UNIVERSITY OF
LEICESTER

# Evaluating $CH_4$ Concentrations and Emissions in the Amazon Basin Using the Greenhouse Gases Observing Satellite and Dedicated $CH_4$ Models

Thesis submitted for the degree of
Doctor of Philosophy at the
University of Leicester

by

Alex James Webb

Department of Physics and Astronomy

30th September 2016

| | |
|---|---|
| Supervisor: | Hartmut Bösch |
| Second Supervisor: | Roland Leigh |

# ABSTRACT

## Evaluating $CH_4$ Concentrations and Emissions in the Amazon Basin Using the Greenhouse Gases Observing Satellite and Dedicated $CH_4$ Models

Alex James Webb

Natural wetlands, such as those in the Amazon, are important sources of methane ($CH_4$), which is the second most important anthropogenic greenhouse gas in terms of radiative forcing. With a short atmospheric lifetime compared to carbon dioxide, reductions in $CH_4$ emissions have the potential to mitigate global warming on much faster time scales. Currently, our understanding of these emissions is limited, with considerable disagreement between modelled wetland emissions estimates. Satellites can provide $CH_4$ observations with high coverage and density that can provide the required observational constraints to improve $CH_4$ emission estimates, especially for regions where in situ observations are sparse, such as the Amazon. In this thesis, I have carried out the first validation of $CH_4$ from the GOSAT satellite using a series of dedicated aircraft in situ profile measurements demonstrating the high quality of GOSAT $CH_4$ observations for this region. I have then used the satellite observations in conjunction with the aircraft profiles to investigate the characteristics of $CH_4$ emissions from wetlands in the Amazon and their representation in state-of-the-art emissions inventories when combined with a chemical transport model. GOSAT observes large methane enhancements of up to 60 ppb between the wet and dry seasons in the Amazon coinciding with large Amazonian wetlands which are underestimated by approximately 15 ppb by models, pointing towards clear shortcomings in the inventories. To further assess the regional $CH_4$ emissions, a simulation system has been developed using a regional transport model based on a high resolution representation of atmospheric transport. This framework allows quick comparisons of different emissions inventories to GOSAT $XCH_4$ on regional scales while giving a better representation of transport compared to global transport models. An assessment against global models and GOSAT data has shown that the model performs well and often agrees better with GOSAT than the global models do.

# PUBLICATIONS

A. J. Webb, H. Bösch, R. J. Parker, L. V. Gatti, E. Gloor, P. I. Palmer, L. S. Basso, M. P. Chipperfield, C. S. C. Correia, L. G. Domingues, L. Feng, S. Gonzi, J. B. Miller, T. Warneke and C. Wilson, (2016). "$CH_4$ concentrations over the Amazon from GOSAT consistent with in situ vertical profile data". *Journal of Geophysical Research: Atmospheres*, *121*, doi:10.1002/2016jd025263.

R. J. Parker, H. Bösch, M. J. Wooster, D. P. Moore, A. J. Webb, D. Gaveau, and D. Murdiyarso, (2016), "Atmospheric $CH_4$ and $CO_2$ enhancements and biomass burning emission ratios derived from satellite observations of the 2015 Indonesian fire plumes", *Atmos. Chem. Phys.*, *16*, 10111-10131, doi:10.5194/acp-16-10111-2016.

R. J. Parker, H. Bösch, K. Byckling, A. J. Webb, P. I. Palmer, L. Feng, P. Bergamaschi, F. Chevallier, J. Notholt, N. Deutscher, T. Warneke, F. Hase, R. Sussmann, S. Kawakami, R. Kivi, D. W. T. Griffith, and V. Velazco, (2015), "Assessing 5 years of GOSAT Proxy $XCH_4$ data and associated uncertainties", *Atmos. Meas. Tech.*, *8*, 4785-4801, doi:10.5194/amt-8-4785-2015.

L. Feng, P. I. Palmer, H. Bösch, R. J. Parker, A. J. Webb, L. G. Domingues, C. S. C. Correia, N. M. Deutscher, D. G. Feist, L. V. Gatti, E. Gloor, F. Hase, R. Kivi, Y. Liu, I. Morino, R. Sussmann, K. Strong, O. Uchino, J. Wang, and A. Zahn, (Submitted 2016), "Consistent regional fluxes of CH4 and CO2 inferred from GOSAT proxy XCH4:XCO2 retrievals, 2010-2014", *Under review: Atmos. Chem. Phys.*.

# ACKNOWLEDGEMENTS

This PhD was funded by the Natural Environment Research Council, NERC.

I would like to thank my supervisor Hartmut Bösch as well as Robert Parker for their help and guidance throughout my studies.

Also, a big thank you to everyone involved with the ACO project, in particular to Luciana Gatti, Manuel Gloor, Caio and Lucas for allowing me the opportunity to work with them in Brazil for two months, and for their brilliant hospitality and friendship during my stay.

I would also like to thank all of the postdocs, the other postgraduate students and the administration staff within the Earth Observation Science group who have often assisted me and who have helped to make my studies enjoyable. With particular mention to Mike Perry, Alex Geddes and Peter Somkuti.

Also, thank you to all of my friends in the wider postgraduate community within the Physics and Chemistry Departments, and to my flatmates Stuart, Matthew and Charlie who have helped to made my time in Leicester memorable.

Finally, I would like to thank my parents for their support over my many years of study.

# DECLARATION

I hearby declare that no part of this thesis has been previously submitted to this or any other University as part of the requirement for a higher degree. The work described herein was conducted by the undersigned except for contributions from colleagues as acknowledged in the text.

Alex J. Webb
September 30, 2016

# CONTENTS

**Abstract** i

**Publications** ii

**Acknowledgements** iii

**Declaration** iv

**1 Introduction** 1
- 1.1 Effects of climate change . . . 1
  - 1.1.1 Atmospheric structure . . . 4
  - 1.1.2 Atmospheric temperature profile . . . 5
- 1.2 Radiative forcing . . . 7
- 1.3 Thesis outline . . . 10

**2 Atmospheric Methane** 14
- 2.1 Introduction to atmospheric methane . . . 14
- 2.2 Methane sources . . . 15
  - 2.2.1 Wetland emissions . . . 17
  - 2.2.2 Landfill, sewage and waste emissions . . . 21
  - 2.2.3 Emissions from ruminants and termites . . . 21
  - 2.2.4 Emissions from ocean and permafrost hydrates . . . 22
  - 2.2.5 Fossil $CH_4$ emissions . . . 23
  - 2.2.6 Biomass burning emissions . . . 25
  - 2.2.7 Direct emissions from trees . . . 26
- 2.3 Methane sinks . . . 26
- 2.4 Atmospheric $CH_4$ trends . . . 29

**3 Satellite Remote Sensing** 32
- 3.1 Basics of remote sensing . . . 32
- 3.2 Atmospheric Absorption . . . 34
- 3.3 Atmospheric Scattering . . . 36
  - 3.3.1 Scattering and absorption due to aerosols . . . 36
  - 3.3.2 Atmospheric transfer applied to a single particle . . . 37
  - 3.3.3 Atmospheric transfer on a column of aerosol . . . 40
  - 3.3.4 Radiative transfer in the atmosphere . . . 45
  - 3.3.5 Non-scattering atmosphere . . . 46
- 3.4 Surface reflectance . . . 47
- 3.5 The role of satellites in $CH_4$ measurements . . . 48
- 3.6 The GOSAT Satellite . . . 51
  - 3.6.1 Operational changes and status since launch . . . 53

3.7 University of Leicester GOSAT retrieval algorithms . . . . . 58
3.7.1 Optimal estimation retrieval . . . . . 58
3.7.2 UoL full physics retrieval . . . . . 63
3.7.3 Leicester Proxy $XCH_4$ retrieval . . . . . 64
3.8 Validation with ground-based measurements . . . . . 65

**4 Validation of GOSAT $XCH_4$ in the Amazon Using in situ Aircraft Measurements 68**
4.1 Introduction . . . . . 68
4.2 Aircraft Data . . . . . 69
4.3 Differences between Rio Branco and Salinópolis . . . . . 71
4.4 AMAZONICA flights . . . . . 73
4.5 Calculation of aircraft total column $XCH_4$ . . . . . 75
4.5.1 Extension of aircraft profiles in the troposphere . . . . . 76
4.5.2 Extension of aircraft profiles in the stratosphere . . . . . 77
4.5.3 Conversion between altitude and pressure . . . . . 83
4.5.4 Final calculation and application of averaging kernels . . . 86
4.6 Error Analysis . . . . . 89
4.7 Extended Aircraft and GOSAT $XCH_4$ Comparison . . . . . 96
4.7.1 GOSAT model $XCO_2$ . . . . . 96
4.7.2 GOSAT-Aircraft comparison . . . . . 97
4.7.3 Seasonal differences in $XCH_4$ . . . . . 103
4.7.4 Co-location criteria . . . . . 104
4.8 Assessing the Impact of the Model $XCO_2$ . . . . . 106
4.9 Paramaribo-FTS Comparisons with GOSAT . . . . . 111
4.10 Conclusions . . . . . 113

**5 Using GOSAT $XCH_4$ and in situ Data to Assess Emissions Inventories Within a Chemistry Transport Model 115**
5.1 Introduction . . . . . 115
5.2 Modelled $XCH_4$ in the Amazon . . . . . 116
5.3 Comparing GEOS-Chem with the Aircraft Profiles . . . . . 117
5.4 Interpreting GOSAT $XCH_4$ Concentrations . . . . . 123
5.4.1 Examining GOSAT $XCH_4$ in the Amazon . . . . . 123
5.5 Comparisons between GOSAT and GEOS-Chem in the Amazon . . 133
5.6 Conclusions . . . . . 153

**6 Development of a High-resolution Regional Transport Model for the Amazon to Evaluate $CH_4$ Emissions Inventories 155**
6.1 Introduction . . . . . 155
6.2 Numerical Atmospheric-dispersion Modelling Environment . . . 156
6.3 NAME model simulation overview and set-up . . . . . 157
6.3.1 Modelling wind directions . . . . . 159
6.3.2 Background calculation . . . . . 161
6.3.3 Emission inventories . . . . . 163
6.3.4 Calculating $CH_4$ enhancements . . . . . 170
6.4 Results . . . . . 171

6.4.1 Comparisons with GOSAT and models . . . . . 173
6.4.2 Regional differences . . . . . 176
6.4.3 MACC-II Enhancements . . . . . 179
6.5 Conclusions . . . . . 182

**7 Conclusions and Future Work** **185**
7.1 Future work . . . . . 190

**List of Figures** **I**

**List of Tables** **XXIII**

**References** **XXV**

# 1 INTRODUCTION

## 1.1 EFFECTS OF CLIMATE CHANGE

The Earth's climate is defined by the state of many meteorological variables including the temperature, humidity, aerosol and cloud distribution, atmospheric pressure, wind profile and precipitation. The state of these variables can describe the weather on a local scale at variable time scales, whilst the climate itself is defined over a much longer scale of approximately several decades. Climate change refers to the change of any one of these meteorological variables over a long time scale. As a result it is often difficult to confidently claim that the climate is changing without a long record of measurements to draw conclusions from.

Climate change has been identified in many different data records, each with potentially far reaching consequences. One of the most evident of these is the change in global mean temperature. Between 1880 and 2012 global average surface temperature increased by between 0.65°C and 1.06°C and the rate of this increase continues to rise (Stocker et al., 2013). Figure 1.1 shows how the global mean land-ocean temperature has changed since 1880 with respect to a 1951-1980 base period. This increase in global mean temperature is observable in many secondary effects, not just by direct measurements of atmospheric temperature itself. Polar ice caps and glaciers have been melting and their coverage area is getting smaller after refreezing each year (Comiso et al., 2011). The global mean sea level is also rising steadily due to thermal expansion as a result of the increase in temperature (McKay, Overpeck, and Otto-Bliesner, 2011). This global warming is overwhelmingly believed to be a result of human activi-

ties with approximately 97% of publishing climate scientists in agreement (Cook et al., 2016).

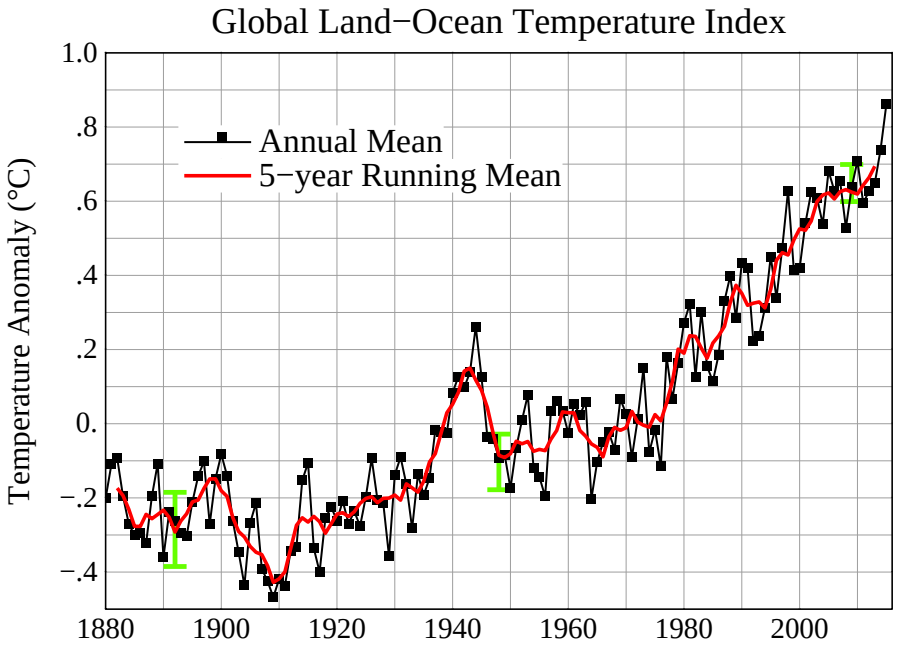


**Figure 1.1:** Global mean land-ocean temperature since 1880, with respect to a 1951-1980 base period. The dotted black line shows the annual mean, the solid red line shows a five year mean, and the green bars show the uncertainty estimate. Data is from the GISS (Goddard Institute for Space Studies) Surface Temperature Analysis (GISTEMP) project (`http://data.giss.nasa.gov/gistemp/`).

Global warming is predicted to have many wide reaching consequences on the planet and the human race with average global temperatures likely to increase by 1-2°C by 2050 and 3-4°C by 2100 (relative to the year 2000). An even larger increase is predicted at high northern latitudes (6-7°C) (McMichael, 2013). Global warming is very likely to increase precipitation in high latitudes, whilst decreasing it throughout the tropics, and it is widely predicted that as the Earth warms the variability of weather patterns will increase, causing extreme events to become more frequent (Thornton et al., 2014). This will increase the number of droughts, fires and flooding events and will lead to many other adverse effects which are expected to have a larger impact on climate than the increases in mean variables alone (Thornton et al., 2014).

The increased frequency of extreme events will have an increasing impact on global economies as the cost in damages due to large weather events (such as storms and flooding) and climate events (such as fires and droughts) have increased eightfold between the 1960s and 1990s, with the cost of extreme weather events in the United States between 1980 and 2004 amounting to 1.4 trillion dollars alone (Thornton et al., 2014). The percentage of land between 60°S and 75°N defined as dry has risen from approximately 17% in the 1950s to 27% in the 2000s, and it is predicted that with rising temperatures, regions such as the United States might see persistent droughts in the next 20-50 years (Dai, 2011). Increases in maximum temperatures are likely to cause severe reductions in the yield of many crops. In drought conditions for example, for each degree day spent above 30°C the yield of maize reduces by 1.7%, whilst rice yields can be reduced by 90% with night temperatures of 32°C compared to their preferable 27°C (Thornton et al., 2014). Decreased animal feed quality and yield due to droughts could also lead to the reduction of livestock populations, with 1.8 million cattle likely to be lost in Kenya alone by 2030 due to an increase in drought frequency (Thornton et al., 2014).

Whilst rainfall is expected to increase globally, it will decrease in the tropics, which coupled with the increased drought frequency will increase freshwater scarcity in these regions in the future. This is expected to affect half of the world's population by 2050 (Rockström et al., 2009). As well as through water scarcity, climate change also poses many other risks on human health. The frequency of heat waves and their magnitude continue to increase, which can be dangerous for the sick and elderly. Many infectious diseases are also highly dependent on precipitation and temperature and it is thought that there could be more epidemics as habitats change and disease carrying mechanisms are able to exist in new regions (Thornton et al., 2014). As some crop yields are expected to struggle there are also health issues associated with getting the nutritional diversity needed from our food, as well as maintaining the number of calories required to stay healthy. Finally, as extreme climate and weather events become more likely, so do issues with human displacement from disasters which often result in relo-

cation in poor and crowded conditions which have negative consequences on health.

In addition to climate and weather variables, as the planet warms, glaciers and sea ice coverage diminish, directly threatening Arctic ecosystems, rising global sea levels and altering the amount of freshwater entering the oceans. It is predicted, based on several different warming magnitudes, that sea levels may rise from anything between 0.26 and 0.98 metres by the year 2100 (Stocker et al., 2013), whilst a complete melting of Antarctic ice sheets could rise sea levels by 17 m within several hundred to a few thousand years (Pollard, DeConto, and Alley, 2015). If global temperatures are to rise by 2°C above pre-industrial temperatures, which is now increasingly likely (Peters et al., 2013), it is estimated by Schaeffer et al. (2012) that sea levels will rise by 75-80 cm. These rises pose a significant threat to coastal and low-lying regions, especially in developing countries where funds to build the necessary flood prevention infrastructure are unavailable.

### 1.1.1 Atmospheric structure

The Earth's atmosphere is comprised of primarily four different gases which make up 99.98% of the air by volume. These are nitrogen (78.08%), oxygen (20.98%), argon (0.93%) and carbon dioxide (0.035%). Neon (0.0018%), helium (0.0005%), hydrogen (0.00005%), krypton (0.001%) and xenon (0.00009%) also exist constantly in the atmosphere (Barry and Chorley, 1992) and all of these gases are well mixed from the surface up to 80 km. Methane is another important gas, comprising 0.0017% of the total atmosphere and is primarily found towards the surface, whilst ozone (0.00006%) is also important but, is primarily found much higher in the atmosphere.

### 1.1.2 Atmospheric temperature profile

The temperature of the Earth's atmosphere contains much variability based on many different factors. The local climate, weather, water vapour content, sunlight exposure and surface properties cause much variation at the surface and dictate how the lower layers of the atmosphere vary with temperature, but above these layers the temperature profile behaves in a more structured manner. Typically the atmosphere firstly cools with ascending altitude, before heating again due to ozone, then cooling for a second time and finally heating again in the upper most layers. This distinct profile allows us to classify the atmosphere into four main parts which we name (in ascending order), the troposphere, stratosphere, mesosphere and thermosphere. Between each of these layers is a region where the temperature lapse rate temporarily halts and the temperature is stable. These regions are named the tropopause (between the troposphere and stratosphere), the stratopause (between the stratosphere and mesosphere), and the mesopause (between the mesosphere and thermosphere). An example temperature profile with these four regions and three separating layers is shown as Figure 1.2. Above the thermosphere is the exosphere which is more than 100 km above the surface and where the pressure is low enough to be defined as the boundary between the Earth's atmosphere and outer space.

At the surface the troposphere typically ranges from 8 km over the poles to approximately 16 km over the equator (`www.weather-climate.org.uk`) and sees a decrease in temperature with altitude until the tropopause where temperatures stop decreasing and above which they begin to increase again. The troposphere contains the majority of the Earth's weather systems and can be very variable and turbulent as the diurnal cycle heats the surface each day (if not at the winter poles) and subsequently releases much of this heat into the lower atmosphere. This warmer air rises by convection but struggles to reach above the tropopause where temperatures begin to increase and halt the convection process, causing most weather to be confined to the troposphere. This limit at the tropopause varies depending on season and latitude and can contain approximately 80% of

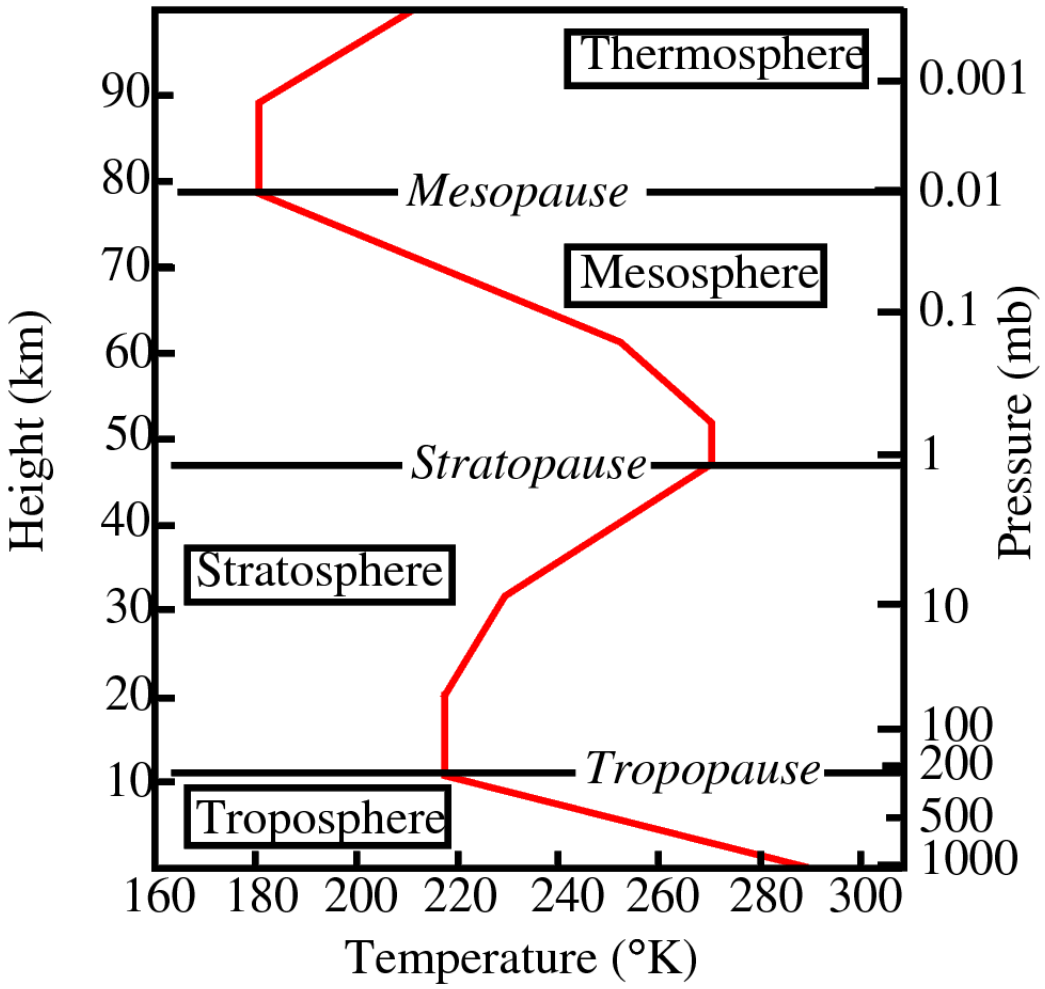


**Figure 1.2:** A graph showing a typical atmospheric temperature profile in Kelvin from the surface to 100 km altitude. The plot also displays the pressure profile in mb, ranging from approximately 0 mb at the top of the atmosphere to approximately 1000 mb at the surface. The profile is split into four parts which are named in boxes, whilst the names for the three transitions are written at these levels in italics (Image source `www.atmos.washington.edu/~hakim/301/climo_sounding.png`).

the mass of the atmosphere and up to 99% of the water vapour in the atmosphere (Keesee, 2014).

Above the tropopause lies the stratosphere which extends up to approximately 50 km above the surface. This region is stable compared to the troposphere and sees temperatures gradually increase with altitude due to the presence of ozone. Approximately 90% of the ozone in the atmosphere resides in the stratosphere where it absorbs incoming solar radiation in the ultra-violet region of the spectrum (290 nm to 320 nm), causing the atmosphere to heat up. Above the stratopause lies the mesosphere where temperatures begin to decrease from

50 km in altitude because this is above the ozone layer, and because of strong radiative cooling from carbon dioxide. This occurs up to approximately 80 km where the atmosphere is at its coldest at the mesopause. Above this is the thermosphere which extends from approximately 80 km to 500 km depending on solar activity, and here the pressure is very low and the particles are far apart. Due to this the temperature can increase dramatically as incoming solar radiation can be absorbed by these few particles, causing large increases in the average kinetic energy per particle. Temperatures in the thermosphere can reach up to 2000 K depending on the strength of the solar activity (Keesee, 2014). A fifth layer of the atmosphere can be defined above the thermosphere (at the exobase), called the exosphere, which extends to the edge of the solar wind where particles are no longer dominated by Earth's gravity.

## 1.2 RADIATIVE FORCING

To understand the processes that contribute to the increase in global temperature it is necessary to consider the Earth's radiative forcing balance. Radiative forcing is a number which, depending on the sign, defines whether the overall effect of a driver in the Earth-Atmosphere system has a net warming or cooling effect on the Earth. It is defined as, "The change in net (down minus up) irradiance (solar plus long-wave; in $\mathrm{Wm}^{-2}$) at the tropopause after allowing for stratospheric temperatures to readjust to radiative equilibrium, but with surface and tropospheric temperatures and state held fixed at the unperturbed values" (Schulz et al., 2006). This radiative forcing is a useful parameter because it directly characterises the way in which a given substance will change the equilibrium surface temperature of the planet. The change in temperature ($\Delta T_s$) is defined mathematically as the instantaneous radiative forcing (RF) multiplied by a factor ($\lambda$), the climate sensitivity factor (Equation (1.1)) with units $^{\circ}\mathrm{C}(\mathrm{W\,m}^{-2})^{-1}$. If a driver has a positive radiative forcing value then the substance has a net positive energy flux on the Earth, causing a net heating of the Earth; whilst a neg-

ative radiative forcing relates to a cooling of the Earth. Figure 1.3 shows the radiative forcing budget for many important atmospheric sources, as well as from land use change and solar irradiance changes. The effective radiative forcing can also be defined as the change in net downward radiation from the top of the atmosphere, after the initial adjustment of atmospheric temperatures, clouds and moisture, but before surface temperatures have responded (Schuckmann et al., 2016). This accounts for radiative feedback which the instantaneous RF cannot.

$$\Delta T_s = \lambda * \mathrm{RF}. \tag{1.1}$$

Figure 1.3 shows that the total net radiative forcing due to well mixed greenhouse gases (GHGs) is 2.83 $\mathrm{Wm}^{-2}$ with the contribution due to carbon dioxide ($CO_2$) the largest single source (1.68 $\mathrm{Wm}^{-2}$), followed by methane ($CH_4$) with 0.97 $\mathrm{Wm}^{-2}$. These greenhouse gases, along with halocarbons, $N_2O$, CO, VOCs (volatile organic compounds), $NO_x$, $SF_6$, HFCs (hydrofluorocarbons) and PFCs (perfluorocarbons), generally increase radiative forcing. Greenhouse gases in the atmosphere increase global temperature because they 'trap' energy by the greenhouse effect. Incoming ultra-violet and visible solar radiation is not absorbed by these gases and passes through the atmosphere to the surface where it is absorbed and re-emitted in the thermal and near infra-red. These wavelengths are absorbed by greenhouse gases, preventing this energy from leaving the Earth-atmosphere system and instead warming the climate.

Aerosols generally have a negative radiative forcing as they reflect a lot of the incoming radiation, instead of absorbing it and heating the planet, (with the exception of black carbon aerosol which does absorb and therefore has a positive radiative forcing effect). Aerosols act on radiative forcing with three different effects, named the direct, indirect and semi-direct aerosol effects. The direct aerosol effect is determined by the scattering and absorbing of radiation 'directly' by the aerosol particles themselves. The indirect and semi-direct aerosol effects instead consider further factors.

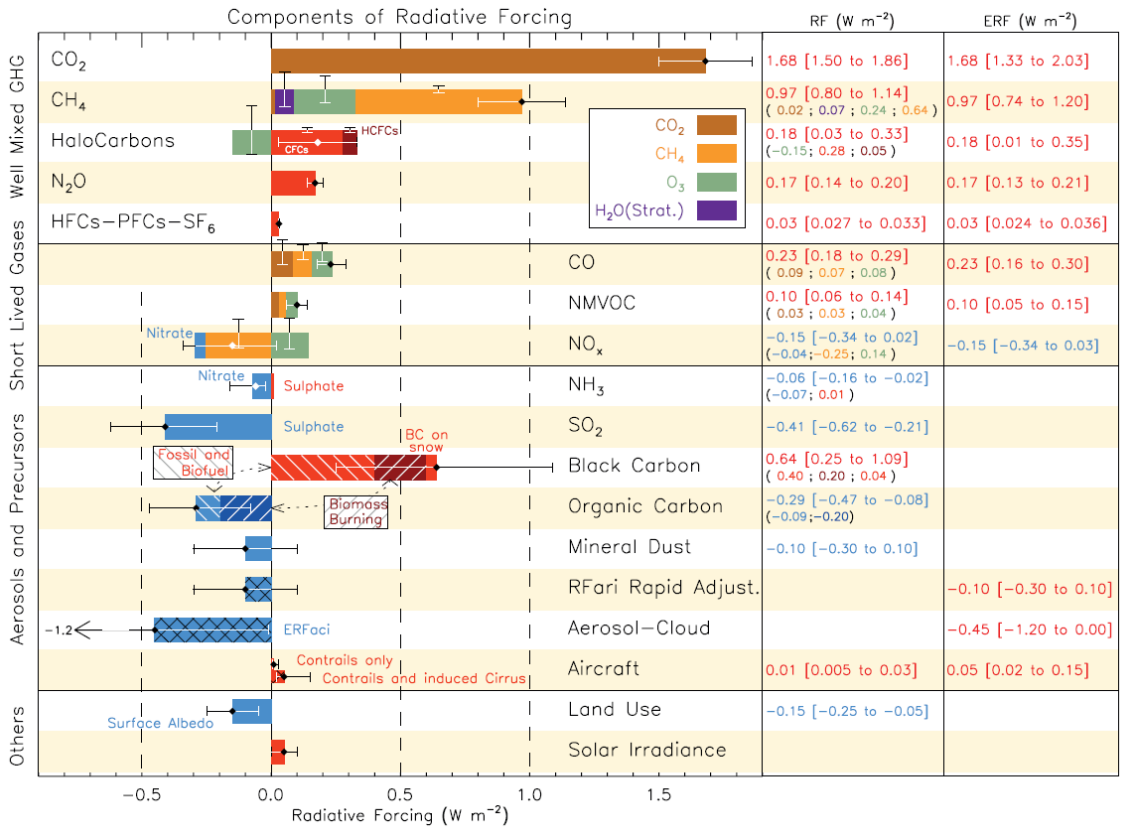


**Figure 1.3:** The radiative forcing (RF) in W m$^{-2}$ of climate change during the Industrial Era (1750 to 2011) for separate components including carbon dioxide ($CO_2$), methane ($CH_4$), nitrogen dioxide ($N_2O$), hydrofluorocarbons (HFCs), perfluorocarbons (PFCs), sulphur hexafluoride ($SF_6$), carbon monoxide (CO), non-methane volatile organic compounds (NMVOCs), ammonia ($NH_3$), sulphur dioxide ($SO_2$), ozone ($O_3$) and water vapour ($H_2O$). Horizontal bars indicate the overall uncertainty (90% confidence) whilst vertical bars are for individual components (vertical bar lengths proportional to the relative uncertainty, with the total length equal to the bar width for a $\pm$50% uncertainty). The ERF column shows the effective radiative forcing due to aerosol-cloud interactions (Stocker et al., 2013).

The first indirect effect, or the 'cloud albedo effect', is where certain aerosols (such as sulphates) are effective cloud condensation nuclei and attach themselves to the water droplets within clouds. This then causes the number of water droplets within the cloud to increase, making each droplet smaller in order to maintain the same mass of water overall in the cloud. As a result this increases the optical depth and the albedo of the cloud because more droplets overall means the water surface area within the cloud has increased, allowing the cloud to reflect more radiation. Increasing the albedo and optical depth of clouds will increase the amount of incoming radiation reflected back out to space and ul-

timately will cause a cooling effect on the climate system. The second way in which aerosols can affect clouds is via the second indirect effect, which is named the cloud lifetime effect. This is another result of some aerosols being cloud condensation nuclei and causing clouds to form with smaller water droplets because these smaller droplets will reach slower terminal velocities and take longer to coalesce and form precipitation. As a result, affected clouds will retain higher liquid water content for longer and will therefore have longer lifetimes. These high albedo, long lasting clouds will therefore have a considerable affect on radiative forcing compared to normal clouds; causing a significant cooling effect on the atmosphere and the planet as a whole (Boucher et al., 2013).

The semi-direct aerosol effect is caused by black carbon aerosols which absorb more radiation than they scatter. This causes the aerosols to heat the surrounding troposphere, decreasing the humidity and therefore evaporating clouds. This decrease in cloud cover will decrease the amount of radiation scattered away from the Earth by clouds in total, therefore increasing radiative forcing. However, this effect is much less important than the indirect effect because the aerosols responsible for increasing cloud lifetime (and hence cloud cover) are more numerous than those responsible for decreasing it, meaning the net effect of the indirect and semi-direct effects is negative over most parts of the Earth (Boucher et al., 2013).

## 1.3 THESIS OUTLINE

In this thesis, I concentrate on the important greenhouse gas, methane. Chapter two discusses the importance of this gas, introduces the sources and sinks of methane and details how its concentration in the atmosphere has changed throughout history. In this Chapter I illustrate the importance of tropical wetland emissions and highlight how there is currently large disagreement regarding the magnitude and distribution of these emissions in current modelled predictions. Starting in Chapter three, I discuss the basics of remote sensing and

describe how satellites can be used to infer the concentration of atmospheric constituents by the use of absorption spectroscopy. I then introduce the GOSAT satellite, the details of its operation, and how the University of Leicester GOSAT retrieval algorithms are designed to estimate methane and carbon dioxide concentrations using an optimal estimation approach and a forward model. Chapter three concludes with a review of GOSAT validation studies and highlights how there is a lack of validation in the tropics, a region which is very important for methane sources.

In Chapter four I present my work from Webb et al. (2016), detailing the first validation study of GOSAT $XCH_4$ in the Amazon. I use in situ measurements from five sites across the Amazon, two of which are part of a campaign which is led by the University of Leicester (ACO project). The two sites were chosen to best represent air before and after travelling across the Amazon basin, with the intention of comparing the two sites to glimpse insights into methane emissions within the Amazon. I also utilise data from a separate campaign of three additional sites (and one which is at the same location as the ACO campaign). These additional flights have a maximum measurement altitude of approximately 4.5 km, whilst the ACO flights reach 7.5 km. The chapter begins by discussing these different aircraft campaigns, looking at the data and seeing how the profiles compare at each site. I then detail the method with which these aircraft profiles are extended and compared with GOSAT measurements, including a full error analysis of the method and exploration of different co-location criteria. The chapter concludes with the results of this comparison and also includes comparisons of $XCH_4$ between GOSAT and a ground-based instrument at Paramaribo in Suriname, which are bought into context with the aircraft-GOSAT comparisons. The main aims of Chapter four are:

- To verify the choice of aircraft measurement sites.
- To determine whether 7.5 km flights provide a worthwhile benefit over (cheaper) 4.5 km flights for the purpose of satellite validation.

- To develop a method for comparing aircraft and GOSAT methane measurements with only small uncertainties introduced so as to provide meaningful validation.
- To validate GOSAT with the aircraft data and determine whether or not GOSAT $XCH_4$ is reliable over the Amazon.

In Chapter five I compare the newly validated GOSAT methane data with the state-of-the-art atmospheric chemistry model GEOS-Chem. $XCH_4$ models in the Amazon, much like GOSAT, have not been extensively validated with in situ data. The chapter begins by introducing the model and comparing it with the extended aircraft profiles. I then examine the large scale patterns of $XCH_4$ which are observed in the Amazon by both GOSAT and GEOS-Chem. The main aims of Chapter five are:

- To validate the state-of-the-art atmospheric chemistry model GEOS-Chem with the extended in situ aircraft profiles in the Amazon for the first time.
- To investigate the behaviour of $XCH_4$ in the Amazon as observed by GOSAT, to learn about the large-scale patterns of $XCH_4$ over multi-year time scales.
- To compare GOSAT measurements with the GEOS-Chem model output to learn where the model is performing well compared to GOSAT, and where there are disagreements.

In Chapter six I detail the development of a high-resolution regional transport model which I use to evaluate methane emission inventories in the Amazon. I introduce the numerical atmospheric-dispersion modelling environment (NAME), which I use to model the transport of $CH_4$ in the Amazon; the emissions inventories, which I use to calculate enhancements of $CH_4$ within the Amazon basin; and the MACC-II model which I use to calculate a background $XCH_4$ concentration. After describing the set-up of the model, I then use the same emissions inventories as the GEOS-Chem model and assess the quality of my model's outputs verses the GEOS-Chem data at GOSAT sounding locations.

Furthermore, I compare the outputs from my simulation system with the MACC-II model (which assimilates in situ data). The main aims of Chapter six are:

- To develop a simulation system which is able to quickly and simply input any emission database and produce high resolution atmospheric $XCH_4$ data at a regional scale that can be assessed against satellite data.
- To test the simulation system by using the same emissions inventories as the GEOS-Chem model and comparing the results with both the GEOS-Chem model and with GOSAT $XCH_4$.
- To verify to what extent my model is able to reproduce the regional variation of $XCH_4$ throughout the Amazon basin, as opposed to simply reproducing the background concentrations which are input into the model.

Chapter seven comprises a summary of conclusions throughout the thesis and aims to bring these all together to evaluate $CH_4$ concentrations and emissions in the Amazon basin. The chapter concludes with a look at the future of $XCH_4$ satellite remote sensing in the Amazon and discusses where the work presented in this thesis could be improved upon by future developments.

# 2 ATMOSPHERIC METHANE

## 2.1 INTRODUCTION TO ATMOSPHERIC METHANE

Methane ($CH_4$) is the second most important anthropogenic greenhouse gas in the atmosphere in terms of its radiative forcing effect (after carbon dioxide, $CO_2$) (IPCC 2013 report chapter 6 (Ciais et al., 2014)). It is responsible for about one-fifth of the increase in radiative forcing by human-linked greenhouse gases since 1750 (Nisbet, Dlugokencky, and Bousquet, 2014), which is considered to be the onset year of the industrial revolution. Since these pre-industrial times, the globally averaged dry air mole fraction of $CH_4$ had increased by a factor of 2.5 by 2009 (from approximately 700 ppb (parts per billion) to 1794 ppb) (Dlugokencky et al., 2011), and as of March 2017 reached 1848 ppb [Ed Dlugokencky, NOAA/ESRL (`www.esrl.noaa.gov/gmd/ccgg/trends_ch4/`), 2017]. $CH_4$ is a stronger absorber of radiation than $CO_2$ per molecule, and over a 20 year period a given mass of $CH_4$ in the atmosphere would trap 86 times as much heat as the same mass of $CO_2$ (Ciais et al., 2014). As well as being a strong greenhouse gas, $CH_4$ contributes towards the formation of surface ozone and directly influences water formation in the stratosphere. The lifetime of $CH_4$ in the atmosphere is approximately 9 years (Dlugokencky et al., 2011). Since this is relatively short in comparison to $CO_2$, reductions in its emissions would quickly benefit the climate and help to mitigate global warming sooner than changes to $CO_2$ emissions could (Dlugokencky et al., 2011). Anthropogenic emissions account for approximately 50–60% of all $CH_4$ emissions, whilst emissions from natural wetlands are the main drivers of the global interannual variability of emissions (Ciais et al., 2014). In this chapter the sources and sinks of $CH_4$ to the atmosphere are presented, and

in particular the Amazonian wetland emissions are detailed, which are relevant to the work in this thesis. The trends in $CH_4$ are also discussed.

## 2.2 METHANE SOURCES

In 2011 the total global emission of $CH_4$ is estimated by models to be 556±56 Tg $CH_4$ $yr^{-1}$, whilst the total loss from the atmosphere is estimated to be 542±56 Tg $CH_4$ $yr^{-1}$; resulting in a net atmospheric increase of 14±3 Tg $CH_4$ $yr^{-1}$ (Ciais et al., 2014). Globally there is only a 10% uncertainty on these estimates, however, individual sources and sinks are highly uncertain. $CH_4$ is emitted to the atmosphere from a large range of natural sources which include wetlands, termites, oceans, marine hydrates, mud volcanoes, geological sources, wild animals and wildfires; as well as many anthropogenic sources from energy production, mining, landfills and waste treatment, ruminants, rice agriculture and biomass burning (O'Connor et al., 2010). Approximately 202±35 Tg $CH_4$ $yr^{-1}$ is emitted from these natural sources (Ciais et al., 2014), with the remainder originating from anthropogenic sources. $CH_4$ emissions can be broadly grouped into three categories: biogenic, pyrogenic and thermogenic (Kirschke et al., 2013). Biogenic methane is the most predominant. It is produced by methanogens (methane generating microbes) which are mainly found in anaerobic environments such as rice paddies and natural wetlands, but also the digestive systems of ruminants and termites. Thermogenic methane is formed through geological processes and is considered a fossil fuel, whilst the other, pyrogenic methane, results from the incomplete combustion of biomass and from wildfires (Kirschke et al., 2013). Figure 2.1 from the 2013 IPCC report (Ciais et al., 2014) shows a schematic of the processes involved in the $CH_4$ cycle including their annual fluxes in Tg $CH_4$ $yr^{-1}$ and $CH_4$ reservoirs in Tg $CH_4$; estimated for the time period 2000-2009.

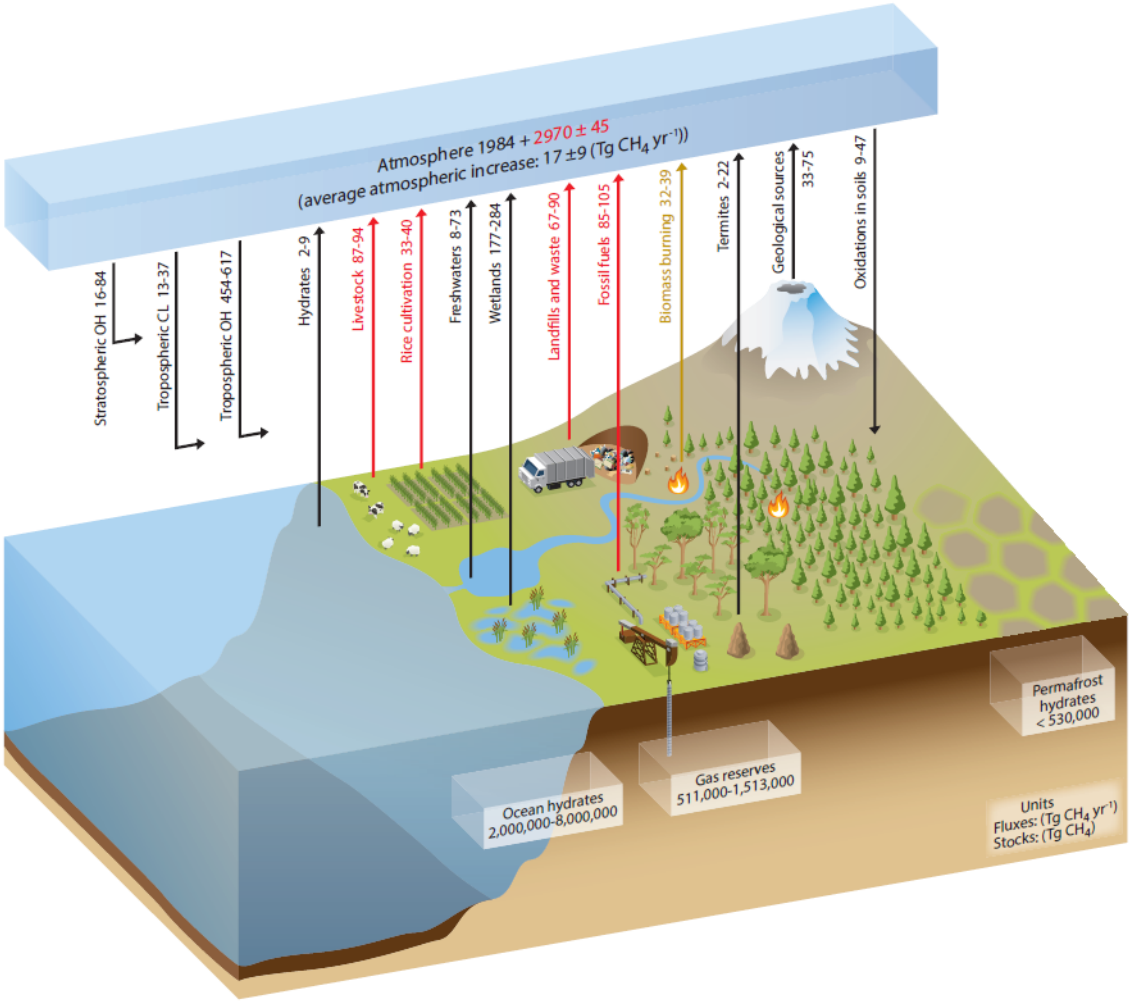


**Figure 2.1:** Schematic showing the fluxes and reservoirs involved with the $CH_4$ cycle in Tg $CH_4$ $yr^{-1}$ and Tg $CH_4$ respectively. These have been calculated for the time period 2000 to 2009. The black arrows denote natural fluxes, the red arrows denote anthropogenic fluxes and the brown arrow represents a combination of both natural and anthropogenic fluxes. The atmospheric reservoir is represented by two numbers; the pre-industrial inventory in black and the increase between 1750 and 2011 given in red (Ciais et al., 2014).

### 2.2.1 Wetland emissions

From Figure 2.1 we can see that the largest single source of $CH_4$ to the atmosphere are natural wetlands, releasing 177 to 284 Tg $CH_4$ each year. The term *wetlands* is used to describe a variety of ecosystems, including swamps, bogs, wet soils and peatlands. $CH_4$ is produced in wetlands by the anaerobic respiration of methanogenic microbes. These methanogens proliferate in aquatic sediments and flooded soils as well as in sewage and landfills (and in the gastrointestinal tracts of animals). In addition to wetlands they can be found in extreme environments which have very high temperatures such as in hot springs or hot vents on the sea floor (Cicerone and Oremland, 1988). The rate of $CH_4$ production in these environments is dependent on a number of factors; particularly on soil temperature and the amount of material available for decomposition, as well as on the position of the water table in the case of wetlands (O'Connor et al., 2010). For these reasons, wetlands are highly susceptible to climate change and the seasonal variabilities of temperature and water volume (Bloom et al., 2010).

Formed under the water surface in anaerobic conditions, this $CH_4$ is transported upwards through diffusion, ebullition (the formation and release of bubbles into the atmosphere) or through the stems of specific plants (O'Connor et al., 2010). Outside of wetlands the non-plant assisted transport still occurs in the water table beneath the surface, however the $CH_4$ is only transported as far as the aerated (non-waterlogged) soils above, and not to the surface. These aerated soils contain methanotrophic bacteria which are highly efficient at oxidising and removing $CH_4$; meaning far less $CH_4$ will reach the surface than in a wetland where this top layer of aerated soil is not present. As a result, most soils emit very little $CH_4$ if the water table is low, and the top layers of soil usually remove more $CH_4$ from the atmosphere than they release, whilst if the water table is high enough or above the surface there is a net $CH_4$ source to the atmosphere.

In many species of wetland plants, the vegetation-assisted pathway for venting $CH_4$ to the surface can allow $CH_4$ to pass directly from the anaerobic soils into

the plant roots, to effectively bypass the above aerobic soils and reach the surface (O'Connor et al., 2010). Recently Pangala et al. (2015) examined stem $CH_4$ emissions from wetland-adapted trees in a temperate wetland and concluded that the $CH_4$ released by trees through the vegetation-assisted venting mechanism contributed a significant amount (up to 27%) to the seasonal flux in the studied wetlands. These tree-assisted emissions are currently not accounted for in trace gas budgets in forested wetlands, but they potentially have an important impact in these ecosystems.

The extent of these wetlands in the Amazon was measured by Hess et al. (2015) using synthetic aperture radar and is shown in Figure 2.2 for the dry season (a.) and wet season (b.). These large differences are partly the reason for the large range in reported wetland emissions.

To a lesser extent, $CH_4$ is also released in freshwater lakes and rivers, as well as in man-made reservoirs. This is done via the same pathways as in wetlands, by ebullition, diffusion and via plant-assisted transport. Bastviken et al. (2011) studied 474 freshwater ecosystems and by up-scaling estimated that 103 Tg $CH_4$ $yr^{-1}$ could be released from these ecosystems, with lakes contributing more than reservoirs and rivers, although they do not give uncertainties for these estimates. The IPCC report quotes a large range for possible $CH_4$ emissions from freshwater lakes and rivers, which could emit between 8 and 73 Tg $CH_4$ $yr^{-1}$. Rice cultivation is also responsible for large $CH_4$ emissions. Rice is a semi-aquatic plant which in agriculture is grown in flooded farmland known as a paddy field. These fields are man-made wetlands and emit $CH_4$ by the same processes as the natural wetlands. It is estimated that these fields emit between 33 to 40 Tg $CH_4$ $yr^{-1}$, of which approximately 90% come from tropical Asia where the fields are most populous (Ciais et al., 2014). A schematic illustrating the different pathways of $CH_4$ release from rice fields is shown as Figure 2.3.

Tropical emissions of $CH_4$ from wetlands have been estimated to be approximately 111 Tg $CH_4$ $yr^{-1}$ (50–60% of the global wetland emissions) from bottom-up models, of which 24% is estimated to have been emitted from Amazonian wetlands (Bloom et al., 2012). These wetlands are typically represented by a mo-

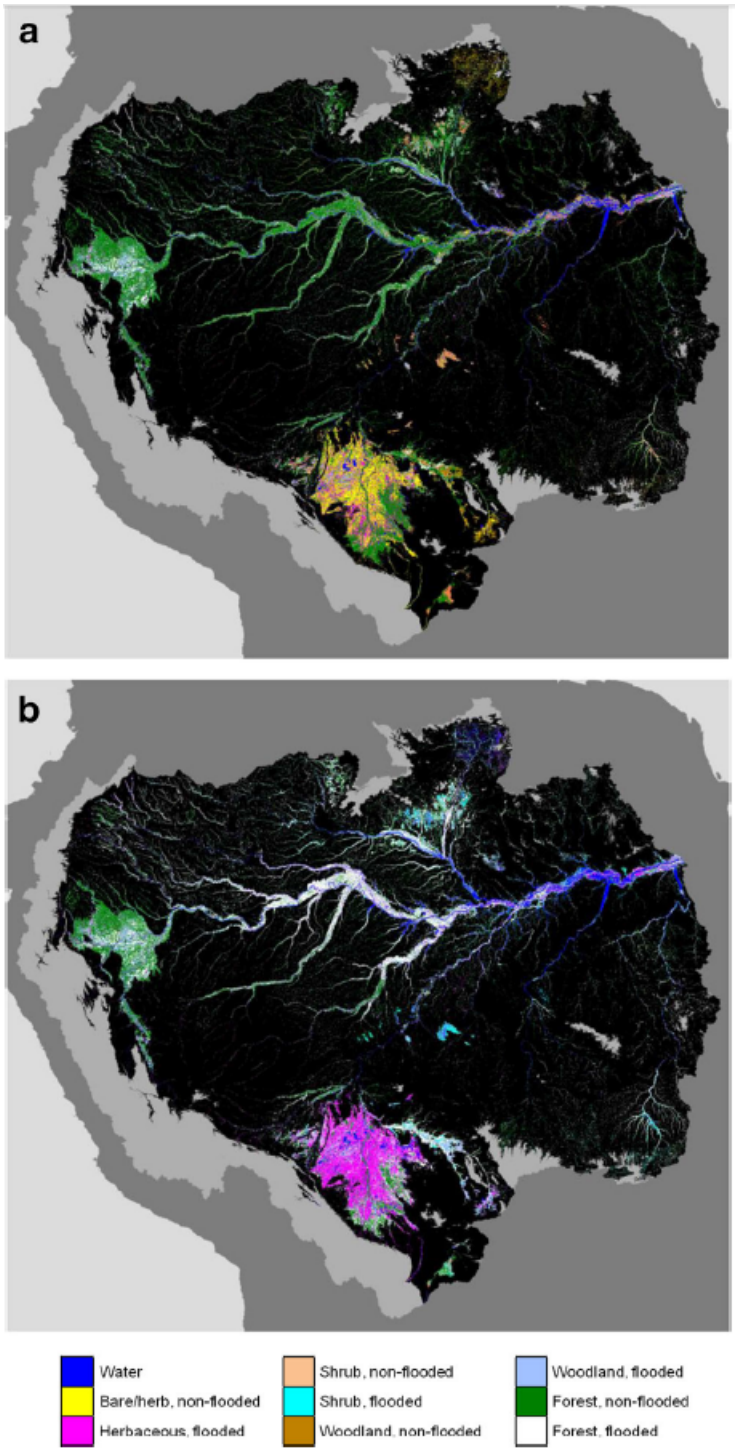


**Figure 2.2:** Amazonian wetland classes mapped during the (a.) dry season (October to November 1995) and the (b.) wet season (May to June 1996) by Hess et al. (2015). Black areas show non-wetland, whilst grey areas show areas within the Amazon Basin which are higher than 500 m in elevation.

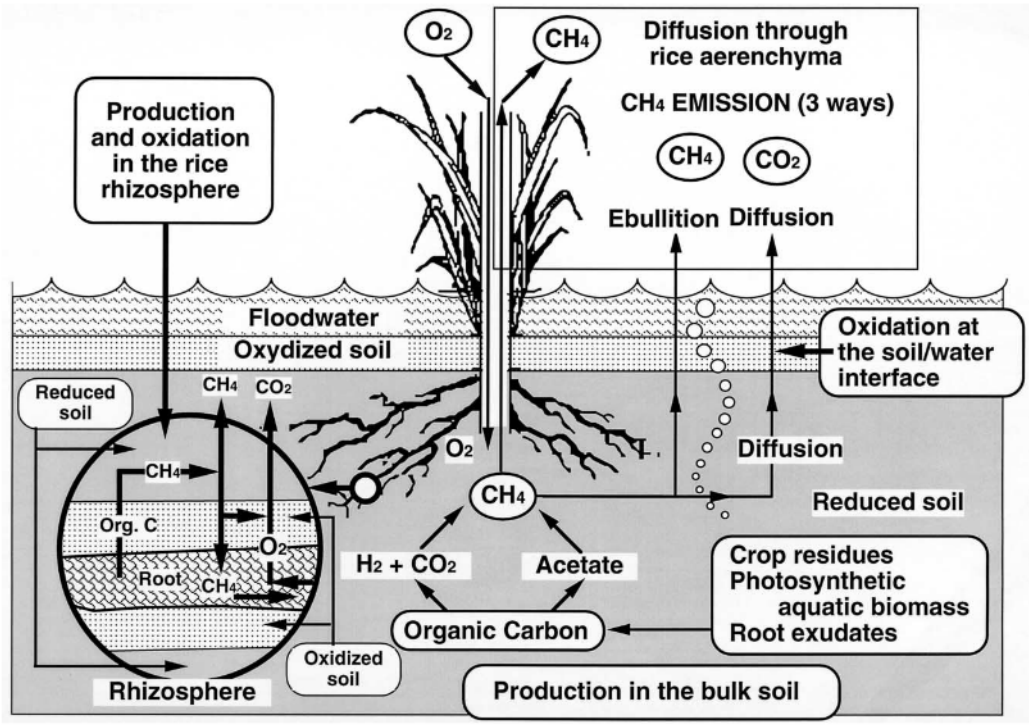


**Figure 2.3:** Schematic showing the production, consumption and transfer of $CH_4$ at the atmosphere in rice fields from Le Mer and Roger (2001) (Figure 1).

saic of lakes and channels (which are open waters), flooded areas, shrublands and woodlands, as well as herbaceous plant communities (Melack et al., 2004). These wetlands exist in depressions which are inundated with water during most of the year. The large range in wetland emissions estimated by models was evaluated by Melton et al. (2013) who compared ten different wetland models of varying complexity and operational methods. They found there to be extensive disagreement between them in their simulations of wetland areal extent and $CH_4$ emissions in both space and time (global $CH_4$ emissions $\pm 40\%$). They further find that atmospheric $CH_4$ observation datasets are inadequate to evaluate typical model fluxes which severely restricts our ability to model global wetland $CH_4$ emissions.

### 2.2.2 Landfill, sewage and waste emissions

Landfills and the waste disposal industry are accountable for 67–90 Tg $CH_4$ released into the atmosphere each year (Ciais et al., 2014). Landfills, livestock manure and waste waters are anaerobic environments where the decomposition of biodegradable organic material by methanogenesis occurs. This process releases $CH_4$ to the atmosphere. The amount of $CH_4$ escaping from a landfill site can vary dramatically from site to site depending on the content and the amount of covering material, if any (Fung et al., 1991).

### 2.2.3 Emissions from ruminants and termites

An important source of $CH_4$ to the atmosphere results from the flatulence and the eructations of animals. Many herbivores feed upon foods which contain a high proportion of cellulose which the majority of animals are unable to break down since they do not produce the required cellulolytic enzymes to do so (Cicerone and Oremland, 1988). As a result many animals, so-called ruminants (sheep, cows, goats, buffalo, deer, elk, camels etc.) have evolved a symbiotic relationship with anaerobic micro-organisms which live within their gastrointestinal tracts. These micro-organisms possess the ability to break down the cellulose into sugars releasing $CH_4$ as a by-product, which in turn is released by the animal's belching. Roughly 30–40% of the gas released is composed of $CH_4$ with the remainder comprising mainly of $CO_2$ with traces of $N_2$, $H_2S$ and $H_2$.

A typical 500 kg domestic cow is capable of producing 200 litres (131.2 g) of $CH_4$ per day (Cicerone and Oremland, 1988), making livestock a considerable source of $CH_4$ to the atmosphere and being responsible for between 87 and 94 Tg $CH_4$ $yr^{-1}$, approximately 16% of the total according to the IPCC report (Ciais et al., 2014). However it is important to consider the contribution of wild ruminants since these were not included in this report, yet they do also provide a source of $CH_4$. Smith et al. (2015) addressed this by considering ruminants and other

$CH_4$ producing variants such as monogastric herbivores, (like elephants, zebras, rhinoceros and warthogs), and concluded that these wild animals could be capable of emitting an additional 3–13 Tg $CH_4$ $yr^{-1}$ depending on estimates for the total numbers of these animals.

Termites are widespread in the tropics and are generally found between 45°N and 45°S. They are found in large communities, or nests, which may range between many sizes both above ground in mount structures or dead trees, or below ground in complex underground networks. Termites typically feed on wood and other organic matter and like ruminants they also have a symbiotic relationship with bacteria in their guts which break down cellulose to produce $CH_4$ (Sanderson, 1996). The flux of $CH_4$ released by termites as shown in Figure 2.1 is estimated to be between 2 and 22 Tg $CH_4$ $yr^{-1}$ (Ciais et al., 2014). One reason for this large uncertainty is that termites emit varying concentrations of $CH_4$ depending on their species, their diet, and on climate variables such as the temperature and humidity (Sanderson, 1996). It is also far harder to accurately estimate the total number and distribution of these animals than for ruminants, due to their abundance in many differing tropical ecosystems and their subterranean habitation where we cannot easily gauge their scale.

### 2.2.4 Emissions from ocean and permafrost hydrates

$CH_4$ exists in large quantities stored in hydrates in deep permafrost and in marine sediments in water depths exceeding 500 m (O'Connor et al., 2010). Hydrates are a type of clathrate, a class of crystalline structures which are formed with an arrangement of *cage-like* structures which trap atoms or molecules within their structure (known as the guest atom or molecule). For hydrates these structures consist of water molecules and on Earth most commonly contain $CH_4$ molecules. This $CH_4$ primarily originates from the breakdown of organic matter, but also from hydrothermal vents at the sea floor. Generally speaking, hydrates are stable at high pressures and low temperatures when there is a high enough concentration of their guest atoms or molecules. Emissions from

hydrates are estimated to be between 2 and 9 Tg $CH_4$ $yr^{-1}$ with estimates of up to 4.5 Tg $CH_4$ $yr^{-1}$ believed to originate from the East Siberian Arctic sheet in permafrost alone (Berchet et al., 2015).

The amount of $CH_4$ thought to be held by ocean hydrates is estimated to be between 2,000,000 and 8,000,000 Tg, with at least a further 530,000 Tg stored in hydrates in the permafrost (Ciais et al., 2014). As global sea temperatures increase and the permafrost continues to warm, it is possible for the hydrates in these regions to become unstable and release a significant amount of $CH_4$ as a result. However the amount which will reach the surface is still widely disputed and estimates suggest that anything from 35 to 940 Pg C could be released over the next several thousand years following a 3° rise in sea-floor temperature (Archer, Buffett, and Brovkin, 2009).

### 2.2.5 Fossil $CH_4$ emissions

$CH_4$ sources can be considered as either 'modern' or 'fossil'. Modern sources of $CH_4$ emissions include wetlands, animals, biomass burning and rice agriculture; whilst fossil emissions are from $CH_4$ which has formed in the Earth's crust in the geological past and are radiocarbon-free due to their long lifetimes (Etiope et al., 2008). These fossil emissions can be both anthropogenic, with sources due to the exploitation of fossil fuels such as coal, oil and natural gas; as well as from natural sources.

Natural sources include seepage from marine and volcanic areas (estimated to be between 18–48 Tg $CH_4$ $yr^{-1}$ and 1.7–6.3 Tg $CH_4$ $yr^{-1}$ respectively), as well as directly from mud volcanoes (5–12.6 Tg $CH_4$ $yr^{-1}$), and from the processes of microseepage and macroseepage (10–25 Tg $CH_4$ $yr^{-1}$, and 2–4 Tg $CH_4$ $yr^{-1}$ respectively) (Etiope et al., 2008). Microseepage is a slow process defined by the continual loss of $CH_4$ from 2–5 km beneath the surface in sedimentary basins where the thermal degradation of organic matter occurs. This leads to the creation of $CH_4$ gas which is driven upwards by the fact that gaseous $CH_4$ is more buoyant

than the connate fluids which are trapped in the pores of the surrounding sedimentary rocks. Mud volcanoes are a type of macroseepage which are formed over faults and caused by the up welling of sediments (mud), usually above oil and gas reservoirs in hydrocarbon basins. The gas emitted from mud volcanoes typically consists of 90–99% $CH_4$ (Etiope and Klusman, 2002). Emissions from these volcanoes can be highly variable over time. The Dashgil volcano in Azerbaijan for example was found to emit anything from 0.14 to 28 tonnes of $CH_4$ per day over a two year period, with an annual average of 5,200 tonnes (Guliyev and Feizullayev, 1997). In geothermal areas, $CH_4$ can be directly out gassed from the mantle at temperatures above 700°C in quantities of approximately a few ppm (parts per million), whilst processes such as the Fischer-Tropsch reactions convert species like $CO_2$ into liquid hydrocarbons and release $CH_4$ as a minor component. Gas vents also release $CH_4$, although the fraction is typically very low (0.01–0.1%) (Etiope and Klusman, 2002). The best estimates for the total of these natural sources are between approximately 42 and 64 Tg $CH_4$ $yr^{-1}$ (Etiope et al., 2008). These natural emissions are illustrated in Figure 2.4.

Anthropogenic fossil $CH_4$ sources result from the burning of the fossil fuels oil, coal and natural gas, as well as from the techniques involved in these industries. These industries are estimated to release between 85–105 Tg $CH_4$ $yr^{-1}$, making them potentially the second largest source to the atmosphere, approximately similar to emissions from livestock and landfills (Ciais et al., 2014). The $CH_4$ content of natural gas is approximately 90% and can escape during several stages during energy production (Fung et al., 1991). Most significantly it is leaked at oil and natural gas wells and importantly can continue to do so long after these wells are abandoned. The loss of gases through pipeline leakage is also non-negligible with an average reported loss of $CH_4$ during transportation estimated to be 1.6% and a maximum reported value of 11% by 174 natural gas companies in the United states for 2011 (Jackson et al., 2014). Coal mining also releases large quantities of $CH_4$ since it is a major component of coal gas (approximately 95%) which is released into the atmosphere both in mining and processing of coal (Fung et al., 1991). It is estimated that approximately 15 L of coal gas is released for every 1 kg of coal mined. Recently there has been much debate about the

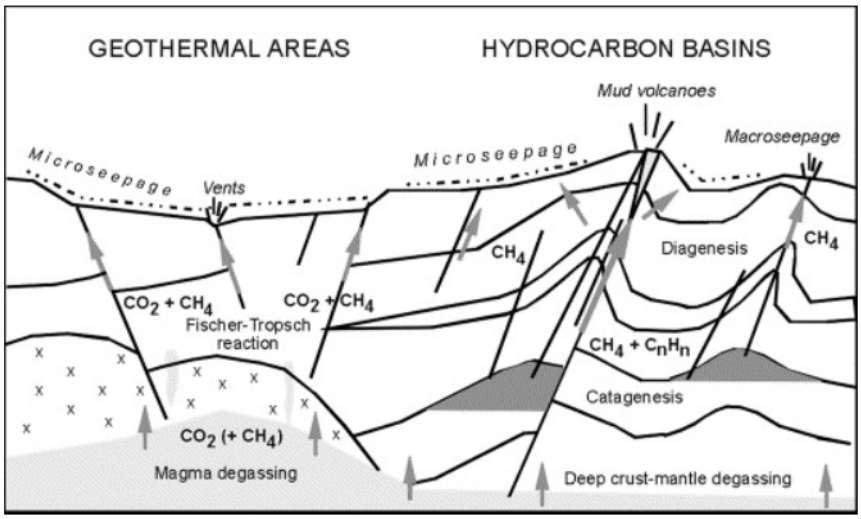


**Figure 2.4:** Illustration showing the geological production and release of $CH_4$ from volcanic (geothermal) areas and hydrocarbon basins (Etiope and Klusman, 2002).

release of $CH_4$ through the process of hydraulic fracturing (or fracking) of shale gas, which allows gas and oil production in tight rock formations (Schneising et al., 2014). In theory this new technique is advantageous for the mitigation of greenhouse gas release into the atmosphere since oil and gas produce less $CO_2$ per unit energy than coal does (approximately 56% for gas and 79% for oil). However, this is only beneficial if less than 3.2% of the gases are leaked, and current studies suggest the amount leaked may be $9.1\% \pm 6.2\%$ (Schneising et al., 2014). These and other studies suggest that the anthropogenic release of fossil $CH_4$ are likely underestimated at current (Schneising et al., 2014; Kort et al., 2014).

### 2.2.6 Biomass burning emissions

Pyrogenic $CH_4$ sources originate as a result of the incomplete combustion of biomass from deforestation and wildfires. These natural and anthropogenic sources are estimated to be a relatively small source compared to wetlands, releasing between 32 and 39 Tg $CH_4$ $yr^{-1}$ into the atmosphere (Ciais et al., 2014). Tropical and boreal forests are thought to contribute 17–21 Tg $CH_4$ to this per year. Worden et al. (2013) used tropospheric methane and CO data from the Aura Tropospheric Emission Spectrometer and CO profile measurements from

the Terra Measurements of Pollution in the Troposphere (MOPITT) satellite to estimate methane emissions of 4.25±0.75 Tg for the period October–November 2006 from Indonesian fires alone. Using a mass balance approach, Basso et al. (2016) estimated that $CH_4$ emissions amounted to 52.8±6.8 mg $CH_4$ $m^{-2}$ $day^{-1}$ over the Amazon Basin, and by using a CO:$CH_4$ emission factor they estimated that the contribution to biomass burning was approximately 15% of the total flux in the dry season.

### 2.2.7 Direct emissions from trees

Keppler et al. (2006) suggested that $CH_4$ is formed in situ in terrestrial plants under aerobic conditions. They observed significant emissions from both intact plants and detached leaves during field and laboratory experiments and suggested a $CH_4$ source of between 62 and 236 Tg $CH_4$ $yr^{-1}$ for living plants, and 1–7 Tg $CH_4$ $yr^{-1}$ for plant litter. Since this study was published there have been new results which do not agree with these findings and the latest consensus is that plants are not a major source of the global $CH_4$ production (Nisbet et al., 2009), and are 'very unlikely' to be a significant source according to Ciais et al. (2014).

## 2.3 METHANE SINKS

Atmospheric $CH_4$ has a lifetime of approximately 9 years in the atmosphere and is removed primarily by photochemistry through reactions with hydroxyl radicals (OH), and on a smaller scale by reactions with chlorine (Cl) atoms (Dlugokencky et al., 2011; Ciais et al., 2014). The chemical reactions which oxidise atmospheric $CH_4$ also affect the chemical state of the atmosphere by removing OH and introducing CO, $CO_2$, $H_2O$, $H_2$ (hydrogen) and $CH_2O$ (formaldehyde) as products. Through secondary reactions these affect the amount of ozone ($O_3$)

and lead to a significant amount of water vapour production in the stratosphere, itself an important greenhouse gas (Cicerone and Oremland, 1988). Stratospheric $CH_4$ reactions with Cl form HCl (hydrogen chloride), and $CH_4$ entering the stratosphere also provides a mechanism to aid the escape of Hydrogen to space, further altering atmospheric chemistry (Cicerone and Oremland, 1988). From Figure 2.1 we see that for 2011 the $CH_4$ removal from the atmosphere was 445–617 Tg $CH_4$ by OH in the troposphere, with a further 16–84 Tg removed by OH in the stratosphere and 13–37 Tg removed by Cl in the stratosphere.

To understand these processes we must consider the key reactions which occur in the atmosphere, starting with the production of OH when ozone reacts with ultraviolet radiation as in Equation (2.1),

$$O_3 + h\nu \longrightarrow O(^1D) + O_2 \quad \lambda < 315\text{nm}, \tag{2.1}$$

where $\nu$ is the frequency of radiation, $h$ is Planck's constant and $\lambda$ is the wavelength. The product, $O(^1D)$, are electronically excited oxygen atoms. About 99% of the atoms are then quenched in collisions with $N_2$ and $O_2$ as in Equation (2.2), losing their energy and resulting in the reformation of ozone in Equation (2.3), where M can be $N_2$, $O_2$, or another particle or molecule capable of stabilising ozone.

$$O(^1D) + N_2 \longrightarrow O + N_2, \tag{2.2}$$

$$O + O_2 + M \longrightarrow O_3 + M. \tag{2.3}$$

However, approximately 1% of the excited oxygen reacts with water vapour instead; producing hydroxyl radicals, which in turn can act upon $CH_4$ and destroy it as in Equation (2.5). Approximately 85% of the $CH_4$ which is emitted into the atmosphere is destroyed in this manner in the troposphere and the remainder is almost all destroyed in the stratosphere by OH and Cl. A very small fraction of $CH_4$ reaches the mesosphere where it is photolytically destroyed directly by very

short wavelength ultraviolet radiation (at 121.6 nm) (Cicerone and Oremland, 1988).

$$O(^1D) + H_2O \longrightarrow 2OH, \tag{2.4}$$

$$CH_4 + OH \longrightarrow H_2O + CH_3. \tag{2.5}$$

The complete oxidation of $CH_4$ ultimately leads to the production of $CO_2$ and water vapour as shown in Equation (2.6); but note that this shows only the resultant net reaction. OH radicals and radiation are required to reach these products as described previously. A schematic illustrating the remainder of this cycle from $CH_3$ to $CO_2$ is shown in Figure 2.5, whilst the full reaction sequences for this can be found in Cicerone and Oremland (1988).

$$CH_4 + 2O_2 \longrightarrow CO_2 + 2H_2O. \tag{2.6}$$

In the stratosphere $CH_4$ is still destroyed by OH, but also by Cl atoms as given by Equation (2.7), which represents an important reaction for stratospheric chemistry, acting to remove Cl atoms which are known to destroy ozone.

$$CH_4 + Cl \longrightarrow CH_3 + HCl. \tag{2.7}$$

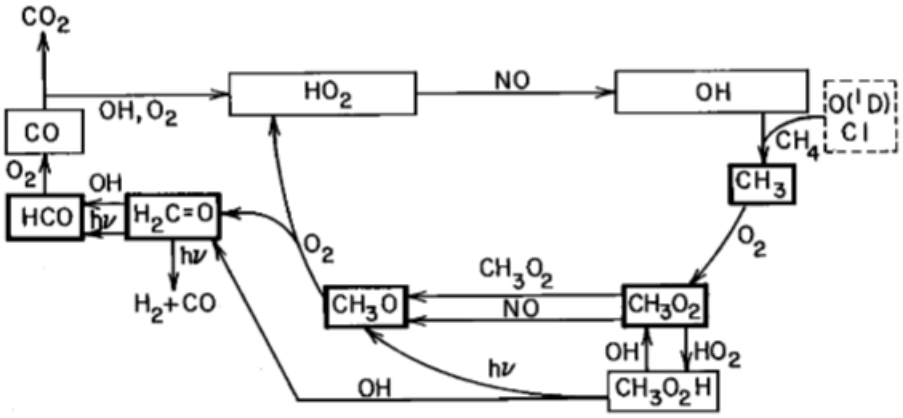


Figure 2.5: The principle reactions in the oxidation of atmospheric $CH_4$ into $CO_2$ and $H_2O$ (Cicerone and Oremland, 1988).

In addition to these aforementioned atmospheric processes, in the marine boundary layer it is thought possible that $CH_4$ can be removed by reactions with Cl, and also by oxidation in well aerated soils (Ciais et al., 2014). These aerobic methane-oxidising methanotrophic bacteria work to oxidise $CH_4$ in a sequential manner, firstly converting $CH_4$ into methanol and then by subsequent oxidations into formaldehyde, formate, and finally into $CO_2$ as shown in Equation (2.8) (Cicerone and Oremland, 1988). As shown in Figure 2.1, the IPCC 2013 report estimates that between 9 and 47 Tg $CH_4$ were removed from the atmosphere by this process in 2011.

$$CH_4 \longrightarrow CH_3OH \longrightarrow HCOOH \longrightarrow CO_2. \tag{2.8}$$

## 2.4 ATMOSPHERIC $CH_4$ TRENDS

Palaeoclimate records of $CH_4$ mole fractions measured from ice cores show that there is a strong coupling between climate and $CH_4$ (Dlugokencky et al., 2011). During cold glacial periods the concentration was approximately 350 ppb, compared to estimates of 700 ppb for warmer interglacial periods. These differences are thought to be mainly driven by changes to boreal wetlands with cold temperatures and the coverage of wetlands by ice sheets reducing $CH_4$ emissions to effectively zero (Dlugokencky et al., 2011). At the beginning of the industrial era (approximately 1750) the atmospheric $CH_4$ concentration was approximately 722 ppb (Ciais et al., 2014), and has risen to 1840 ppb since then. Total $CH_4$ emissions in the pre-industrial era were approximately 215 Tg $CH_4$ $yr^{-1}$. This is similar to natural emissions today, although land use changes since 1750 have likely decreased the total emissions by natural sources by approximately 10% (Dlugokencky et al., 2011). Figure 2.6 shows the variation in $CO_2$, $CH_4$ and $N_2O$ over ten thousand years up until the year 1900.

Atmospheric $CH_4$ mole fractions have increased by approximately 150% since the beginning of the industrial era. From the 1980s until 1992 concentrations

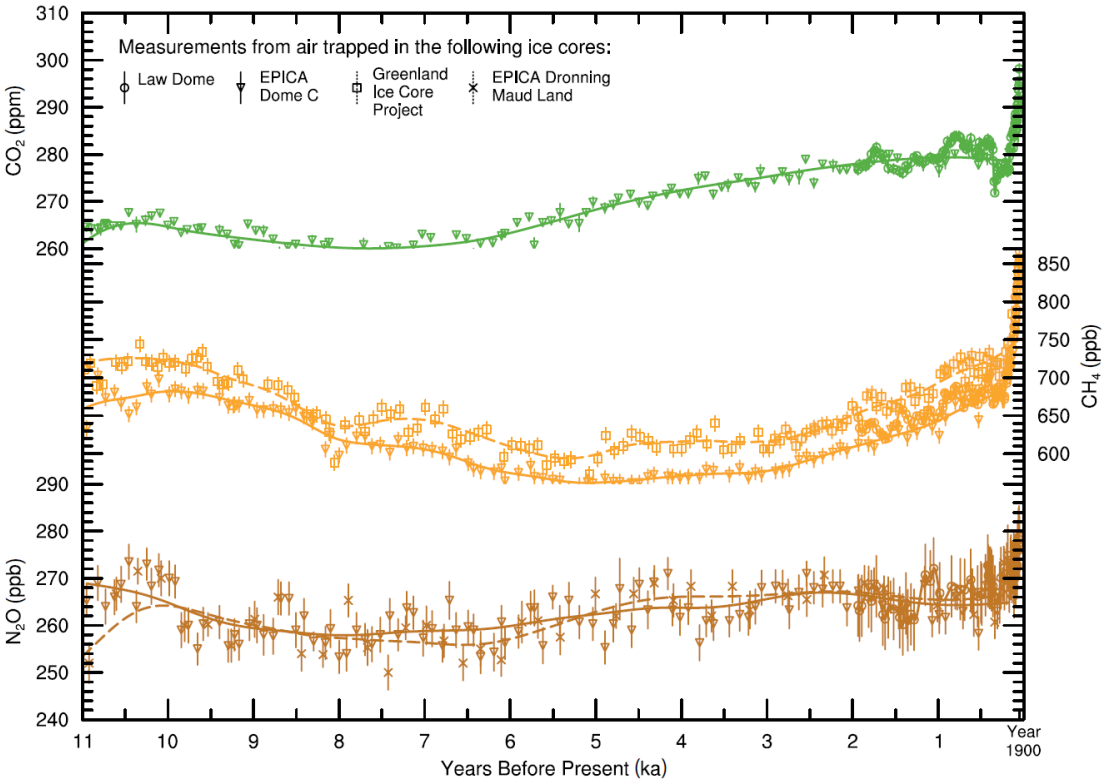


**Figure 2.6:** Showing ice core records for the concentrations of $CO_2$, $CH_4$ and $N_2O$ over ten thousand years up until the year 1900 (Ciais et al., 2014).

rose by an average of about 12 ppb year$^{-1}$, before slowing throughout the 1990s to a near zero average growth between 2000 and 2006 (Dlugokencky et al., 1994; Dlugokencky, 2003). In 2007 concentrations began to rise again by an average of approximately 6 ppb year$^{-1}$ (Rigby et al., 2008; Nisbet, Dlugokencky, and Bousquet, 2014) and have recently increased by approximately 12.6 ppb in 2014, 9.9 ppb in 2015 and 7.7 ppb in 2016 (NOAA `www.esrl.noaa.gov/gmd/ccgg/trends_ch4/`). The reasons for these recent changes still remain incompletely understood. Figure 2.7 shows this changing global average concentration of $CH_4$ between 1983 and September 2016.

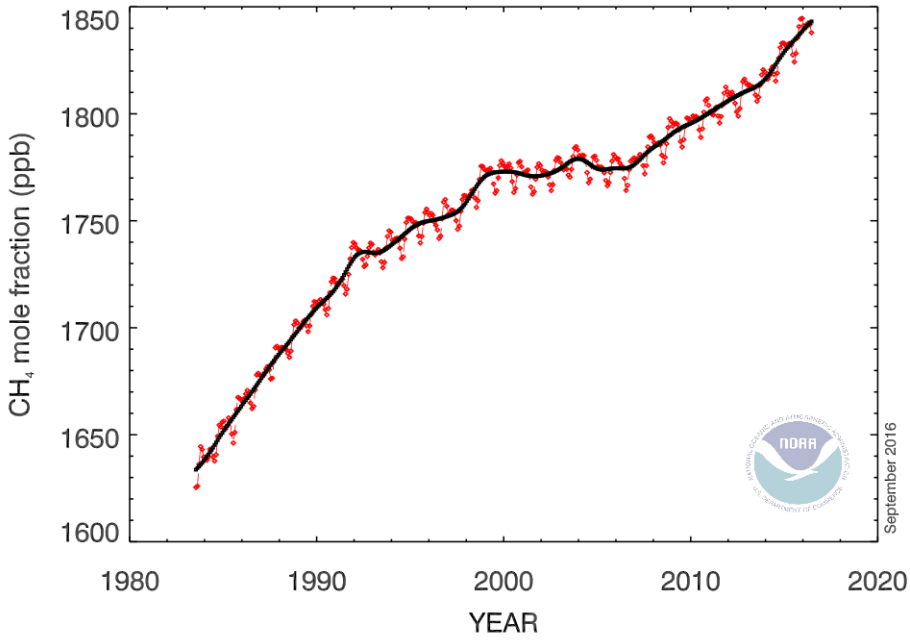


**Figure 2.7:** Time series of the globally averaged $CH_4$ concentration in ppb, from 1983 to September 2016. Showing the globally averaged monthly mean values in red, (centred on the middle of each month); and the long-term trend (similar to a 12-month running mean) in black, where the average seasonal cycle has been removed. This Figure is from the National Oceanic and Atmospheric Administration (NOAA), Earth System Research Laboratory (`www.esrl.noaa.gov/gmd/ccgg/trends_ch4/`).

# 3 SATELLITE REMOTE SENSING

## 3.1 BASICS OF REMOTE SENSING

To measure the concentration of gases in the atmosphere we need to understand the radiative transfer processes which govern the transfer of electromagnetic radiation through the atmosphere. This radiation is affected by absorption, emission and scattering caused by the molecules and aerosol particles of which the atmosphere is comprised. These molecules and particles affect the electromagnetic spectrum differently as a result of their different properties and abilities to absorb, emit and scatter radiation in unique ways depending on the wavelength of radiation incident upon them. As a result, the composition and concentrations of gases in the atmosphere can be inferred given the correct knowledge of these processes by measuring the resultant radiation after having passed through the atmosphere. In this chapter we describe how the processes of absorption, scattering and emission are reliant on the optical properties of the molecules and particles in the atmosphere. We further describe how satellite measurements of electromagnetic radiation which has travelled through the atmosphere and has been affected by these processes can be used to calculate the abundance of a gas such as $CH_4$ or $CO_2$ in the atmosphere.

Typically the radiation measured by satellites either originates from the Sun or is emitted by the Earth or atmosphere; although LIDARs and RADARs on satellites can directly produce their own radiation for this purpose. The radiation used depends on the absorption features in the gases which we are interested in retrieving, although $CH_4$ is typically retrieved in the infra-red (IR) or short wave infrared (SWIR) parts of the spectrum. This was first done by the SCIAMACHY instru-

ment, utilising the SWIR part of the spectrum as detailed in Buchwitz, Rozanov, and Burrows (2000).

To measure the total concentration of $CH_4$ in the atmosphere it is important to sample the entire column from the surface to the top of the atmosphere (TOA). From the Earth's surface this can be done effectively by measuring directly upwards at the Sun, as is the case for most ground-based spectrometers. From satellites it is possible to measure by directly looking at the Sun if in limb sounding mode, although this method is more inaccurate towards the surface as the total amount of atmosphere being sampled increases. The alternative is to sample in the nadir where the instrument is aligned to look downwards at the Earth's surface and measures either reflected sunlight in the SWIR or emitted radiation in the IR. In the SWIR case this radiation has twice travelled through the atmosphere, from the Sun, to the surface and back to the satellite. The presence of $CH_4$ in the atmosphere causes radiation at specific wavelengths to be absorbed, decreasing the signal strength at these wavelengths compared to that before the radiation had entered the atmosphere. By measuring this relative decrease in electromagnetic radiation at the correct wavelengths it is possible to infer the concentration of $CH_4$ which would have caused this change in signal. This absorption spectroscopy is the basic principle of remote sensing and relies on having an accurate knowledge of the absorption properties of all gases in the atmosphere, as well as knowing the solar spectrum. We discuss the processes which cause this absorption in Section 3.2. However, calculating the correct atmospheric composition from these measurements also relies on an accurate knowledge of the radiation path-length through the atmosphere. This is highly dependent on atmospheric scattering processes, which are discussed in Section 3.3.

## 3.2 ATMOSPHERIC ABSORPTION

Radiation is absorbed in the atmosphere via two main processes; by aerosols (described in more detail in Section 3.3), and by molecular absorption from gases such as $CH_4$. Atoms and molecules absorb electromagnetic radiation at discrete energy levels which are dependent on their atomic structure, described by Equation (3.1),

$$\Delta E = h\nu, \tag{3.1}$$

where $h$ is Planck's constant and $\nu$ is the frequency of the absorbed radiation. This absorption energy takes several forms, each described by the nature of how the absorbed radiation affects the atom or molecule. These take the form of either electrical, vibrational, rotational or nuclear energy changes to the atom or molecule, or can result as a combination of several or all of these different transitional forms. The combination of these energies must always equal an allowed energy transition exactly. These allowed transitions therefore only allow the atom to absorb radiation of specific wavelengths which in total describe the atom or molecule's atomic structure and hence allow us to determine which gases are present when performing absorption spectroscopy.

In the SWIR the electronic and nuclear energies resultant from absorption are large compared to those associated with rotational and vibrational transitions. The rotational transitional energy can be represented by considering that the molecule gains inertia $I$ in one of the three axes of direction ($A$, $B$ and $C$), such that the rotational energy is given by,

$$E_{Rotational} = \frac{1}{2} I_A {\omega_A}^2 + \frac{1}{2} I_B {\omega_B}^2 + \frac{1}{2} I_C {\omega_C}^2, \tag{3.2}$$

where $\omega$ is the angular velocity around each axis. This energy is proportional to the angular velocity and the moment of inertia around each axis, which depend on the structure of the molecule. Molecules can therefore be categorised depending on their structure. $CH_4$ is classified as a spherical top because all

three moments of inertial are equal to each other ($I_A = I_B = I_C$). Due to its symmetry $CH_4$, and all spherical tops, have no pure rotational transitions.

Vibrational transitions occur with a set number of vibrational modes which depends on the number of degrees of freedom, for which a molecule of $X$ atoms has $3X$ degrees of freedom. However three of these describe the translational motion of the molecule moving in a given direction, and three more represent the rotation of a particle about one of the axes; therefore six of the degrees of freedom do not represent vibrational modes. Therefore a molecule of $X$ atoms will have $3X-6$ degrees of freedom. $CH_4$ therefore, has nine fundamental modes of vibration, but due to symmetry five of these are degenerate. The four remaining fundamental modes of $CH_4$ vibration are shown in Figure 3.1, although only two of them are active in the IR (v3 at 3.3 $\mu$m and v4 at 7.7 $\mu$m where the Carbon atom is in motion). Figure 3.13 shows an example of atmospheric spectra between 1.55 $\mu$m and 1.72 $\mu$m with the regions containing methane absorption lines indicated.

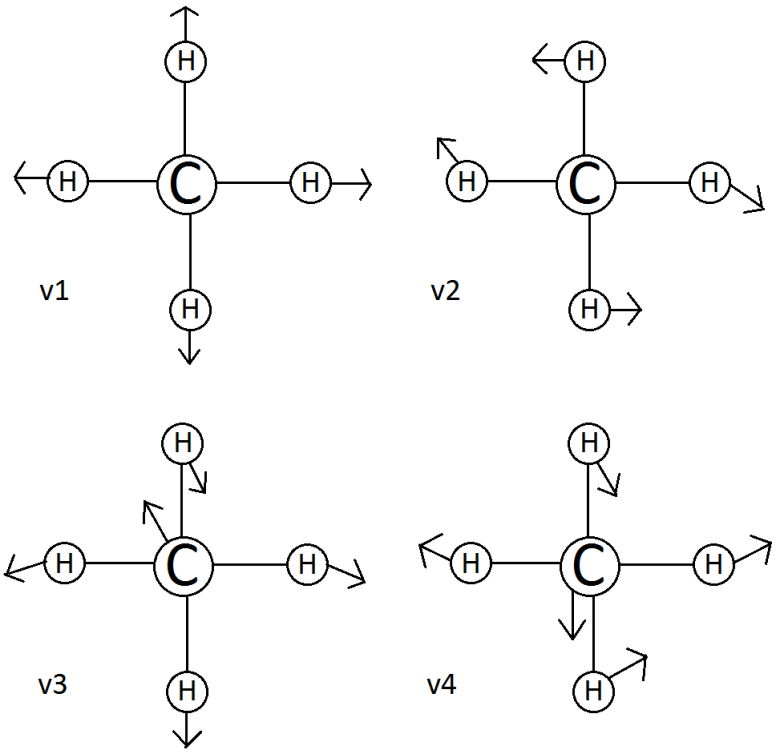


Figure 3.1: Illustration of the four fundamental modes of vibration for the $CH_4$ molecule.

## 3.3 ATMOSPHERIC SCATTERING

### 3.3.1 Scattering and absorption due to aerosols

In the ideal case, solar radiation travels directly from the Sun to the Earth's surface, is reflected, and then travels directly to the satellite's detectors. The light-path would be known and absorption due to different gases could be accurately calculated. The largest uncertainty in the ideal case arises from the properties in the satellite instrument although thorough calibration can reduce this. In reality the largest uncertainty in satellite measurements in the near infra-red is due to the scattering effects of aerosol and clouds which act to alter the path length of radiation (Aben, Hasekamp, and Hartmann, 2007). These effects are illustrated in Figure 3.2 where light path 1 represents the ideal case. If radiation is scattered towards the satellite by clouds or aerosols before reaching the surface then it does not travel through the entire atmosphere, as represented by light paths 2 and 3. The satellite will not be sampling the entire atmosphere and will yield underestimates for the total amount of methane in a column. Typically the radiation will reach the surface unless reflected by clouds or scattered under heavy aerosol conditions, but aerosols are always present to some degree and will alter the light path slightly, as illustrated by light path 4; meaning that even the clearest scenes will suffer from uncertainties of this nature. The radiative transfer equation relates the absorption, scattering and reflection properties of the atmosphere to the light path length and the intensity of radiation measured at each wavelength due to its interaction with the atmosphere along this path. We will now derive this relationship and discuss the important terms and their physical representations.

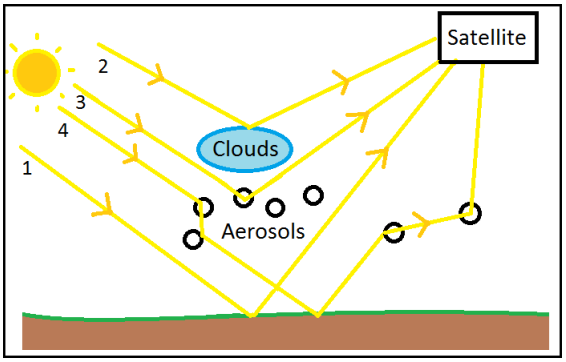


**Figure 3.2:** Illustration of possible radiation paths between the Sun and a satellite. Some interacting with aerosols and clouds to shorten or lengthen the path length compared to the non-scattered case (path 1).

### 3.3.2 Atmospheric transfer applied to a single particle

We consider the optical properties of a simple system of particles in order to ultimately produce a value for the radiative forcing caused by this system. Whilst this is a simplified model of the atmosphere it will show which parameters and properties are needed to determine the extinction of radiation as it travels through the atmosphere.

Firstly we consider the case when a flux of incoming radiation is incident on a single spherical aerosol particle. The incident flux will be considered as a flux per unit wavelength, $F_{in}(\lambda)$. The power which is absorbed ($P_{abs}$ in Joules per second) will be equal to the incident flux (in $joules m^{-2} s^{-1}$) multiplied by the absorption cross section of the aerosol, ($\sigma_{abs}$ in $m^2$) as shown in Equation (3.3). This cross section represents the area through which, if an incoming light beam is incident, it will interact with the particle. The power which is scattered ($P_{sca}$) can also be expressed in the same way where $\sigma_{sca}$ is the scattering cross section.

$$P_{\text{abs}} = F_{\text{in}}(\lambda)\sigma_{\text{abs}}, \tag{3.3}$$

$$P_{\text{sca}} = F_{\text{in}}(\lambda)\sigma_{\text{sca}}. \tag{3.4}$$

The cross sectional areas in Equations (3.3) and (3.4) are functions of the size of the aerosol particles, the wavelength of incident radiation, and the refractive index. These cross sections can be expressed as an extinction cross section, which

is the sum of the absorption and scattering cross sections. From this, the single-scattering albedo can also be defined as the scattering cross section divided by the extinction cross section. This single-scattering albedo, $\omega$, is therefore a measure of the relative importance of scattering and absorption. The smaller the single-scattering albedo, the more absorbing the aerosol is. The extinction cross section, $\sigma_{ext}$, and $\omega$ are defined in Equations (3.5) and (3.6) respectively. Another useful term is the aerosol size parameter, $\alpha$, which can be expressed in terms of the with radius $r$, and wavelength $\lambda$. This is given in Equation (3.7).

$$\sigma_{\text{ext}} = \sigma_{\text{sca}} + \sigma_{\text{abs}}, \tag{3.5}$$

$$\omega = \frac{\sigma_{\text{sca}}}{\sigma_{\text{ext}}}, \tag{3.6}$$

$$\alpha = \frac{2\pi r}{\lambda}. \tag{3.7}$$

The refractive index is expressed with a real ($\Re$) and an imaginary ($\Im$) component which represent the scattering and absorption terms respectively. This is both wavelength and temperature dependent although we are assuming, for this treatment of an aerosol, that the refractive index is a constant throughout the particles (the particles are homogeneous). This refractive index is therefore,

$$m(\lambda, T) = \Re(m(\lambda, T)) + \Im(m(\lambda, T))i. \tag{3.8}$$

Now that we have defined the absorption and scattering cross sections, we need to consider the scattering in more detail. Radiation which is incident within the scattering cross sectional area is scattered in all directions, although not uniformly. The radiation is scattered as a function of the scattering angle $\theta$ and is dependent on the radius of the aerosol particle and the wavelength of incident radiation. Depending on the wavelength and radius, either the Rayleigh or the Mie scattering approximations are used. The scattering angle is defined in Figure 3.3 where an angle of $0^\circ$ represents total forward scattering and $180^\circ$ represents total backscattering.

For particles which have a radius which is much smaller than the incident wavelength of radiation ($r << \lambda$), we use the Rayleigh scattering approximation. This

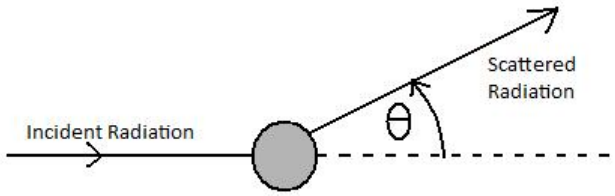


**Figure 3.3:** Diagram to illustrate the scattering angle $\theta$.

is where these small particles become excited and emit like a dipole which is almost isotropic. However there is a slight decrease in scattered radiation around 90 and -90 degrees.

Rayleigh scattering is only a good approximation when the radius of the aerosol particle is much less than the wavelength of incoming radiation. When the radius is much larger than the wavelength ($r >> \lambda$) we instead need to use the Mie scattering approximation which has a predominately forward scattering profile and scatters as shown in Figure 3.5.

The asymmetry factor $g$ can now be defined. This is a single number which describes the scattering of an aerosol. The asymmetry function is defined as the integral over all of the possible scattering angles of the scattering phase function multiplied by $\cos\theta$. The scattering phase function, $P(\theta)$, is equal to one when integrated over all of the scattering angles and will be defined shortly. Before looking at this, the asymmetry factor should be fully understood.

$$g = \int P(\theta)\cos\theta \mathrm{d}\Omega. \tag{3.9}$$

This can be seen to take values between -1 and 1, (3.10). For completely forward scattering ($\theta = 0°$), the asymmetry factor is equal to 1; and when $g = 0$ this rep-

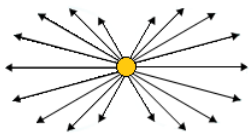

**Figure 3.4:** Diagram representing the directions of scattered radiation for Rayleigh scattering. The relative lengths of the arrows represent the relative amount of radiation scattered in each direction.

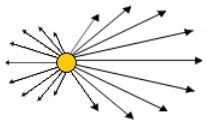

**Figure 3.5:** A diagram showing the relative directions of scattering radiation for the Mie scattering approximation, (the radiation is incident from the left and so there is more radiation scattered in a forward direction; to the right). The relative lengths of the arrows represent the relative amount of radiation scattering in each direction.

resents isotropic scattering. When there is complete backscattering, $\theta = 180°$, then the asymmetry factor equals -1; although this does not occur naturally. This can be understood by considering the intensity scattered at each angle for both Rayleigh and Mie scattering, as depicted in Figure 3.6.

Although the asymmetry factor can be a useful parameter to know, in practice it is more important to know the scattering phase function $P(\theta)$. This is a function which describes the scattering angle profile of a given particle and it is defined in terms of the differential scattering cross section divided by the scattering cross section. This allows the integral of the scattering phase function over the entire sphere to equal one, as previously mentioned.

$$g = \int P(\theta) \cos\theta \mathrm{d}\Omega, \tag{3.10}$$

$$P(\theta) = \frac{1}{\sigma_{\mathrm{sca}}} \left( \frac{\mathrm{d}\sigma_{\mathrm{sca}}}{\mathrm{d}\Omega} \right). \tag{3.11}$$

### 3.3.3 Atmospheric transfer on a column of aerosol

Previously we considered a single aerosol particle which has radiation incident upon it, but now we consider a population of aerosols. This will allow us to model an entire column of the atmosphere which consists of many aerosol particles. Firstly we define new variables, the scattering coefficient, $k_{sca}$, and the absorption coefficient, $k_{abs}$, (both with units of reciprocal distance). These are de-

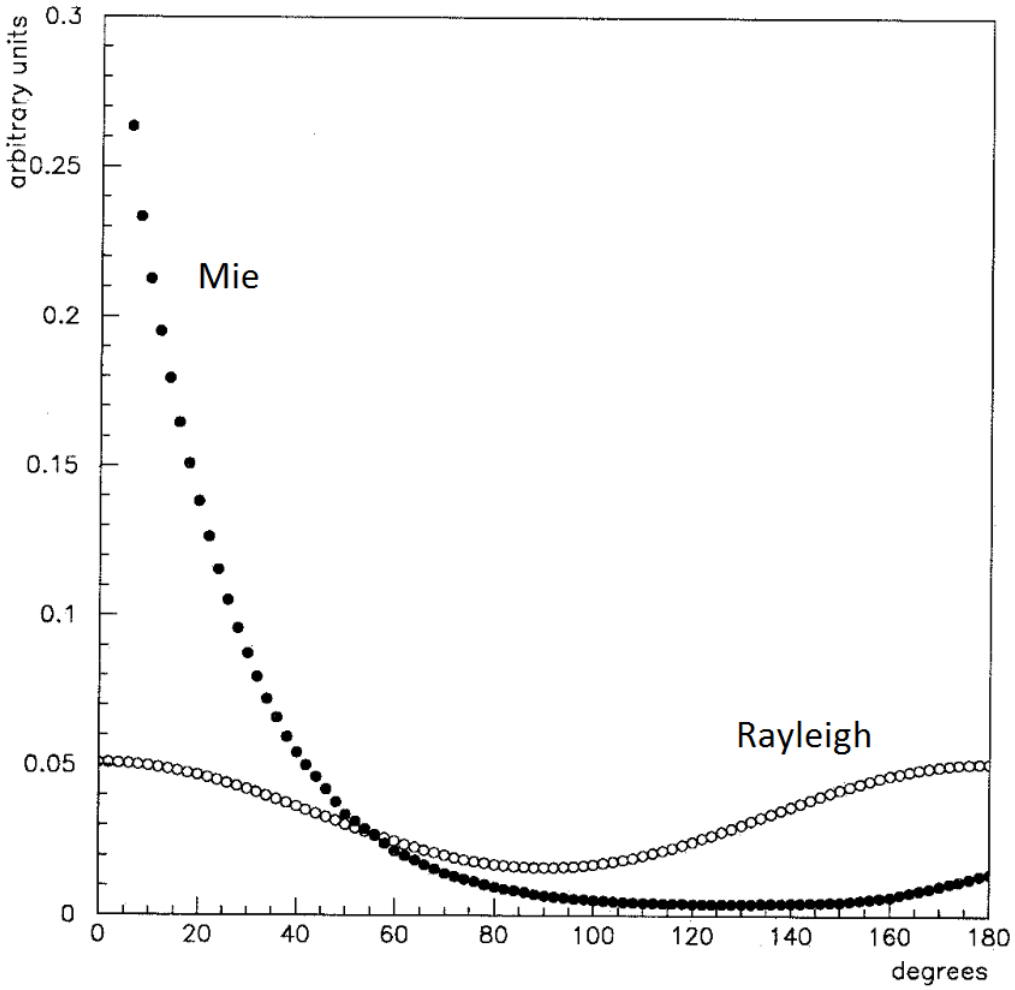


**Figure 3.6:** Graph showing intensity against scattering angle for Mie (solid dotted line) and Rayleigh scattering. It can be seen than when $\theta = 0°$, the scattering is dominated by Mie scattering showing that larger particles (with respect to the incident wavelength) have larger values of $g$ (Mumford, 2000).

fined as the integral of the scattering or absorption cross section, over the entire particle size distribution.

$$k_{\text{sca}} = \int_0^{r_{\max}} \sigma_{\text{sca}}(\lambda, r, m) N(r) \mathrm{d}r, \tag{3.12}$$

$$k_{\text{abs}} = \int_0^{r_{\max}} \sigma_{\text{abs}}(\lambda, r, m) N(r) \mathrm{d}r, \tag{3.13}$$

where $N(r)$ is the number of particles per metre cubed of radius $r$. From these, the extinction coefficient, $k_{\text{ext}}$, can be defined as the sum of the scattering and absorption coefficients (3.14). The extinction coefficient represents the fraction of radiant flux which is lost from aerosol scattering and absorption per unit thickness of aerosol; it has a unit of reciprocal metres. From this we can also define the population single-scattering albedo, $\omega_{\text{pop}}$, (3.15).

$$k_{\text{ext}} = k_{\text{sca}} + k_{\text{abs}}. \tag{3.14}$$

$$\omega_{\text{pop}} = \frac{k_{\text{sca}}}{k_{\text{ext}}}. \tag{3.15}$$

It is worth noting here that the population single-scattering albedo is not equal to the sum of all the individual single-scattering albedo's of the particles in the size distribution. This will only be equal if all of the particles are the same.

$$\omega_{\text{pop}} \neq \int \omega N(r) \mathrm{d}r. \tag{3.16}$$

Now that we have defined the extinction coefficient we can define a very important optical property of aerosols; the optical depth, $\tau$. This is defined as the length over which a direct beam will decrease by a factor of the exponential $e$ whilst travelling through the aerosol layer. This is given as the integral of the extinction coefficient over altitude, $z$.

$$\tau = \int k_{\text{ext}} \mathrm{d}z. \tag{3.17}$$

The optical depth is often used to represent the amount of aerosol in a vertical column in an optical sense. Part A of Figure 3.7 shows how optical thickness varies over the oceans, as measured by the POLDER (POLarization and Directionality of the Earth's Reflectance) radiometer aboard the ADEOS (ADvanced Earth Observing Satellite) platform at 865 nm (Deuzé et al., 1999). In the Atlantic Ocean, to the west of Africa, we can see that there is an increase in optical thickness. This is due to sand which is blown out to sea from the Sahara desert. Measurements of the optical depth over water and land are very different. This is because the albedo over the land varies by a vast amount depending on the terrain; whereas over water the albedo is relatively constant. Changes in the optical depth with respect to wavelength are characterised by the angstrom exponent. High values of this exponent are indicative of small particles and low values are indicative of large particles. Part B of Figure 3.7 shows the angstrom exponent over the ocean.

The scattering phase function for the population of aerosols can now be defined. This is given as the integral over all particle radii of the scattering phase functions for each individual particle multiplied by the number of particles which have each of these radii (particle size distribution) and the scattering cross section of each particle. This is divided by a similar integral over the scattering cross sections for each particle in the size distribution in order to keep the total integral of the scattering phase function over all angles equal to one. This is displayed in Equation (3.18).

$$P_{\text{pop}}(\theta) = \frac{\int_0^{r_{\max}} P(\lambda, r, m, \theta) N(r) \mathrm{d}r \sigma_{\text{sca}}(\lambda, r, m)}{\int_0^{r_{\max}} N(r) \sigma_{\text{sca}}(\lambda, r, m) \mathrm{d}r}. \tag{3.18}$$

From Equation (3.18) it can be seen that the population scattering phase function is a function of the wavelength of the incident radiation, the radius of the particles, the refractive index of the particles, the scattering angle and the particle number size distribution. This would in practise also become a function of the particle shape, although not without dramatically complicating the equation.

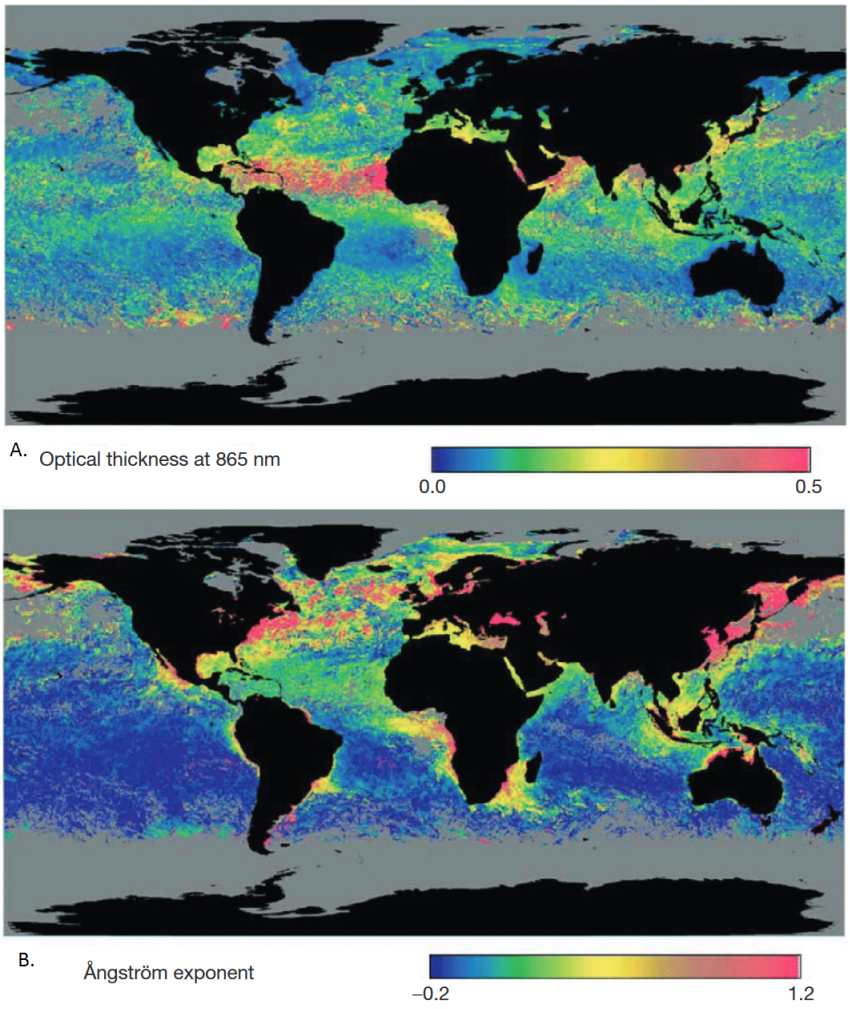


**Figure 3.7:** Part A (top): Showing the aerosol optical thickness at 865 nm over the Earth's water surfaces, and part B (bottom), showing the anstrom exponent. Both measured by the POLDER radiometer aboard the ADEOS satellite (Buseck and Schwartz, 2003).

### 3.3.4 Radiative transfer in the atmosphere

The extinction of solar intensity can now be considered as it travels through the atmosphere. This change in intensity, $I_\nu$, with respect to distance through the aerosol, $s$, can be expressed in terms of an extinction term and a source function (3.19).

$$\frac{\mathrm{d}I_\nu}{\mathrm{d}s} = -k_{\text{ext}}(I_\nu + S_\nu), \tag{3.19}$$

where $k_{\text{ext}}$ is the extinction coefficient ($\mathrm{m}^{-1}$) and $S_\nu$ is the source function ($\mathrm{Wm}^{-2}\mathrm{sr}^{-1}\mathrm{m}^{-1}$). For this source function we need to consider the different scattering geometries within an aerosol column of length $\mathrm{d}s$ and incident radiation intensity $I$. The radiation which passes through the layer will be a function of the initial incident radiation (multiplied by the extinction coefficient), and a function of the radiation from other directions which is scattered into the radiative beam. We express this extra incoming radiation as a cone ($\mathrm{d}\Omega'$) which needs to be scattered at an angle represented by another cone ($\mathrm{d}\Omega$) for it to be included with the measured intensity at the end of the column. From this the source function can be represented as Equation (3.20).

$$S_\nu(\tau, \hat{\Omega}) = [1 - a(\tau, g, \omega)]B(\tau) + \frac{a(\tau, g, \omega)}{4\pi} \int \mathrm{d}\Omega' P(\tau, \hat{\Omega}', \hat{\Omega}) I(\tau, \hat{\Omega}'), \tag{3.20}$$

where $a(\tau, g, \omega)$ is the albedo of the aerosol particles, which is a function of the optical depth, $\tau$, the asymmetry factor, $g$, and the single-scattering albedo for the population $\omega$. The source function has two components. The first component consists of the co-albedo multiplied by the Planck function and this represents the emission term of the aerosol particles. The second term represents the contribution from radiation which enters the column from an angle $\mathrm{d}\Omega'$ and is scattered into the angle $\mathrm{d}\Omega$. This term is dependent on the scattering phase function (which is also dependent on both of these angles and the optical depth); and is integrated over all possible angles of incidence, $\mathrm{d}\Omega'$. This means that we have gone from considering a single particle, to considering a column of par-

ticles, and are now considering the extinction of radiation due to all particles scattering radiation in from all directions. The final equation for the extinction of intensity through the atmospheric layer can then be given as,

$$\frac{\mathrm{d}I_\nu}{\mathrm{d}s} = -k_{\mathrm{ext}} I_\nu + [1 - a(\tau, g, \omega)]B(\tau) + \frac{a(\tau, g, \omega)}{4\pi} \int \mathrm{d}\Omega' P(\tau, \hat{\Omega}', \hat{\Omega}) I(\tau, \hat{\Omega}'). \tag{3.21}$$

This version of the radiative transfer equation describes how radiation travels through the atmosphere and how different factors influence the intensity received at the end of a column of atmosphere. The extinction coefficient depends on the absorption and scattering of radiation by particles throughout the particle size distribution so is a function of particle radius, particle number distribution, the incident radiation wavelength and refractive index of the particles. In addition to these parameters, the equation is a function of the scattering albedo which relies on the asymmetry factor. These therefore both rely on the scattering phase function, the scattering angle and the shape of the particles. The equation also relies on the Planck function which determines how the aerosols re-emit radiation. Furthermore, this extinction is also a function of the directions of scattering radiation from outside the column of aerosol and on how the scattering phase function describes how this radiation will be scattered.

### 3.3.5 Non-scattering atmosphere

For the case where there is no scattering, the relation between the incoming intensity of radiation and the observed intensity a distance $s'$ into a medium is given by the Beer-Lambert law. This can be derived from Equation (3.19) by firstly disregarding the source function term which gives the scattering and emission components. The result is Equation (3.22).

$$\frac{\mathrm{d}I}{\mathrm{d}s} = -k_{\mathrm{ext}} I_\nu, \tag{3.22}$$

By rearranging this equation and integrating over $s$ from zero to the distance $s'$ we get Equation (3.23),

$$\int_0^{s'} \frac{\mathrm{d}I}{I} = -\int_0^{s'} k_{\text{ext}} \mathrm{d}s. \tag{3.23}$$

By performing this integral on the left hand side of the equation and substituting the right hand side for $-\tau$ as given by Equation (3.17) (where in this case $z = s$); the equation becomes,

$$\ln\left(\frac{I_{s'}}{I_0}\right) = -\tau. \tag{3.24}$$

This then rearranges to the Beer-Lambert law as given in Equation (3.25), where $I_{s'}$ is simply $I$, the radiation observed by the detector.

$$I = I_0 \exp^{-\tau}. \tag{3.25}$$

## 3.4 SURFACE REFLECTANCE

In addition to absorption, emission and scattering, observing the atmosphere from space requires knowledge of how radiation reflects from the Earth's surface. Generally, the relationship between incident and reflected light depends upon a quantity called the bidirectional reflectance distribution function (BRDF), which is a function of the incident and viewing geometry. To simplify these calculations a Lambertian surface is assumed, for which the BRDF is a constant, only dependent on the surface albedo $\rho$. Thus, the reflected intensity depends only upon $\rho$ and $\theta_s$, the angle at the surface between the incoming solar radiation and the zenith angle. For a slanted path which has angle $\theta$ between

the original co-ordinate system and the line-of-sight, the Beer-Lambert law becomes,

$$I = I_0 \exp\left(-\frac{\tau}{\cos\theta}\right), \tag{3.26}$$

Equation (3.27) describes the radiance at the top of the atmosphere as seen by an observer at angle $\theta_v$ from the zenith,

$$I_s = I_0 \exp\left(-\frac{\tau}{\cos\theta_s}\right) \exp\left(-\frac{\tau}{\cos\theta_v}\right) \frac{\rho \cos\theta_s}{\pi}, \tag{3.27}$$

where $\tau$ is the optical depth for the entire atmosphere.

## 3.5 THE ROLE OF SATELLITES IN $CH_4$ MEASUREMENTS

To properly measure atmospheric greenhouse gases and to understand their large scale fluxes, it is necessary to observe their transport and their sources and sinks over large regions. These are especially difficult to measure over tropical regions due to a number of factors. To do so would require a vast network of ground based detectors of atmospheric measurements to monitor gases over what is a very large geographical area. This is difficult to achieve in tropical regions such as the Amazon rainforest, not only due to its size, but due to the difficulty in accessing the terrain and maintaining the infrastructure required to run a permanent measurement site in such a remote region. Figure 3.8 shows a map of the ground and aircraft based measurement network of $CH_4$ from 2009 from the GLOBALVIEW-CH4 product. Co-ordinated by NOAA, this is a co-operative effort among many organizations and institutions to make a database of high-quality $CH_4$ measurements. Across all of these organizations and institutions there were no measurement sites in the Amazon Basin in 2009. More recently was a GLOBALVIEW-CO2 product in 2013. The locations for these

measurements are shown in Figure 3.9 and the vast majority of sites which measure $CO_2$ are the same as those which, from Figure 3.8, we see also measured $CH_4$ in 2009. By 2013 the number of measurement sites in the Amazon had increased with the addition of aircraft and ground-based measurements conducted by the University of São Paulo as a part of the AMAZONICA project (Gloor et al., 2012), who also measure $CH_4$, but generally the measurement coverage in the Amazon is still far behind that of temperate latitudes.

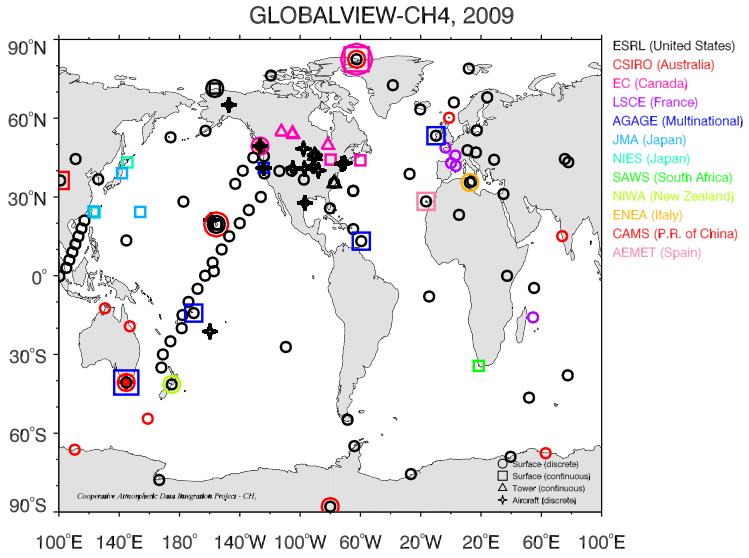


**Figure 3.8:** Global sampling locations of instruments measuring $CH_4$ in 2009 from the ground, from towers, and with aircraft (`www.esrl.noaa.gov/gmd/ccgg/globalview/ch4/ch4_sites.html`).

Satellite remote sensing allows us to fill in the gaps between ground-based and aircraft measurements by providing near-global coverage on a regular repeat cycle. They currently provide the best coverage over the tropics (Aben, Hasekamp, and Hartmann, 2007) and are ideal for measuring the transport, sources, and sinks of greenhouse gases over large areas due to their global coverage which is unaffected by the remoteness of terrain and political boundaries which often prevent in situ measurements. However, satellite measurements will often be less accurate than surface measurements, but they still require a high precision and accuracy to study greenhouse gases (variations on the scale of 2.5 ppm on an $8° \times 10°$ footprint (Rayner and O'Brien, 2001) for $CO_2$).

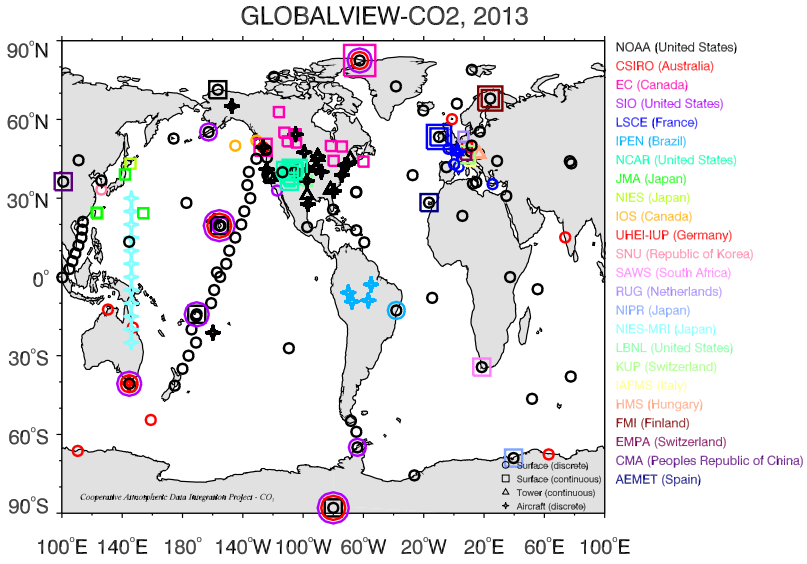


**Figure 3.9:** Global sampling locations of instruments measuring $CO_2$ in 2013 from the ground, from towers, and with aircraft (`www.esrl.noaa.gov/gmd/ccgg/globalview/co2/co2_observations.html`).

## 3.6 THE GOSAT SATELLITE

On January 23rd 2009 the Japanese Aerospace Exploration Agency (JAXA) launched the first dedicated greenhouse gas observing satellite, GOSAT (Yokota et al., 2009). The scientific instrument on board GOSAT is the Thermal And Near-infrared Sensor for carbon Observation (TANSO), which comprises two separate sensors; a Fourier Transform Spectrometer (FTS) and a Cloud Aerosol Imager (CAI). GOSAT is in a sun-synchronous orbit at $666 \pm 0.6$ km with a 13:00$\pm$15 minutes local solar overpass time with an inclination angle of $98.0^\circ \pm 0.1^\circ$ (Kuze et al., 2009). TANSO-CAI measures in the ultraviolet, visible, near infra-red and short wave infra-red and is designed to detect cloud and aerosol for use in the TANSO-FTS data correction and cloud screening (Kuze et al., 2009). An example image from TANSO-CAI is shown as Figure 3.10.

TANSO-FTS comprises of a Michelson interferometer which splits radiation into two separate paths. These paths have varying path lengths caused by a double pendulum design. These two beams are then recombined and undergo either constructive or destructive interference depending on the wavelength difference caused by the varying path length. A schematic of this is shown in Figure 3.11. The result is an interferogram which is conveniently the Fourier transform of the spectra, allowing us to produce the original spectra by performing an inverse Fourier transform operation on the measured interferogram.

The TANSO-FTS instrument measures in the short wave infrared (SWIR) and the thermal infrared (TIR) and can detect three narrow bands between 0.758-0.775 $\mu$m, 1.56-1.72 $\mu$m and 1.92-2.08 $\mu$m, and one wide band between 5.56 and 14.3 $\mu$m (Crisp et al., 2012). Figure 3.12 from Kuze et al. (2009) shows the relative positions of these spectral bands and indicates some of the important absorbing regions for $CO_2$, $CH_4$, $O_2$ and $O_3$ which TANSO-FTS can measure. Bands 1, 2 and 3 are shown in more detail in Figure 3.13. TANSO-FTS performs a cross-track scanning pattern, defining a lattice of measurements which can be varied from one to nine per cross track scan; each having a field of view of 15.8 mrad

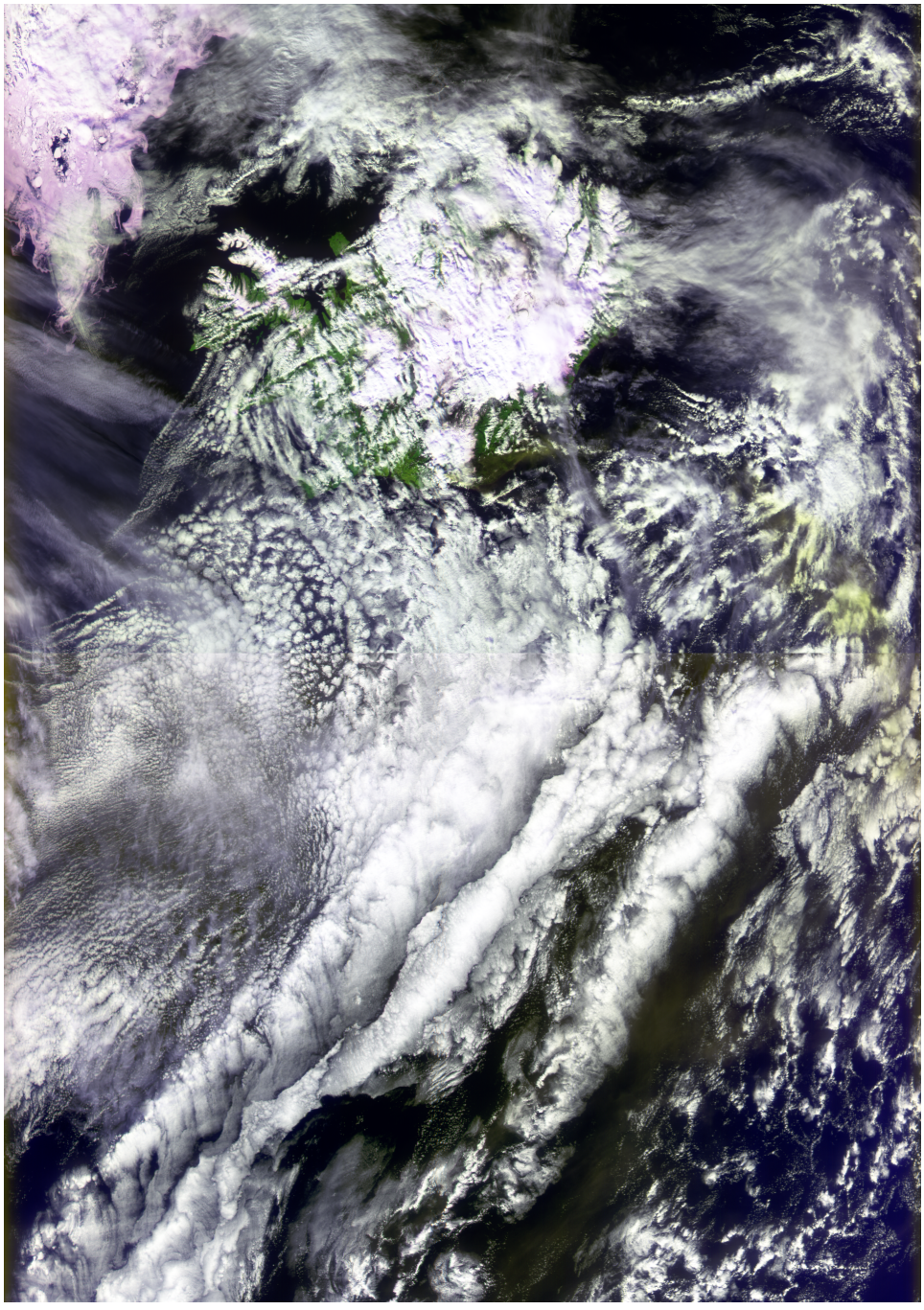

**Figure 3.10:** Example image from the TANSO-CAI instrument on-board GOSAT. Showing the eruption of the Eyjafjallajökull volcano in Iceland in 2010.

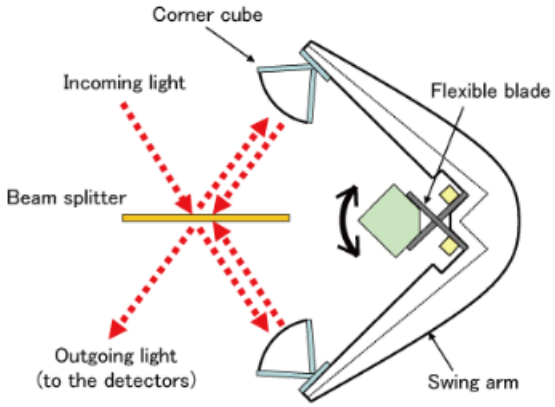


**Figure 3.11:** Schematic of a Michelson interferometer as used for a Fourier transform spectrometer with a double pendulum design such as for GOSAT (NIES, 2009).

(equivalent to 10.5 km projected onto the Earth's surface) (Cogan et al., 2012). The satellite has a ground track repeat cycle of three days.

### 3.6.1 Operational changes and status since launch

Before August 2010 the satellite utilised a 5-point cross-track (CT) scanning pattern. After which the pattern was changed to a 3-point CT pattern where each point was sampled three times. Figure 3.14 shows the GOSAT sampling pattern for the first three days of each month in 2010, clearly highlighting the change in August 2010. GOSAT also has the ability to enter a targeting mode where it can be tasked to specifically point at particular locations which were predetermined. These are usually special target sites such as validation or calibration sites, or emission sources (Kuze et al., 2016). Since 2014 a dithering observation has been used over the Amazon to increase the amount of clear-sky observations as shown in Figure 3.15 compared to the usual sampling technique. This new pattern still uses a 3-point CT approach, except the three repeated observations at each point are separated, allowing the same number of observations to cover more of the Amazon and reduce the likelihood of sampling cloudy scenes. Over the oceans the satellite can be set to operate in a sun-glint mode which involves targeting the location on the water's surface where the incoming sunlight

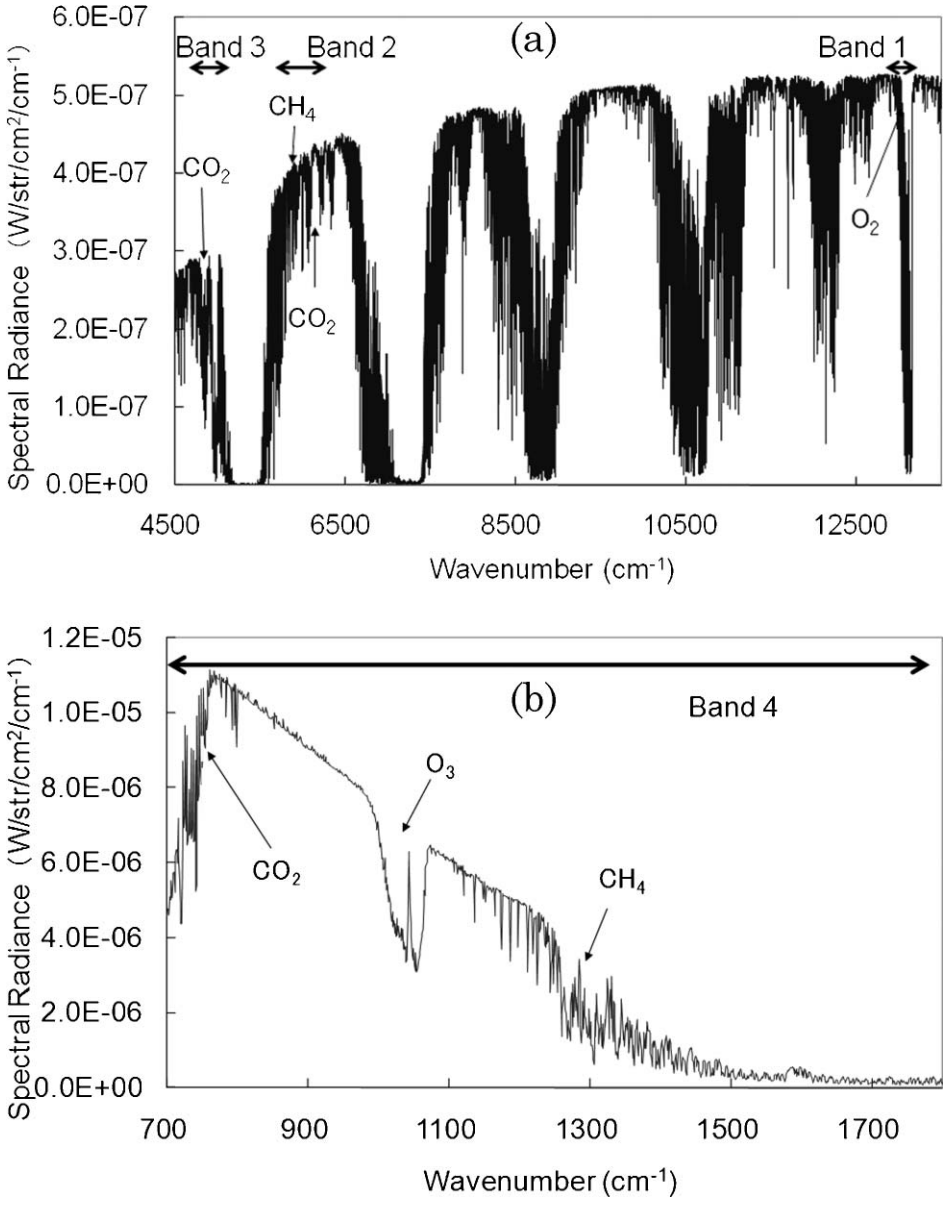


**Figure 3.12:** Simulated spectral coverage of TANSO-FTS. (a) The SWIR region showing bands 1, 2 and 3. (b) The TIR region showing band 4 (Kuze et al., 2009).

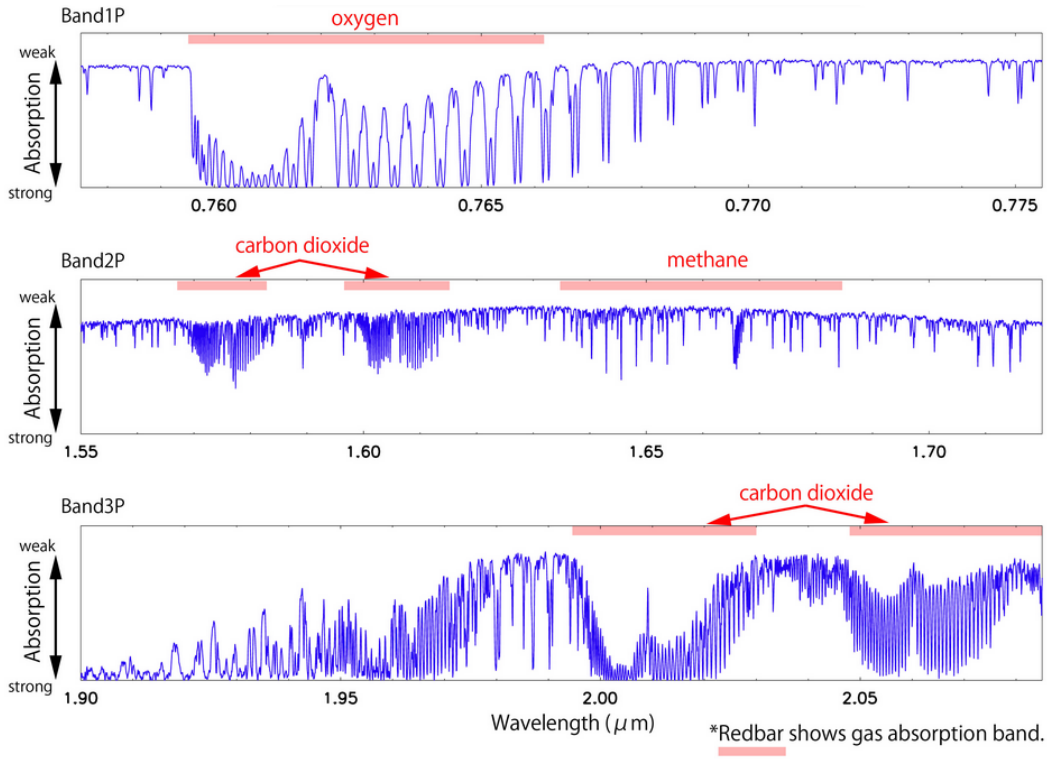


**Figure 3.13:** Example atmospheric spectra measured by GOSAT for bands 1, 2 and 3, indicating the regions where oxygen, carbon dioxide and methane absorption are prominent (Japan Aerospace Exploration Agency, 2009).

is most strongly reflected back at the satellite. This allows limited measurement over the oceans where the surface is generally too dark in the SWIR to make useful measurements, except within these specific sun-glint angle thresholds. The latitudes for which sun-glint measurements are possible will vary throughout the year as the Sun's height in the sky varies.

Since its launch in 2009, GOSAT has encountered three major anomalies which have affected the satellite operation (Kuze et al., 2016). Firstly, between the 24th and 30th of May 2014 the failure of one of the satellite's two solar paddles caused both TANSO-FTS and CAI to cease operations for this short period. Target mode observations were suspended from December the 15th 2014 due to an instability with the primary satellite pointing system, which had slowly been degrading as the satellite aged. These were resumed again on August the 30th 2015 after switching to the secondary pointing system and completing calibration testing. Thirdly, on the 2nd of August 2015 use of the thermal infra-red band of the TANSO-FTS instrument was suspended due to a sudden shutdown of the cryocooler which caused the temperature of the detector to rise from the oper-

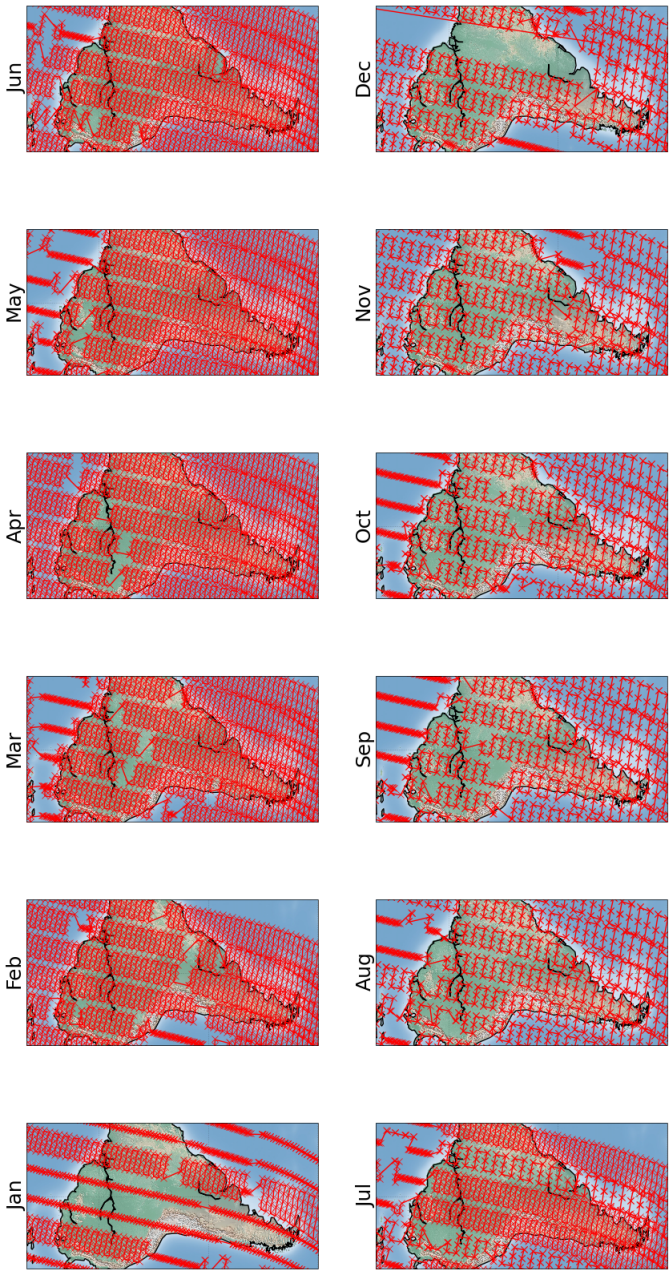


**Figure 3.14:** GOSAT sampling patterns for the 1st, 2nd and 3rd day of each month in 2010.

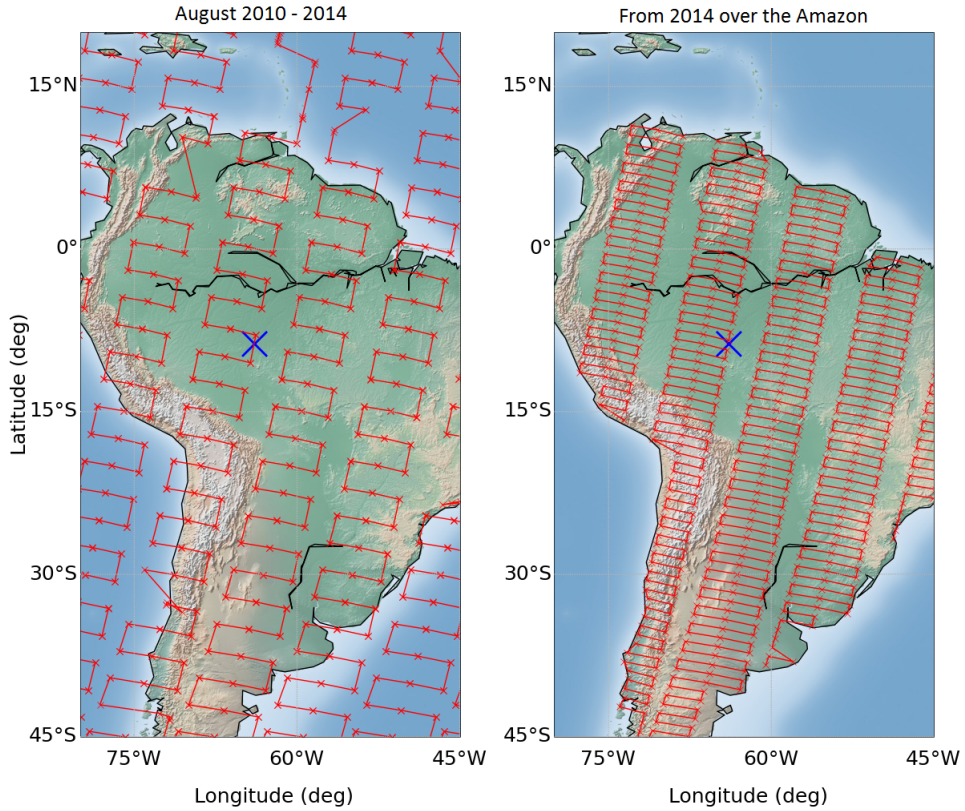


**Figure 3.15:** Example of the GOSAT 3-point CT scanning pattern for the usual case (left) and the newer dithering case (from 2014), on the right.

ational 70 K to ambient temperature. On the whole, despite having surpassed its intended operational lifetime, GOSAT is still performing well after six years, with radiation degradation of TANSO-FTS and CAI becoming very low. Further detailed information can be found in Kuze et al. (2016).

## 3.7 UNIVERSITY OF LEICESTER GOSAT RETRIEVAL ALGORITHMS

### 3.7.1 Optimal estimation retrieval

The retrieval of atmospheric spectra from GOSAT is dependent on many parameters, some of which we are interested in learning, and others which we may or may not already accurately know. This leads to an under-constrained situation where it becomes necessary to introduce additional (a priori) information about the system to keep the solution constrained to realistic values. See O'Dell et al. (2012), Crisp et al. (2012), Boesch et al. (2006), Boesch et al. (2011), Connor et al. (2008), Parker et al. (2011) and Cogan et al. (2012)).

For the retrieval of $XCO_2$ and $XCH_4$ we use a forward model which simulates spectra based on the geometry and state vectors. Here we will detail the use of this for the retrieval of $XCH_4$, although the principle is the same for $XCO_2$. The measurement vector, $\mathbf{y}$, represents the GOSAT radiances and has an associated error $\mathbf{e}$. The state vector, $\mathbf{x}$, is a function of all of the parameters which we wish to retrieve. For our $XCH_4$ retrievals these are $CH_4$, $CO_2$ and scaling factors for $H_2O$, temperature, surface albedo and a spectral shift. The parameters which we are not retrieving, but which the measurement vector still depends on, are given by the vector $\mathbf{b}$. We can relate the measured spectra to the parameters which determine it by use of a Forward function $\mathbf{F}$, given by Equation (3.28).

$$\mathbf{y} = \mathbf{F}(\mathbf{x}, \mathbf{b}) + \mathbf{e}. \tag{3.28}$$

The Forward model consists of three main modules, a radiative transfer model, a solar model and an instrument model. These are used within the main retrieval to describe the spectrum and to generate the noise with respect to the instrument line shape when simulating spectra.

The measurements are non-linear so we are required to first linearise the Forward model before we can utilise it; and we do that around a reference state $\mathbf{x}_0$. Linearising Equation (3.28) will give,

$$\mathbf{y} - \mathbf{F}(\mathbf{x}_0) = \frac{\partial \mathbf{F}(\mathbf{x})}{\partial \mathbf{x}}(\mathbf{x} - \mathbf{x}_0) + \mathbf{e}, \tag{3.29}$$

where the partial derivative gives the sensitivity of the Forward model to the change in the state vector $\mathbf{x}$. This quantity is called the Jacobian and is given by $\mathbf{K}$. Figure 3.16 shows examples of the Jacobian for $CH_4$ for the three SWIR GOSAT bands. This illustrates that the measured spectra is sensitive to $CH_4$ in bands 2 and 3, which is what we would expect as these bands were chosen for GOSAT because they are sensitive to $CH_4$. Band 1 is the Oxygen A Band which has no dependence on $CH_4$; which is shown by the Jacobian having a value of zero throughout the band (the measured spectra in this band has no sensitivity to $CH_4$).

The variance in the state vector for each level of the atmosphere can be expressed with a probability density function where the value will lie within a Gaussian distribution. In reality the distribution for each level will rely on the variance at the levels either side of it because if we have a high value of $CH_4$ in one atmospheric level then we would expect to have a high value in the adjacent level (not simply

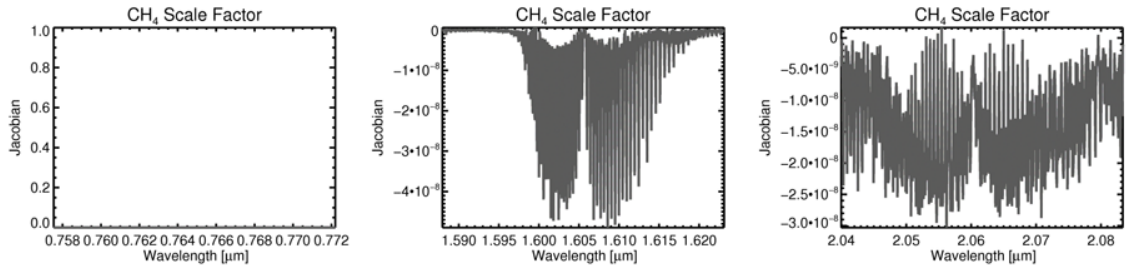


**Figure 3.16:** Showing the three SWIR GOSAT TANSO-FTS bands with example Jacobians for $CH_4$ at each band (Cogan, 2013).

a random concentration given by the Gaussian distribution). We can express the correlation between the different elements of a particular state vector with a covariance matrix and the correlation between these different elements is given in Equation (3.30). The covariance of the measured parameter is expressed using the measurement covariance matrix $\mathbf{S}_y$; and for the a priori data $\mathbf{S}_a$.

$$\mathbf{S}_{ij} = \epsilon\{(\mathbf{y}_i - \hat{\mathbf{y}}_i)(\mathbf{y}_j - \hat{\mathbf{y}}_j)\} \neq 0, \tag{3.30}$$

where $\mathbf{S}_{ij}$ represents the covariance between $\mathbf{y}_i$ and $\mathbf{y}_j$, and $\epsilon$ is the expected value operator (Rodgers, 2000).

As previously mentioned, when we have an under-constrained scenario it is necessary to include extra information to constrain our solution to realistic values. This is the case when we have fewer measurements than unknown parameters in the state vector $\mathbf{x}$, and the information we introduce is called "a priori" information. The optical estimation approach which our retrieval algorithm follows uses this a priori information to estimate the state vector and obtain reasonable solutions to the state of the system. However, there is no unique solution so we have to settle for the optimal solution. There are two ways we can consider the optimal solution; by finding the most probable state (where Equation (3.31) is satisfied) or the expected state $\hat{\mathbf{x}}$, as given by Equation (3.32).

$$\frac{\mathrm{d}\mathbf{P}(\mathbf{x},\mathbf{y})}{\mathrm{d}\mathbf{x}} = 0, \tag{3.31}$$

$$\hat{\mathbf{x}} = \int \mathbf{x}\mathbf{P}(\mathbf{x}|\mathbf{y})\mathrm{d}\mathbf{x}, \tag{3.32}$$

where $\mathbf{P}$ gives the probability density function.

The most probable state is found by minimising the cost function, $\chi^2$, which represents the minimum costs obtained by optimising the difference between the simulated and measured spectra, as well as the difference between the a priori and the state vector (Rodgers, 2000). We define the cost function as follows,

$$\chi^2 = (\mathbf{y} - \mathbf{K}_x)^T \mathbf{S}_y{}^{-1}(\mathbf{y} - \mathbf{K}_x) + (\mathbf{x} - \mathbf{x}_a)^T \mathbf{S}_a{}^{-1}(\mathbf{x} - \mathbf{x}_a), \tag{3.33}$$

where $T$ denotes the transpose matrix and $\mathbf{x}_a$ is the a priori estimate of the state vector. From this we can define the most probable state for a linear problem as,

$$\hat{\mathbf{x}} = \mathbf{x}_a + (\mathbf{K}^T \mathbf{S}_y{}^{-1} \mathbf{K} + \mathbf{S}_a{}^{-1})^{-1} \mathbf{K}^T \mathbf{S}_y{}^{-1} (\mathbf{y} - \mathbf{K}\mathbf{x}_a), \tag{3.34}$$

Using the most probable state we can define the Gain matrix, $\mathbf{G}$, which represents how the solution to the state vector is affected by changes in the measurement vector $\mathbf{y}$. The Gain matrix is given by Equation (3.35) and we can express the most probable state vector in terms of the Gain matrix as shown in Equation (3.36).

$$\mathbf{G} = \frac{\mathrm{d}\hat{\mathbf{x}}}{\mathrm{d}\mathbf{y}} = (\mathbf{K}^T \mathbf{S}_y{}^{-1} \mathbf{K} + \mathbf{S}_a{}^{-1})^{-1} \mathbf{K}^T \mathbf{S}_y{}^{-1}, \tag{3.35}$$

$$\hat{\mathbf{x}} = \mathbf{x}_a + \mathbf{G}(\mathbf{y} - \mathbf{K}\mathbf{x}_a). \tag{3.36}$$

The retrieval uses an iterative approach to obtain the optimal solution because the Jacobian is dependent on the state vector. It is therefore necessary to rerun the Forward model and recalculate the Jacobians for each iteration step as we aim to minimise the cost function. If the retrieval is linear we could use a Gauss-Newton iteration solution, however if the optimal solution is far from the true solution or if the retrieval is too non-linear then we must use a Levenberg-Marquardt approach instead. The iteration in this case is given by,

$$\mathbf{x}_{i+1} = \mathbf{x}_i + [(1+\gamma)\mathbf{S}_a{}^{-1} + \mathbf{K}_i{}^T \mathbf{S}_e{}^{-1} \mathbf{K}_i]^{-1} (\mathbf{K}_i{}^T \mathbf{S}_e{}^{-1} [\mathbf{y} - \mathbf{F}(\mathbf{x}_i)] - \mathbf{S}_a{}^{-1} [\mathbf{x}_i - \mathbf{x}_a]), \tag{3.37}$$

where the a priori state vector $\mathbf{x}_a$ is used for the first iteration $\mathbf{x}_0$; $\mathbf{S}_e$ is the covariance matrix of $\mathbf{e}$, and $\gamma$ is the Levenberg-Marquardt Algorithmic parameter (Gavin, 2011). The parameter $\gamma$ is changed after each iteration by an amount which depends on the cost function. If the cost function increases after an iteration, gamma is increased in an attempt to deduce the cost function and the iteration is repeated. If the cost function decreases then gamma can be decreased, the state vector updated and the next iteration can begin.

After each iteration three tests are performed to determine if the retrieval has converged to the optimal solution. The first test takes the cost function from the latest iteration plus the old cost function and compares this with the cost function forecast plus the old cost function. This is expressed as a ratio. If the ratio is less than 0.25 then the model has diverged away from the measured spectra, if it is between 0.25 and 0.75 then the model has become closer to the measurement but not close enough. If the ratio is larger than 0.75 then the model and measurement are considered to have converged. The second test compares the error variance derivative, $d\sigma^2$, of the current iteration with that of the previous. Convergence has been achieved when the difference between these is less than or equal to the number of state vector elements. The error variance derivative is given as,

$$d{\sigma_i}^2 = d\mathbf{x}_{i+1}^T \hat{\mathbf{S}}^{-1} d\mathbf{x}_{i+1}, \tag{3.38}$$

where $\hat{\mathbf{S}}$ is the covariance of the retrieved state. The third condition, which is not required for convergence but is used as grounds to remove retrievals, considers the goodness of fit between the model and the measured spectra. We calculate the goodness of fit, $\chi^2$, which is done by considering the residual between the model and the measured GOSAT spectra. If $\chi^2 < 1$ the fit is considered to be good. Between 1 - 10 the fit is considered to be reasonable; and above 10 the fit is considered to be poor.

The column averaged $CH_4$ mixing ratio, $XCH_4$, can be obtained from the retrievals by using the pressure weighting operator $\mathbf{h}$ (O'Dell et al., 2012) which is zero for all non-$CH_4$ elements and this acts to collapse the retrieved $CH_4$ profile down into $XCH_4$.

$$XCH_4 = \mathbf{h}^T \hat{\mathbf{x}}. \tag{3.39}$$

Finally the error for the measurement can be calculated. For this we need to consider the column averaging kernel, $\mathbf{a}$, which is used to express the ability of the retrieval to constrain the solution to the true state of the system, and is given in Equation (3.40). The averaging kernel, $\mathbf{A}$, is given by Equation (3.41) and repre-

sents whether adding one particle to a particular level of the state vector yields in that level increasing by a value of 1 after the retrieval. It is ideally 1 in the diagonal and 0 elsewhere, as none of the other levels would see an increase in an ideal case.

$$\mathbf{a}^T = \mathbf{h}^T\mathbf{A}, \tag{3.40}$$

$$\mathbf{A} = \frac{\mathrm{d}\hat{\mathbf{x}}}{\mathrm{d}\mathbf{x}} = \mathbf{S}\mathbf{K}^T\mathbf{S}_e\mathbf{K}, \tag{3.41}$$

where **S** is the a posteriori error covariance, given by,

$$\mathbf{S} = (\mathbf{K}^T\mathbf{S}_e\mathbf{K} + \mathbf{S}_a{}^{-1})^{-1}, \tag{3.42}$$

and finally the $XCH_4$ error variance can be expressed as,

$$\boldsymbol{\sigma}^2{}_{XCH_4} = \mathbf{h}^T\mathbf{S}\mathbf{h}. \tag{3.43}$$

### 3.7.2 UoL full physics retrieval

The University of Leicester Full Physics retrieval algorithm (UoL-FP) is used to retrieve column information for $CO_2$ and $CH_4$. The retrieval is based on the algorithm which was intended for NASA's Orbiting Carbon Observation satellite (OCO) but has been modified for use with GOSAT data (O'Dell et al., 2012). Firstly, all GOSAT measurements undergo a pre-filtering process to remove scenes with a low signal to noise ratio and to take only measurements over land surfaces. A basic cloud screening process based on the Oxygen A Band at 760 nm is then used to remove the scenes which contain high levels of scattering. The retrieval process then takes differing approaches for both $CO_2$ and $CH_4$ to retrieve both gases, and following this it is necessary to perform post-filtering.

Before the main optical estimation retrieval is attempted it is necessary to do a preliminary cloud screening step to remove the scenes which are the most obviously cloudy and which would have very little chance of converging to a re-

alistic solution. This cloud screening method involves measuring the surface pressure using the oxygen A band (GOSAT band 1). This band ranges between 759 - 771 nm. This region is used because the absorption lines depend only on the absorption due to $O_2$, the scattering due to clouds and aerosol, and the geometry of the observation. The geometry is known accurately and the profile of $O_2$ is also very well defined in the atmosphere; allowing us to perform a quick retrieval of the surface pressure if we assume there is no scattering due to clouds and aerosols (Taylor et al., 2012). In reality there will be errors introduced in the measured surface pressure due to clouds and aerosols and these will increase with the aerosol and cloud optical depths. We therefore compare this measured surface pressure with that from a model provided by the European Centre for Medium-Range Weather Forecasts (ECMWF) and if the difference between these two surface pressures is above a threshold value (30 hpa) then the scene is said to be too cloudy and is not further analysed.

### 3.7.3 Leicester Proxy $XCH_4$ retrieval

At the University of Leicester we use different approaches to retrieve $XCH_4$ and $XCO_2$. The $CH_4$ retrieval is much simpler and does not require the use of the UoL-FP retrieval, meaning we can retrieve methane quickly and relatively easily. The method is simpler because we are able to remove the effects of aerosol and clouds and therefore do not need to deal with them in the retrieval. Following the preliminary cloud screening, we use GOSAT band 2 we do a quick retrieval on both methane and carbon dioxide at the same time, as described in Section 3.7.1. These measurements will be incorrect because we do not take into account the effects of clouds and aerosol, but importantly we can assume these effects to be the same on both the $CH_4$ and $CO_2$ retrievals. We can make this assumption because $CO_2$, at 1.61 $\mu$m, and $CH_4$, at 1.65 $\mu$m, are spectrally very close. Post-filtering checks are performed to check that the outcome of the retrievals were successful and that the Chi-squared values for $XCH_4$ and $XCO_2$ are between 0.4 and 1.5. In addition to these checks, we include thresholds

on the a posteriori error of 20 ppb and 3 ppm for $XCH_4$ and $XCO_2$ respectively. We also remove all soundings where the raw retrieved $XCH_4$ and $XCO_2$ values fall below 1650 ppb and 350 ppm respectively (Parker, 2015). We then use the "quickly retrieved" $XCO_2$ as a proxy for the light path by taking the $XCH_4$ retrieval and dividing through by the $XCO_2$ retrieval to remove the effects of clouds and aerosols. The final "Proxy $XCH_4$" is calculated by multiplying this result by a modelled $XCO_2$ value as shown in Equation (3.44). This method does introduce a dependency on the error in the modelled $XCO_2$ (Schepers et al., 2012).

$$\text{Proxy } XCH_4 = \frac{XCH_4}{XCO_2} \times \text{Model } XCO_2, \tag{3.44}$$

The main disadvantage of the Proxy method is its reliance on an accurate and unbiased model $XCO_2$. To mitigate and quantify the uncertainty from the model $XCO_2$ in the Proxy $XCH_4$ retrieval, we use a model ensemble as described in Parker et al. (2015). Here it is found that each individual $XCO_2$ model used in the ensemble agrees well with validation data (discussed in Section 3.8), with correlation coefficients ranging from 0.94 to 0.97. However, none of the models are shown to be a better choice than the others. The median $XCO_2$ value of the ensemble is found to have a smaller scatter against the validation data (with a standard deviation of 0.92 ppm) than any of the individual models, whilst maintaining a small bias of 0.15 ppm. The models used in this ensemble are GEOS-Chem from the University of Edinburgh, LMDZ/MACC-II and NOAA CarbonTracker as described in Parker et al. (2015).

## 3.8 VALIDATION WITH GROUND-BASED MEASUREMENTS

With GOSAT we aim to measure sources and sinks of $CO_2$ and $CH_4$ over tropical regions and determine the magnitude and location of fluxes between the tropical land sink and the atmosphere. To achieve this using satellites we need high

accuracy and precision in the order of 2.5 ppm on an $8^\circ \times 10^\circ$ footprint, corresponding to errors of less than one percent. To validate both the Proxy $XCH_4$ and $XCO_2$ we use measurements from the Total Carbon Column Observing Network (TCCON), which is a network of ground based Fourier transform spectrometers which measure columns of $CO_2$, $CH_4$ and other atmospheric gases (Wunch et al., 2011). Comparisons of our data with TCCON agree relatively well for the majority of TCCON sites (see Figure 3.17), showing a bias of 4.80 ppb with a standard deviation of 13.44 ppb across all sites (Parker et al., 2015). We see that our uncertainties are less than the 1% required (Cogan et al., 2012). Currently there are no TCCON sites in the tropics, or South America, which means we are currently unable to validate our uncertainties over the regions we are most interested in using TCCON (a map with the locations of TCCON sites is shown as Figure 3.18). A site at Manaus in Brazil temporarily operated for the final three months in 2014 but is currently not operational (Dubey et al., 2014).

Reuter 2013, conducted a study which compared seven $XCO_2$ retrieval algorithms for SCIAMACHY and GOSAT (Reuter et al., 2013). This included the University of Leicester's (UOL-FP v3.0, (Boesch et al., 2006; Boesch et al., 2011)), the ACOS v2.9 algorithm from the University of Colorado (O'Dell et al., 2012; Crisp et al., 2012), BESD v01.00.01 from the University of Bremen (Reuter et al., 2010; Reuter et al., 2011), the NIES v02.xx and PPDF-D algorithms from the NIES team in Japan (Yoshida et al., 2011; Oshchepkov et al., 2012), RemoteC v1.0 from the Karlsruhe Institute of Technology (Butz et al., 2011) and the WFMD v2.2bcv7b also from the University of Bremen (Schneising et al., 2012; Heymann et al., 2012). The study compared the different algorithms with TCCON sites and found that the UoL-FP retrieval algorithm had an average single measurement precision of 2.3 ppm, which roughly relates to an uncertainty of 0.59% using a value of 390 ppm for the atmosphere (Reuter et al., 2013). This study shows that the uncertainties in UoL v3.0 retrievals of $CO_2$ were of the precision required (at the TCCON sites) and also shows the retrieval to have a comparable precision with the work of the other groups. Version 6.0 of the UoL retrieval is an updated version which has been further analysed by Parker et al. (2015).

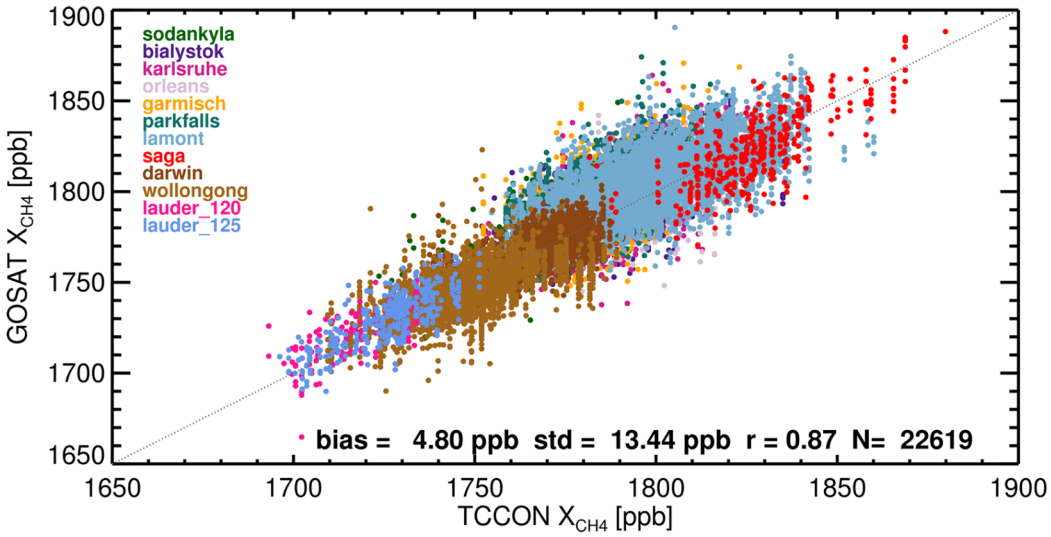


**Figure 3.17:** Correlation plot showing the $CH_4$ measured by GOSATv6 vs that measured by the TCCON ground based sites. The data was matched so that the GOSAT measurements were required to be within $\pm 5°$ of the TCCON site and within two hours of the measurement taken by TCCON. The different TCCON sites are colour coded as given in the figure (Parker et al., 2015).

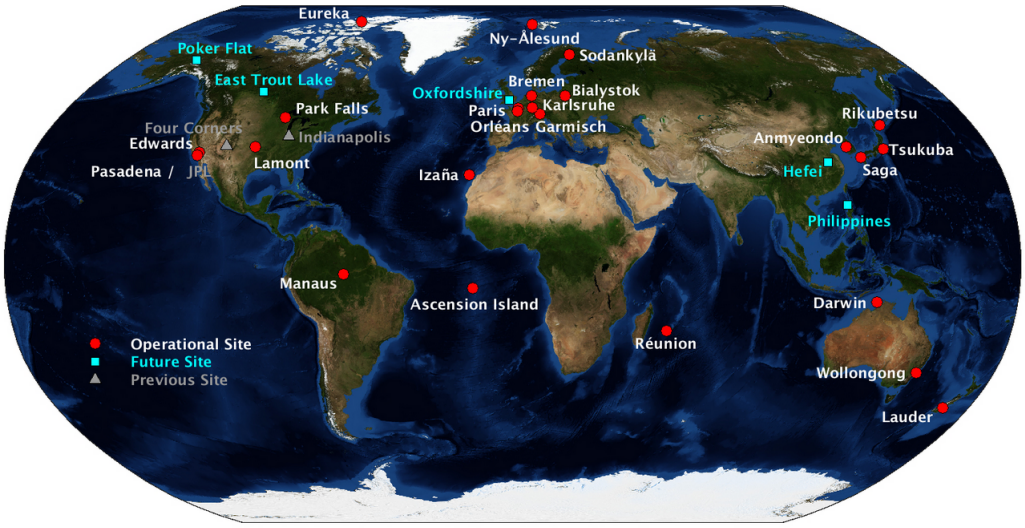


**Figure 3.18:** Map showing the location of current, future and past TCCON site locations in 2014 (Wunch et al., 2011).

# 4 VALIDATION OF GOSAT $XCH_4$ IN THE AMAZON USING IN SITU AIRCRAFT MEASUREMENTS

## 4.1 INTRODUCTION

Satellites such as GOSAT are capable of measuring $XCH_4$ on a global scale, providing valuable insights into tropical regions where in situ measurements are sparse. Currently there is much disagreement in the tropics between wetland models with regards to the areal extent of wetlands and their $CH_4$ emissions in both space and time. Melton et al. (2013) describe this, in their words "extensive disagreement", by comparing ten different wetland models of varying complexity and operational methods. They further write that atmospheric $CH_4$ observation datasets are inadequate to evaluate typical model fluxes and that this severely restricts our ability to model global wetland $CH_4$ emissions. Validation of GOSAT in the Amazon is now especially important as more studies begin to assimilate this satellite data into atmospheric $CH_4$ models (Fraser et al., 2013; Alexe et al., 2015) and find that tropical South America and tropical Asia yield the largest differences between the GOSAT data and forward model output (Fraser et al., 2014). Validating these satellite measurements is therefore critical to understand if the differences between models and satellites can reflect new insights into tropical methane fluxes that can improve emission models.

GOSAT is typically validated using TCCON stations, of which there are none in South America and very few in the tropics in general. Presented in this chapter are the first known attempts to validate GOSAT data in the Amazon. This validation involves the use of aircraft profile data which was explicitly measured for this purpose as part of the Amazonian Carbon Observatory (ACO) project

which was led by the University of Leicester. Since these data are new, the profiles themselves are first examined and the seasonal and spatial differences between profiles are discussed. The method used for comparing aircraft profiles with GOSAT $XCH_4$ measurements is then described. This involves the extension of the profiles with modelled stratospheric data, from which the total column is then calculated. The uncertainties involved with this method are evaluated and placed in context with the uncertainties expected from GOSAT. A comparison between the aircraft profiles and GOSAT is then presented and the effects of altering the co-location and model $XCO_2$, which is inherent in the GOSAT Proxy $XCH_4$ retrieval process, are examined.

## 4.2 AIRCRAFT DATA

As part of the NERC/FAPESP (National Environment Research Council/Fundação de Amparo à Pesquisa do Estado de São Paulo) Amazonian Carbon Observatory (ACO) Project, air samples from aircraft have been collected approximately once a month since January 2013 at two sites in the Amazon. The aircraft captured air samples in 0.7 litre flasks, which were pressurised to 2.7 atm, whilst descending in a spiral starting at approximately 7.5 km asl (above sea level) and ending at approximately 300 m asl; typically these consist of 17 separate flask measurements which are approximately equally spaced in altitude (Gatti et al., 2014). The samples were taken between 12:00 and 13:00 local time, making them comparable in time with measurements from the GOSAT satellite at approximately 13:00 local time, and were only performed in clear sky conditions. The flasks were analysed at the IPEN (Instituto de Pesquisas Energéticas e Nucleares) and INPE (Instituto Nacional de Pesquisas Espaciais) laboratories in Brazil where the gases were measured relative to the WMO X2004 scale. They measure the greenhouse gases $CH_4$ and $CO_2$, as well as CO, $SF_6$ and other gases. The uncertainty on these measurements of $CH_4$ is $\pm 2$ ppb, as defined by repeated measurements of whole air sampled from a high

pressure cylinder. Figure 4.1 shows the Mitsubishi MU-2 aircraft used at one of the aircraft sites and a close-up of the air inlet pipe and the instrument used on-board the aircraft to collect the air samples.

**Figure 4.1:** Top: The aircraft used to perform measurements for the Amazonian Carbon Observatory project. Bottom left: Close-up of the air inlet. Bottom right: Air collection flasks and control box.

The two ACO sites are located near Rio Branco (RBH) at the western side of Brazil, and near Salinópolis (SAH) on the eastern coast of Brazil next to the Atlantic Ocean. They were chosen to best represent air before and after travelling across the Amazon Basin. This will be true most of the time since air entering the Amazon basin is dominated by tradewind easterlies coming from the tropical Atlantic Ocean (Miller et al., 2007). Figure 4.2 shows the locations of the sites and backward trajectories calculated from the NOAA HYSPLIT model (HYbrid Single-Particle Lagrangian Integrated Trajectory) (Draxler and Hess, 1997). These trajectories were calculated from Rio Branco at 4.5 km altitude and show the typical route taken by air over the previous five days for an ensemble of releases which are calculated by altering the altitude, latitude and longitude by a small amount. This date was chosen as an example due to its good representation of the average wind trajectories and because it illustrates how air arriving at Rio Branco has typically travelled across the entire Amazon from the direction of Salinópolis.

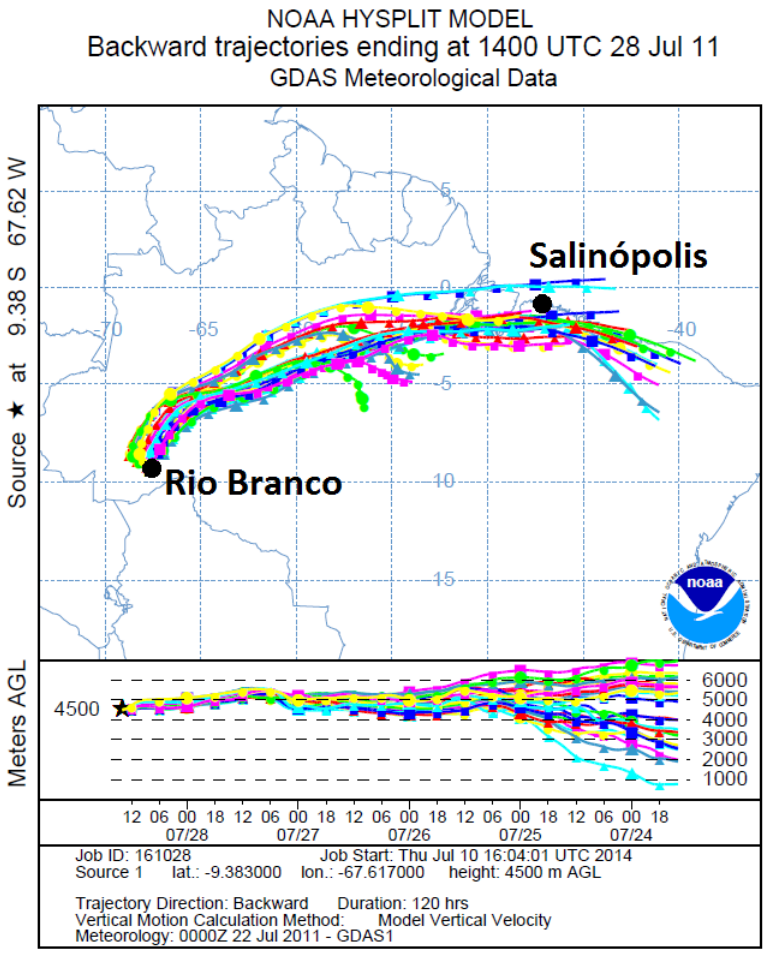


**Figure 4.2:** 120-hour back-trajectories from Rio Branco at 4.5 km on the 28th July 2011 at 14:00 UTC; calculated using the HYSPLIT model.

Figures 4.3 and 4.4 show the aircraft profiles at Rio Branco and Salinópolis respectively, for $CO_2$, $CH_4$ and CO between January and August 2013.

## 4.3 DIFFERENCES BETWEEN RIO BRANCO AND SALINÓPOLIS

Figure 4.5 shows every ACO aircraft profile up until the end of June 2015 color-coded to represent the season in which they were measured (blue for the wet season, red for the dry season, gray for intermediate months). The wet season is defined to be approximately between January and April, the same as was used

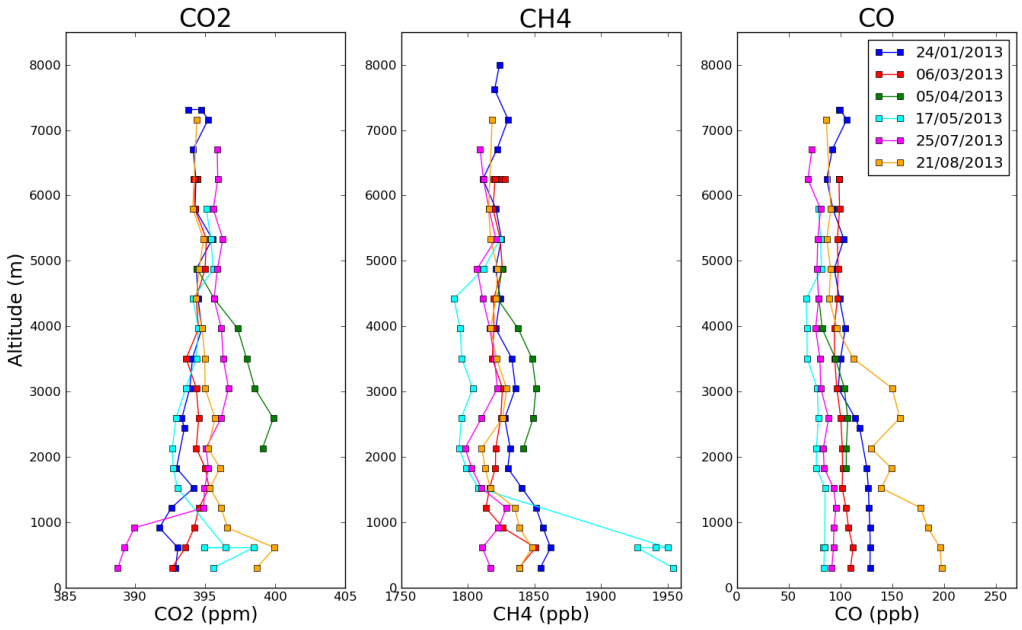


**Figure 4.3:** ACO aircraft profiles between January and August 2013 at Rio Branco, showing $CO_2$ on the left in ppm, $CH_4$ in the middle in ppb, and CO on the right, also in ppb.

by Gatti et al. (2014). Gatti et al. (2014) defined the dry season as the rest of the year, whilst I have excluded the two months between each season to account for yearly variations in the timing and length of the seasons, ensuring that 'dry season' measurements are not affected by the wet season overrunning or beginning earlier than usual (therefore the dry season is defined as July-October).

The profiles in Figure 4.5 from the background site Salinópolis typically have lower values of $CH_4$ throughout most of the altitude range than those at the inland site (Rio Branco), especially for the first few levels above the surface (average $CH_4$ across all altitude levels and profiles is 1834 ppb for RBH and 1815 ppb for SAH). This difference in profile shape arises due to RBH being in the Amazon Basin where the surface air is likely influenced by local wetlands, whilst the coastal air measured at SAH will be relatively free from wetland influence. The wet and dry season profiles are more similar at SAH (1812 ppb and 1811 ppb respectively), while there is a more distinct separation at RBH (1840 ppb for the wet season and 1825 ppb in the dry season), with the profiles measured in the wet season containing elevated $CH_4$ concentrations in the low and mid-altitude range. Enhanced $CH_4$ emissions in the wet season are to be expected due to

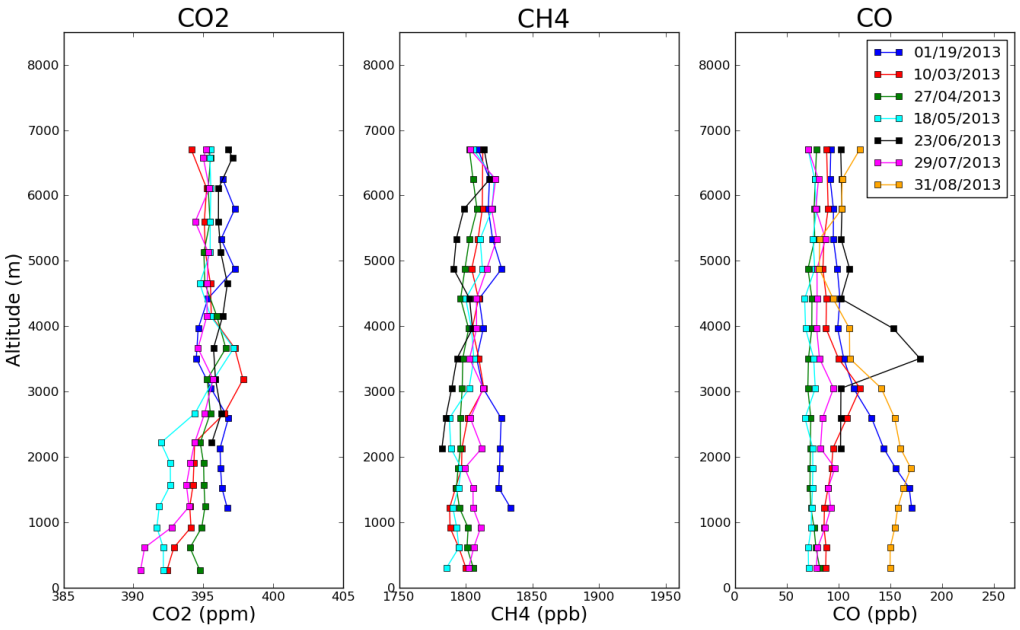


**Figure 4.4:** ACO aircraft profiles between January and August 2013 at Salinópolis, showing $CO_2$ on the left in ppm, $CH_4$ in the middle in ppb, and CO on the right, also in ppb.

the increased flooded area from seasonal wetlands. The profiles show that during the wet season there is atmospheric uptake of $CH_4$ as the air travels from the background site to the inland site at mid-altitudes, whilst there is less of a difference near the surface and at higher altitudes.

## 4.4 AMAZONICA FLIGHTS

Since GOSAT was launched in 2009 and the ACO flights only started in 2013; additional aircraft measurements are used from four sites across the Amazon Basin performed during the AMAZONICA project (Gloor et al., 2012; Wilson et al., 2016). These flights were performed by the same team as the ACO flights and use the same sampling and analysis techniques. The only difference being that AMAZONICA flights used a different aircraft which allowed them to only reach an altitude of 4.5 km instead of 7.5 km. These flights typically sampled 12 separate altitudes instead of the 17 of ACO flights as a result. The sampling sites

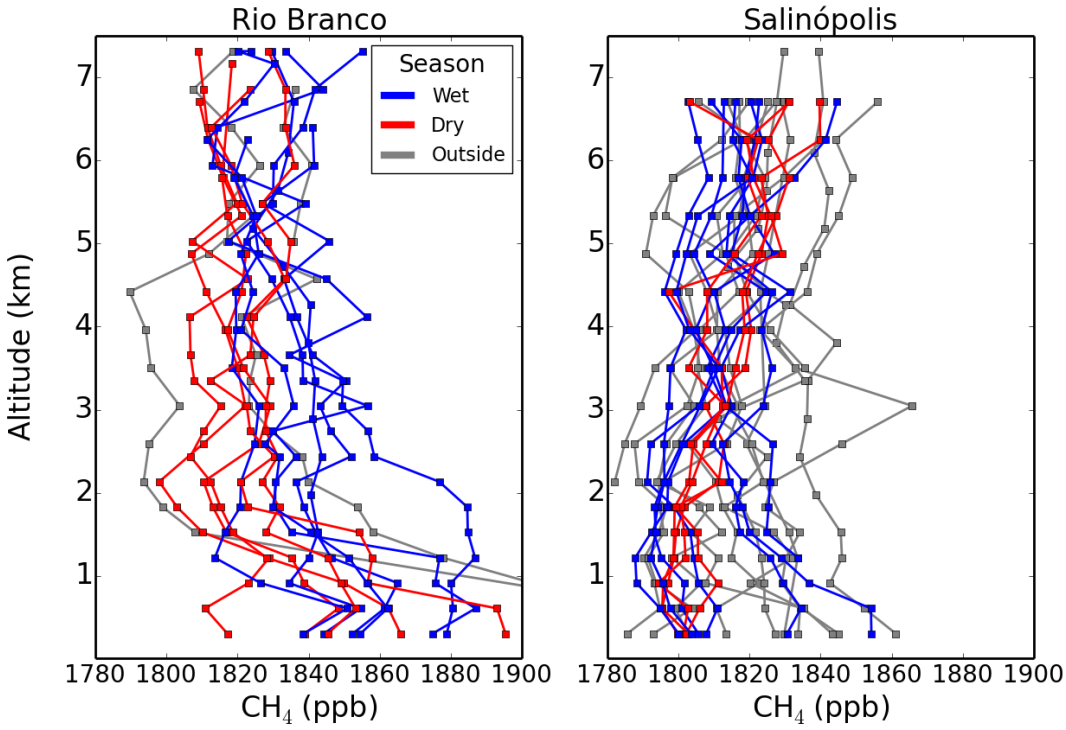


**Figure 4.5:** Amazonian Carbon Observatory aircraft measured $CH_4$ vertical concentration profiles taken between 2013 and June 2015 at Rio Branco and Salinópolis. Profiles measured between January-April are shown in blue, July-October in red, and May-June and November-December in grey.

for AMAZONICA profiles are at Rio Branco (RBA), Tabatinga (TAB), Alta Floresta (ALF) and Santarém (SAN). The Rio Branco flights were not measured at exactly the same location as for the ACO profiles at Rio Branco since these were moved to coincide with the GOSAT overpass pattern. The flights operated at all four sites from 2010 although started as early as 2003 at Santarém. They were typically performed twice monthly (where weather conditions allowed), and continued at all four sites until the end of 2012. As of 2016 the flights are still ongoing at Rio Branco. The locations of these four sites, in addition to the ACO sites, are shown in Figure 4.6.

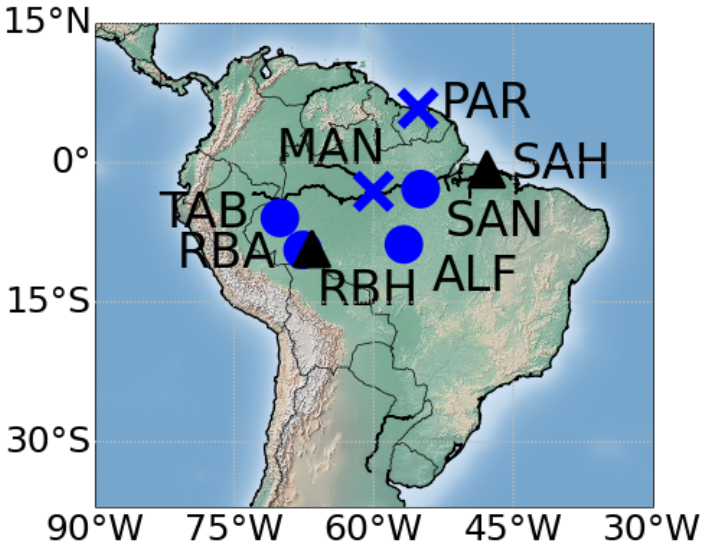


**Figure 4.6:** Map showing the locations of AMAZONICA sites Rio Branco (RBA), Tabatinga (TAB), Alta Floresta (ALF) and Santarém (SAN) as blue circles, in addition to ACO sites Rio Branco (RBH) and Salinópolis (SAH) as black triangles. Additionally the ground-based TCCON site at Manaus (MAN) and TCCON-like site at Paramaribo (PAR) are also shown as blue crosses.

## 4.5 CALCULATION OF AIRCRAFT TOTAL COLUMN XCH$_4$

GOSAT measures the total column XCH$_4$ of the atmosphere, resulting in a single value which represents the entire atmospheric profile and is dependent on the sensitivity of the satellite to measure CH$_4$ at each altitude. The aircraft profiles are a set of point measurements ranging from 300 m to either 4.5 km or 7.5 km. To compare the two it is necessary to calculate the total column XCH$_4$ from the aircraft profiles. They must therefore be extended to cover the entire atmosphere vertically. After extending the aircraft profiles, the XCH$_4$ can then be calculated and the GOSAT averaging kernels applied to account for the varying sensitivity of the satellite with altitude. The method of extending the aircraft profiles is similar to that detailed by Miyamoto et al. (2013). The lowest aircraft measurement value is extended down to the surface, the region between the aircraft profile and the tropopause is extrapolated upwards, and a modelled CH$_4$ profile is used for the stratosphere.

### 4.5.1 Extension of aircraft profiles in the troposphere

In the tropics the troposphere typically corresponds to the lowest-most 15 km of the atmosphere. The aircraft profile needs to be extended in two directions. Firstly, the mole fraction between the lowermost aircraft measurement and the surface is assumed to hold the same value as the lowest aircraft measurement. This is reasonable for mid-day measurements because we expect there to be strong vertical mixing in the planetary boundary layer by 13:00 hours and the aircraft profiles already extend down as far as 300 m asl. Secondly, the mole fractions throughout the altitude range between the uppermost aircraft measurement and the tropopause are assumed to be the same as at the highest aircraft measurement level since it is expected that at these higher altitudes the air will have become more well-mixed.

The tropopause altitude is calculated from ECMWF ERA Interim data using the method outlined in Reichler, Dameris, and Sausen (2003), which uses a thermal definition of the tropopause based on a threshold lapse-rate. The tropopause is defined as the lowest level at which the lapse-rate decreases to 2°K per km or less, provided that the average lapse-rate between this level and all higher levels within 2 km does not exceed 2°K per km. The ECMWF data is used to calculate the tropopause height at the location and time of each aircraft profile. Given the rapid decrease of $CH_4$ mole fraction in the stratosphere (Wunch et al., 2010), the tropopause height is a very sensitive parameter in constructing a total column using aircraft data. To address this, I have compared our calculated tropopause altitudes with values from the NOAA NCEP/NCAR Reanalysis 1 dataset (Kalney et al., 1996) for every flight. Figure 4.7 shows the ECMWF temperature profiles at Salinópolis for 11 flight dates. The NCEP tropopause height is shown in blue, whilst the calculated altitude is shown in red. This shows that generally the calculated value is closer to where we would expect the tropopause height to be (where the temperature is lowest throughout the altitude range plotted). We would expect to be better than NCEP in this comparison since I am directly calculating the tropopause height from the ECMWF profiles themselves, whilst NCEP

use alternative models and data for their calculation. Average differences between the two tropopause heights are found to be a few hundred meters at all sites, ranging from 359±458 m to 763±395 m (uncertainties are the one sigma standard deviations of the differences). Typically, NCEP is higher than the values I have calculated, as illustrated in Figure 4.8, which shows histograms of this difference at each site (calculated for each flight). Although examination of the profiles suggests that the results are correctly calculating the tropopause height from the ECMWF data, and that this difference is not due to the method calculating the height at too low an altitude.

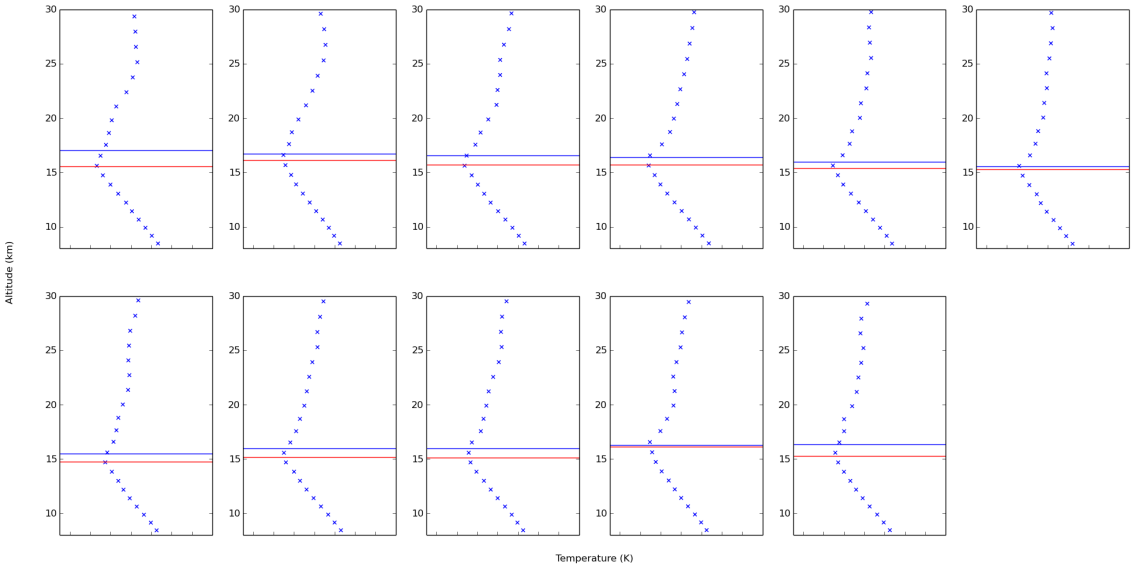


**Figure 4.7:** ECMWF temperature profiles at Salinópolis for 11 flight dates, showing the calculated tropopause height in red and the NCEP tropopause height in blue.

### 4.5.2 Extension of aircraft profiles in the stratosphere

For the stratosphere I use a dedicated stratospheric model. This full chemistry simulation (run ID 570) of the TOMCAT atmospheric chemistry model from the University of Leeds was tailored for the stratosphere (Chipperfield, 1999). This model run is constrained by observed global monthly mean surface $CH_4$ mole fractions and simulates atmospheric transport based on wind and transport fields from the ECMWF ERA-Interim reanalysis, whilst also simulating the loss

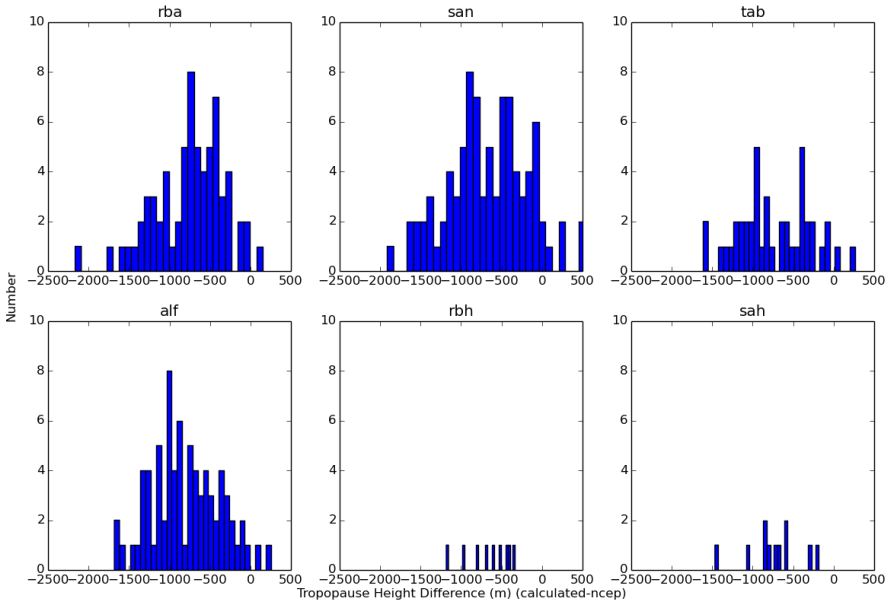


**Figure 4.8:** Histograms showing the difference between the calculated tropopause height and that given by NCEP for every flight date at each of the six aircraft sites.

of $CH_4$ from chemical reactions. The model also uses the Prather second-order moments advection scheme to reduce numerical diffusion (Prather, 1986). The run has a resolution of approximately $2.8^\circ \times 2.8^\circ$ with 32 levels from the surface to 60 km and provides monthly mean output. The model is sampled for the month of each aircraft flight at the location of the site and every modelled altitude level above the calculated tropopause height is used. Figure 4.9 shows an example global map of TOMCAT $XCH_4$ for January 2010 at 68.13 hpa, which is approximately 18.6 km and towards the lower altitudes of the stratosphere in the tropics. This figure illustrates how $CH_4$ concentrations at this altitude are higher in the tropics than temperate regions, since the tropopause height is higher and $CH_4$ concentrations do not begin to drop-off with altitude until higher in the atmosphere.

To validate the TOMCAT model I have compared it against ACE-FTS satellite profiles, TCCON apriori modelled profiles, and Aircore balloon profiles. Figure 4.10 shows ACE-FTS profiles compared to TOMCAT and TCCON. Comparisons for May 2009 are shown at all six sites with coincident data (the month where there were the most ACE matches within $\pm 5^\circ$ of TCCON sites) and the ACE profiles are found to be in closer agreement with TOMCAT than TCCON. This is expected

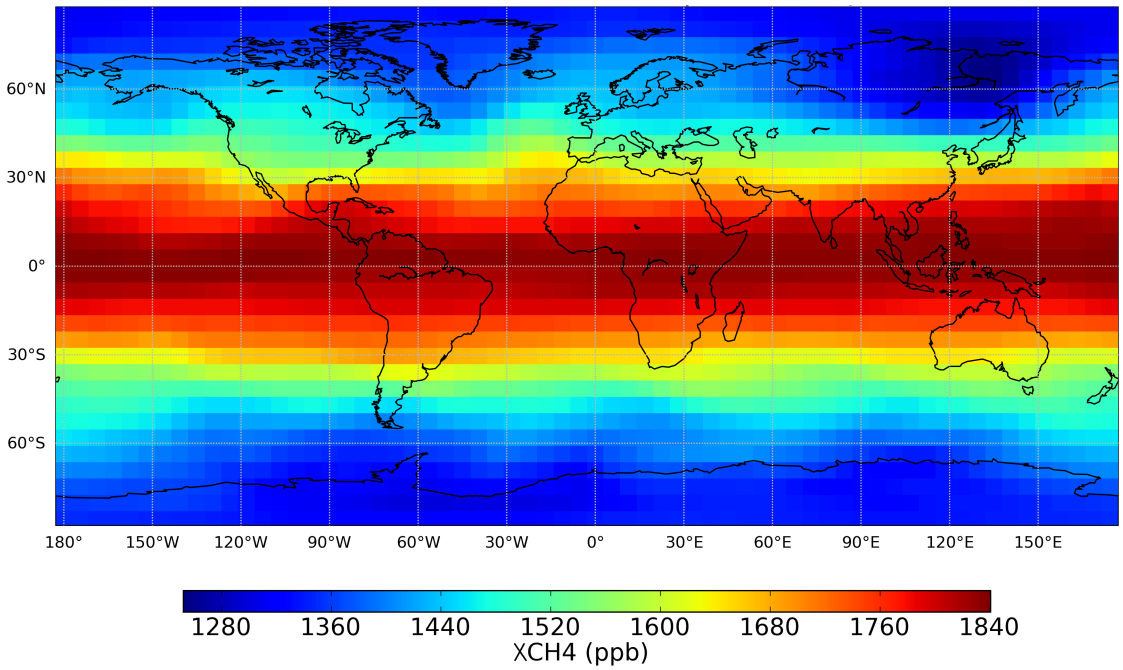


**Figure 4.9:** Map showing modelled $XCH_4$ data in ppb from the TOMCAT model, at 68.13 hpa (approximately 18.6 km) for January 2010.

since TOMCAT is a dedicated stratospheric model, whilst the TCCON apriori profiles are not required to have the same complexity. The results of the TOMCAT comparison along with eight Aircore profiles are displayed in Figure 4.11. These show a generally good agreement, with TOMCAT coming very close to the profile shape from the in situ data. The model does not capture the variability within each profile since they are monthly model mean profiles.

To evaluate TOMCAT's performance in the tropics (where there are no TCCON sites or Aircore flights), I have taken all ACE profiles between $\pm 20^\circ$ of the equator for comparison with the model. These results show that the stratospheric $CH_4$ profile is well represented by TOMCAT as illustrated in Figure 4.12. In this figure, TOMCAT is shown compared with 7 ACE profiles from May 2009 above 350 hpa (approximately 8.1 km). In total there are 163 ACE profiles within $\pm 20^\circ$ of the equator for 2008-2012, (an average of less than 4 per month). I have calculated the stratospheric $XCH_4$ for these ACE profiles and compared them with TOMCAT $XCH_4$ which are calculated for the same altitude range. The mean difference in $XCH_4$ between ACE and TOMCAT was found to be $4.34\% \pm 4.58\%$ (of the TOMCAT $XCH_4$). These differences are smaller than the expected uncertainty in the ACE profiles (Mazière et al., 2008), suggesting that TOMCAT and ACE are in

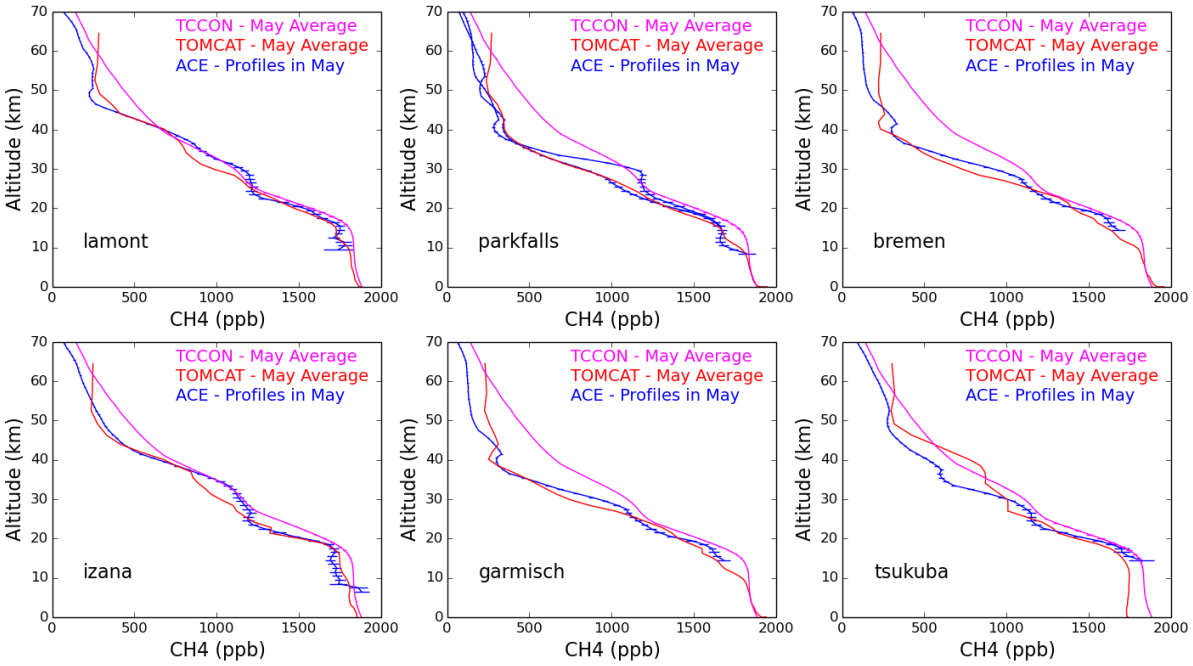


**Figure 4.10:** $CH_4$ profiles from the TOMCAT model (in red) sampled at six TCCON sites (Lamont, Parkfalls, Bremen, Izana, Garmisch and Tsukuba), for May 2009. Compared with the TCCON apriori profiles for the same month in magenta; and with ACE-FTS satellite profiles (in blue) for the same month and sampled within $\pm 5^\circ$ of the TCCON site. Uncertainties in the TOMCAT profile are not shown, whilst those of the TCCON and ACE profiles are displayed.

agreement for these profiles in the tropics. In summary, TOMCAT is found to perform well in the tropics as it compares favourably with ACE measurements. This justifies my use of TOMCAT data in the stratosphere.

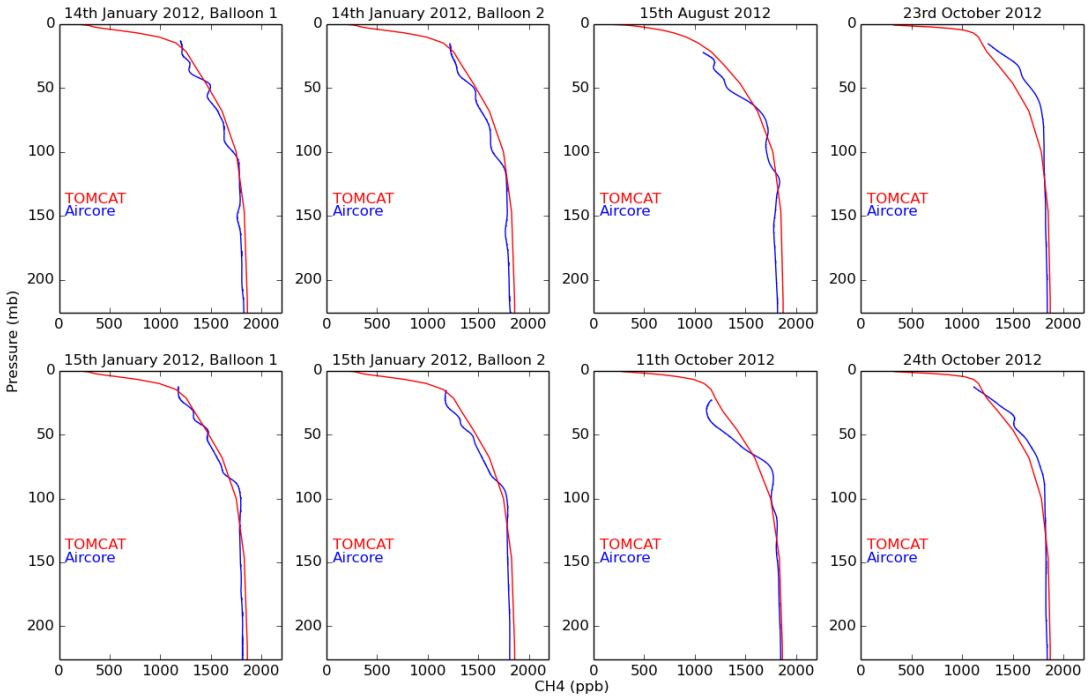


**Figure 4.11:** Monthly average TOMCAT $CH_4$ profiles sampled at the locations of eight Aircore balloons launched in 2012. Since the balloons drift, GOSAT is sampled at the latitude and longitude which the balloons were each at upon reaching 10 km asl, since I am only interested in the stratosphere for this comparison. On the $14^{th}$ and $15^{th}$ of January 2012 there were two balloons released on each day, labelled here as balloons 1 and 2 for each date. TOMCAT is shown in red and the Aircore profiles in blue.

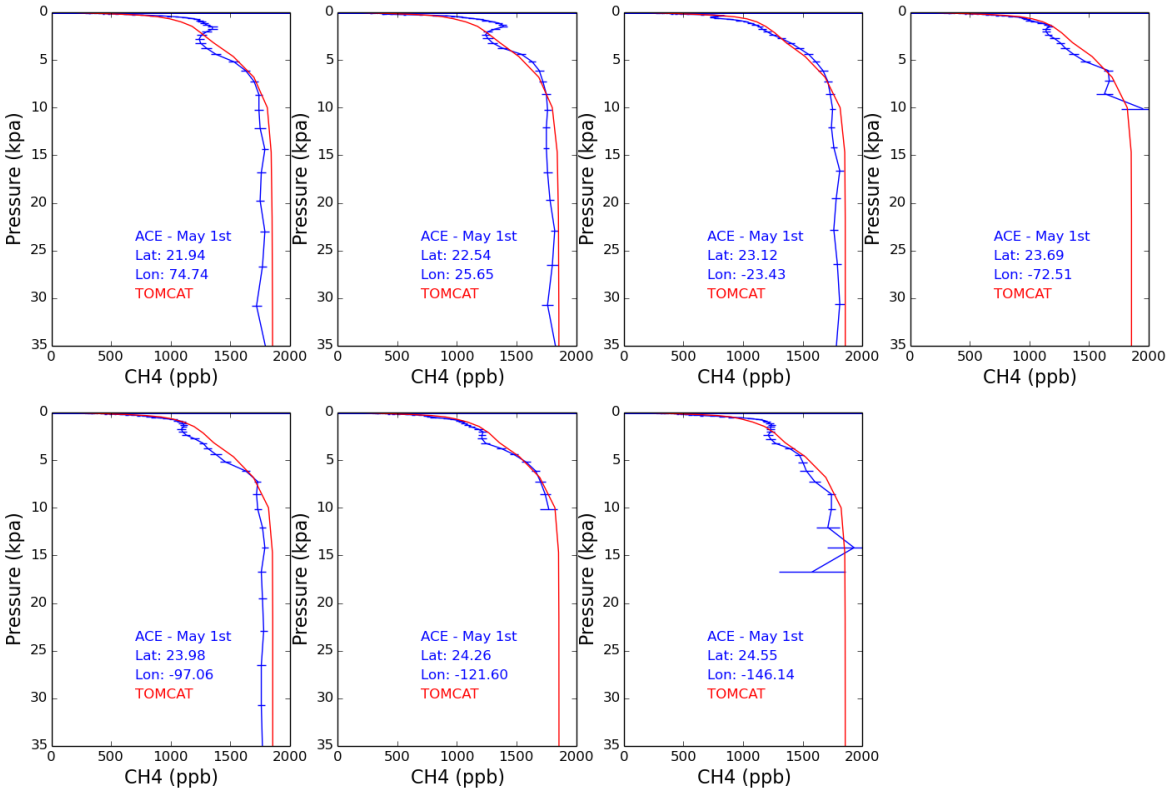


**Figure 4.12:** TOMCAT $CH_4$ profiles for May 2009 (in red) compared with every ACE-FTS profile from this month which was made within $\pm 20^\circ$ of the equator, in blue. The latitudes and longitudes of these profiles are displayed on the figure and the y-axis extends from 35 kpa (approximately 8.1 km) to the top of the atmosphere.

### 4.5.3 Conversion between altitude and pressure

The ACO and AMAZONICA aircraft profiles are provided with an altitude in metres, and from its definition the tropopause height also needs to be calculated in metres. Meanwhile the TOMCAT model is given in pressure and in order to piece the components of the atmospheric profile together and calculate an $XCH_4$ value it is necessary to express the entire profile in terms of pressure. It is important to convert between altitude and pressure as accurately as possible; but this conversion is reliant on additional atmospheric properties (temperature and humidity), which are acquired from the same ECMWF data from which the tropopause height has been calculated.

Pressure decreases roughly exponentially with altitude in the atmosphere, varying from an average sea level pressure of 101,325 Pa to 0 Pa at the edge of space where the atmosphere ends. The exact variations are dependent on the temperature ($T$) and density ($\rho$) of the air, which in turn are dependent on the humidity. The equation to relate the altitude $z$ with the pressure $P$ under hydrostatic equilibrium is given in Equation (4.1) where $g$ is the acceleration due to gravity,

$$dP = -\rho g dz. \tag{4.1}$$

Using the ideal gas equation $PV = nRT$ where $V$ is the volume of the gas, $n$ is the number of moles of gas and $R$ is the universal gas constant, the number of moles can be substituted out for the total mass of the gas divided by the molar mass $M$, and the density can be introduced as the total mass divided by the volume of gas. This gives Equation (4.2), relating the pressure to the density and temperature.

$$P = (\rho RT)/M. \tag{4.2}$$

The relationship between pressure and altitude is derived by dividing (4.1) by the pressure, substituting in Equation (4.2) and integrating the equation to get

Equation (4.3) where $H$ is the scale height defined by Equation (4.4), and $P_0$ is the pressure at the surface ($z = 0$).

$$P = P_0 \exp^{-\frac{z}{H}}, \tag{4.3}$$

$$H = \frac{RT}{Mg}. \tag{4.4}$$

This scale height assumes that temperature, gravitational acceleration and molar mass are all constant and represents the altitude over which the pressure will decrease by a factor of $e$. In the troposphere this height is approximately 8,500 m assuming a temperature of 290 K. However, these parameters are not constant throughout the entire atmosphere so to convert between pressure and altitude profiles accurately it is necessary to consider small changes in pressure and calculate the small changes in altitude these relate to using Equation (4.5). By starting at the surface with an accurately measured surface pressure it is possible to calculate the altitude profile referring to a pressure profile with the use of temperature and humidity data on the condition that these data are of high enough vertical resolution that hydrostatic equilibrium can be assumed over each $\Delta P$ increment.

$$\Delta P = -\rho g \Delta z. \tag{4.5}$$

The density can be calculated by rearranging Equation (4.2) for $\rho$ where the total pressure $P$ is considered as the contribution of the pressure from dry air $P_d$ and the pressure from water vapour $P_v$, i.e. $P = P_d + P_v$. In this case the universal gas constant $R$ needs to be substituted for the specific gas constants for dry air $R_d$ and for water vapour, $R_v$, using $R = M_d R_d = M_v R_v$, where $M_d$ and $M_v$ are the molar masses of dry air and of water vapour respectively. Substituting these together causes the molar masses to cancel and the density is given by Equation (4.6),

$$\rho = \frac{P_d}{R_d T} + \frac{P_v}{R_v T}. \tag{4.6}$$

The pressure of dry air can be eliminated from the equation by substituting for $P = P_d + P_v$ and then substituting this equation for $\rho$ back into Equation (4.5) to get Equation (4.7).

$$\Delta P = -\left(\frac{P - P_v}{R_d T} + \frac{P_v}{R_v T}\right) g \Delta z. \tag{4.7}$$

The pressure due to water vapour depends upon the specific humidity, $\omega$, which is defined as the ratio of the mass of water vapour ($m_v$) to the mass of air ($m_v + m_d$), Equation (4.8). Meanwhile, the mass mixing ratio ($W$) is defined as the ratio of the mass of water vapour to the mass of dry air. Therefore, $\omega = W/(W+1)$. Since the fraction of the total pressure relating to $P_v$ depends on the fraction of the total molecules of water vapour and dry air ($n_v$ and $n_d$ respectively), Equation (4.9), and $n_x = m_x / M_x$, these two equations can be combined with the definition of $W$ and rearranged to derive an equation for $W$ (Equation (4.10)) in terms of $P_v$, $P$ and the term $B$ which is given as $M_v / M_d$.

$$\omega = \frac{m_v}{m_v + m_d}, \tag{4.8}$$

$$P_v = \frac{n_v}{n_v + n_d} P, \tag{4.9}$$

$$W = \frac{B P_v}{P - P_v}. \tag{4.10}$$

Equation (4.10) is then substituted into $\omega = W/(W+1)$ and rearranged for $P_v$ to get Equation (4.11). Therefore, Equation (4.7) is solved by using Equation (4.11) to calculate $\Delta z$ for a small change in pressure ($\Delta P$) such that the temperature and specific humidity can be considered as constants at pressure $P$.

$$P_v = \frac{P\omega}{\omega + B - B\omega}. \tag{4.11}$$

Utilising the above equations, a high resolution relationship between pressure and altitude can be determined for each aircraft profile, allowing for an easy conversion between the two where necessary. This is also important when calculating the uncertainties involved with the extended aircraft profiles.

### 4.5.4 Final calculation and application of averaging kernels

The extended aircraft profile is converted into a total column by applying scene-specific pressure weighting functions and scene-dependent GOSAT averaging kernels to each level. The method outlined in O'Dell et al. (2012) is used to calculate the pressure weighting function on each level of the profile, $h_i$ for levels $i = 1$ to $N$; as given by Equation (4.12).

$$h_i = \begin{cases} (1 - f_i)h'_1, & i = 1. \\ f_{i-1}h'_{i-1} + (1 - f_i)h'_i, & i = 2..N - 2. \\ f_{N-2}h'_{N-2} + (1 - f_s f_{N-1})h'_{N-1}, & i = N - 1. \\ f_s f_{N-1}h'_{N-1}, & i = N \end{cases} \tag{4.12}$$

where $i = 1$ represents the upper-most level and $i = N$ represents the lower-most level. $f$ is an interpolation variable relating the $CH_4$ mole fraction at a layer centre to that at its two boundaries, which will equate to one half, if there are sufficient levels to assume that $CH_4$ varies linearly between levels. $f_s$ refers to the interpolation parameter at the surface, given in Equation (4.13), which is dependent on the surface pressure ($P_s$), the pressure at the lowest level in the model ($P_N$) and the pressure in the second lowest level ($P_{N-1}$). In my case $P_N \equiv P_s$. $h'_i$ is the pressure weighting function on the pressure layers and is given by Equation (4.14).

$$f_s = \frac{P_s - P_{N-1}}{P_N - P_{N-1}}, \tag{4.13}$$

$$h'_i = \frac{\bar{c}_i \Delta P_i}{\sum_{i=1}^{N-1} \bar{c}_i \Delta P_i}, \tag{4.14}$$

where $\bar{c}_i$ is the average of the column density of dry air per unit pressure ($c$) on level $i$. This is given by Equation (4.15).

$$c = \frac{1 - \omega}{g M_{dry}}, \tag{4.15}$$

where $\omega$ is the specific humidity, $g$ is the local acceleration due to gravity, and $M_{dry}$ is the molar mass of dry air. ECMWF data is used for the specific humidity and $g$ is calculated using Equation (4.16) from Swick (1942), since this will change with altitude and latitude. Figure 4.13 shows an example of the newly calculated pressure layers calculated for the levels of an extended aircraft profile with the blue points showing the initial pressure levels and red and green points showing the upper and lower pressures for the layer calculated on each level.

$$g = 9.780327(1 + 0.0053024(\sin\phi)^2 - 0.0000058(\sin 2\phi)^2) - 0.000003086z. \tag{4.16}$$

where $\phi$ is the latitude and $z$ is the altitude above sea level.

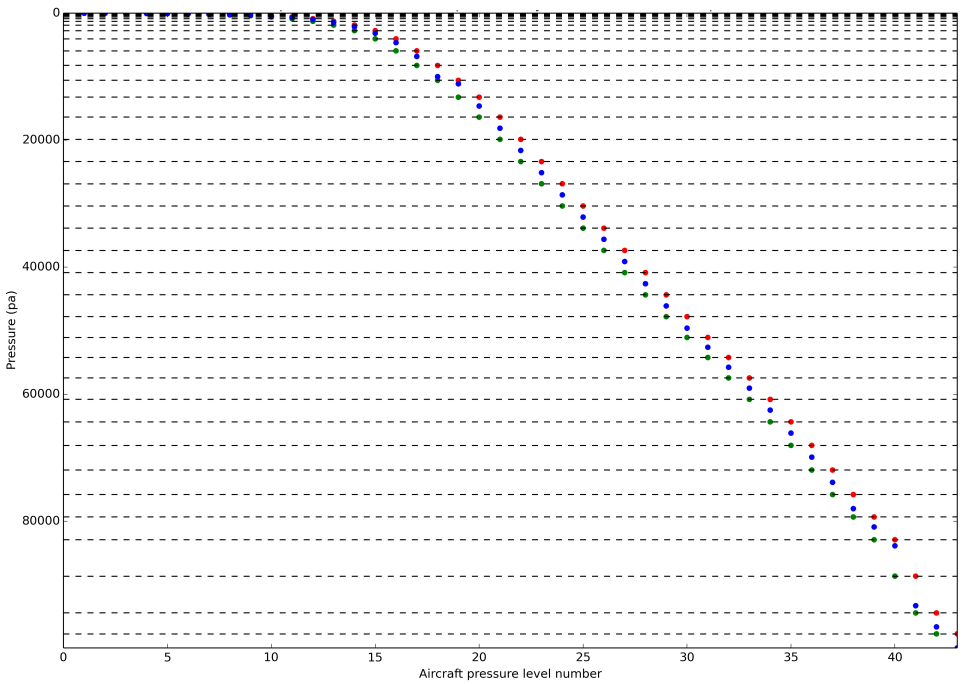


**Figure 4.13:** An example extended aircraft profile with pressure levels in blue. The calculated upper (red) and lower (green) pressure levels corresponding to a pressure layer centred on the original level are shown.

The final $XCH_4$ value is simply calculated as the sum of the pressure weighting function multiplied by the $CH_4$ concentration for each level. However, the GOSAT averaging kernels also need to be applied for fair comparison with the

satellite. This requires Equation (4.17) and uses the GOSAT averaging kernels and apriori profiles. Every cloud free GOSAT retrieval within a $\pm 5^\circ$ grid box around the aircraft location for the same day as the flight are used to calculate the averaging kernel corrected $XCH_4$ for each GOSAT retrieval, and the average is used as the final corrected $XCH_4$ for the extended aircraft profile. When there were no GOSAT observations on the same day the selection criteria were extended to an additional day on either side, and for the rare occasions where there were still no matches an average correction was applied which was calculated using the other flights at that site (0.49 ppb at RBA, 0.61 ppb at SAN, 0.51 ppb at TAB, 0.54 ppb at ALF, 0.57 ppb at RBH and 0.80 ppb at SAH). To interpolate the apriori profiles onto the extended aircraft profile, a method which first converts the profiles into partial columns and then integrates them vertically to give a cumulative column is used. This column is interpolated onto the aircraft pressure levels and is then converted back into volume mixing ratios on the new pressure grid. This method ensures that the total column value is maintained in the interpolation and will reduce errors caused here by a regular interpolation.

$$\mathrm{XCH_4} = \sum h_i(\mathrm{AK}_i(\mathrm{AircraftCH4}_i - \mathrm{AprioriCH4}_i) + \mathrm{AprioriCH4}_i). \tag{4.17}$$

The application of satellite averaging kernels results in the aircraft $XCH_4$ decreasing by 0.49-0.80 ppb, depending on the site. Figure 4.14 shows an example profile before and after extension from an ACO flight on the 16th August 2014. The average $XCH_4$ contribution of the aircraft data to the total column at the ACO sites RBH and SAH is 55.5% and 54.3% respectively, whilst the AMAZONICA sites which only extend to 4.5 km contribute between 39-40% on average for the 4 sites. The part between the surface and the lowest aircraft measurement contributes approximately 0.5% to the total column. The extrapolated region between the top of the aircraft profile and the tropopause contributes approximately 50-51% for the AMAZONICA sites and 34-35% for the ACO sites. The stratospheric component comprises approximately 10% of the total $XCH_4$.

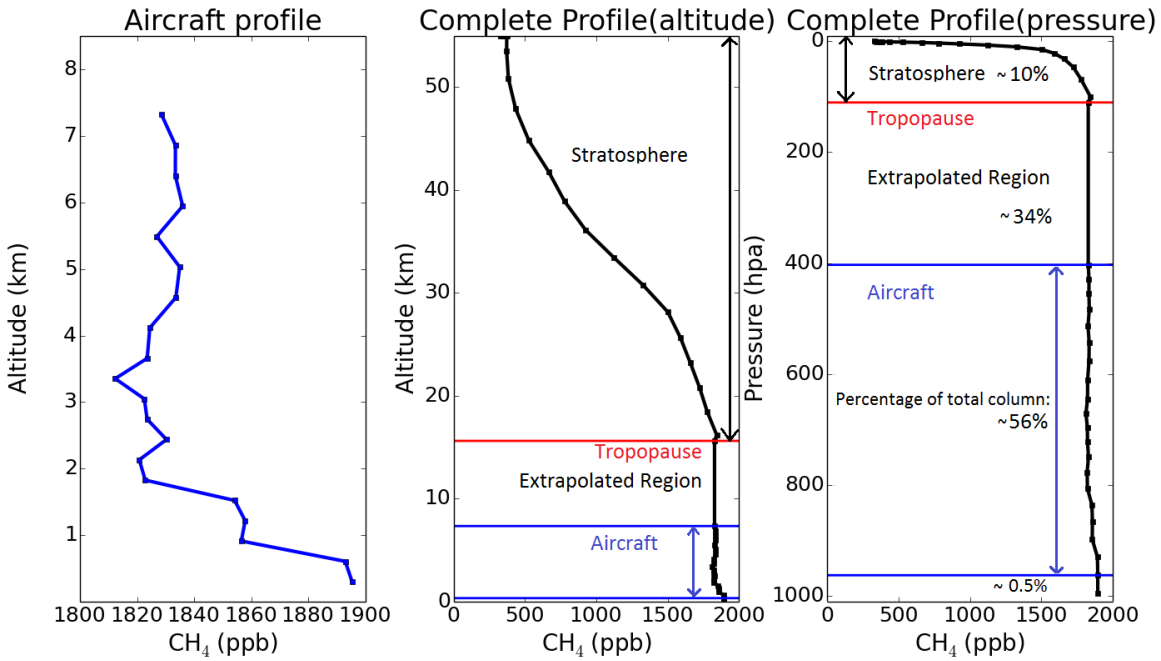


**Figure 4.14:** Example of the extended aircraft profile for the ACO flight at Rio Branco on the 16th August 2014. The left panel shows the measured aircraft profile. The middle and right panels show the final complete profile with altitude and pressure on the y-axis respectively. On the right panel, the percentage contribution to the $XCH_4$ from each part is displayed (these are average values for all of the RBH extended profiles).

## 4.6 ERROR ANALYSIS

To estimate the uncertainty of the $XCH_4$ columns derived from the extended aircraft profile, uncertainties are assigned to each section of the profile individually since they are constructed using different methods and with different data sources. Throughout the height of the aircraft profile the uncertainty used is from the air sample analysis. The uncertainty at the surface was assumed to be the same as the uncertainty in the lowest aircraft measurement. Between the top of the aircraft profile and the tropopause, the uncertainty is estimated by examining the variability of $CH_4$ in a high resolution model. For the stratosphere, the method of Wunch et al. (2010) is used. This method shifts the stratospheric values up and down by one kilometre to calculate the difference in total column, which is used as an estimate of the uncertainty in the location of the tropopause and therefore for the stratospheric contribution.

Between the maximum altitude of the aircraft measurements, approximately 4.5 km for AMAZONICA flights and 7.5 km for ACO flights, and the tropopause the uncertainty was estimated from the ECMWF high resolution MACC model for 2012 which is driven by ERA-Interim operational high resolution meteorology, including real time biomass burning. The horizontal resolution is 16 km with a 3 hourly output on 91 vertical levels. For each day in 2012 the $XCH_4$ partial column for this height range was calculated by taking the model value at either 4.5 km or 7.5 km to represent the highest aircraft measurement and using a) the model concentrations for each level above these in this altitude range or b) by using a constant value for these levels based on the concentration at this altitude. The difference in $XCH_4$ using these two methods then represents the estimated error of the method for this height range. Figure 4.15 shows histograms of the difference for $XCH_4$ between methods a and b (model calculated $XCH_4$ minus the linear calculated $XCH_4$) starting from 4.5 km. These are shown for each month in 2012, for which the model outputs from every grid-box within $\pm 5^\circ$ of the site and for each day of the month are taken. The differences were calculated at every site and results are shown here for the Rio Branco site. Figure 4.16 shows the same analysis at Rio Branco but starting from 7.5 km to represent the higher altitude ACO flights. In both of these figures the dotted red line shows the mean of the distribution and the numbers in red indicate how many of the cases fall on each side of a 0 ppb difference. These values do not sum up to exactly the same value for the 4.5 km and 7.5 km cases, because within $\pm 5^\circ$ of Rio Branco there are mountains which are taller than 4.5 km and the model data over this area was not used for the 4.5 km case (all are smaller than 7.5 km).

Figures 4.15 and 4.16 show that there is both a random distribution in the differences between the two methods and a systematic offset from zero. The random distribution is more wide-spread for the 4.5 km case than for the 7.5 km case. This is particularly noticeable for the months from January-April and in December. This variation typically ranges from -20 ppb to 20 ppb, although the majority of cases are within $\pm 10$ ppb of zero. For many of the months the mean difference is not centred around zero but instead is offset by up to 4 ppb depending on the month. From these histograms I have further calculated the median absolute de-

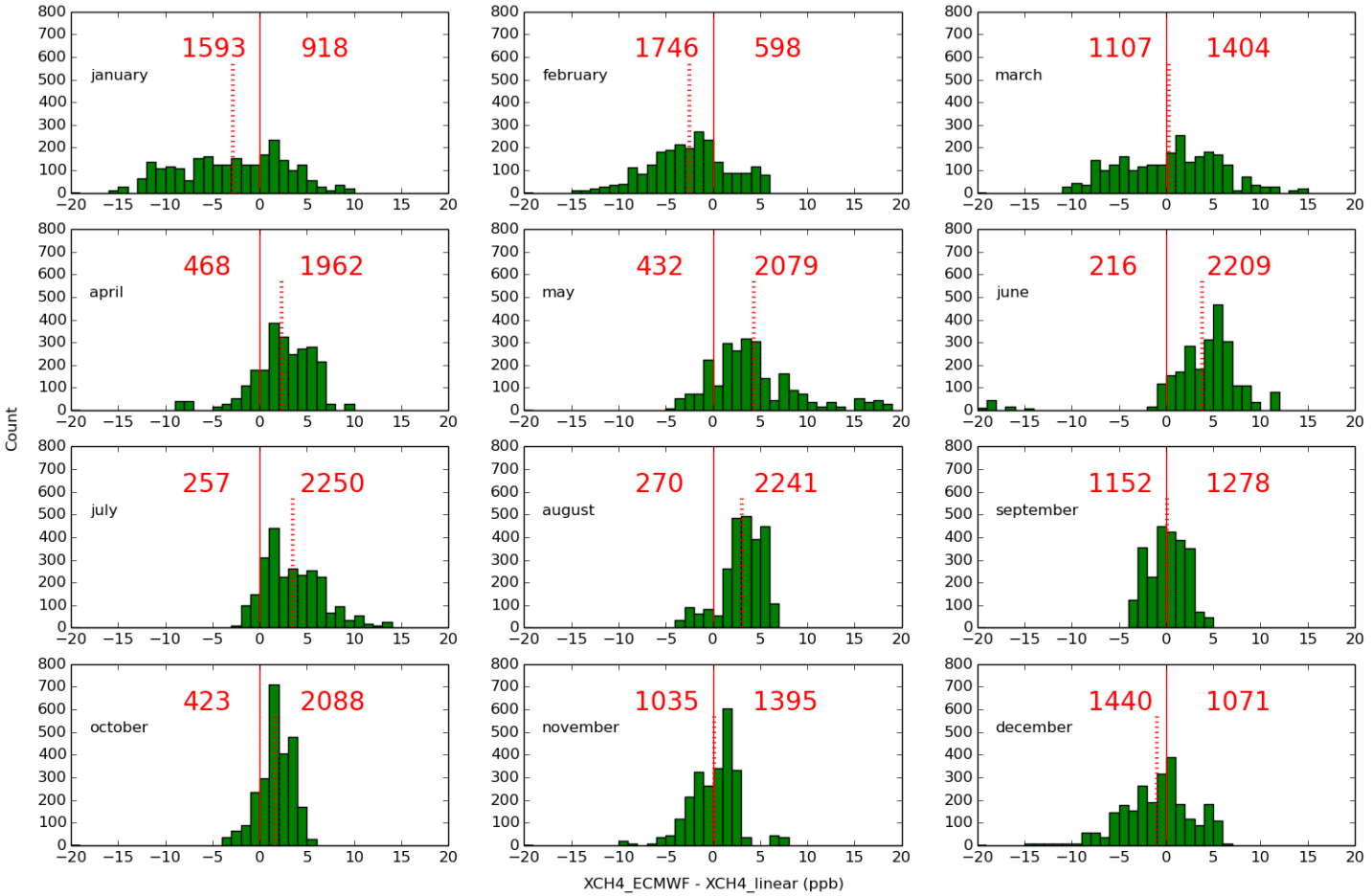


**Figure 4.15:** Monthly histograms of 2012 showing the difference in $XCH_4$ (partial column between 4.5 km and the tropopause) as measured by a high resolution model output (MACC ERA-Interim) and by assuming a constant $CH_4$ concentration throughout this region given by the model value at 4.5 km. The model was sampled for each day and at each grid-box within $\pm 5^\circ$ of Rio Branco, resulting in approximately 2400 comparisons per month. The solid red line marks a difference of zero ppb whilst the dotted red line marks the mean difference for that month. The numbers in red indicate the number of occurrences either side of zero.

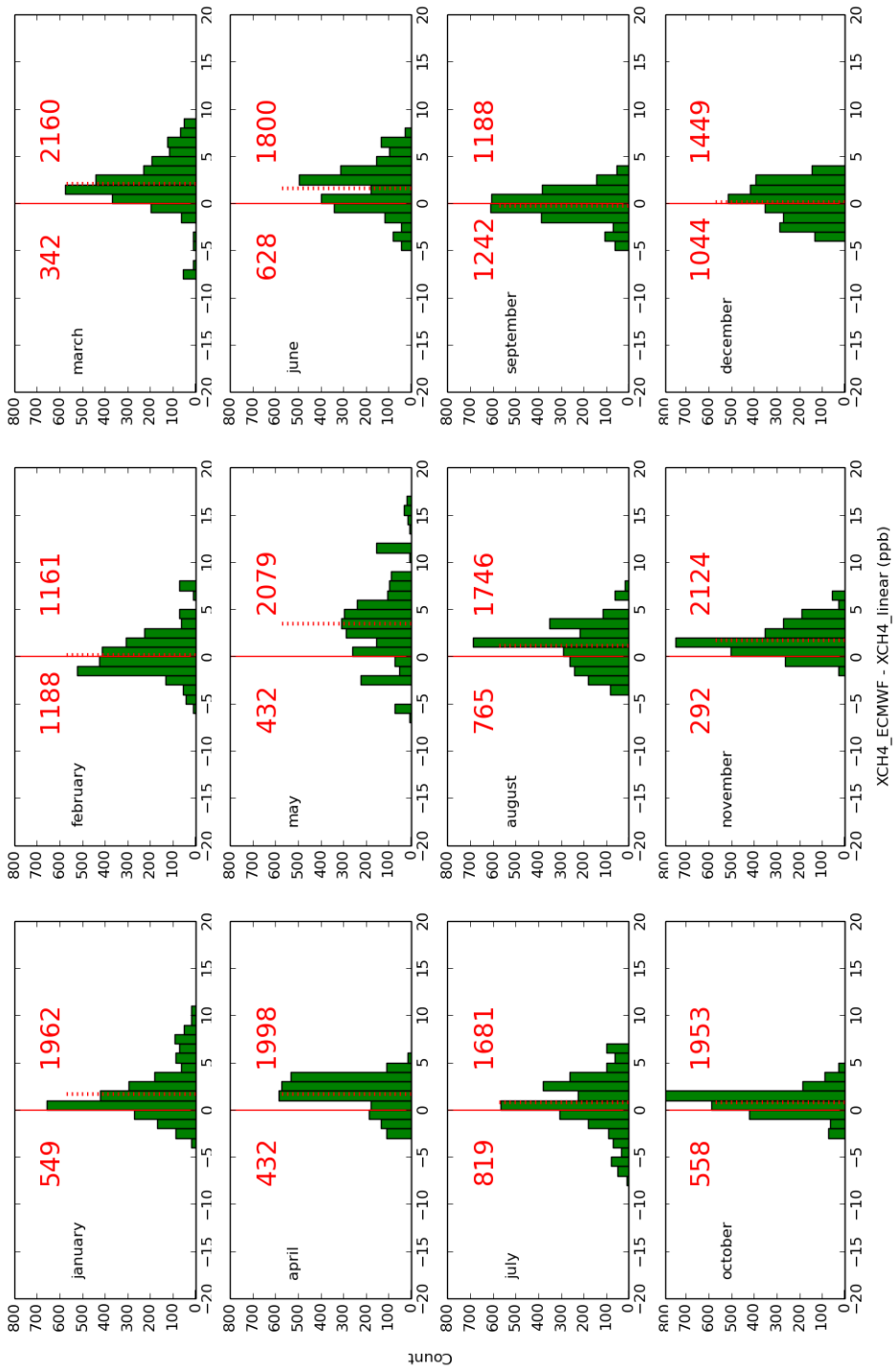


Figure 4.16: Monthly histograms of 2012 showing the difference in $XCH_4$ (partial column between 7.5 km and the tropopause) as measured by a high resolution model output (MACC ERA-Interim) and by assuming a constant $CH_4$ concentration throughout this region given by the model value at 7.5 km. The model was sampled for each day and at each grid-box within $\pm 5^\circ$ of Rio Branco, resulting in approximately 2400 comparisons per month. The solid red line marks a difference of zero ppb whilst the dotted red line marks the mean difference for that month. The numbers in red indicate the number of occurrences either side of zero.

viation of all of these values for each month to give an estimate for the variation of $XCH_4$ in this extrapolated region, representing the random uncertainties for this range. The median of the difference represents a systematic error with the method as described. Figure 4.17 shows time series for the monthly median and median absolute deviations for both the 4.5 km and 7.5 km cases at Rio Branco, Tabatinga, Alta Floresta and Santarém; allowing for a better examination of these monthly differences.

The uncertainty for the extrapolated region for a flight height of 4.5 km is seen to be between about 1.5 ppb and 4 ppb, with January and March for Rio Branco being exceptions with values up to 6 ppb. The median shows a systematic behaviour with a possible bias of between -4 ppb and +5 ppb which is dependent on the month. During the wet season the model data is typically higher for the extrapolated region than the linear method, because there are higher $CH_4$ emissions and the model predicts enhanced features in the profile higher in the troposphere than it does during the dry season. The benefit of extending the height of the flights up to 7.5 km is shown by the difference in both the median standard deviation and the median in the extrapolated region between the two heights. The systematic uncertainty and the variability are decreased significantly when using higher altitude flights, suggesting that air higher in the troposphere is more well mixed. The average variability for Rio Branco decreases from 3.3 ppb to 2.1 ppb when going to the 7.5 km case, with the other sites behaving similarly (2.6-1.8 ppb for ALF, 2.9-1.6 ppb for SAN and 3.0-1.8 ppb for TAB). The average absolute difference from zero across all months ranges from 2.1 ppb to 1.3 ppb when going to the 7.5 km case for Rio Branco. Again results for the other sites are similar (2.7-1.1 ppb at ALF, 2.9-1.1 ppb for SAN and 2.0-1.4 ppb for TAB).

As previously mentioned, the uncertainty in the stratosphere is calculated using the method of Wunch et al. (2010) where the entire stratospheric profile is shifted by $\pm 1$ km. This is designed to account for both the uncertainty in the tropopause position and in the stratospheric profile. From the previous comparison to NCEP tropopause data, the calculated tropopause height was shown to vary from the model by on average only a few hundred meters at all sites, ranging from $359 \pm 458$ m to $763 \pm 395$ m. Therefore placing an uncertainty of $\pm 1$ km on

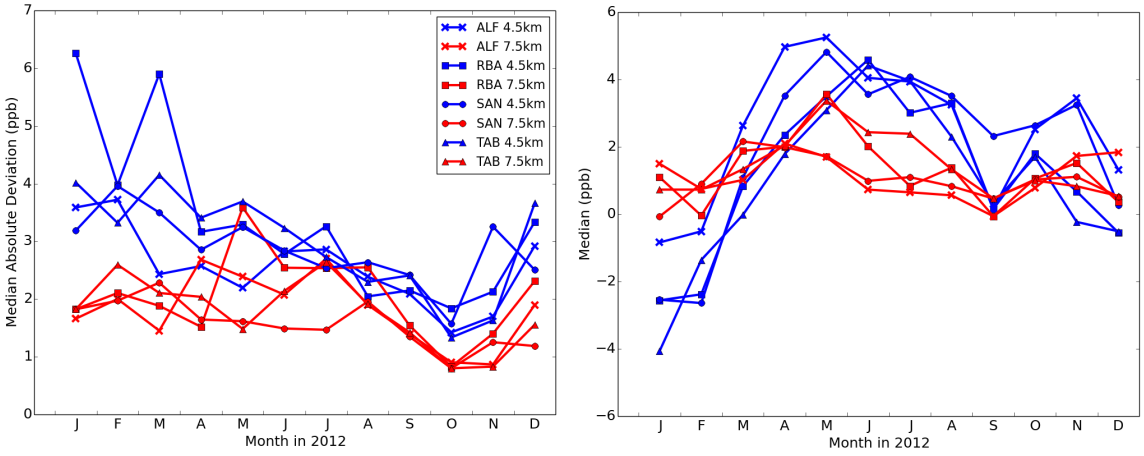


**Figure 4.17:** The median absolute deviation of (left), and median of (right) the difference in partial $XCH_4$ column (from 4.5 km to the tropopause (blue) or 7.5 km to the tropopause (red)) between a model $CH_4$ profile and a linear extrapolation method (based on the model $CH_4$ concentration at either 4.5 or 7.5 km). The model has been sampled for each day and each grid-box within $\pm 5^\circ$ of a target location to generate approximately 2400 difference values per month from which to calculate the monthly median absolute deviations and medians for 2012. The locations studied are Alta Floresta (marked by crosses), Rio Branco (marked by squares), Santarém (marked by circles), and Tabatinga (marked by triangles).

its position should easily account for the uncertainty in the tropopause height. Figure 4.18 shows TOMCAT and ACE-FTS profiles at six TCCON site locations (Bialystok, Bremen, Garmisch, Karlsruhe, Orleans and Sodankyla) for January 2011. The TOMCAT profile is given in black and has been shifted by $\pm 1$ km and plotted in red to indicate this change. For the majority of the coincident ACE-FTS profiles there is a good agreement between this TOMCAT range and the satellite considering that these $\pm 1$ km limits are treated to represent $\pm 1$ standard deviation and also considering that TOMCAT is a monthly mean whilst ACE profiles are individual measurements.

The combined random uncertainty for all parts of the extended aircraft profile is (as a mean across all flights) 3.6 ppb. This is smaller than the individual GOSAT measurement uncertainties (mean single sounding precision across all flights = 10.8 ppb) and also smaller than the standard error of the ensemble (reflecting the spread of GOSAT $XCH_4$ retrievals) of all coincident GOSAT data for a single day (mean for all days and flights = 6.6 ppb). In the majority of months the magnitude of the random error and systematic error combined are still smaller than

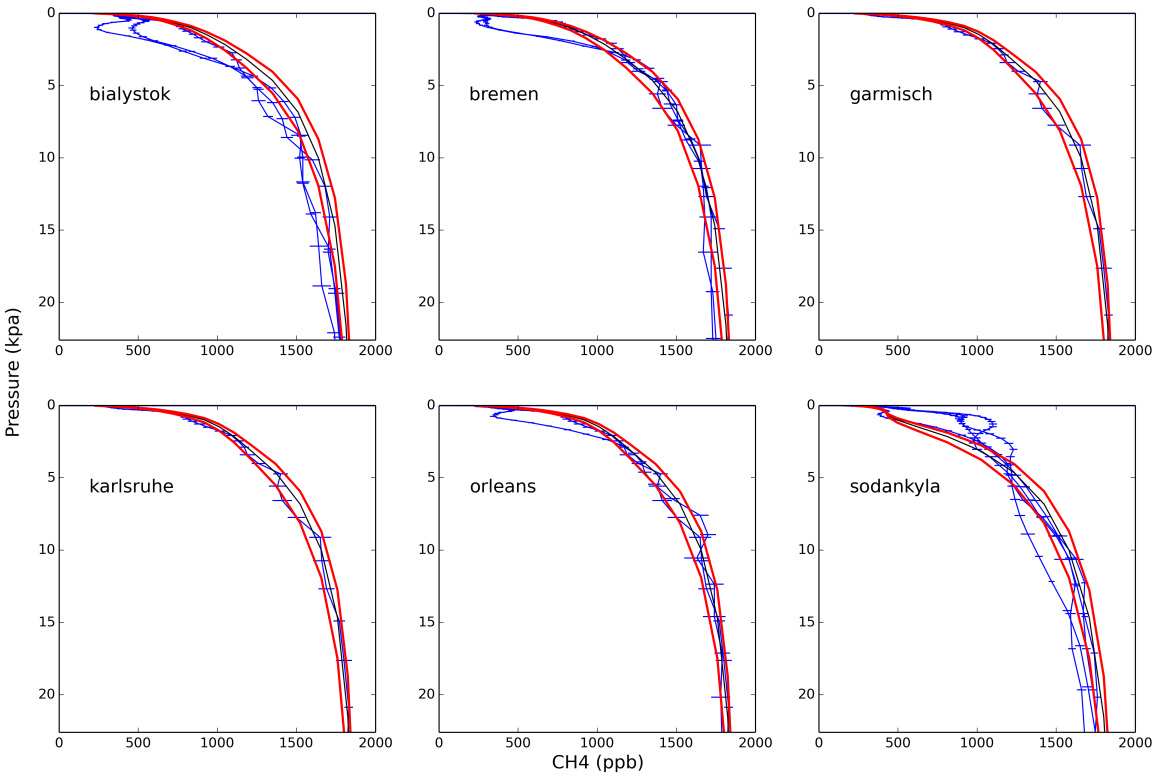


**Figure 4.18:** Comparison of TOMCAT (black) monthly mean profiles sampled at six TCCON sites for January 2011, and coincident ($\pm 5^\circ$ and same month) ACE-FTS profiles (blue). The TOMCAT profile has been shifted by $\pm 1$ km and plotted in red to indicate the scale of the uncertainty placed on the stratosphere in this analysis.

the standard error of the coincident GOSAT soundings. Approximately 3-6% of the assigned random uncertainty in the total column is due to the actual aircraft measurements, about 42-52% is from the stratosphere and the remaining 42-54% is from the extrapolated region. In this extrapolated region a mean systematic error of approximately 1.65 ppb for the AMAZONICA sites and 1.13 ppb for the ACO sites has been estimated. This is about 43% and 34% of the estimated random errors respectively.

## 4.7 EXTENDED AIRCRAFT AND GOSAT $XCH_4$ COMPARISON

### 4.7.1 GOSAT model $XCO_2$

Now that the aircraft profiles have been extended, treated with GOSAT averaging kernels and converted into total column measurements, they can be compared with GOSAT measurements. The usual GOSAT Proxy $XCH_4$ product from the University of Leicester uses a model ensemble for its $XCO_2$ as described in Chapter 3 and Parker et al. (2015), however not all of the models of the employed ensemble are available for our entire time series of aircraft flights. Therefore for 2014 some of the model outputs from 2013 are repeated with the calculated global growth rate from NOAA applied. To use this $XCO_2$ would therefore be inconsistent for the years 2009 to 2013 and 2014. As a result I have chosen to use only data from one $XCO_2$ model for consistency instead of the ensemble. These data are model fields from the University of Edinburgh (simulation version 2.02), which are based on the global chemistry transport model GEOS-Chem v9.02. This is run at a spatial resolution of $4^\circ \times 5^\circ$ and is driven by GEOS-5 meteorological analyses from the Global Modelling and Assimilation Office Global Circulation Model. The surface $CO_2$ fluxes are inferred from $CO_2$ mole fractions from NOAA's in situ Global Greenhouse Gas Reference Network by using an Ensemble Kalman

Filter (Feng et al., 2009; Feng et al., 2011). Figure 4.19 shows a time series of GOSAT data from 2009 until the end of 2014 within $\pm 5^\circ$ of each of the six aircraft sites. It shows the difference in $XCH_4$ between the Proxy product with the usual model ensemble $XCO_2$ and with only the GEOS-Chem $XCO_2$. The data are shown as daily averages with the uncertainties shown as the standard deviation of daily GOSAT data. The mean daily value is displayed with a black line to highlight it clearly and just above the x-axes the yearly average values are given for each full year of data. These show that the average differences (for all sites) between the GEOS-Chem calculated and the ensemble calculated $XCH_4$ are 0.63 ppb for 2010, 0.64 ppb for 2011, 0.80 for 2012 and 1.05 for 2013, compared to 3.79 ppb for 2014. This difference in 2014 is considerably larger than for the earlier years and illustrates why I have chosen to use one model instead of the ensemble for consistency with results before and during 2014.

### 4.7.2 GOSAT–Aircraft comparison

To compare GOSAT $XCH_4$ and the extended aircraft $XCH_4$, all GOSAT soundings (which pass the quality filter) within $\pm 5^\circ$ of each aircraft site are used. Figure 4.20 shows a time series of this comparison where GOSAT is displayed as a daily average with the uncertainties representing the standard deviation of $XCH_4$ for each day. For all sites, the $XCH_4$ calculated from the extended aircraft profiles is found to show a similar seasonal cycle to that seen from GOSAT methane data: enhanced methane in the wet season and lower values in the dry season. The figure shows a large variation in $XCH_4$ values of approximately 10-20 ppb for flights during the dry season in 2011 for Rio Branco and Alta Floresta and to a lesser extent around June-July 2010 for Rio Branco. The differences in $XCH_4$ at Rio Branco were analysed using the wind trajectory model HYSPLIT to determine whether wind speed or wind direction could be causing these variations. Generally, in the higher value $XCH_4$ cases, air is slow moving and remains local to the site, whereas for lower $XCH_4$ values the wind speed is generally much higher, suggesting that the higher values result from slower moving air which has had more time to pick

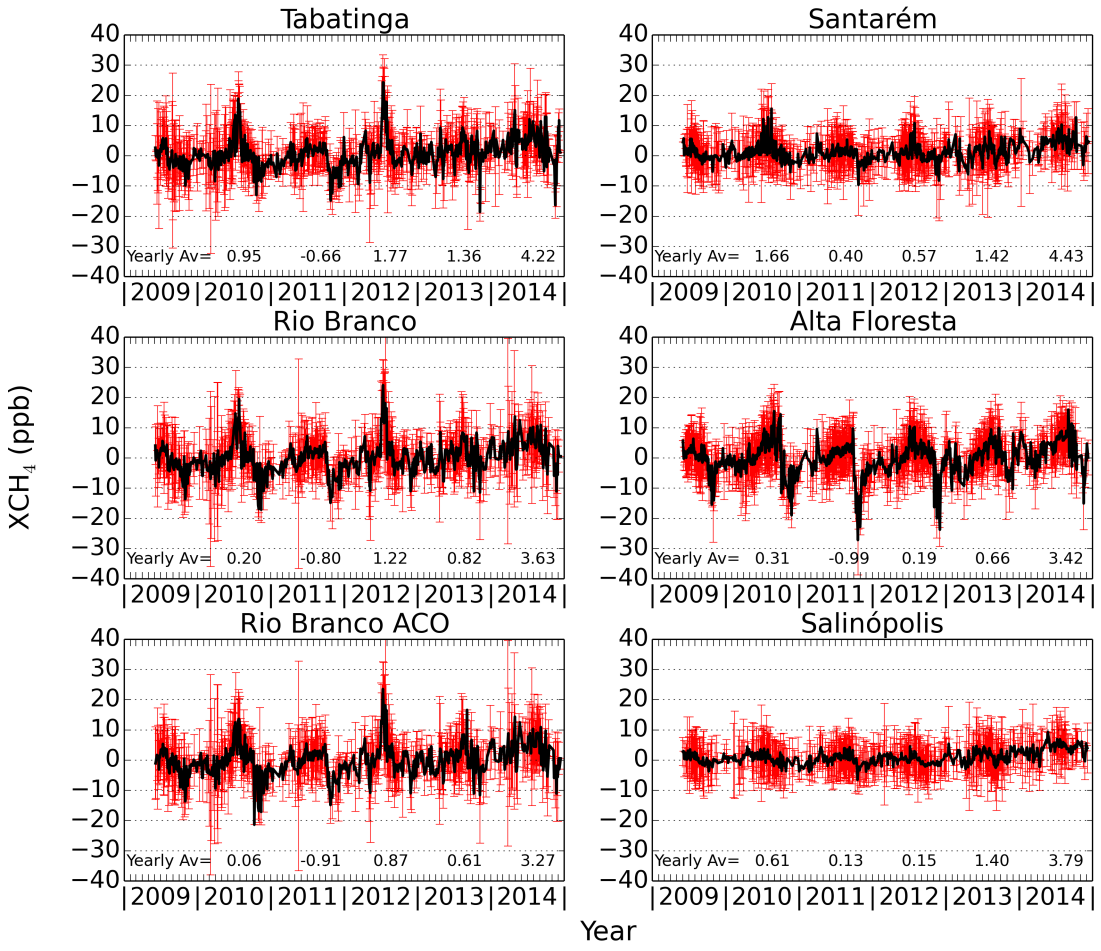


**Figure 4.19:** Time series showing the difference in daily averaged GOSAT Proxy $XCH_4$ when calculated using the usually employed model ensemble $XCO_2$ and when using GEOS-Chem alone for the $XCO_2$ (ensemble minus GEOS-Chem). GOSAT data are used within $\pm 5^\circ$ of the four AMAZONICA sites and two ACO sites. Red data show GOSAT daily averaged results with the daily standard deviation used for the error bars. The black line shows the daily mean value. The yearly mean value is displayed above the x-axes for all years of full data.

up local methane emissions. This is very promising as it indicates that GOSAT has the power to observe variations of $XCH_4$ over short time scales (between subsequent overpasses) and that it can see variations at regional scales within the Amazon Basin. Figure 4.21 shows HYSPLIT wind trajectories for the four flights with the highest $XCH_4$ throughout 2010 and 2011 (top row) and also shows trajectories for the four flights with the lowest $XCH_4$ for the same period (bottom row). There is a clear difference between the high and low $XCH_4$ cases, with trajectories from the high $XCH_4$ flights remaining over land for all trajectories for the entire 120 hours and coming from many different directions, often changing direction also. Meanwhile, in three of the four low $XCH_4$ cases all of the trajectories have reached the Atlantic Ocean and in all cases the wind is coming from the East. It is also notable that for the high $XCH_4$ cases the trajectories are generally coming from lower than 4.5 km with all dates having several trajectories lower than 1 km, whilst for dates with low $XCH_4$ the trajectories all remain above 2 km and generally increase in altitude whilst over land.

Figure 4.22 shows scatter plots between the aircraft profiles at each site and the daily average of the GOSAT data within $\pm 5^{\circ}$. The corresponding correlations and biases for these comparisons are detailed in Table 4.1 for varying co-location criteria. The correlation is examined to understand the scatter and the variability between the aircraft and satellite measurements, whilst the offset indicates the bias between them. The average offset for each site is calculated with a linear fit between the datasets with the slope set to unity, as illustrated in Figure 4.22.

The offsets at Rio Branco are within their uncertainties for both the lower altitude AMAZONICA flights and the higher altitude ACO flights (-1.9$\pm$2.2 ppb for RBA, 3.6$\pm$4.3 ppb for RBH), with the larger uncertainties at RBH a result of having four times fewer flights. At the other sites GOSAT is on average higher by a few ppb than the aircraft values and the bias is larger than the variability (3.6$\pm$1.7 ppb for SAN, 8.1$\pm$2.1 ppb for ALF, 6.6$\pm$2.6 ppb for TAB and 9.7$\pm$2.8 ppb for SAH). A student's t-test calculated on these offsets without considering the weighting of the different flights (which are used for the offset and Pearson's r value calculations) indicates that the offsets observed are not significantly different from zero for TAB, SAN, RBA and RBH, whilst at ALF and SAH the offsets are significant on

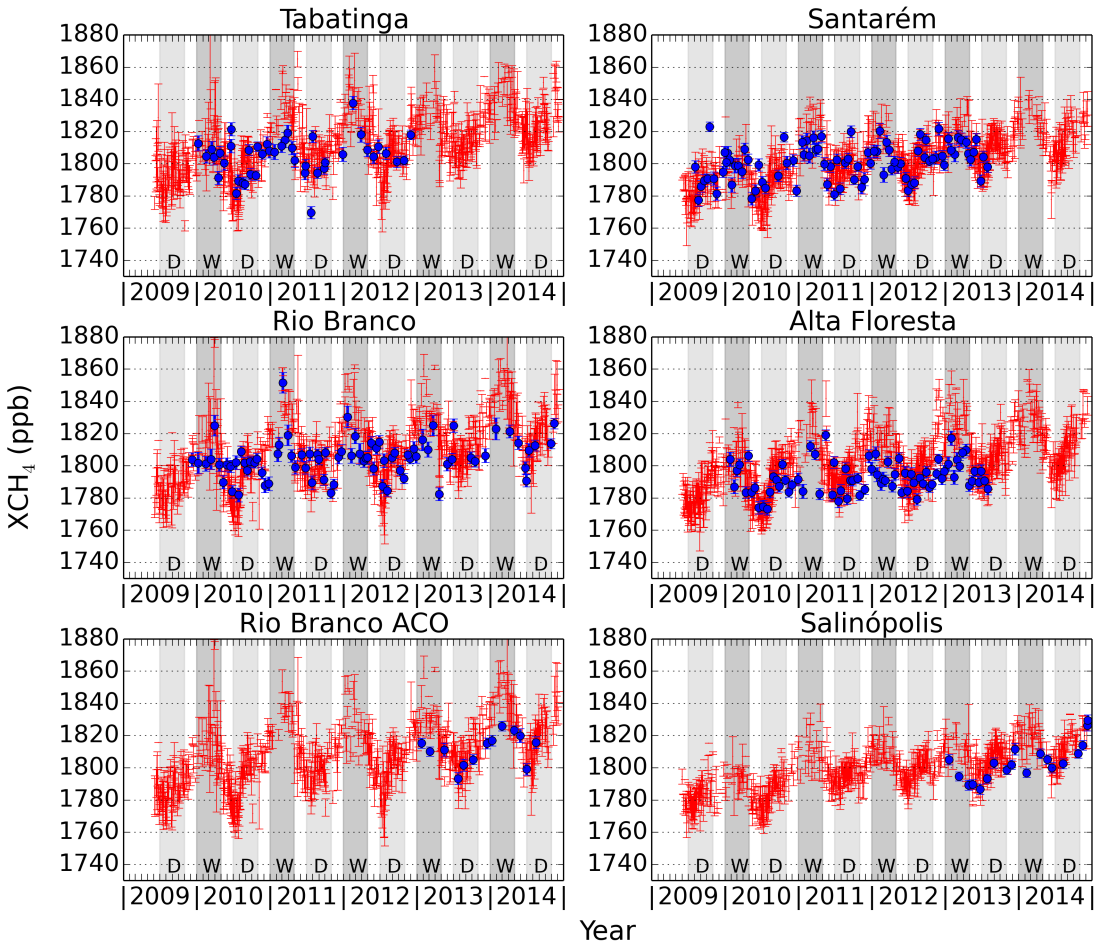


**Figure 4.20:** Time series showing daily averaged GOSAT $XCH_4$ (red) with error bars representing the standard deviation of data for each day. Extended aircraft $XCH_4$ is shown in blue. The approximate wet and dry seasons in the Amazon are displayed on the figure with 'W' and 'D' markers, respectively.

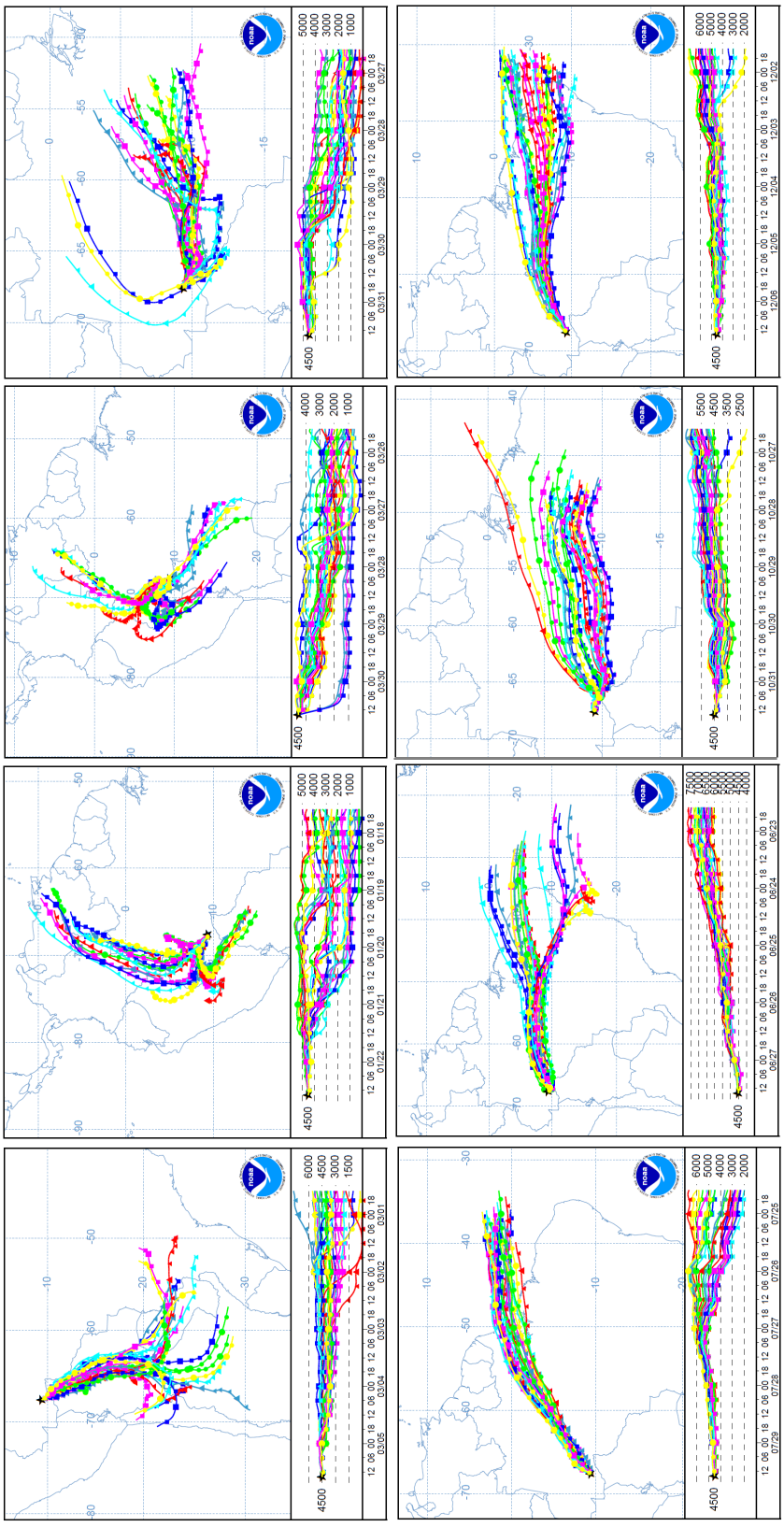

Figure 4.21: Ensemble of back-trajectories from the HYSPLIT model for Rio Branco, released from 4.5 km for 120 hours. The top row in order left to right show the four flight dates with the highest $XCH_4$ measurements in 2010-2011 in order starting with the highest. The bottom row shows trajectories for the four dates with the lowest $XCH_4$ values starting with the lowest.

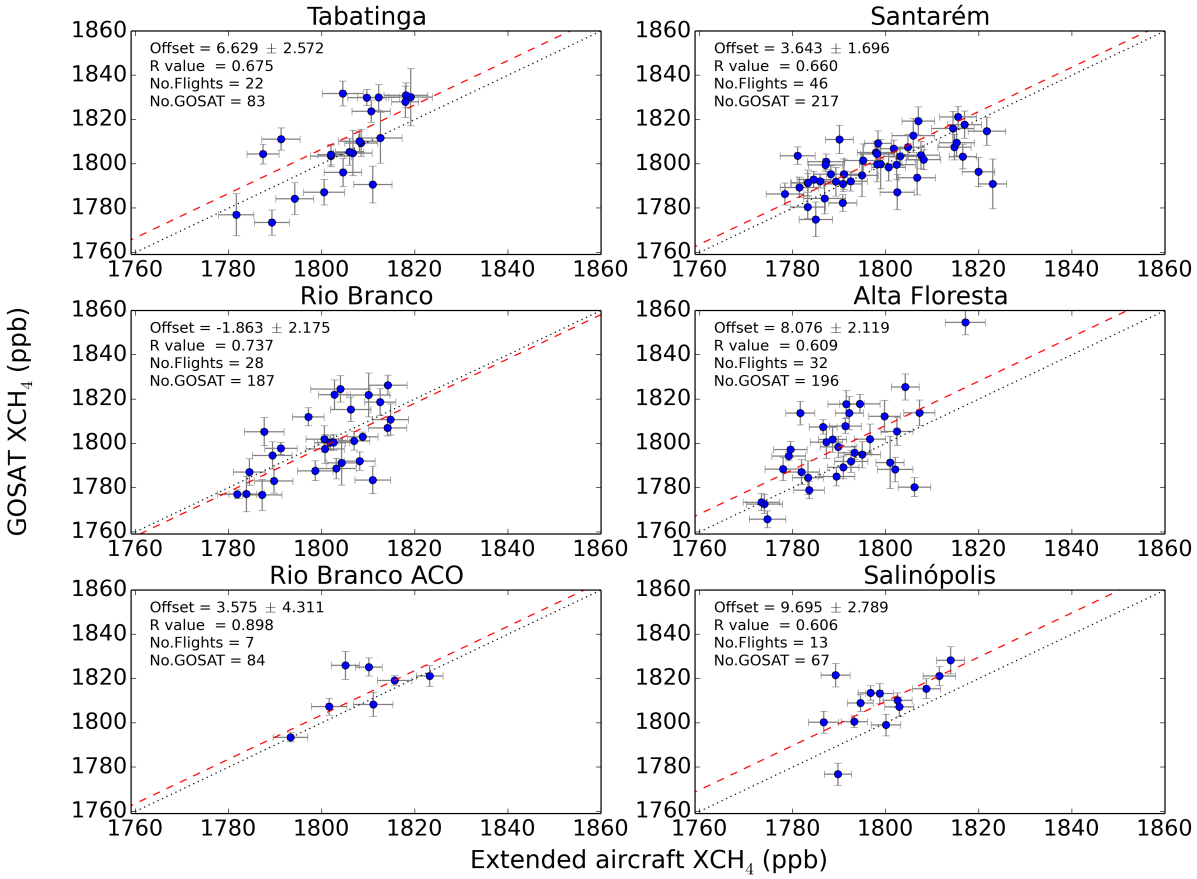


**Figure 4.22:** Correlation plot to illustrate the data shown in Table 4.1 for the case when the co-location criteria is $\pm 5$ degrees. Showing the GOSAT $XCH_4$ on the y-axis versus the aircraft $XCH_4$ on the x-axis for the four AMAZONICA sites and two ACO sites. The black dotted line shows the one to one correlation line. The red dashed line shows the result of a linear regression with the slope set to one. From this the offset values given in Table 4.1 are the difference in intercept of each line on the y-axis, giving the mean offset between GOSAT and aircraft $XCH_4$.

a 95% but not a 98% level. The correlation coefficients (Pearson's r) are all above 0.6, showing that there is a reasonable to good agreement between aircraft and GOSAT $XCH_4$ at all of the sites. They are 0.74, 0.66, 0.61 and 0.68 for RBA, SAN, ALF and TAB respectively and 0.90 and 0.61 for ACO sites RBH and SAH (using a $\pm 5^\circ$ co-location).

Of the AMAZONICA sites for which there are far more flights, the largest offset in $XCH_4$ is at Alta Floresta. This site also shows the largest variation in both the correlation coefficient and the offset over different co-location criteria (see Table 4.1). Furthermore, the largest difference in the $XCO_2$ between the offsets for different co-location criteria are also at ALF. This could be due to the location of the site which is at the edge of the tropical Amazon, closer to the Cerrado ecosystem than the other aircraft sites. Fires are more prevalent in this region and so ALF is likely more influenced by fires during the fire season than the other sites (Gloor et al., 2012). $CH_4$ emission inventories are examined in Chapter 6, where Figure 6.9 shows monthly maps of fire emissions, indicating the prevalence of fires near ALF. Previous studies (Ross et al., 2013; Parker et al., 2016) have shown that GOSAT measurements do show significantly changed total-column $CH_4$ mole fractions in the presence of wildfires; particularly those featuring smouldering combustion which can occur in the types of damp biomass found in the Amazon rainforest.

### 4.7.3 Seasonal differences in $XCH_4$

To examine if the differences which are observed between GOSAT and aircraft $XCH_4$ are dependent on the season, a colour-coded plot, otherwise the same as Figure 4.22, is used to differentiate between aircraft flights which are in the dry and wet seasons (where the wet season has been extended to include the intermediate months). This is Figure 4.23 which shows the dry season flights in red and wet season flights in blue, including the intercepts, r-values and the number of flights in the same colours specific to each month (the black numbers refer to all of the flights). This analysis would show if there are any large differences

between the seasons as observed between GOSAT and the aircraft profiles. No difference between the dry and wet season flights was observed from this figure. The intercepts calculated for the separate seasons are found to be within the uncertainties of each other for all sites with the exception of Tabatinga (8.0±3.0 ppb for the wet season and 2.5±5.1 ppb for the dry season), although there are only 5 flights in the dry season in this case. For Rio Branco and Alta Floresta the number of flights in the two seasons are the same as each other, yet the r-values are similar, (RBA: 0.61 (wet) and 0.76 (dry), ALF: 0.60 (wet) and 0.57 (dry)). It is also not possible to remark whether outliers are more prevalent in the wet or dry season, with the scatter of data from the trend lines appearing indiscriminate of season. These findings suggest that GOSAT and aircraft $XCH_4$ values are both affected to the same degree by differences between the wet and dry seasons, as there is no identifiable relation to separate them in these results. Although the data is sparse so a relationship can not be ruled out entirely.

### 4.7.4 Co-location criteria

I have assessed the impact of the co-location criteria on the sampling of GOSAT $XCH_4$ by considering the use of different criteria (±5°, ±4°, ±3° and ±2°, as shown in Table 4.1). The inferred offset values at RBA, RBH and TAB each agree within their uncertainties across all co-location criteria, whilst at SAN they do all agree between ±5° and ±3°, and ALF and SAH between ±5° and ±4°. However at ±2° around SAN and ±3° around ALF the number of flights which have matching GOSAT soundings decreases to only 13 and 9, respectively, compared to 46 and 32 at ±5°, which do not allow a robust correlation coefficient to be calculated with these small sample sizes. At SAH there are also only 9 flights with coincident GOSAT soundings at ±3°, but more than half of the GOSAT soundings are lost compared to ±5°. When using a stricter coincidence criterion the coefficient of correlation remains consistent within 0.14, except at ALF where the difference is 0.25. The correlation and bias between GOSAT and the aircraft remain consistent with progressively smaller co-location criteria until the case where

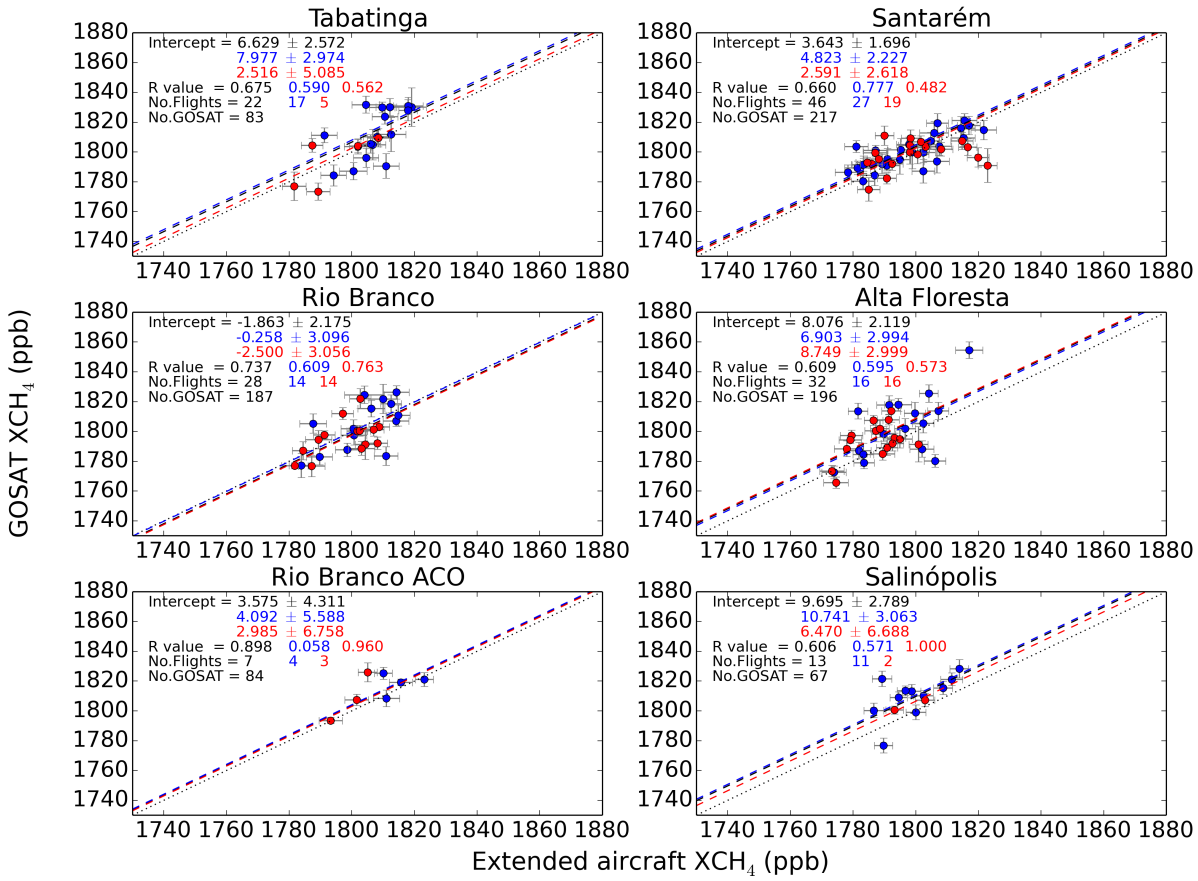


**Figure 4.23:** Correlation plot showing the aircraft $XCH_4$ on the x-axis versus the average GOSAT $XCH_4$ (for the same day, within $\pm 5^\circ$ of the site) and on the y-axis for the four AMAZONICA sites and two ACO sites. The black dotted line shows the one to one correlation line. The dashed lines show the result of a linear regression with the slope set to one, for all of the flights (in black), for only flights in the dry season in red and for only flights in the wet season in blue. The intercept values quoted are the difference in intercept of each line on the y-axis (colour-coded by season). The correlation coefficients (r-values) are also quoted, along with the number of flights and the corresponding averaged GOSAT soundings.

there are too few matches. Therefore I have chosen to use the $\pm 5^\circ$ co-location criteria.

## 4.8 ASSESSING THE IMPACT OF THE MODEL $XCO_2$

It is important to understand the extent to which the model $XCO_2$ used in the proxy $XCH_4$ calculation introduces biases in the GOSAT $XCH_4$ data. Parker et al. (2015) have studied the importance of this previously and concluded that in South America the uncertainties in $XCH_4$ are often smaller than the mean $XCH_4$ observed there, although in 2010 they are comparable due to South America exhibiting a complicated seasonal behaviour in $XCH_4$. To better quantify these biases I have compared the model $XCO_2$ to columns of $XCO_2$ calculated from the aircraft data by following the same method as detailed previously for $XCH_4$. For the stratosphere the MACC-II v13r $CO_2$ model which utilizes surface flux observation networks has been used. This has not been validated to the same extent as the TOMCAT modelled data for $XCH_4$ because $CO_2$ is less problematic to model in the stratosphere than $CH_4$ (Verma et al., 2017). For the extrapolated region error analysis a high resolution run was used which is driven by ERA-Interim operational high resolution ECMWF meteorology. Histograms showing the difference between the model and a linear approach in the extrapolated region (in the same way as has been previously detailed for $CH_4$) have been calculated. These are shown in Figure 4.24 for the 7.5 km case. This shows that $CO_2$ is far less variable than $CH_4$ in this region and shows that all differences are less than 0.2 ppm on average, with no clear seasonal offset observable.

The $XCO_2$ total columns are then calculated for each aircraft flight and compared with the GEOS-Chem model (which has been used in the Proxy $XCH_4$ GOSAT retrieval) using the same method detailed previously for the $XCH_4$ profiles. The results for all co-location criteria of this study are shown in Table 4.2 and the correlation plot for the $\pm 5^\circ$ case is shown in Figure 4.25 and shows that there is only a small difference between the aircraft and model $XCO_2$. This difference is less

| Co-Location Criteria | (degrees) | | | |
|---|---|---|---|---|
| | ±5 | ±4 | ±3 | ±2 |
| **Rio Branco (RBA)** | | | | |
| No. Flights | 28 | 18 | 11 | 9 |
| No. GOSAT | 187 | 128 | 67 | 33 |
| R Value | 0.74 | 0.75 | 0.79 | 0.78 |
| Offset (ppb) | -1.86 | -1.42 | -2.92 | 3.44 |
| Offset Error | 2.18 | 2.69 | 3.56 | 3.83 |
| **Santarém (SAN)** | | | | |
| No. Flights | 46 | 33 | 20 | 13 |
| No. GOSAT | 217 | 136 | 68 | 39 |
| R Value | 0.66 | 0.66 | 0.70 | 0.74 |
| Offset | 3.64 | 4.08 | 4.12 | 8.46 |
| Offset Error | 1.63 | 1.99 | 2.52 | 3.04 |
| **Alta Floresta (ALF)** | | | | |
| No. Flights | 32 | 28 | 9 | 9 |
| No. GOSAT | 196 | 116 | 50 | 50 |
| R Value | 0.61 | 0.37 | 0.63 | 0.63 |
| Offset | 8.08 | 10.14 | 15.64 | 15.64 |
| Offset Error | 2.12 | 2.34 | 3.53 | 3.53 |
| **Tabatinga (TAB)** | | | | |
| No. Flights | 22 | 14 | | |
| No. GOSAT | 83 | 39 | | |
| R Value | 0.68 | 0.68 | | |
| Offset | 6.63 | 8.51 | | |
| Offset Error | 2.57 | 3.21 | | |
| **Rio Branco ACO (RBH)** | | | | |
| No. Flights | 7 | 7 | 5 | |
| No. GOSAT | 84 | 77 | 52 | |
| R Value | 0.90 | 0.89 | 0.96 | |
| Offset | 3.58 | 4.92 | 3.20 | |
| Offset Error | 4.31 | 4.31 | 5.35 | |
| **Salinópolis (SAH)** | | | | |
| No. Flights | 13 | 13 | 9 | |
| No. GOSAT | 67 | 52 | 27 | |
| R Value | 0.61 | 0.65 | 0.50 | |
| Offset | 9.70 | 10.15 | 16.60 | |
| Offset Error | 2.79 | 2.84 | 3.60 | |

**Table 4.1:** Correlation results with varying degrees of filtering criteria for the extended aircraft profile $XCH_4$ vs same day averaged GOSAT $XCH_4$. Only criteria with at least 10 coincident GOSAT retrievals are shown. Offset is calculated as described in text.

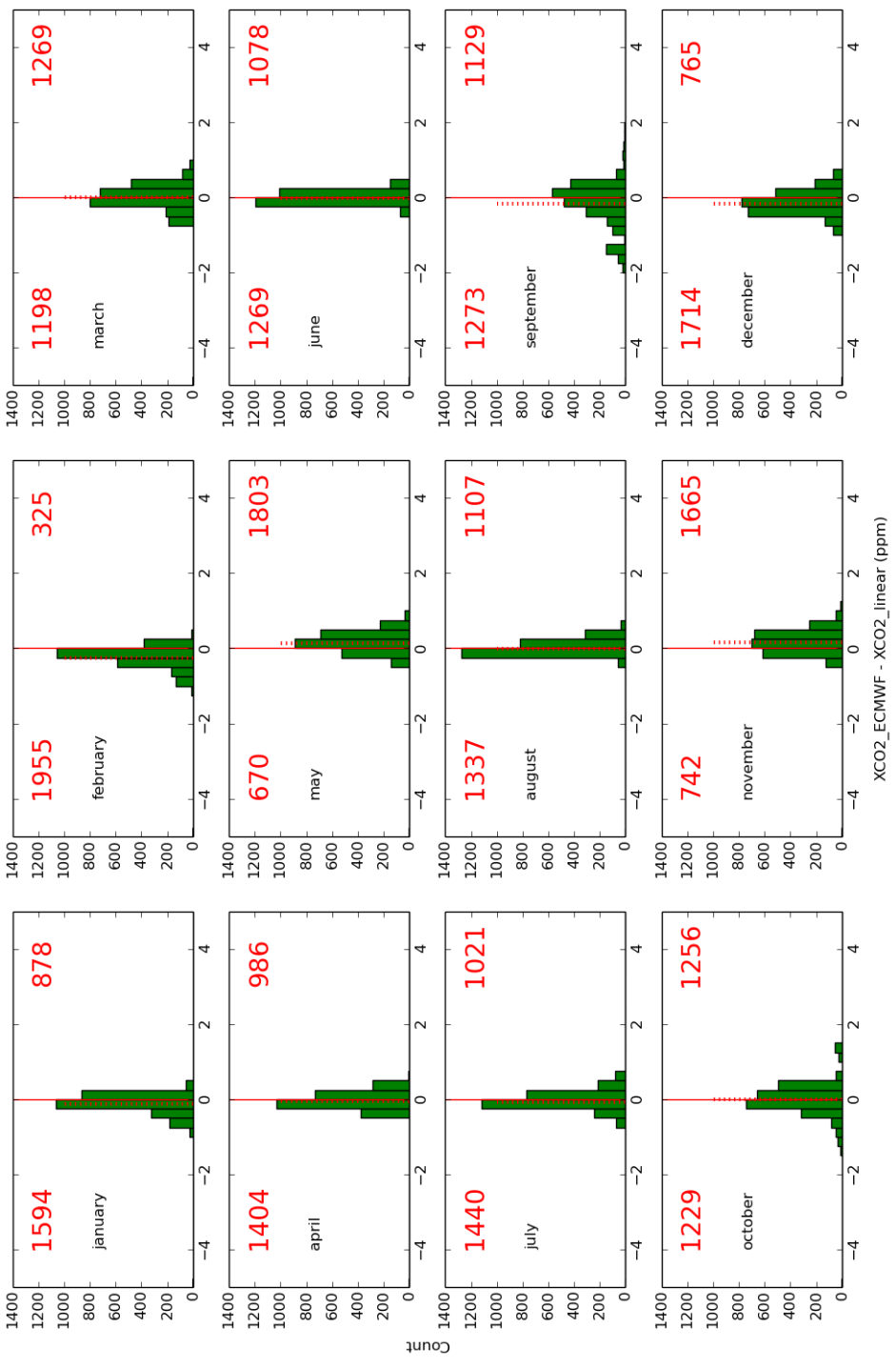


Figure 4.24: Monthly histograms of 2012 showing the difference in $XCO_2$ (partial column between 7.5 km and the tropopause) as measured by a high resolution model output (MACC-II v13r $CO_2$) and by assuming a constant $CO_2$ concentration throughout this region given by the model value at 7.5 km. The model was sampled for each day and at each grid-box within $\pm 5°$ of Rio Branco, resulting in approximately 2400 comparisons per month. The solid red line marks a difference of zero ppm whilst the dotted red line marks the mean difference for that month. The numbers in red indicate the number of occurrences either side of zero.

than 0.58 ppm for every site and co-location criteria except for Rio Branco. Here the difference ranges between 0.92 and 1.13 ppm. This difference in the model $XCO_2$ of 0.58 ppm to 1.13 ppm leads to differences in methane of approximately 2.6 ppb to 5.09 ppb, respectively, which are within GOSAT $XCH_4$ uncertainties. At $\pm 5^\circ$ co-location criteria the difference is particularly small at SAN, ALF and TAB, relating to $XCH_4$ differences of less than 1 ppb at these sites (as small as 0.3 ppb at ALF) with uncertainties between 0.9-1.7 ppb. The correlation coefficients between the model and aircraft $XCO_2$ are high at all of the AMAZONICA sites and are above 0.9 at Alta Floresta, Rio Branco and Santarém for all co-location criteria (0.93, 0.97, 0.90 and 0.76 for RBA, SAN, ALF and TAB respectively for $\pm 5^\circ$). The correlation coefficients are low at the ACO sites which are only compared with flights in 2013 since the high resolution model data was not available for 2014 (5 flights with GOSAT matches for RBH $\pm 5^\circ$ and 8 for SAH). The good correlation coefficients and small biases between the model $XCO_2$ used in the proxy retrieval and $XCO_2$ from aircraft suggest the $XCO_2$ model is unlikely to be causing the significant bias we observe at ALF in the Proxy $XCH_4$, however, it could be contributing towards part of the biases at other sites. At Rio Branco this comparison suggests that the model $XCO_2$ could be low by approximately 0.92 ppm (for $\pm 5^\circ$ co-location criteria), which is equivalent to approximately 4.1 ppb in $XCH_4$. This difference may explain why GOSAT $XCH_4$ values at RBA are the lowest compared to aircraft of all of the sites (see Table 4.1).

| Co-Location Criteria | (degrees) | | | |
|---|---|---|---|---|
| | ±5 | ±4 | ±3 | ±2 |
| **Rio Branco (RBA)** | | | | |
| Offset (ppm) | -0.92 | -0.95 | -1.02 | -1.13 |
| Offset Error | 0.42 | 0.55 | 0.60 | 0.52 |
| R Value | 0.93 | 0.93 | 0.95 | 0.94 |
| **Santarém (SAN)** | | | | |
| Offset | -0.22 | -0.24 | -0.25 | -0.49 |
| Offset Error | 0.19 | 0.23 | 0.29 | 0.32 |
| R Value | 0.97 | 0.97 | 0.98 | 0.99 |
| **Alta Floresta (ALF)** | | | | |
| Offset | -0.06 | 0.03 | 0.58 | 0.58 |
| Offset Error | 0.38 | 0.41 | 0.84 | 0.84 |
| R Value | 0.90 | 0.90 | 0.92 | 0.92 |
| **Tabatinga (TAB)** | | | | |
| Offset | -0.22 | -0.02 | | |
| Offset Error | 0.35 | 0.40 | | |
| R Value | 0.76 | 0.74 | | |
| **Rio Branco ACO (RBH)** | | | | |
| Offset | -0.44 | -0.44 | -0.19 | |
| Offset Error | 0.65 | 0.66 | 0.90 | |
| R Value | 0.33 | 0.33 | 0.96 | |
| **Salinópolis (SAH)** | | | | |
| Offset | 0.54 | 0.52 | 0.51 | |
| Offset Error | 0.38 | 0.38 | 0.37 | |
| R Value | 0.46 | 0.49 | 0.72 | |

Table 4.2: Correlation results with varying degrees of filtering for extended aircraft profile $XCO_2$ vs same day averaged model $XCO_2$ which is used in the University of Leicester Proxy methane retrieval (GEOS-Chem in this study). The aircraft profile $XCO_2$ is calculated in the same way as for the $XCH_4$ but instead using an ECMWF MACC $CO_2$ model for the stratosphere and a high resolution version for the extrapolated region error analysis. The offset is calculated as the intercept on the Model $XCO_2$ axis when a linear function of gradient 1 is fit to the data.

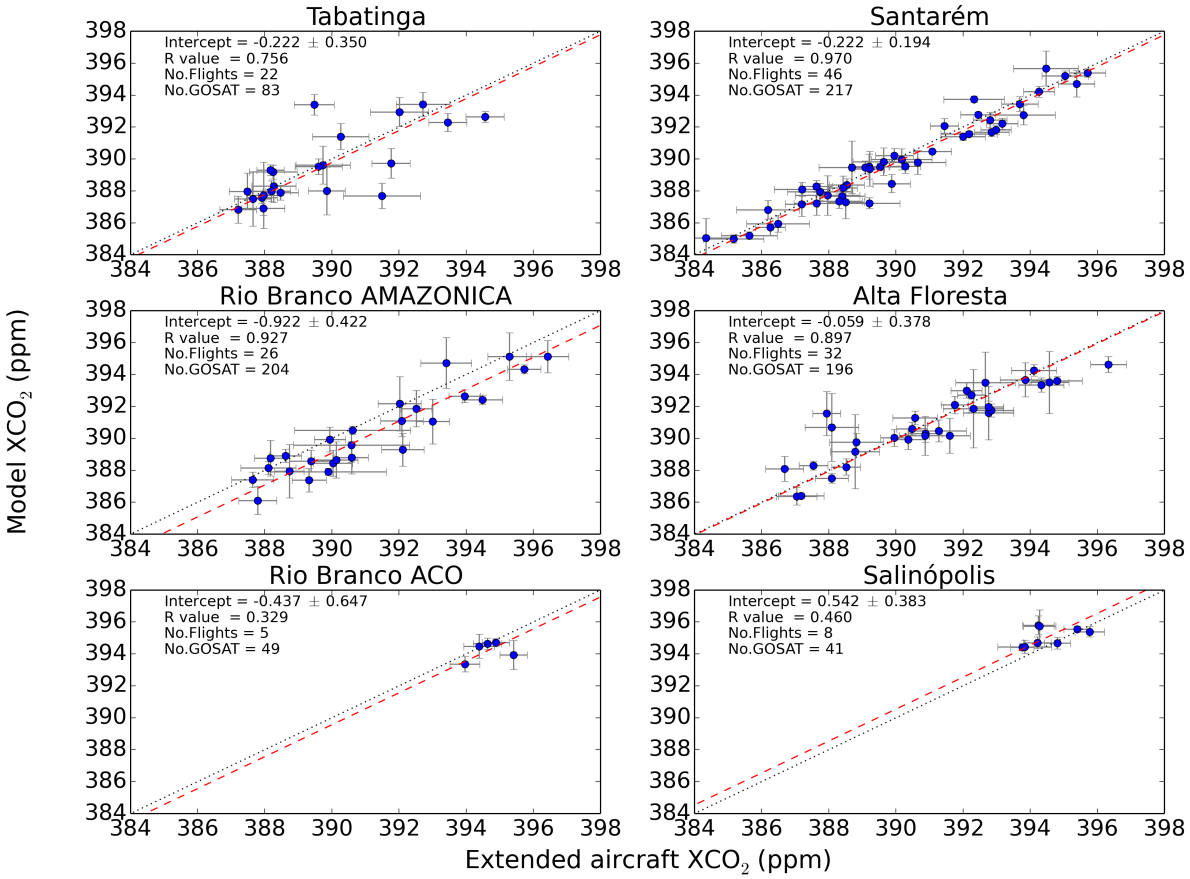


**Figure 4.25:** Correlation plot to illustrate the data shown in Table 4.2 for the case when the co-location criteria is ±5 degrees. Showing the GEOS-Chem model $XCO_2$ on the y-axis versus the aircraft $XCO_2$ on the x-axis for the four AMAZONICA sites and two ACO sites. The black dotted line shows the one to one correlation line. The red dashed line shows the result of a linear regression with the slope set to one. From this the offset values given in Table 4.2 are the difference in intercept of each line on the y-axis, giving the mean offset between the model and aircraft $XCO_2$.

## 4.9 PARAMARIBO–FTS COMPARISONS WITH GOSAT

Results of the aircraft campaigns are supported by comparisons between $XCH_4$ from GOSAT and a ground-based instrument at Paramaribo, Suriname, (location shown in Figure 4.6). The instrument measures $XCH_4$ using a Bruker 120M Fourier Transform Spectrometer (Warneke et al., 2010). Since the launch of GOSAT in 2009 these measurements have been made during an approximately two week period in November each year. Between mid-2009 and 2013

there were five measurement campaigns, providing 306 ground-based $XCH_4$ measurements with, in total, 109 coincident GOSAT soundings within $\pm 1$ day and $\pm 5^\circ$ of these measurements. In Figure 4.26, these measurements are shown in context with the spatially coincident GOSAT soundings for the entire time period. To highlight the campaign periods further, the averages over these time periods are plotted (with the x-axis error bars indicating the time period and the y-axis error bars indicating the standard deviation of the encompassed $XCH_4$ data). The $XCH_4$ measured at the FTS site agrees well with the GOSAT data (r = 0.89) and GOSAT tends to be higher by $3.4 \pm 2.1$ ppb across all campaigns, although the uncertainties do overlap for each of these periods.

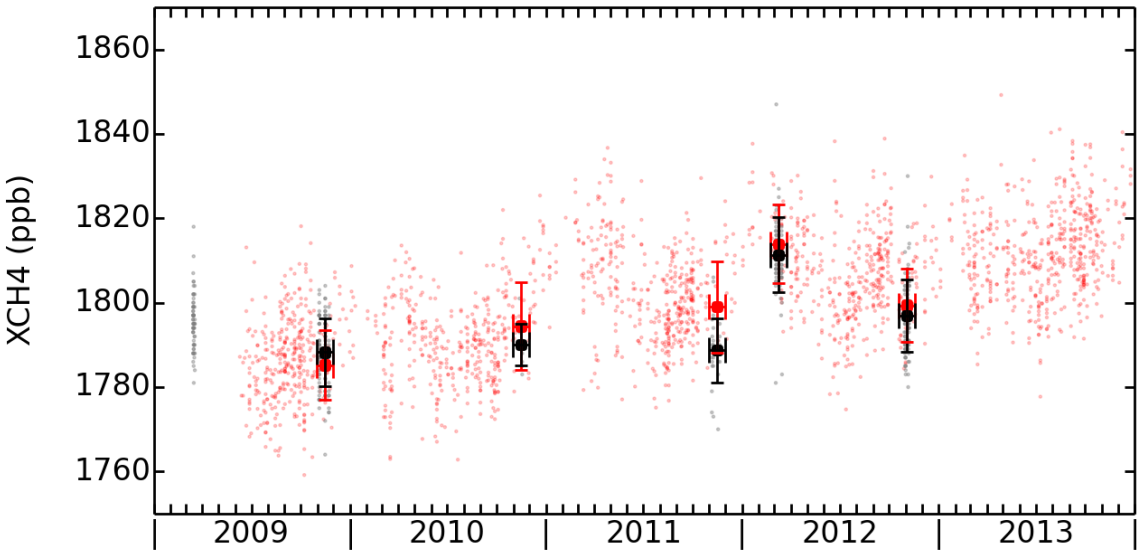


**Figure 4.26:** Showing comparisons between Paramaribo-FTS (black) and GOSAT (red) for $XCH_4$. The lighter shaded scatter points show all of the Paramaribo-FTS data between 2009 and 2013 and all GOSAT until the end of 2013 which is within $\pm 5^\circ$ of the site. The average of Paramaribo-FTS data (standard deviation given in y-direction error bars) for each campaign period (shown in x-direction error bars) and coincident GOSAT within the same time period is averaged and also plotted.

## 4.10 CONCLUSIONS

The tropics are an important region for $CH_4$ fluxes to the atmosphere. However, tropical greenhouse gas concentrations are strongly under-sampled. Satellites such as GOSAT can potentially provide much needed observations here, but their current usefulness is limited due to their lack of validation in the tropics. Recently, vertical profile data measured in situ over the Amazon have become available and I present new measurements up to 7.5 km altitude taken between 2013 and mid 2015 at two sites in the Amazon, chosen specifically to represent air before and after travelling across the basin. These profiles show a distinct seasonality, with the inland site exhibiting enhanced $CH_4$ concentrations in the wet season compared to those at the coastal site. These data are used for the first time to validate GOSAT remote sensing $XCH_4$ retrievals over the Amazon and determine whether or not they agree with in situ vertical $CH_4$ profiles sampled at these two sites in the Amazon. Additional profiles extending up to 4.5 km altitude measured during the AMAZONICA project have also been used at a further three sites. The aircraft profiles, which extend up to 4.5 km and 7.5 km, were extended using a stratospheric chemistry model and by extrapolating throughout the remainder of the troposphere. The uncertainties involved in this method were estimated by examining the variation of methane in a high resolution model, and the difference between the 4.5 km and 7.5 km heights was evaluated. The analysis into the effect of using our newer 7.5 km aircraft profiles compared to 4.5 km profiles shows that the uncertainties can be significantly reduced by measuring at higher altitudes.

A good agreement is found between in situ data extrapolated throughout the atmosphere and the remote sensing data from GOSAT in respect to the seasonality of $XCH_4$ measurements. The absolute concentrations agree within uncertainties or show no significant difference (student's t-test) at three of the aircraft sites ($-1.9\pm2.2$ ppb for RBA, $3.6\pm4.3$ ppb for RBH, $3.6\pm1.7$ ppb for SAN, and $6.6\pm2.6$ ppb for TAB), whilst the other two show GOSAT to be slightly higher than aircraft measurements, by up to approximately 10 ppb in the most differing case

(8.1±2.1 ppb for ALF and 9.7±2.8 ppb for SAH). Uncertainties introduced by the model $XCO_2$ in the proxy $XCH_4$ method could account for part of these biases, especially at RBA where the model is shown to be lowest compared to aircraft measurements. This may explain why $XCH_4$ at RBA is also low compared to aircraft data. Measurements from a ground-based FTS at Paramaribo have also been compared with GOSAT and are found to be in agreement within their uncertainties. The fairly small difference between the extrapolated in situ observations and the GOSAT remote sensing data is encouraging evidence that remotely sensed atmospheric $XCH_4$ data from GOSAT has a small bias over the Amazon and can provide new insights into wetland $CH_4$ emissions in the Amazon. The better understanding of bias in GOSAT $XCH_4$ measurements can therefore provide us with improved top-down surface flux estimates of $CH_4$ in the Amazon, which could help to resolve some of the discrepancies between models, as were highlighted by Melton et al. (2013). This will allow for better confidence when assessing modelled $XCH_4$ columns driven by emissions inventories.

# 5 USING GOSAT $XCH_4$ AND IN SITU DATA TO ASSESS EMISSIONS INVENTORIES WITHIN A CHEMISTRY TRANSPORT MODEL

## 5.1 INTRODUCTION

In this chapter the chemistry transport model GEOS-Chem (ran by the University of Edinburgh) is assessed in the Amazon. This model represents the current state-of-the-art in our ability to model $XCH_4$ on a global scale and utilises some of the most accurately considered $CH_4$ source emission inventories. I compare these GEOS-Chem modelled outputs with the in situ ACO and AMAZONICA aircraft measurements, and then with the GOSAT $XCH_4$ measurements, which have already been validated in Chapter 4 and found to be in good agreement with in situ data. There are two main aims of this chapter. The first is to investigate the behaviour of $XCH_4$ in the Amazon as observed by GOSAT, to learn about the large-scale patterns of $XCH_4$ over multi-year time scales now that we have five and a half years of measurements. Secondly, to compare these GOSAT measurements with the GEOS-Chem model output to learn where the model is performing well compared to GOSAT, and where there are disagreements.

Bloom et al. (2016) (who's wetland $CH_4$ emissions are used in the GEOS-Chem model), find that estimates of Amazon river basin wetland $CH_4$ emissions range between 16% - 29% of the global wetland emissions source and explain that their methods to determine emissions in densely vegetated wetland areas such as in the Amazon are ill-equipped for these regions. They therefore anticipate

errors in seasonal and inter-annual variability to be larger within densely vegetated wetland areas like the Amazon. By examining where GOSAT and GEOS-Chem are in disagreement, the locations and seasons in which GOSAT disagrees with GEOS-Chem can be determined; providing insights into the Amazonian methane environment. These differences should highlight where state-of-the-art emission inventories are currently lacking in understanding.

## 5.2 MODELLED $XCH_4$ IN THE AMAZON

To model $CH_4$ in the Amazon, climate models utilise emission inventories which account for all of the sources and sinks of $CH_4$ as accurately as possible. These 'bottom-up' datasets are often based on ground-based and laboratory measurements of 'typical' ecosystems or sources, and are scaled-up and extrapolated to cover larger areas. As a result the models which use these inputs need to be well validated because, particularly in the Amazon, it is not possible to measure the emissions from every source at every location, so these up-scaling processes may misrepresent the true variability and scale of emissions in a particular area.

The outputs used are from version v9-02 of the GEOS-Chem global 3-D chemistry transport model (Bey et al., 2001; Fraser et al., 2014). The model is driven by assimilated meteorological fields from the Goddard Earth Observing System v5 from the Global Modelling and Assimilation Office Global Circulation model which is based at NASA Goddard. The model is used at a horizontal resolution of $4^\circ \times 5^\circ$, with 47 levels spanning from the surface to 0.01 hPa. Of these levels, typically 30 are within the troposphere. The 3-D meteorological data is updated every 6 hours, and boundary layer and tropopause heights are updated every 3 hours. The model uses biomass burning emissions from the Global Fire Emissions Database (GFED v3), which include both seasonal and inter-annual variations (Werf et al., 2010), with biofuel burning emissions from Yevich and Logan (2003). Anthropogenic sources of coal mining, oil and gas production, and from

ruminants are from the EDGAR 3.2 FT database (Emissions Data Base for Global Atmospheric Research, Fast Track) (Van Aardenne et al., 2005). Natural sources from oceans (Houweling et al., 1999), termites, and hydrates are also included, as well as a soil sink (Fung et al., 1991). The rice and wetland emissions are detailed in Bloom et al. (2012). The OH sink in the model is described by monthly mean 3-D OH fields from a full chemistry Ox-NOx-VOC run of the model (Fiore et al., 2003). Loss rates of methane in the stratosphere are adapted from a 2-D stratospheric model (Wang et al., 2004).

## 5.3 COMPARING GEOS-CHEM WITH THE AIRCRAFT PROFILES

GEOS-Chem simulated $CH_4$ profiles are sampled at each GOSAT time and location within the co-location criteria of each aircraft site and are converted into $XCH_4$ total columns using the GOSAT averaging kernels. These are then compared with the extended aircraft profiles in the same way we have previously compared them with GOSAT in Chapter 4. These results are shown in Table 5.1 for varying co-location criteria ($\pm 5^\circ$, $\pm 4^\circ$, $\pm 3^\circ$ and $\pm 2^\circ$ of each aircraft site and on the same day as the flight). Figures 5.1 and 5.2 show the time series of GEOS-Chem and the aircraft flights and the correlation plot for the $\pm 5^\circ$ case respectively, which are analogous to Figures 4.20 and 4.22 which showed GOSAT instead of GEOS-Chem. GEOS-Chem values are considerably lower than the aircraft values and also GOSAT. This difference is largest in the northern AMAZONICA sites (Santarém and Tabatinga) where the offset between GEOS-Chem and aircraft for the $\pm 5^\circ$ co-location criteria is -26.0$\pm$0.6 ppb at Santarém and -19.8$\pm$1.0 ppb at Tabatinga. The offset with both the high and low altitude Rio Branco flights is smaller yet similar for both; -15.7$\pm$1.9 ppb and -15.0$\pm$0.9 ppb respectively. The other two sites show smaller offsets still and are more similar to the offsets seen between GOSAT and aircraft, albeit in the opposite direction (-12.1$\pm$1.1 ppb at Salinópolis and -7.3$\pm$0.8 ppb at Alta Floresta compared

to 9.7±2.8 ppb and 8.1±2.1 ppb for GOSAT). At all but one site the correlation between GEOS-Chem and aircraft is lower than that between GOSAT and aircraft for the larger co-location criteria.

Figure 5.3 shows a time series of a direct comparison between GEOS-Chem and the aircraft sites, plotting the difference between them for each flight. This further illustrates that for the majority of flights GEOS-Chem has a lower concentration than the calculated aircraft $XCH_4$. At Tabatinga this is true for 95% of the flights; 98% for Santarém, 91% for Rio Branco, 92% for Salinópolis, and 75% at Alta Floresta. This figure illustrates that despite the offset between GEOS-Chem and the aircraft $XCH_4$, there is no obvious change to this offset with time, with the offset at each site remaining consistent over the entire measurement time-line.

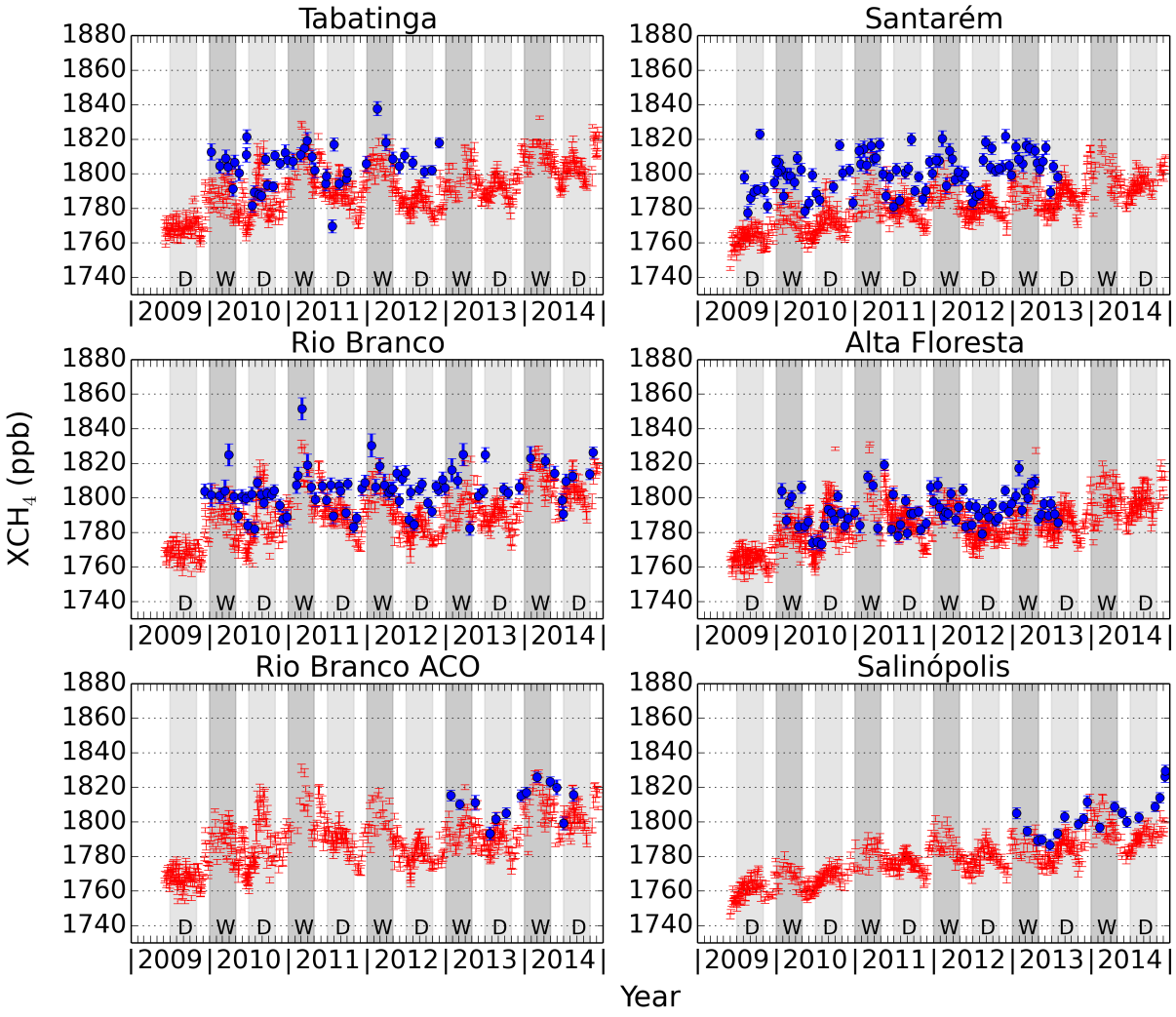


**Figure 5.1:** $XCH_4$ concentration in parts per billion against the date of measurements for daily averaged GEOS-Chem sampled at GOSAT soundings within $\pm 5^\circ$ of the aircraft sites in red (error bars representing the standard error), and extended aircraft $XCH_4$ in blue. The approximate dry seasons (July–October) and wet seasons (January–April) are marked with D and W respectively.

| Co-Location Criteria | (degrees) | | | |
|---|---|---|---|---|
| | ±5 | ±4 | ±3 | ±2 |
| **Rio Branco** | | | | |
| No. Flights | 28 | 18 | 11 | 9 |
| No. GOSAT | 187 | 128 | 67 | 33 |
| R Value | 0.501 | 0.473 | 0.435 | 0.505 |
| Offset (ppb) | -14.988 | -10.916 | -12.478 | -13.227 |
| Offset Error | 0.891 | 1.127 | 1.433 | 1.542 |
| **Santarém** | | | | |
| No. Flights | 46 | 33 | 20 | 13 |
| No. GOSAT | 217 | 136 | 68 | 39 |
| R Value | 0.163 | 0.187 | 0.543 | 0.548 |
| Offset | -25.966 | -24.710 | -22.348 | -23.692 |
| Offset Error | 0.639 | 0.745 | 0.959 | 1.165 |
| **Alta Floresta** | | | | |
| No. Flights | 32 | 28 | 9 | 9 |
| No. GOSAT | 196 | 116 | 50 | 50 |
| R Value | 0.416 | 0.516 | 0.411 | 0.411 |
| Offset | -7.300 | -5.603 | 0.111 | 0.111 |
| Offset Error | 0.770 | 0.781 | 1.393 | 1.393 |
| **Tabatinga** | | | | |
| No. Flights | 22 | 14 | | |
| No. GOSAT | 83 | 39 | | |
| R Value | 0.370 | 0.710 | | |
| Offset | -19.772 | -15.689 | | |
| Offset Error | 0.959 | 1.161 | | |
| **Rio Branco ACO** | | | | |
| No. Flights | 7 | 7 | 5 | |
| No. GOSAT | 84 | 77 | 52 | |
| R Value | 0.804 | 0.788 | 0.619 | |
| Offset | -15.734 | -15.949 | -10.898 | |
| Offset Error | 1.860 | 1.821 | 2.104 | |
| **Salinópolis** | | | | |
| No. Flights | 13 | 13 | 9 | |
| No. GOSAT | 67 | 52 | 27 | |
| R Value | 0.704 | 0.618 | 0.746 | |
| Offset | -12.058 | -10.971 | -13.560 | |
| Offset Error | 1.052 | 1.009 | 1.178 | |

Table 5.1: Correlation results with varying degrees of filtering for the extended aircraft profile $XCH_4$ verses the same day averaged GEOS-Chem $XCH_4$ sampled at the same GOSAT locations. Only criteria with at least 10 coincident GOSAT retrievals are shown.

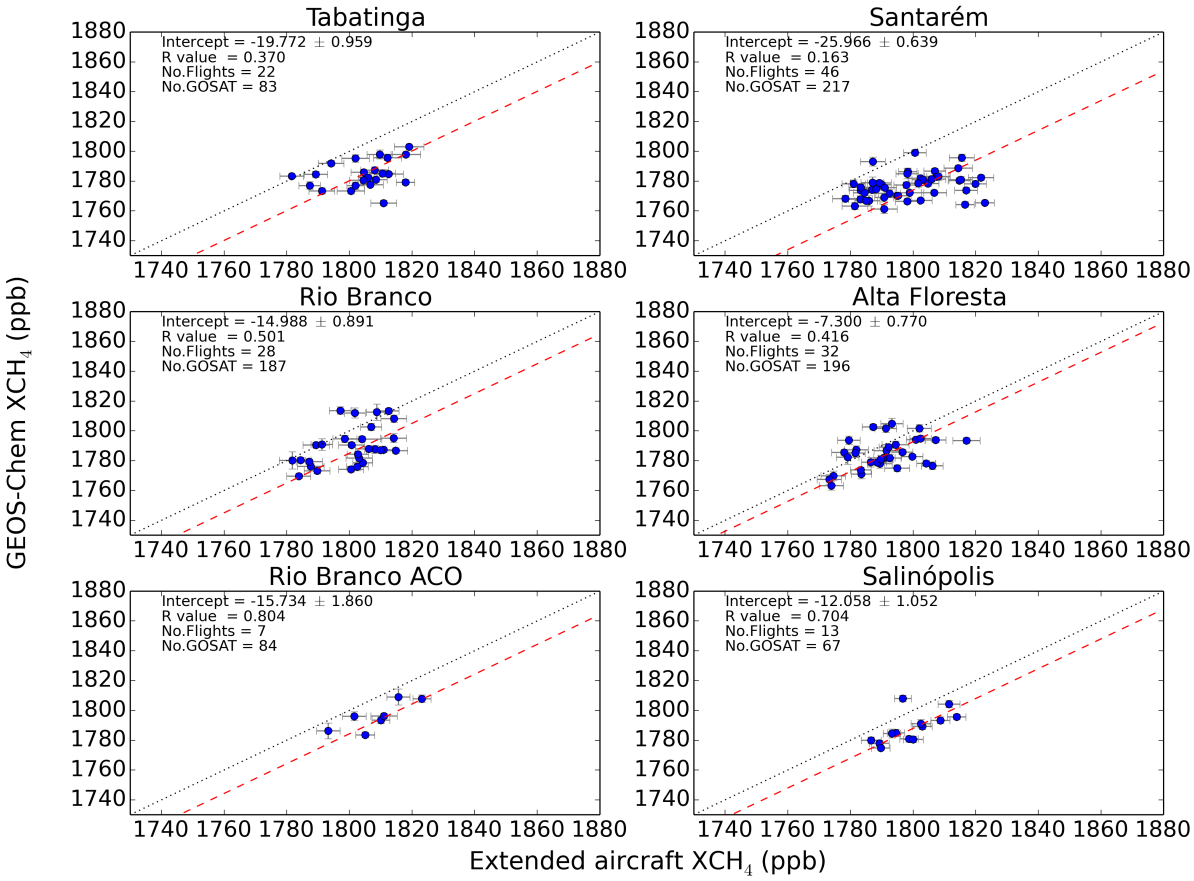


**Figure 5.2:** Correlation plot showing GEOS-Chem $XCH_4$ on the y-axis versus the aircraft $XCH_4$ on the x-axis for the four AMAZONICA sites and two ACO sites. The black dotted line shows the one to one correlation line. The red dashed line shows the correlation line when the gradient is set to one. From this the offset values given in Table 5.1 are the difference in intercept of each line with the y-axis, giving the mean offset between GEOS-Chem and aircraft $XCH_4$.

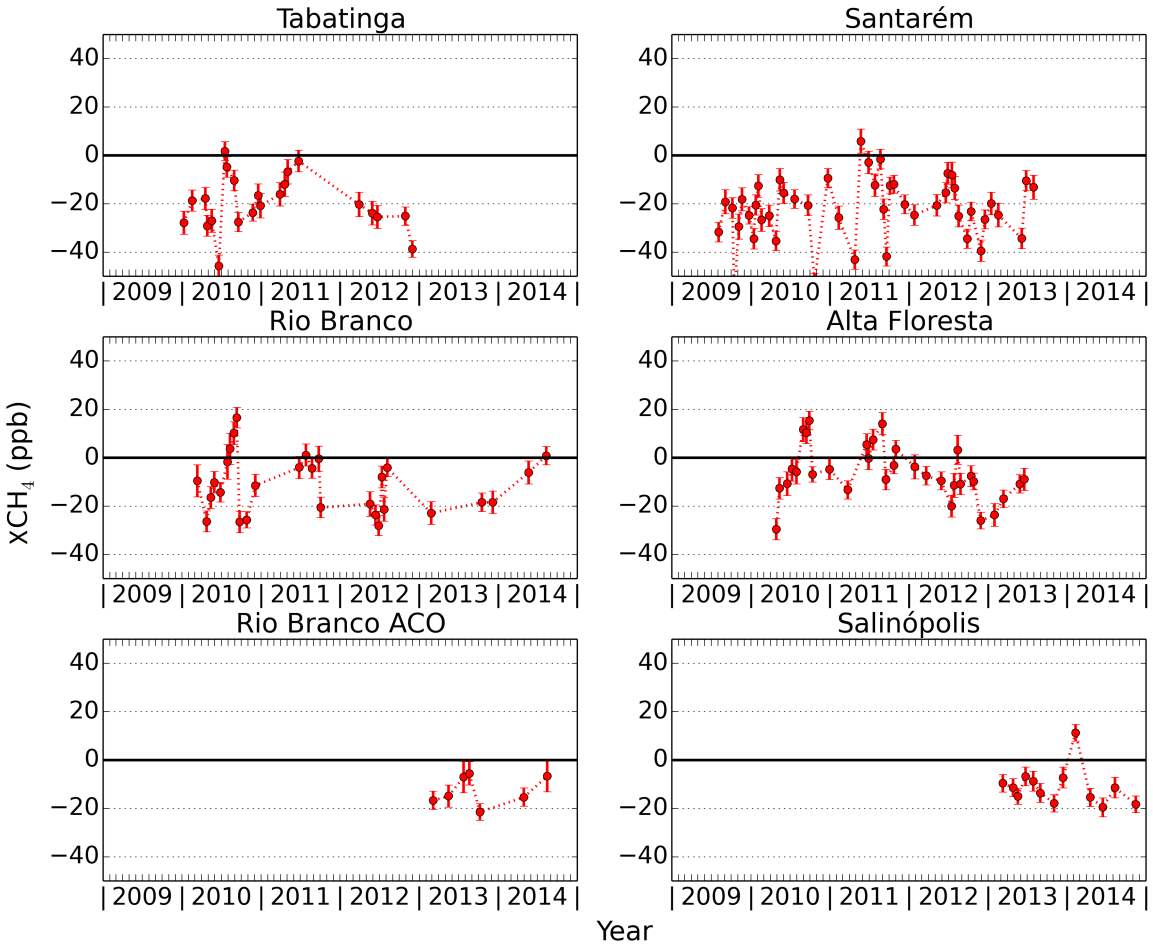


**Figure 5.3:** Time series of the difference between GEOS-Chem and aircraft $XCH_4$ in ppb (GEOS-Chem minus aircraft) with GEOS-Chem sampled at GOSAT sounding locations within $\pm 5^\circ$ and same day co-location of the flights.

## 5.4 INTERPRETING GOSAT $XCH_4$ CONCENTRATIONS

Figure 5.4 shows the yearly average of GOSAT Proxy $XCH_4$ v6 for all cloud-free retrievals in 2011. This data has been binned onto a $2^\circ \times 2^\circ$ grid. From this it can clearly be seen that average $CH_4$ concentrations are highest in South East Asia, Central Africa and in tropical South America; compared to temperate regions. GOSAT also shows the north-south gradient in $XCH_4$, with the Southern Hemispheric values in the region of 1710-1780 ppb, whilst the majority of the Northern Hemisphere (excluding Greenland) is typically between 1760-1800 ppb on average. Figure 5.5 shows three month averages of global GOSAT $XCH_4$ from June 2009 until the end of 2014. From this figure, global concentrations of $XCH_4$ are seen to have risen over this time frame, with concentrations becoming higher each year as shown by each row in the plot. Concentrations in 2009 and 2010 are typically closer to 1770 ppb in the Northern Hemisphere, whilst in the same geographical regions the concentrations increase each year and by autumn (September-November) 2014 these concentrations are typically well in excess of 1810 ppb in the Northern Hemisphere. This figure also shows several features of the GOSAT measurement technique. Sun-glint measurements over the oceans move north and south with the seasons. In the Northern-Hemisphere summer the satellite measures over the oceans in the Northern Hemisphere, whilst in winter the measurements are over the Southern Hemisphere. A lack of daylight over the northern latitudes during winter is also seen to limit the upper latitude at which GOSAT can measure $XCH_4$.

### 5.4.1 Examining GOSAT $XCH_4$ in the Amazon

The remainder of this chapter concentrates on $XCH_4$ in South America. Figures 5.6, 5.7, 5.8, 5.9, 5.10 and 5.11 show monthly averages of GOSAT $XCH_4$ for 2009, 2010, 2011, 2012, 2013 and 2014 respectively. From these figures the global growth rate of $CH_4$ can be seen to change throughout the Amazon, with concen-

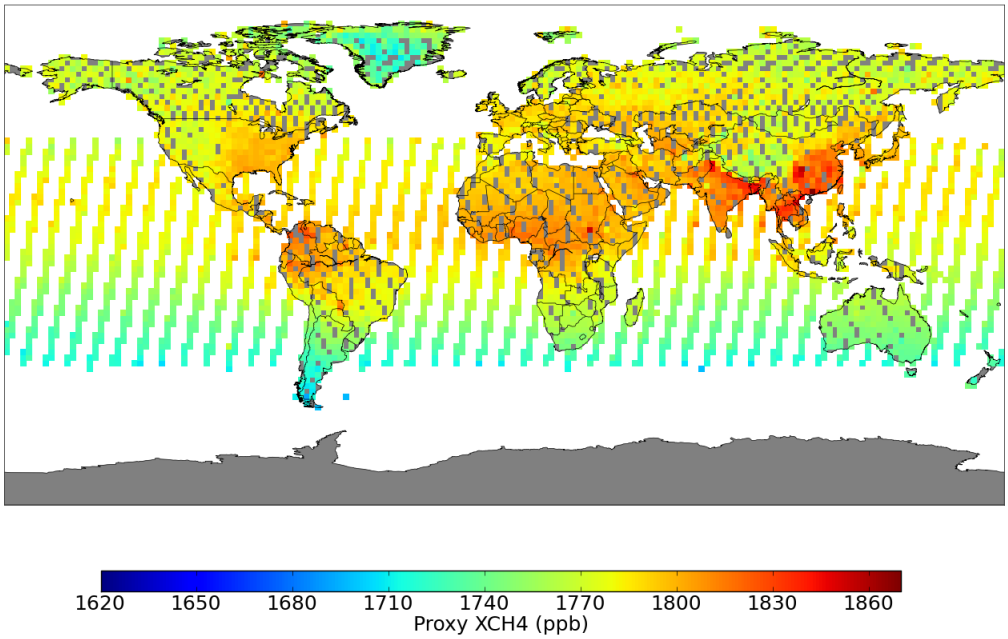


**Figure 5.4:** GOSAT Proxy $XCH_4$ v6 UoL retrieval (in ppb) averaged for 2011. The data is plotted to a $2^\circ \times 2^\circ$ grid.

trations becoming gradually higher each year. Changes in the GOSAT sampling pattern are also observable between July and August 2010, resulting in data gaps between overpasses and the appearance of having less coverage, as explained in Chapter 3. In 2014 these gaps were filled by the Amazonian dithering overpass technique as can be clearly seen for September 2014. These maps also illustrate the impact of the wet and dry seasons on the data coverage. In Figure 5.8 where the sampling pattern remains the same for the entire year, the best coverage is seen between June and September, which is roughly speaking the dry season in the Amazon. Whilst coverage is especially poor in the central Amazon between January and April, which corresponds to approximately the wet season in the Amazon. This pattern is observable in all years of GOSAT data and is especially noticeable in 2010 with the original GOSAT sampling pattern when comparing the lack of data in January and February to the almost full coverage of June and July. GOSAT $XCH_4$ is also seen to follow a seasonal pattern where there are higher values in the north of the Amazon compared to the south in the drier months. Whereas in the wet season the higher values extend further south. Figure 5.10 for 2013 in particular shows heightened concentrations over Bolivia in January-March and in December, whilst there are no such enhancements in the middle of the year.

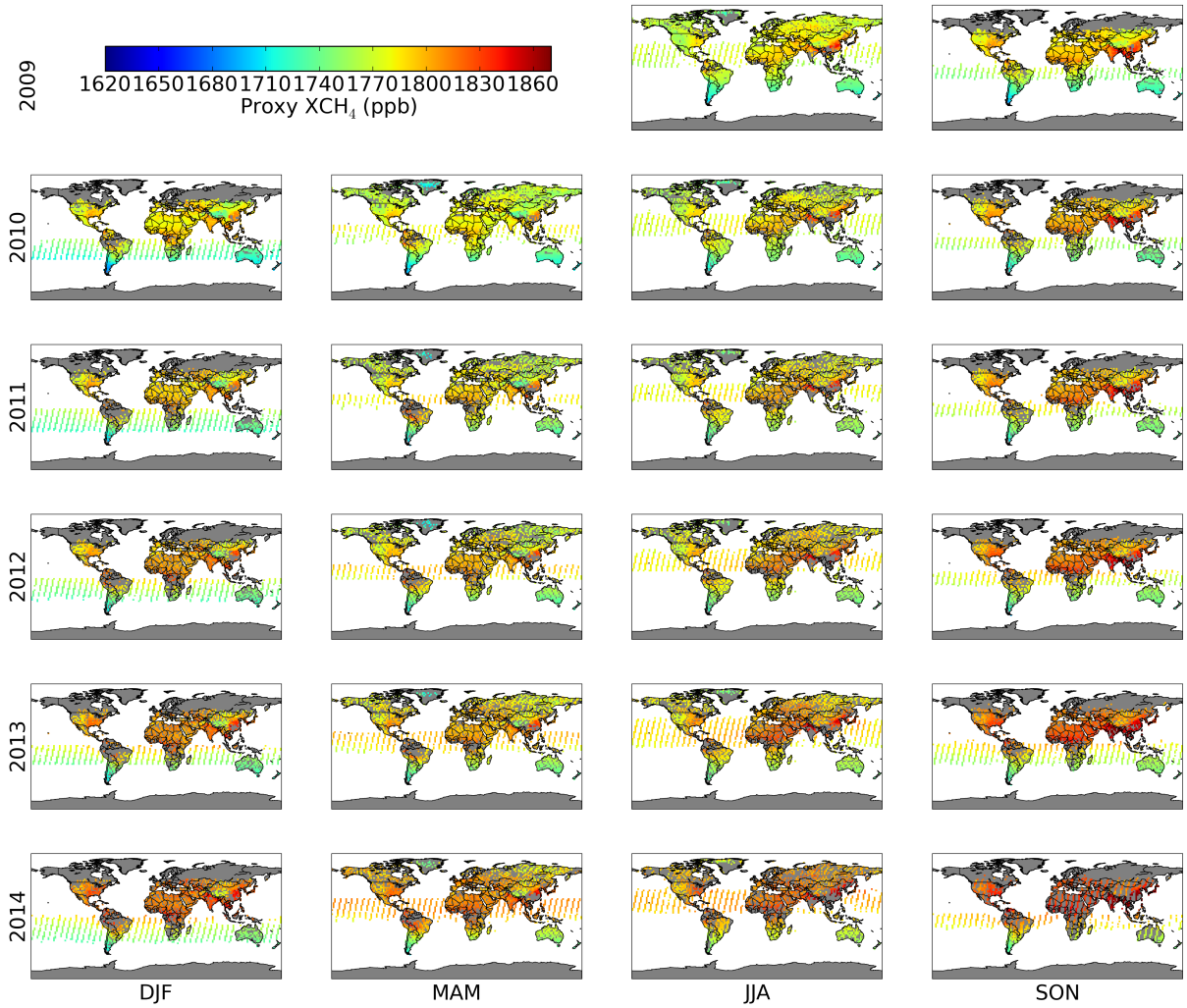


**Figure 5.5:** GOSAT Proxy $XCH_4$ v6 UoL retrieval (in ppb). Showing averages for the Northern Hemisphere seasons, December-February, March-May, June-August and September-November for the years 2009 to 2014 (winter seasons at the beginning of the year and using December from the previous year). The data is plotted to a $2^\circ \times 2^\circ$ grid.

The seasonality of GOSAT $XCH_4$ in the Amazon can be better assessed by looking at seasonal averages of the data, with January, February, March and April representing the wet season, and July, August, September and October representing the dry season. Data from the months which are intermediary between the two seasons are excluded. Figure 5.12 shows these seasonally averaged GOSAT $XCH_4$ data for the different wet and dry seasons between 2010 and 2014, including the difference between the seasons in each year. These maps show that, compared to the rest of the Amazon, northern South America (particularly around the border of Colombia and Venezuela) has higher concentrations in the dry season (by up to approximately 30 ppb), whilst in the wet season the values are higher

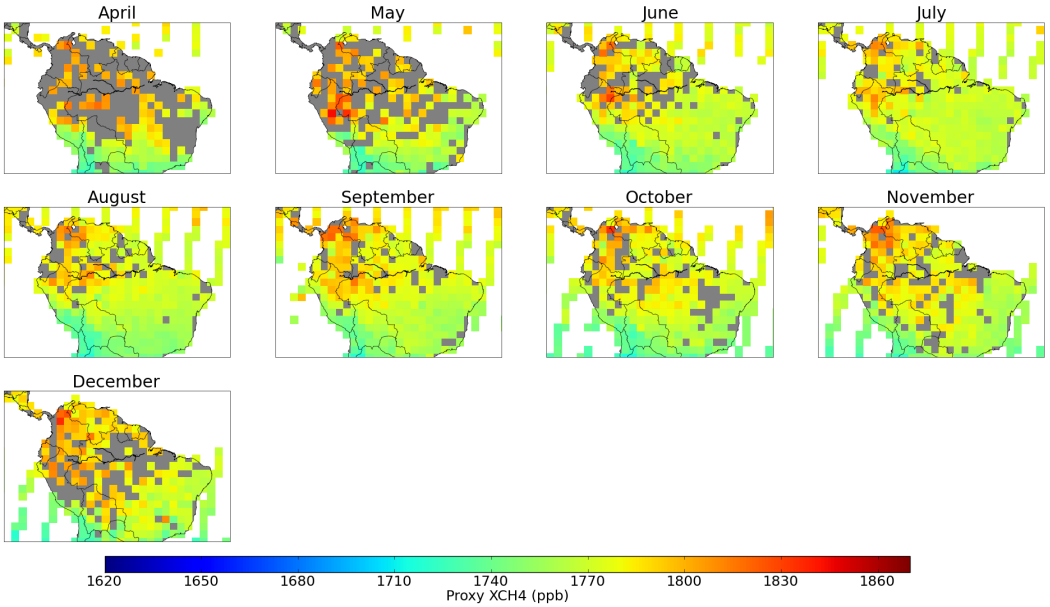


**Figure 5.6:** Monthly averaged GOSAT $XCH_4$ for 2009. The data is plotted to a $2^\circ \times 2^\circ$ grid.

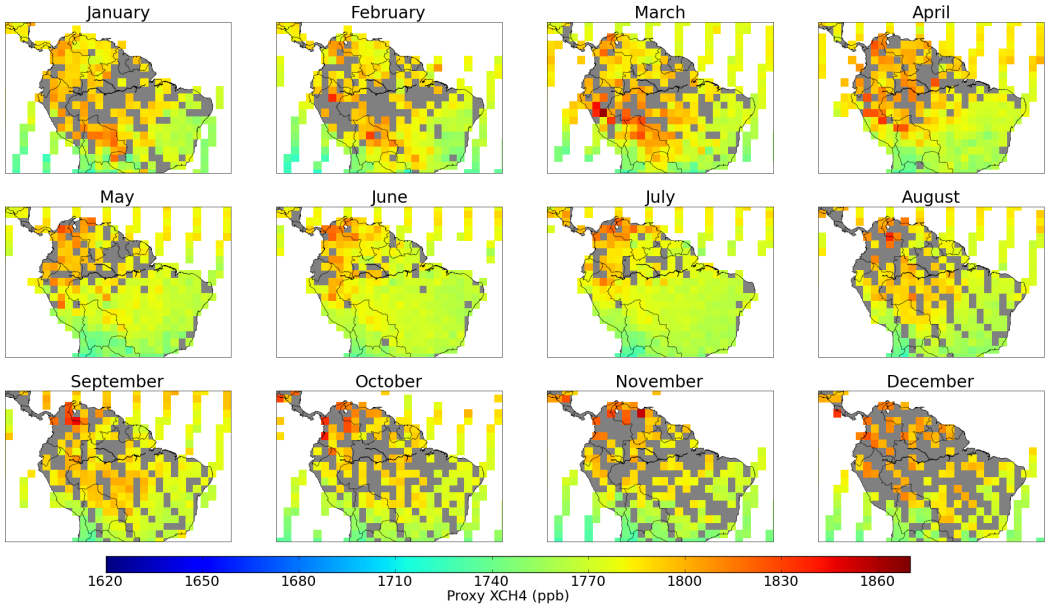


**Figure 5.7:** Monthly averaged GOSAT $XCH_4$ for 2010. The data is plotted to a $2^\circ \times 2^\circ$ grid.

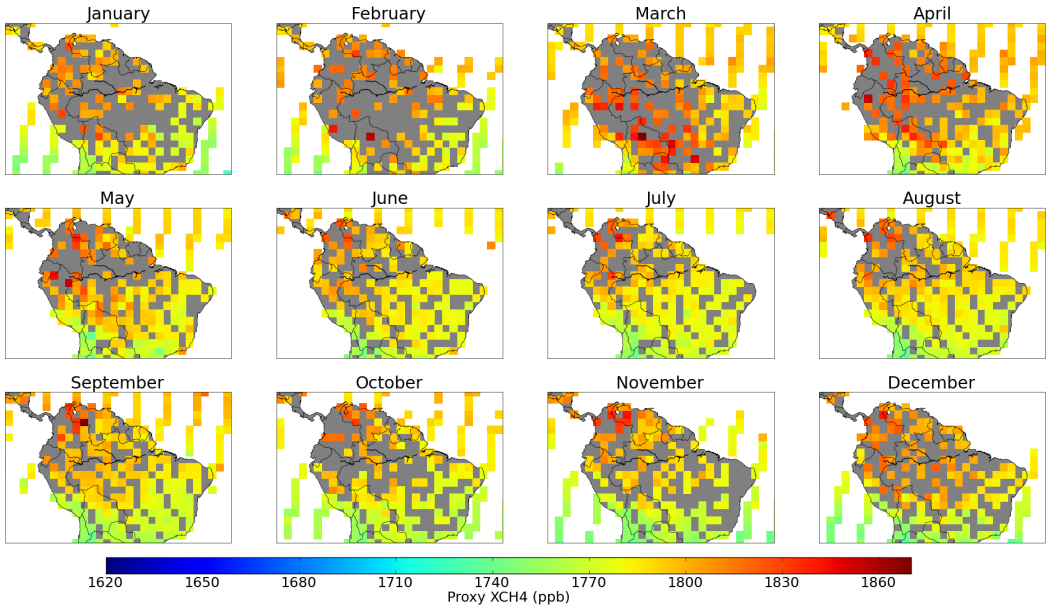


**Figure 5.8:** Monthly averaged GOSAT $XCH_4$ for 2011. The data is plotted to a $2^\circ \times 2^\circ$ grid.

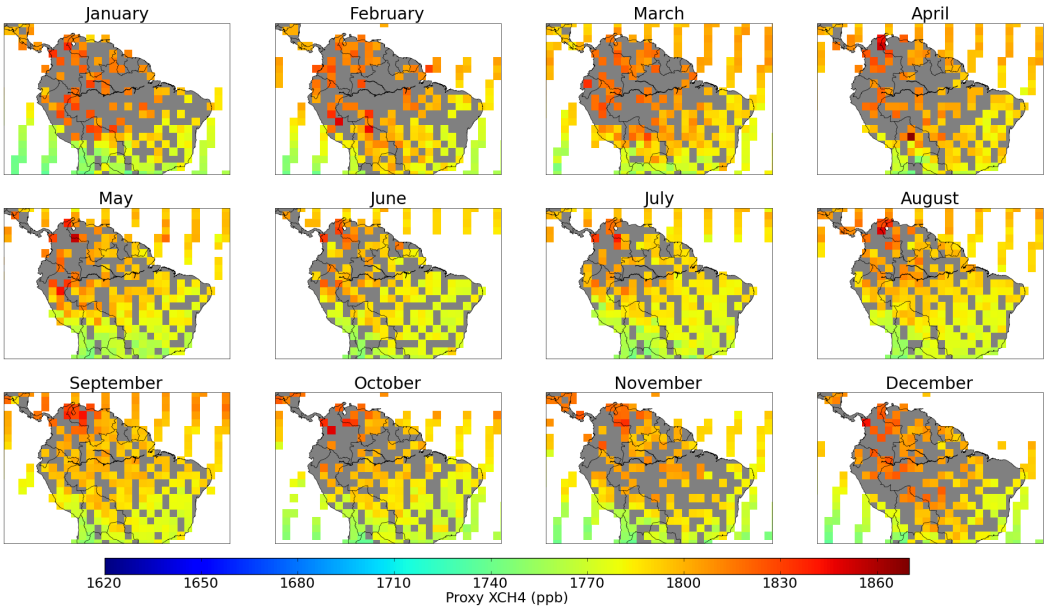


**Figure 5.9:** Monthly averaged GOSAT $XCH_4$ for 2012. The data is plotted to a $2^\circ \times 2^\circ$ grid.

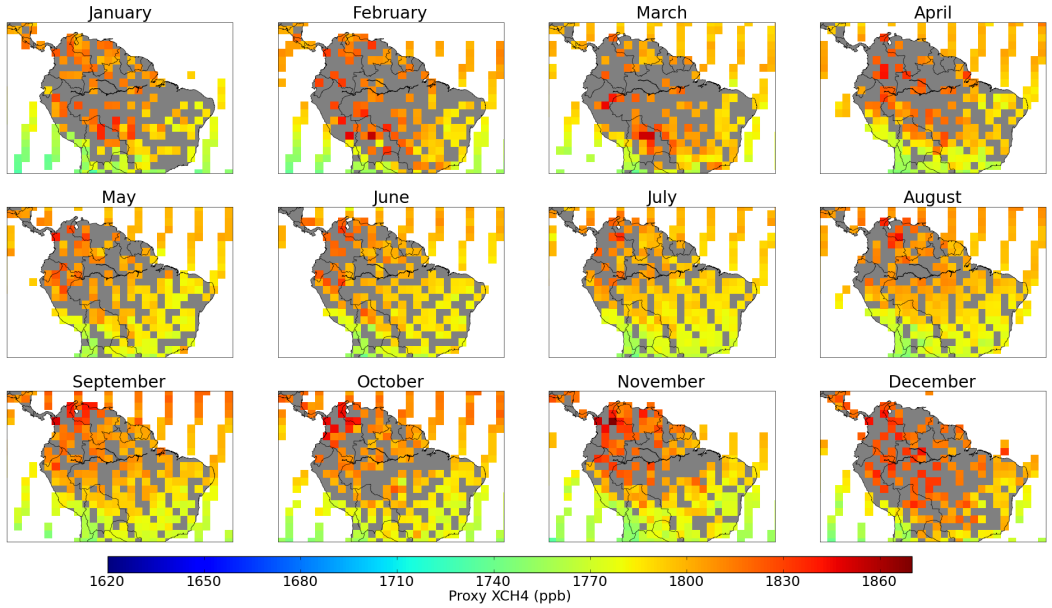


**Figure 5.10:** Monthly averaged GOSAT $XCH_4$ for 2013. The data is plotted to a $2° \times 2°$ grid.

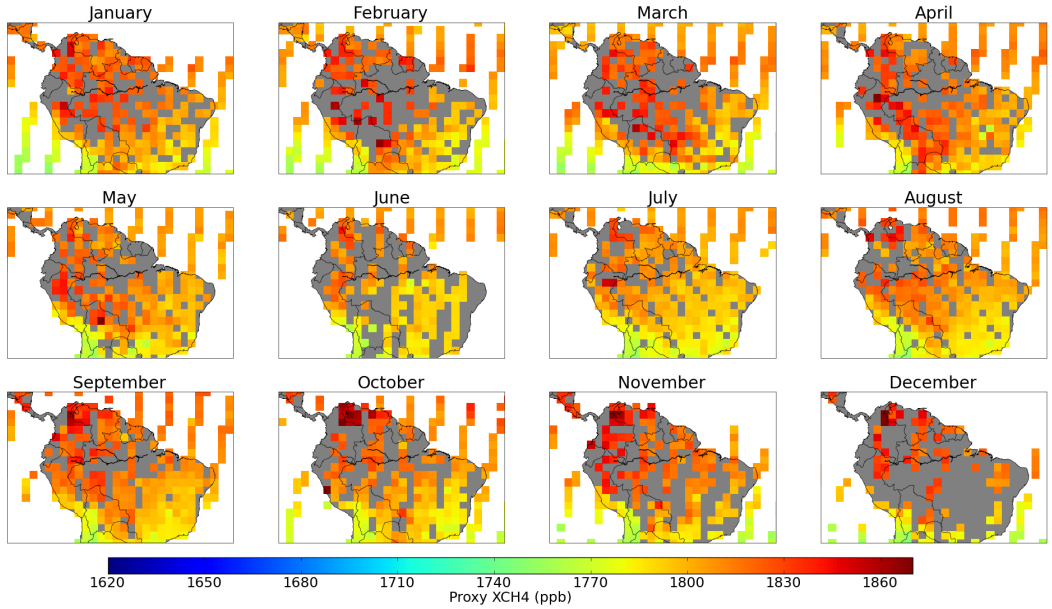


**Figure 5.11:** Monthly averaged GOSAT $XCH_4$ for 2014. The data is plotted to a $2° \times 2°$ grid.

across the Amazon Basin further south (by typically up to 45 ppb, and in 2011 by as much as 60 ppb). These wet season enhancements are highest in the western Amazon, with the largest differences in or around Bolivia. Hess et al. (2015) studied the extent and location of wetland area in lowland Amazonia and show that there are extensive wetlands in Bolivia which are consistent with where we find the largest differences between the wet and dry season with GOSAT. Figure 2.2 (in Chapter 2) is from Hess et al. (2015), showing the extent of wetlands in the Amazon during high and low water months in 1996. The largest difference observed is for 2011, which agrees well with observations that this was an anomalously wet year (Gatti et al., 2014). $XCH_4$ over the Atlantic Ocean shows little difference between the wet and dry seasons compared to those over land. This indicates that the enhanced concentrations in the Amazon for the wet season are a result of local emissions and not from $XCH_4$ transported across the Atlantic.

To quantify these $XCH_4$ differences and to better understand where they occur, the Amazon is now divided into five subregions for study. Figure 5.13 shows GOSAT $XCH_4$ averaged for the dry season of 2009 (the other dry seasons and all wet seasons are shown in Figure 5.12). From this figure it is apparent that the highest values in this dry season, as discussed previously for subsequent years, are in the north west of the Amazon in the two regions which have been marked as region 1 (most northerly) and region 2 (middle row, west). Region 5 (south east) contains the lowest concentrations, whilst regions 3 (middle row, east) and 4 (south west) are in-between. Figure 5.14 shows a time series of the average monthly $XCH_4$ of all GOSAT data within each of the five regions. Regions 1, 2, 3, 4 and 5 are shown in red, green, magenta, blue and cyan respectively. In the wet seasons (January-April), enhanced values are seen in the Amazon regions compared to the rest of the year. These enhancements are highest in regions 4 (blue) and 2 (green) which are both in the western Amazon, but the difference between the wet and dry seasons are more pronounced in region 4 which contains the Bolivian wetlands.

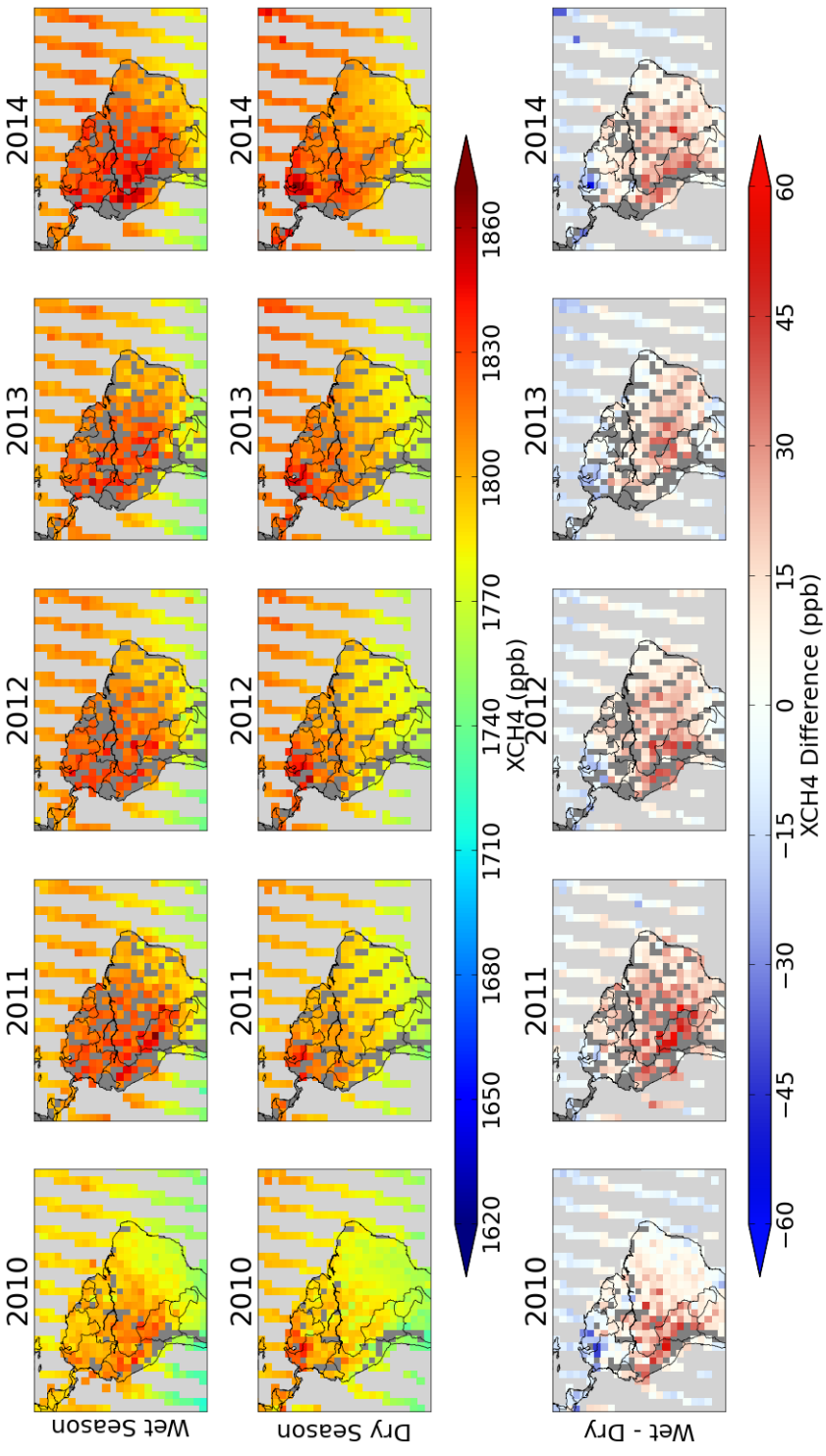


Figure 5.12: GOSAT $XCH_4$ averaged for the wet seasons (January-April) and dry seasons (July-October) in 2010 to 2014. The third row shows the difference (wet season minus dry season) for the seasons in each year. The data is plotted to a $2^\circ \times 2^\circ$ grid.

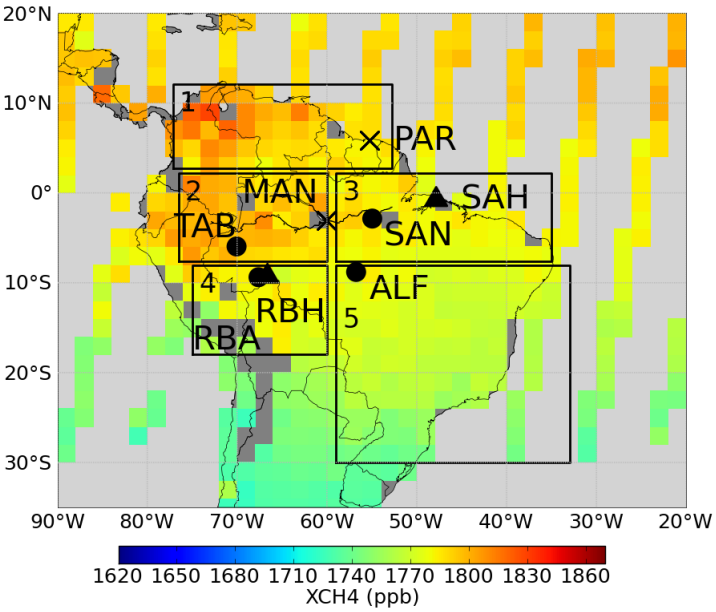


**Figure 5.13:** GOSAT $XCH_4$ averaged for the 2009 dry season (July–October). The locations of the aircraft and Paramaribo-FTS sites are shown, in addition to the Manaus TCCON site, MAN. The five regions referred to in the text are also shown. The data is plotted to a $2^\circ \times 2^\circ$ grid.

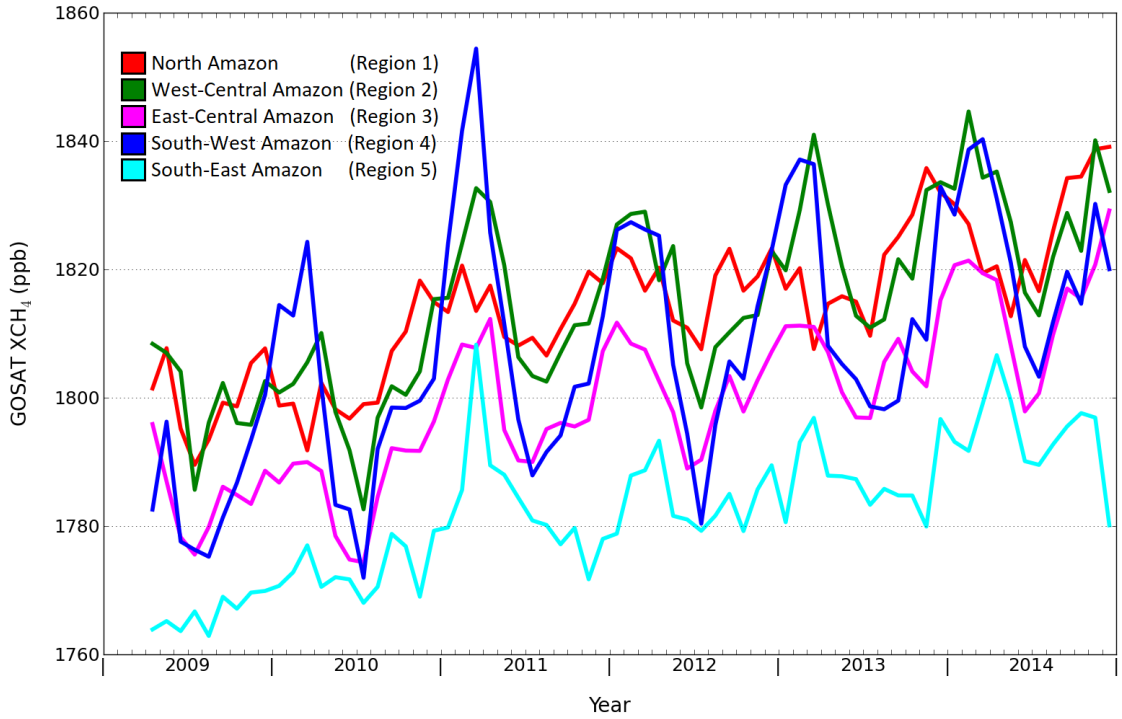


**Figure 5.14:** Time series of monthly averaged GOSAT $XCH_4$ (in ppb) calculated from all cloud-free soundings coincident within the five sub-regions in the Amazon, as specified by Figure 5.13. Region 1 (the North Amazon) is given by the red line, region 2 (West-Central Amazon) by the green line, region 3 (East-Central Amazon) by the magenta line, region 4 (South-West Amazon) by the blue line, and region 5 (South-East Amazon) by the cyan line.

## 5.5 COMPARISONS BETWEEN GOSAT AND GEOS-CHEM IN THE AMAZON

Since GEOS-Chem values are lower than the aircraft measurements in the northern AMAZONICA sites than they are in the southern sites, a tagged tracer run of GEOS-Chem is introduced to see if transport from the Northern Hemisphere could be causing these differences in the model. The location of the ITCZ (Intertropical Convergence Zone) varies with season in the Amazon and depending on its location the Amazon becomes more or less influenced by the Northern Hemisphere which generally has higher $XCH_4$ values than the Southern Hemisphere. Between August and September (in the dry season) the ITCZ is north of the equator at about 14°N; whilst between March and April (in the wet season) it is slightly south of the equator at about 2°S (Basso et al., 2016). The aircraft sites are all further south than 2°S except for Salinópolis at 0.75°S which therefore could see some influence from the Northern Hemisphere during a few months of the wet season. Santarém (2.86°S) and Tabatinga (5.96°S) are close enough that the $\pm 5°$ co-location area extends above 2°S, whilst it is unlikely that the two more southern sites are affected by the movement of the ITCZ at any times of the year.

The tagged tracer model run was conducted by the University of Edinburgh using the same model set-up used to produce the $XCH_4$ output which is utilised throughout the rest of this study, making the output directly comparable to my other results. The run tracks the origins of $CH_4$ emissions from 11 regions defined by The Atmospheric Tracer Transport Model Intercomparison Project (TRANSCOM). The first day of each month in 2010 is considered and the $XCH_4$ contribution is calculated from the past one month period from every global subregion specified by the model. The model is sampled at every grid box within the five regions defined in Figure 5.13, and all of the values within these areas are averaged. Figure 5.15 shows the relative contributions of the TRANSCOM regions for emissions during April 2010 as affecting the average $XCH_4$ concentration on May 1st 2010 for each of the five bounded areas in South

America. The northern-most area is entirely above the equator and show that Tropical South America and Northern Africa both have the largest impact on the $XCH_4$ for this month. The area below this (upper-middle panel of the figure) also shows the largest contributions from Tropical South America and Northern Africa, but with more of the emissions originating from South America than Africa and considerably fewer from North America. The third area (upper-right panel) shows more emission from Northern Africa than from South America, perhaps unsurprisingly as this region is on the east coast and would be the most influenced by incoming background air off of the Atlantic. For the two more southerly areas (lower panels) contributions from South America are the most dominant, but still with significant contributions from Northern Africa.

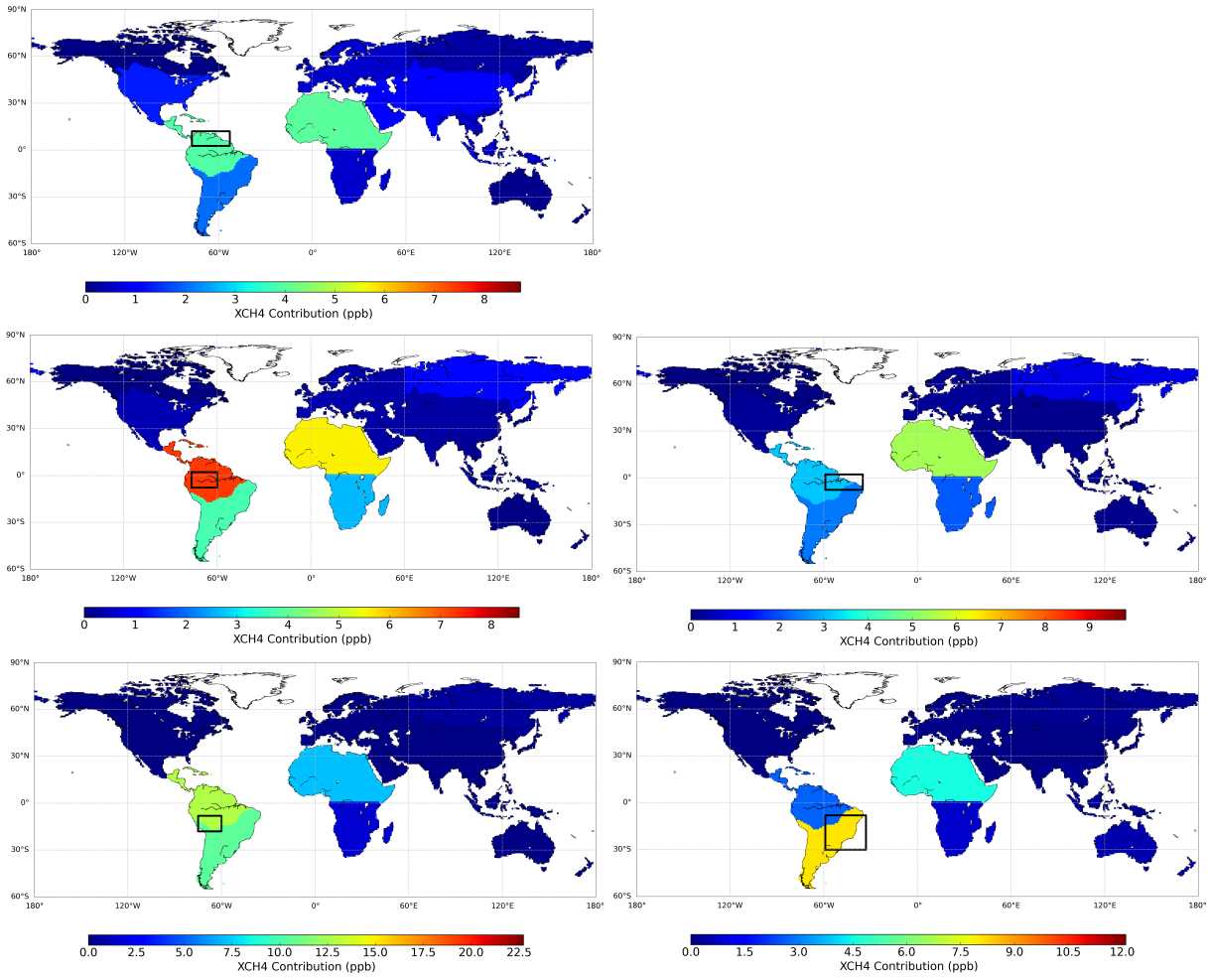


**Figure 5.15:** Maps showing the $XCH_4$ contributions from April 2010 to five different regions on May 1st 2010. The contributions are given for 11 TRANSCOM regions used in the tagged tracer run, which are coloured according to their contribution. The five geographical regions considered are bordered by black rectangles.

Figure 5.16 shows stacked time series of the contributions to each of the five regions from the different TRANSCOM regions. The contributions from the 'rest of the world', which are all parts of the Northern Hemisphere besides Northern Africa, are highest in the northern-most Amazon region and lowest in the two southern-most regions throughout the year. The northern-most region and the eastern-most 'coastal' region show the least influences from South America, whilst region 4 (over the wetlands in Northern Bolivia) is the most strongly influenced by South American $CH_4$ emissions. Region 4 also shows the largest seasonal cycle from South American influences. The contribution of $XCH_4$ from North Africa is very prominent in all of the regions and shows that all of South America is greatly influenced by wetland emissions in Africa according to the GEOS-Chem tagged tracer run.

The tagged tracer analysis suggests that North African $CH_4$ emissions are very important to concentrations of $XCH_4$ observed in the Amazon. GEOS-Chem concentrations over the Amazon are also found to be significantly lower than that measured by the aircraft profiles, whilst GOSAT $XCH_4$ does not share the same bias. To determine whether these differences arise due to the treatment of emissions outside of the Amazon, GOSAT and GEOS-Chem are compared in Figure 5.17. Here, the dry and wet seasonal averages for 2009 and 2010 respectively (which are the first of each to be measured by GOSAT after launch) are plotted. The upper row shows GOSAT $XCH_4$ and, on the right, the difference between these two seasons. The middle row shows the same for GEOS-Chem, sampled at the same GOSAT sounding locations and times, and the lower row shows the differences between GOSAT and GEOS-Chem (GOSAT minus GEOS-Chem) for the two seasons, and a difference plot of the differences. It is immediately apparent that throughout the entire Amazon there is a systematic offset between the two which can be seen over both the continent and over the Atlantic Ocean, as illustrated by the difference plots between GOSAT and GEOS-Chem which are almost entirely at the positive (red) end of the colour scale. Despite this bias however, the dry minus wet season plots show a very similar behaviour for GOSAT and GEOS-Chem. They both indicate that the wet season values are high in the western Amazon and in Bolivia where there are known to be vast wetlands. GOSAT

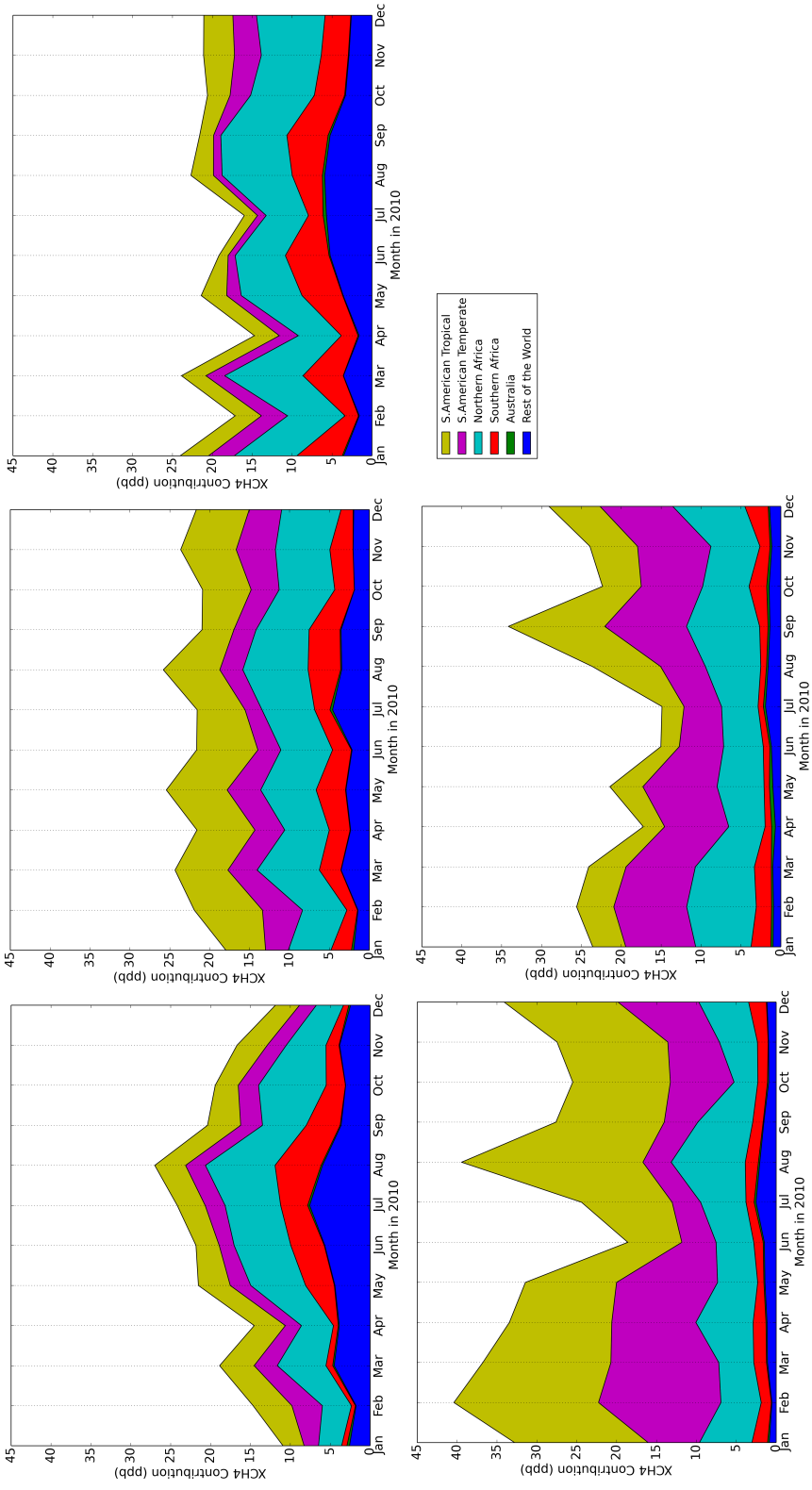


Figure 5.16: Stacked time series showing the contribution of $XCH_4$ from each month in 2010 to the first day of the next month from five of the TRANSCOM regions (Tropical South America in gold, Temperate South America in magenta, Northern Africa in cyan, Southern Africa in red, Australia in green), and the sum of the others (in blue). The five regions (labelled 1-5 in Figure 5.13 are displayed with 1-3 on the top row and 4 and 5 on the second row (both left to right).

has a 10.5 km footprint at the surface and GEOS-Chem has a resolution of 4° × 5°, so all GOSAT soundings in mountainous regions (where the surface altitude is higher than 3 km) have been removed to avoid large discrepancies between GEOS-Chem and GOSAT total column measurements. Figure 5.18 shows the altitude of GOSAT soundings as a monthly average for 2010 as a representation of where these soundings are removed.

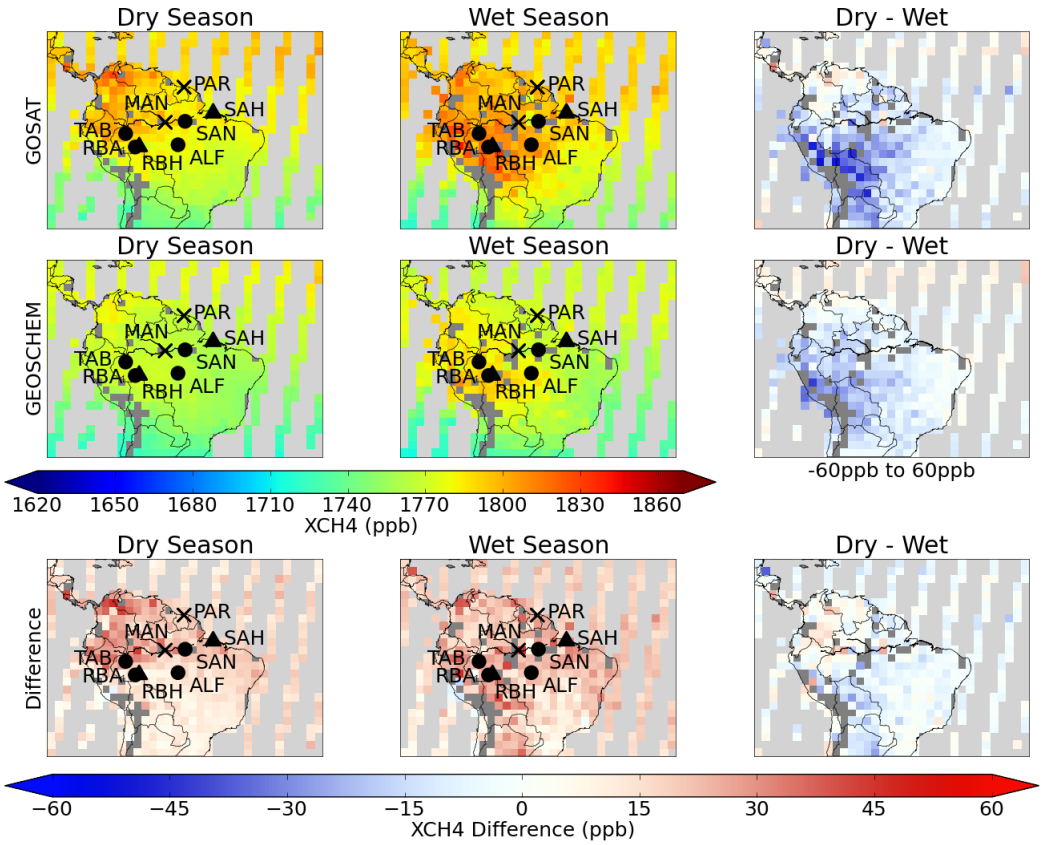


**Figure 5.17:** GOSAT and GEOS-Chem $XCH_4$ distributions for the 2009 dry season (July–October) and 2010 wet season (January–April) with difference plots. Dry minus wet season difference plots are in column three on rows one and two, and are represented by the lowermost colour bar. The bottom row is the GOSAT minus GEOS-Chem $XCH_4$ field, and in column three is the difference between these two difference plots. All plotted to a 2° × 2° grid.

Since I am interested in only South America I have calculated a correction to apply to the GEOS-Chem data to remove the biases from outside of the Amazon, allowing the differences between GOSAT and the model to be examined in the Amazon. This is justified by the Northern Hemisphere $XCH_4$ concentrations in GEOS-Chem over the Atlantic Ocean which we see are far lower than those from GOSAT, indicating that the bias is indeed an issue arising from outside of

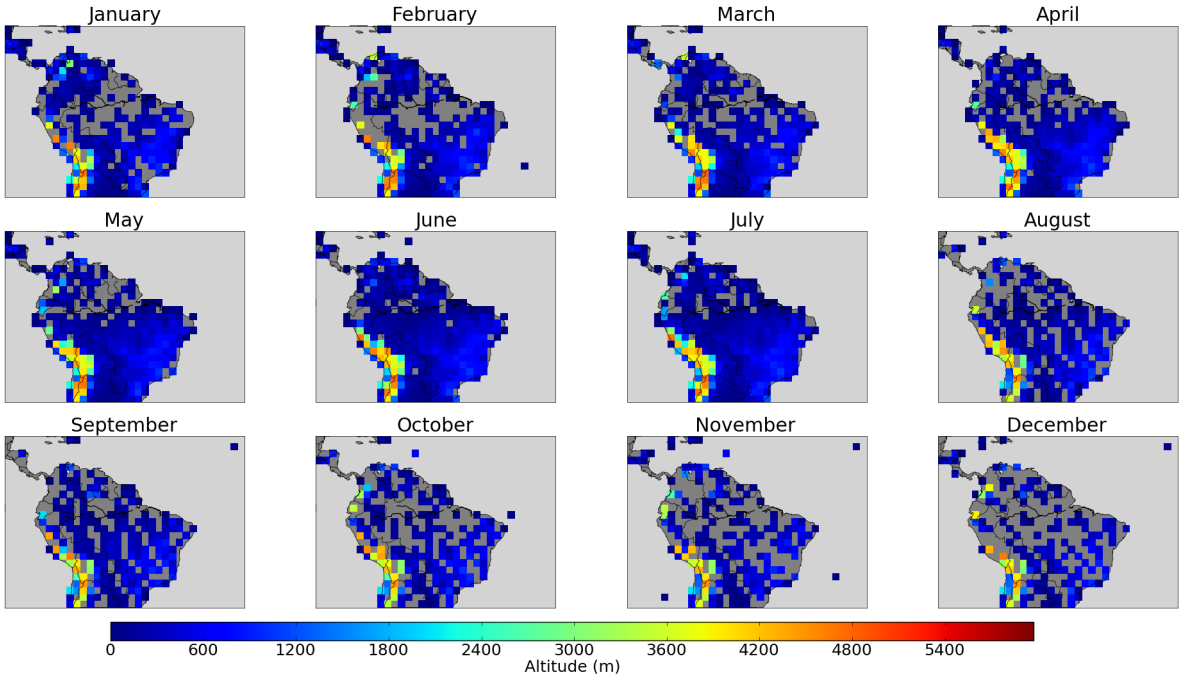


**Figure 5.18:** Surface altitude at GOSAT sounding locations shown as monthly averages for 2010 and plotted on a $2^\circ \times 2^\circ$ grid.

the Amazon itself. Ideally this offset would be calculated using the difference between GEOS-Chem and GOSAT over the Atlantic Ocean, but due to the sparse and seasonal nature of GOSAT ocean observations it was not possible to make this calculation for all months of the year. Instead the offset is calculated by removing the mean difference over the entirety of South America above 30°S (the region plotted in Figure 5.17). This method removes the large scale difference between the two datasets whilst retaining the regional differences which are of interest. Figure 5.19 shows how this corrective value varies monthly and compares it to one which only uses Atlantic Ocean values for the months where they are available. This shows that both corrections are comparable to within the standard deviation of the data involved in the calculation and justifies the use of this correction to remove the background from GEOS-Chem which originates from outside of the Amazon and which is not of interest here.

The original GEOS-Chem $XCH_4$ was calculated as a monthly average for each of the five regions in the Amazon specified in 5.13 (an average of GEOS-Chem sampled at GOSAT sounding locations). This is shown in Figure 5.20 and can be compared to Figure 5.21 showing the same data with the background correction applied. These show that the offset does not significantly alter the patterns

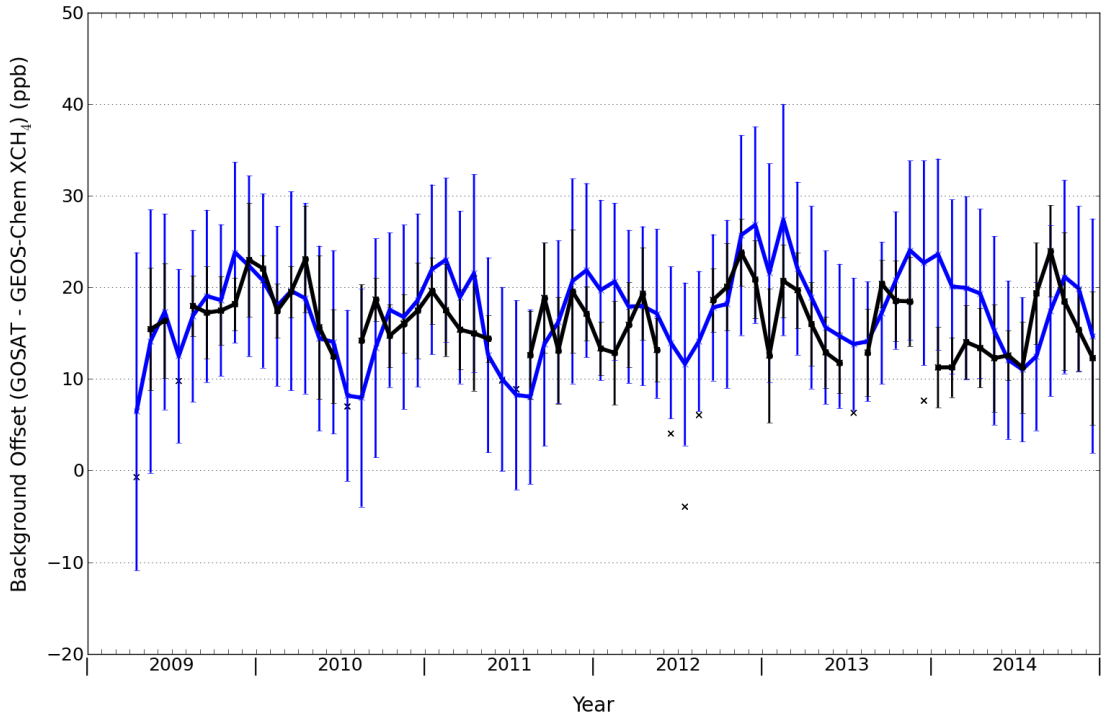


**Figure 5.19:** Showing the monthly varying correction between GOSAT and GEOS-Chem for the case where all of the GOSAT values between 20°N, 30°S, 90°W and 20°W are used in blue, and in black where just values over the Atlantic Ocean between ±4° of the equator are used. The black crosses represent measurements in the Atlantic Ocean correction where there are less than 10 grid boxes that contain GOSAT data (72 total). The uncertainties shown represent the standard deviation of the data.

and seasonality observed by GEOS-Chem. We can further compare these GEOS-Chem time series with the corresponding GOSAT time series shown previously in Figure 5.14, and I plot the difference between GOSAT and the corrected GEOS-Chem in Figure 5.22. From this comparison, the difference between GOSAT and GEOS-Chem is seen to remain uniform over the six years studied, with no divergence of the two datasets over time. The largest variations are seen in the South-West Amazon (region 4 in blue), where the highest concentrations in both of the individual time series are typically seen, suggesting that GOSAT and the model emissions do not agree on the magnitude and time scales of these emissions. There is a clear overall difference between the three northern-most regions (1, 2 and 3) and the two southern-most regions (4 and 5). For the northern regions GOSAT concentrations are generally larger than GEOS-Chem concentrations, whilst in the southern regions the opposite behaviour is typically observed with a similar magnitude for the difference.

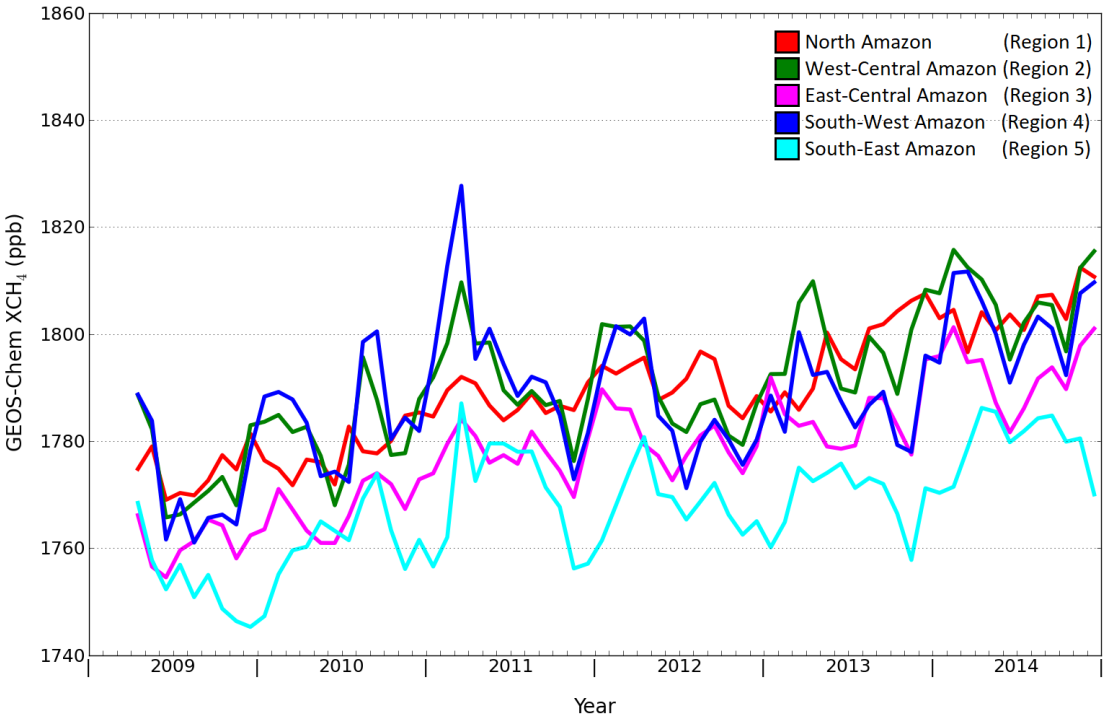


**Figure 5.20:** Time series of monthly averaged GEOS-Chem $XCH_4$ (in ppb) calculated by sampling at the locations of all cloud-free GOSAT soundings coincident within the five sub-regions in the Amazon, as specified by Figure 5.13. Region 1 (the North Amazon) is given by the red line, region 2 (West-Central Amazon) by the green line, region 3 (East-Central Amazon) by the magenta line, region 4 (South-West Amazon) by the blue line, and region 5 (South-East Amazon) by the cyan line.

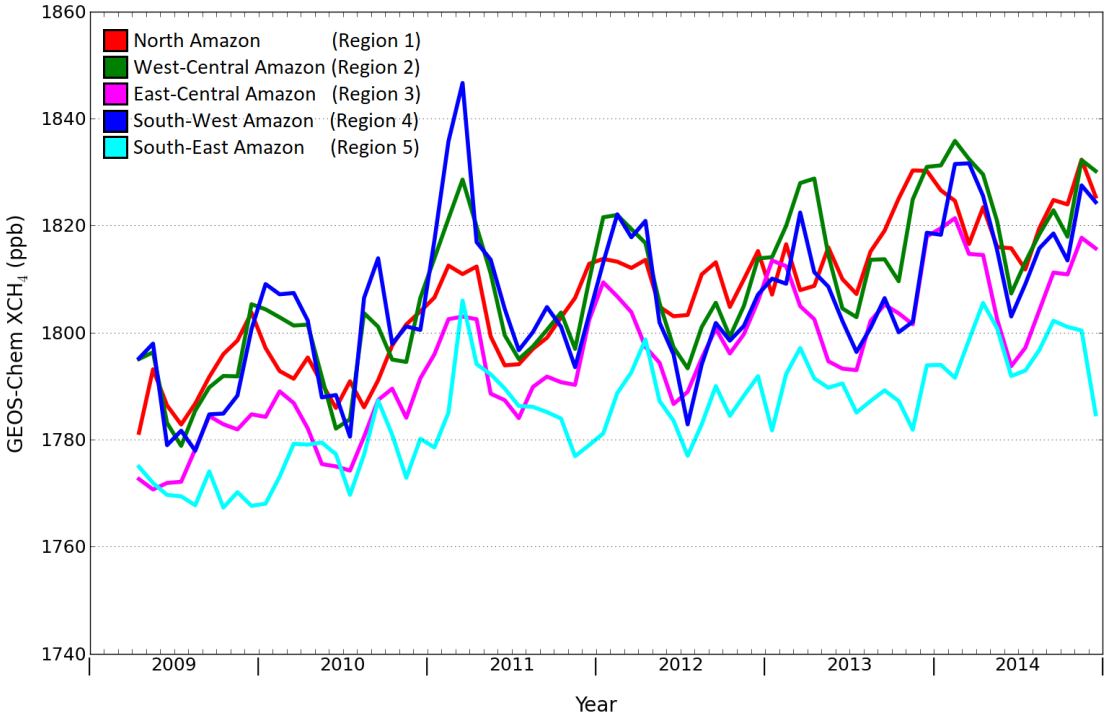


**Figure 5.21:** Time series of monthly averaged GEOS-Chem $XCH_4$ (with the background correction applied) calculated by sampling at the locations of all cloud-free GOSAT soundings coincident within the five sub-regions in the Amazon, as specified by Figure 5.13. Region 1 (the North Amazon) is given by the red line, region 2 (West-Central Amazon) by the green line, region 3 (East-Central Amazon) by the magenta line, region 4 (South-West Amazon) by the blue line, and region 5 (South-East Amazon) by the cyan line.

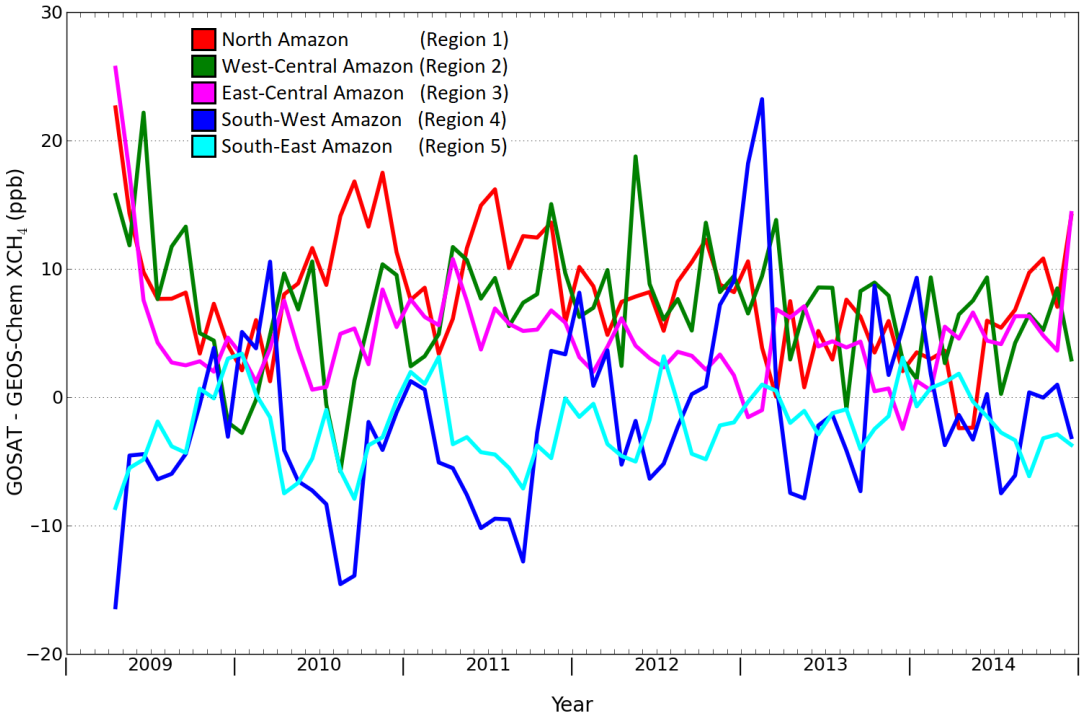


**Figure 5.22:** Time series showing the monthly averaged GOSAT $XCH_4$ minus GEOS-Chem $XCH_4$ (with the background correction applied) calculated from all cloud-free GOSAT soundings coincident within the five sub-regions in the Amazon, as specified by Figure 5.13, and using GEOS-Chem model values sampled at these locations. Region 1 (the North Amazon) is given by the red line, region 2 (West-Central Amazon) by the green line, region 3 (East-Central Amazon) by the magenta line, region 4 (South-West Amazon) by the blue line, and region 5 (South-East Amazon) by the cyan line.

Figure 5.23 shows seasonally averaged GOSAT and GEOS-Chem for the dry season in 2009 (July–October) and the wet season in 2010 (January–April) and is the same as Figure 5.17 except now with the background correction applied to the GEOS-Chem data. In these plots the difference between GOSAT and GEOS-Chem over the Atlantic Ocean is considerably more uniform and closer to zero than before the background offset was applied, providing confidence that the observed differences over the continent are a result of processes in the Amazon. Both GOSAT and GEOS-Chem show a very similar seasonal difference as shown in the difference plots in the third column; very similar to what was seen before the background correction was applied, with the largest differences between the wet and dry seasons found in the south-west Amazon. This region also shows significant emissions in the Bloom 2010 wetland emission inventory which is utilised by GEOS-Chem, as shown in Figure 5.24. GOSAT and GEOS-Chem do differ notably in the dry season, as shown by the bottom row, with GOSAT values higher than GEOS-Chem in the north and lower in the south. The wet season in 2010 shows a mixture of values which are more difficult to diagnose from this one season alone, so now all of the different wet and dry seasons are examined.

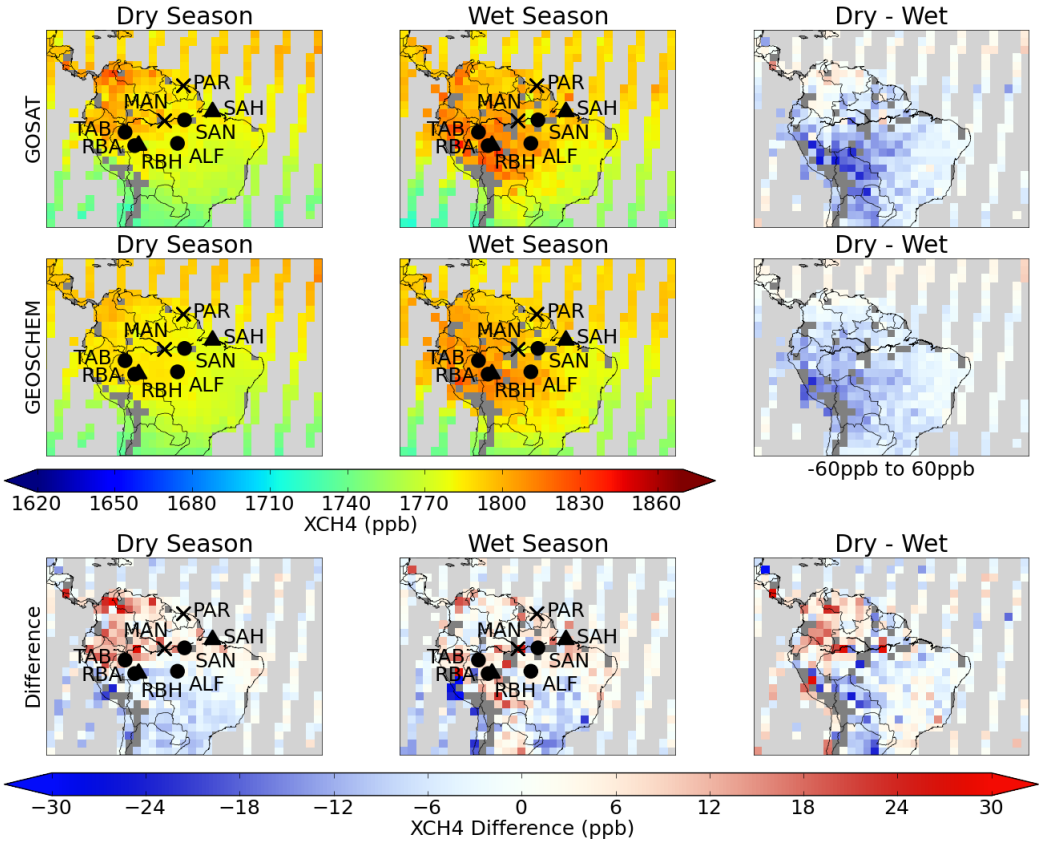


**Figure 5.23:** GOSAT and GEOS-Chem $XCH_4$ distributions for the 2009 dry season (July–October) and 2010 wet season (January–April) with difference plots. Dry minus wet season difference plots are in column three on rows one and two, and are represented by the lowermost colour bar, except with twice the range. The bottom row is the GOSAT minus GEOS-Chem $XCH_4$ field, and in column three is the difference between these two difference plots. The locations of the aircraft and Paramaribo-FTS sites are shown, in addition to the Manaus TCCON site, MAN. All plotted to a $2^\circ \times 2^\circ$ grid.

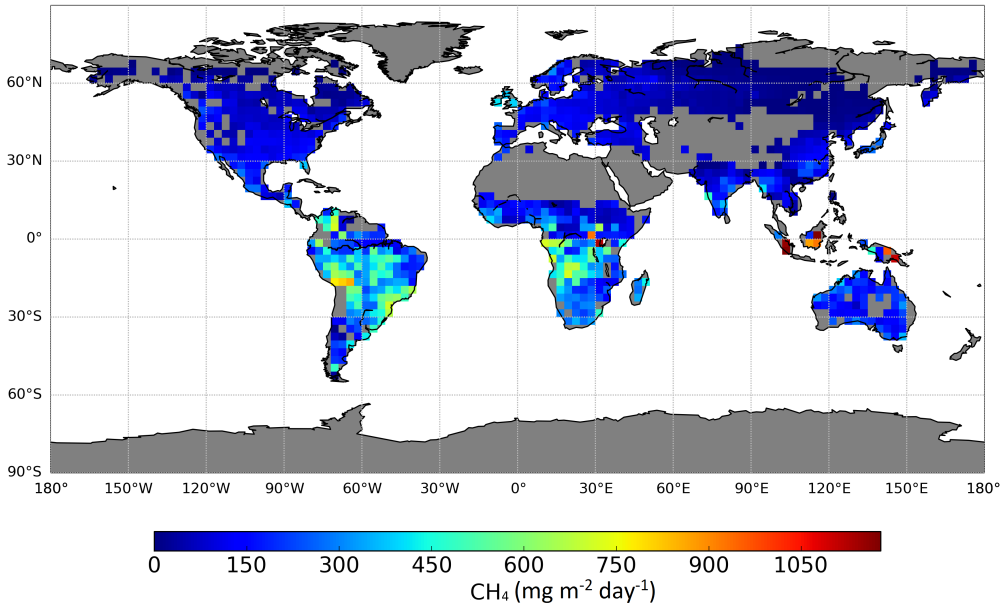


**Figure 5.24:** The Bloom wetland $CH_4$ emissions used in the GEOS-Chem model, for March 2010. Plotted to a $2^\circ \times 2^\circ$ grid.

Figures 5.25 and 5.26 show the dry and wet seasons respectively for GOSAT and GEOS-Chem for multiple years to analyse how they compare over the entire GOSAT time period. The dry seasons from 2009 to 2014 generally agree very well with each other; showing the same higher GOSAT values in the north and higher GEOS-Chem values in the south. These differences are originating in the Amazon as the same north-south gradient can not be seen in the values over the Atlantic Ocean. GEOS-Chem values are noticeably more pronounced than GOSAT in the south (and Bolivian wetland region) for 2010 and 2011. This is interesting because 2010 was an anomalously dry year in the Amazon (Gatti et al., 2014) and less rainfall would result in less wetland $CH_4$ emission. It is possible that this was not correctly attributed in the model, resulting in $XCH_4$ emissions being higher than those seen by GOSAT in 2010, which could have had a knock-on effect on the beginning of 2011. The wet season differences shown in Figure 5.26 typically indicate that GOSAT values are higher in central Amazon and in Northern Bolivia where high $CH_4$ emissions are expected. The heightened GOSAT concentrations in the north of the continent in the dry seasons are not a feature in the wet seasons, with GOSAT and GEOS-Chem typically in agreement. As with the dry seasons there are no features over the Atlantic Ocean which continue over the continent.

Figure 5.27 shows the difference between GEOS-Chem $XCH_4$ concentrations averaged for the wet seasons, and for the dry seasons in each year from 2010 to 2014. This figure is comparable to Figure 5.12 which showed the same comparison for GOSAT data. The difference in $XCH_4$ between the seasons are much smaller than are seen with GOSAT data. In 2010 the wet and dry seasons in GEOS-Chem are very similar, showing no significant geographical differences on this colour-scale in $XCH_4$ concentrations; compared to GOSAT (which is plotted on the same colour-scale) where wet season emissions are considerably higher in the Amazon Basin than they are in the dry season. Across all of the years the differences between the seasons for GOSAT are considerably more pronounced than they are in GEOS-Chem; with GEOS-Chem typically showing less than a 30 ppb difference between the seasons, even in region 4. Whilst GOSAT concentrations differ by 30-50 ppb in the same region.

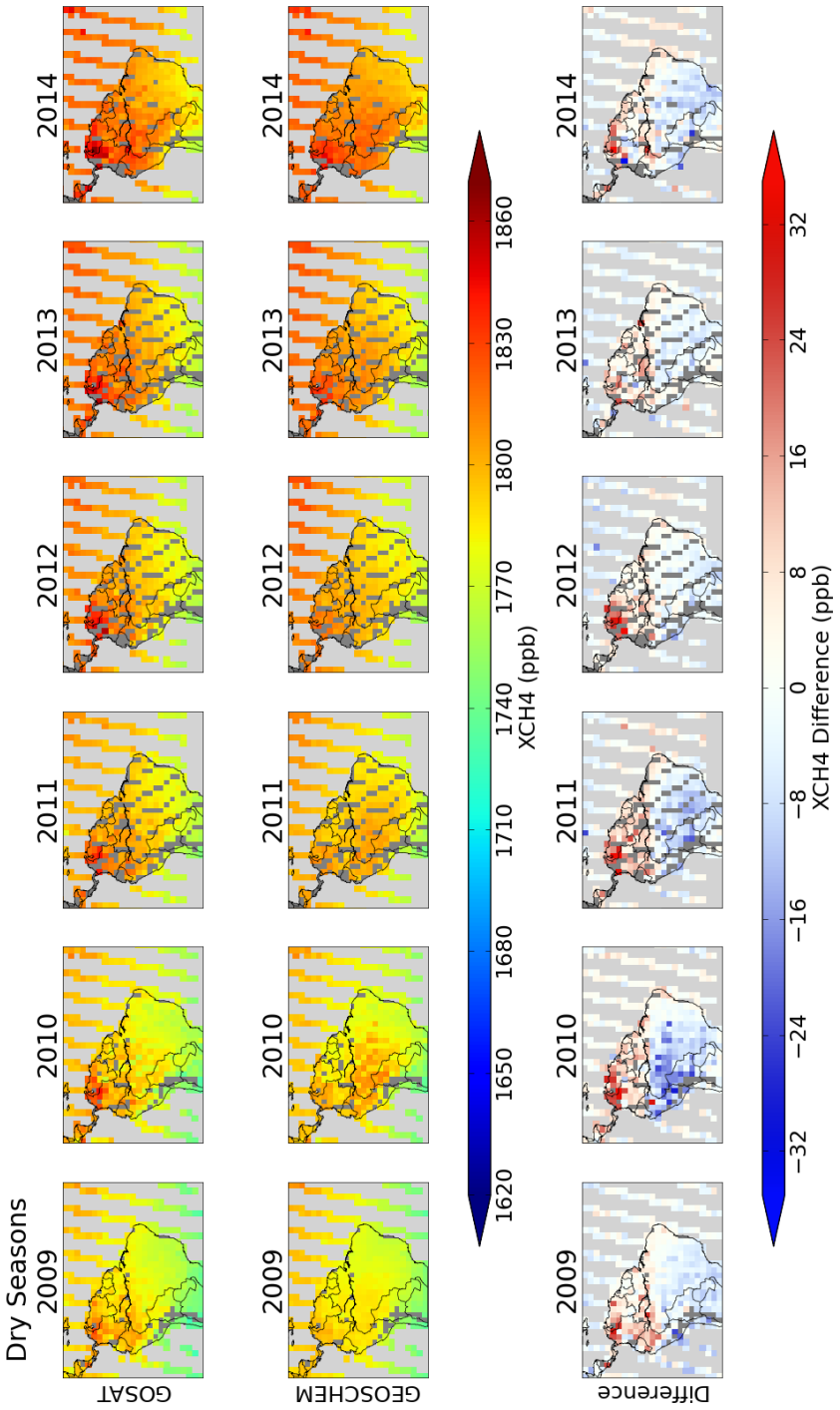


Figure 5.25: Showing GOSAT and GEOS-Chem $XCH_4$ distributions for multiple dry seasons (July–October) with difference plots.

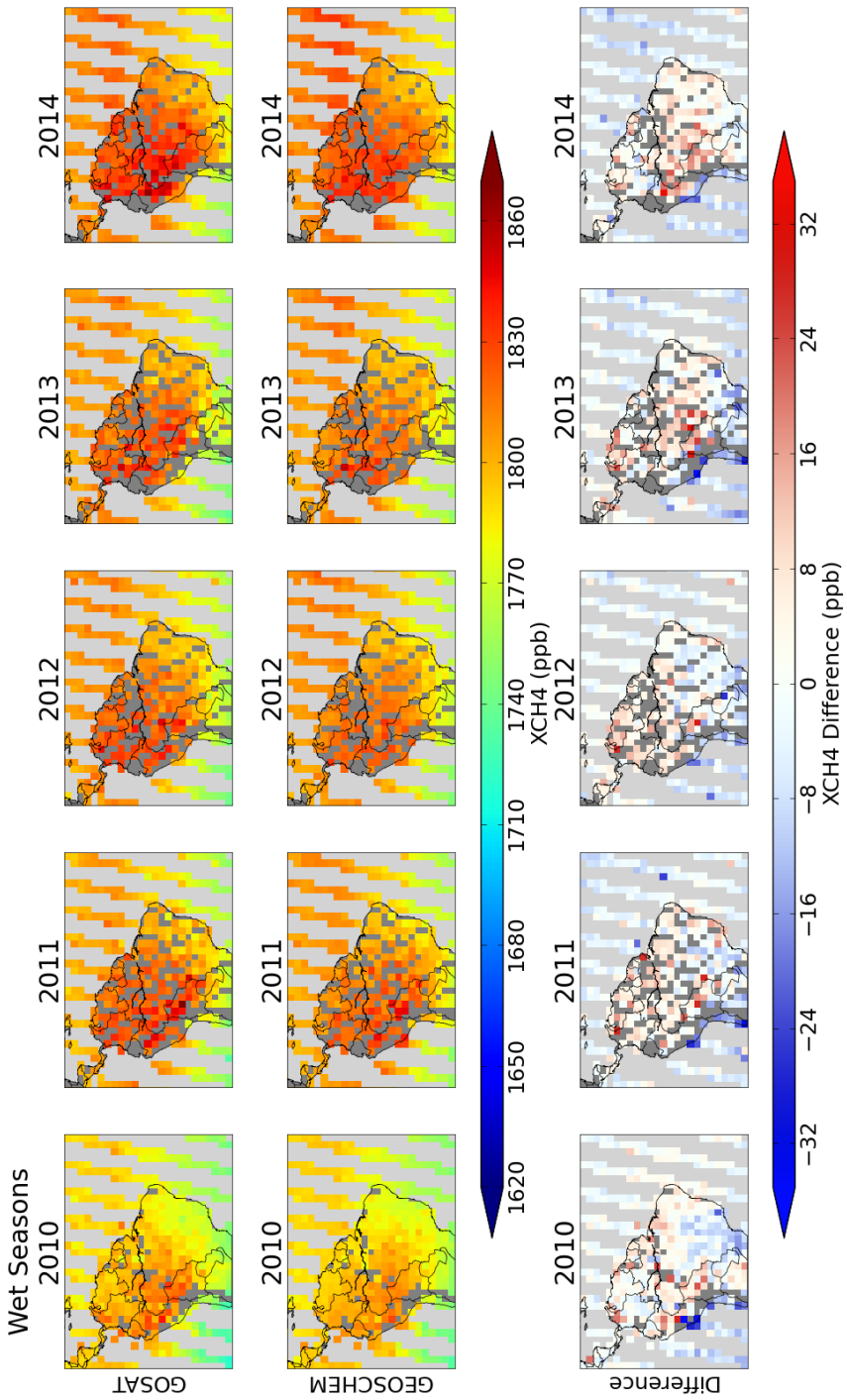


Figure 5.26: Showing GOSAT and GEOS-Chem $XCH_4$ distributions for multiple wet seasons (January–April) with difference plots.

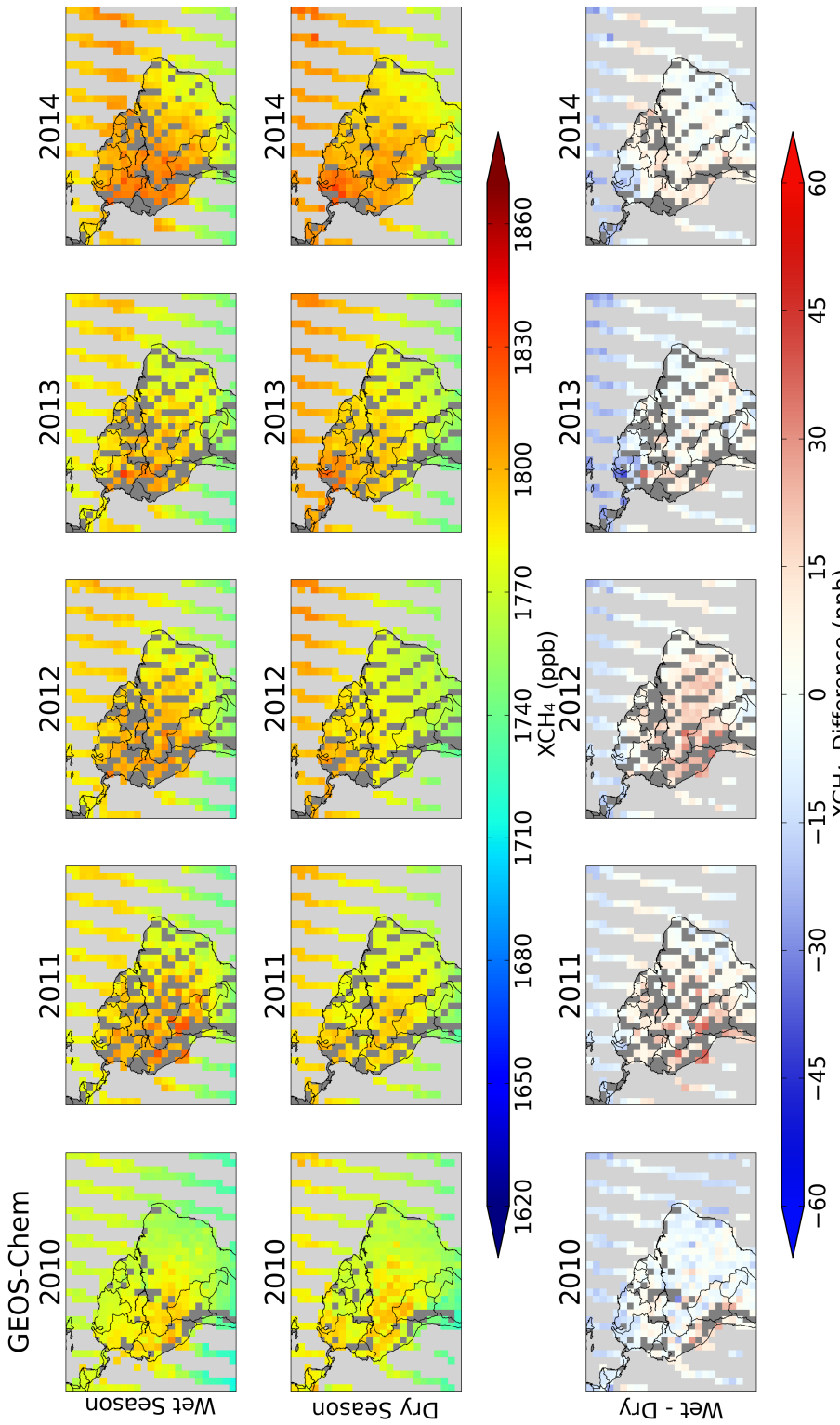


**Figure 5.27:** GEOS-Chem $XCH_4$ averaged for the wet seasons (January-April) and dry seasons (July-October) in 2010 to 2014. The third row shows the difference (wet season minus dry season) for the seasons in each year. The data is plotted to a $2° \times 2°$ grid.

To further analyse how these patterns vary between the years, Figures 5.28 and 5.29 show the yearly differences between consecutive years for the dry and wet seasons, on a $4^\circ \times 4^\circ$ resolution. As expected the dry seasons shown in Figure 5.28 exhibit the largest differences between 2009–2010, 2010–2011 and 2011–2012 as the years 2010 and 2011 were most notably different from the others in Figure 5.25. Interestingly the largest yearly increase in $XCH_4$ by GEOS-Chem was between 2009 and 2010, with 2010 shown to be considerably higher than 2009 (by up to 30 ppb, compared to GOSAT where 2010 concentrations were approximately 10 ppb higher than 2009 for the same region). The wet seasons shown in Figure 5.29 show a large difference between 2010 and 2011 which is very similar in GOSAT and GEOS-Chem data. This shows that there was much more $XCH_4$ throughout the entire Amazon in 2011 than in 2010, and the 2011–2012 plot shows a difference in the opposite direction; that there was much more $XCH_4$ in 2011 than in 2012. This is consistent with observations that 2011 was a far wetter year than those around it (Gatti et al., 2014).

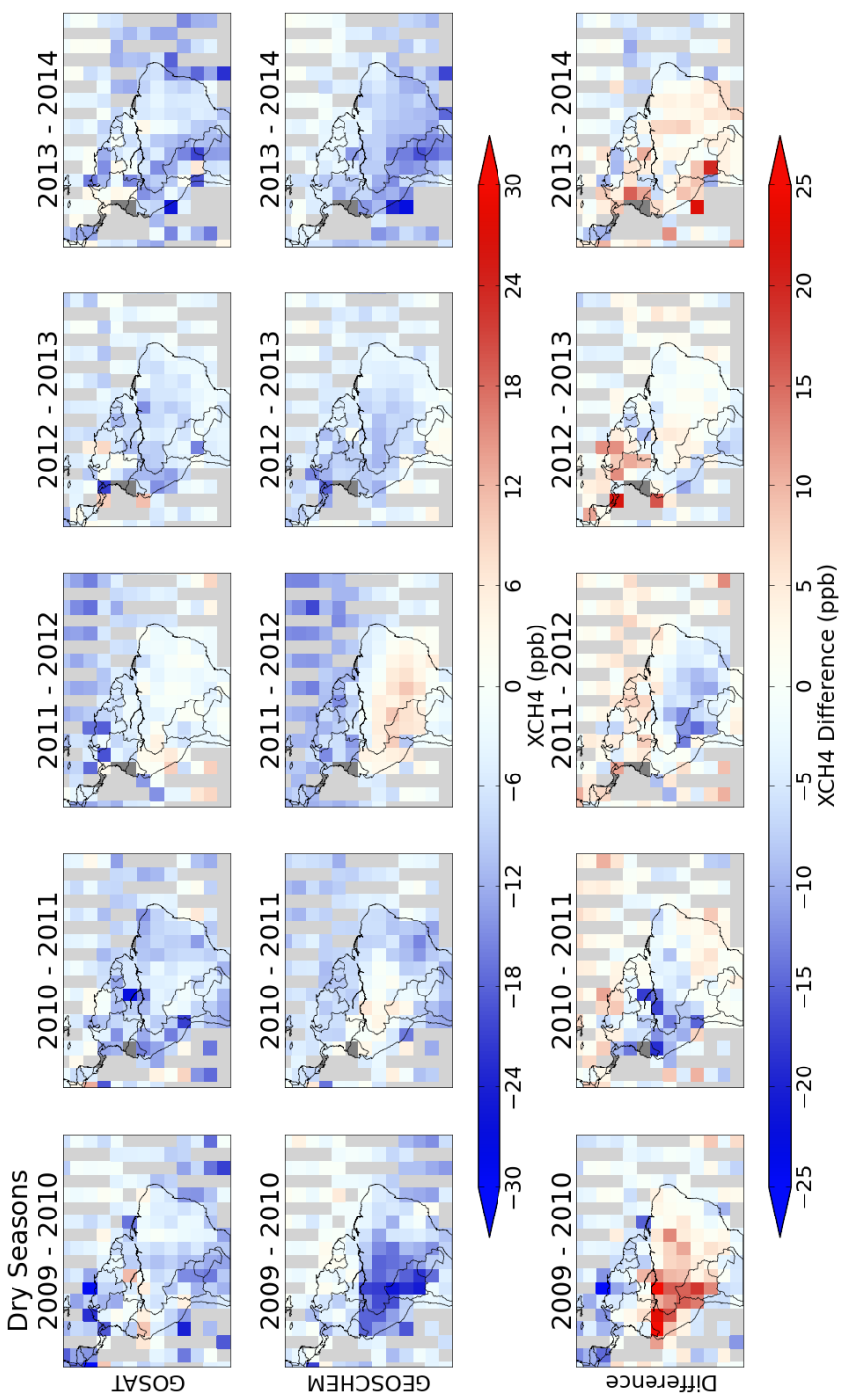


Figure 5.28: Showing the difference between GOSAT and GEOS-Chem $XCH_4$ distributions for consecutive dry seasons (July–October).

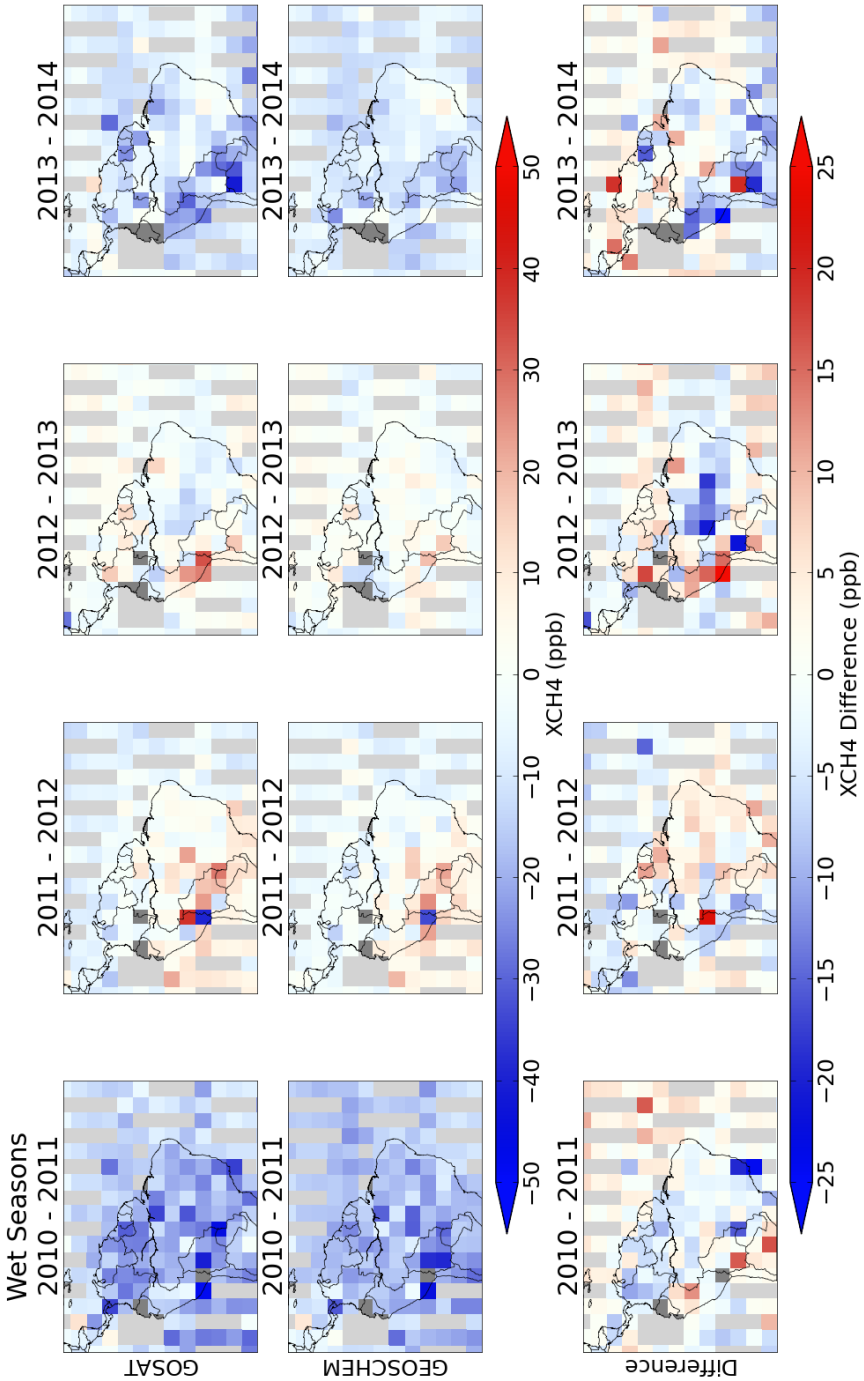


Figure 5.29: Showing the difference between GOSAT and GEOS-Chem $XCH_4$ distributions for consecutive wet seasons (January–April).

## 5.6 CONCLUSIONS

In this chapter I set out to investigate the behaviour of $XCH_4$ emissions in the Amazon as Observed by both GOSAT and a state of the art 3-D chemistry transport model (GEOS-Chem). Observations from GOSAT show that $XCH_4$ concentrations in the northern-most parts of South America (particularly around the border of Colombia and Venezuela) are higher in the dry season by up to 30 ppb than they are in the wet season. However, in the wet season, GOSAT concentrations are generally higher throughout the rest of the Amazon Basin by typically 45 ppb (and as much as 60 ppb). GOSAT observes the largest differences in the wet season in or around Bolivia, a region known to contain the extensive Pantanal wetlands.

Comparisons between GEOS-Chem $XCH_4$ and the in situ aircraft data find that GEOS-Chem concentrations are considerably lower with offsets which range from -26.0$\pm$0.6 ppb at Santarém to -7.3$\pm$0.8 ppb at Alta Floresta. Analysis with a tagged tracer run of GEOS-Chem suggests that this large offset could be partly due to transport from Northern Africa which is found to have a big impact on GEOS-Chem concentrations in the Amazon.

The second aim of this chapter was to compare GOSAT and GEOS-Chem $XCH_4$ concentrations in the Amazon to observe how well modern $CH_4$ emissions inventories represent observed patterns of $XCH_4$ from GOSAT in the Amazon. A correction based on the difference between the GOSAT and GEOS-Chem background was calculated and applied to the GEOS-Chem data to remove the large-scale offset caused by emissions from outside of the Amazon. GOSAT shows elevated $CH_4$ concentrations in the north-west corner of South America compared to the model simulations in the dry seasons. The seasonality between the wet and dry seasons looks similar between GOSAT and GEOS-Chem geographically, although the magnitudes are not similar. There are some large differences of more than $\pm$15 ppb, especially in regions containing the Bolivian wetlands where the largest $XCH_4$ concentrations from both GEOS-Chem and GOSAT are seen. For every year from 2010 to 2014 the seasonality seen by GOSAT is larger

(in magnitude) than that modelled by GEOS-Chem. Due to its low resolution it is possible that GEOS-Chem may be missing transport, so this will be assessed in Chapter 6. Since GOSAT $XCH_4$ is found to be in better agreement with the extrapolated in situ observations than GEOS-Chem is, this is encouraging evidence that GOSAT data can be utilised to improve the underlying emissions inventories used in the model. This should be particularly beneficial in regions with high $CH_4$ emissions which show the largest differences between GOSAT and GEOS-Chem, providing new insights into wetland emissions in the Amazon.

# 6 DEVELOPMENT OF A HIGH-RESOLUTION REGIONAL TRANSPORT MODEL FOR THE AMAZON TO EVALUATE $CH_4$ EMISSIONS INVENTORIES

## 6.1 INTRODUCTION

In Chapter 5 I compared $XCH_4$ from the GEOS-Chem model with GOSAT measurements in the Amazon. The model output and satellite measurements disagree on the magnitude of the seasonality of $CH_4$ between the wet and dry seasons; especially in regions which are known to contain extensive wetlands. These differences highlighted shortcomings in the model which are either a result of the model transport or of the underlying emissions inventories. The aim of this chapter is to develop a simulation system which is able to quickly and simply input any emission database and produce high resolution atmospheric $XCH_4$ data at a regional scale that can be assessed against satellite data. The transport in these simulations is calculated using high resolution back-trajectories, simulated by the Met Office's Numerical Atmospheric-dispersion Modelling Environment (NAME). This is demonstrated at the times and locations of every GOSAT $XCH_4$ sounding over the period of one year (in the Amazon), and using the most up to date versions of the emission inventories used for the GEOS-Chem model. The results for these simulations are compared with the GOSAT $XCH_4$ concentrations, as well as GEOS-Chem and MACC-II modelled $XCH_4$.

## 6.2 NUMERICAL ATMOSPHERIC-DISPERSION MODELLING ENVIRONMENT

NAME is an atmospheric dispersion model which was developed by the UK Met Office. It is a Lagrangian model which uses Monte Carlo random-walk techniques to represent the turbulent transport of pollutants in the atmosphere (Jones, 2015). The model is designed to simulate emissions into the atmosphere by creating a large quantity of model objects which are referred to as 'particles'. The particles are advected through a modelled atmosphere with the turbulent nature of their dispersion simulated by these random-walk methods. The model was originally developed as a response to the Chernobyl nuclear disaster in 1986, although has been used as a more general purpose atmospheric dispersion model for a variety of applications since then, including the tracking of volcanic ash and to simulate the outbreak of air-borne diseases (Manning et al., 2011; Devenish et al., 2012; Gloster et al., 2007). The model is capable of being run in both a forward and backward scheme. NAME has traditionally been utilised 'in-house' by the UK Met Office, although there is a growing community of external users using the model for new research purposes (Jones, 2015).

In this study I utilise the NAME model at individual GOSAT sounding locations and model the transport of air from these starting locations in a backwards model run to examine the origins of the air that was measured at these exact locations. The model is designed to be usable with the Met Office's meteorological data from their own Unified Model (MetUM), which is a world leading Numerical Weather Prediction (NWP) model (Jones et al., 2007). This data is available globally with a 3-hourly resolution and contains important parameters such as the wind direction and speed with are used by NAME to simulate the particle back-trajectories. For further details on NAME see Jones et al. (2007) and the NAME-III user guide (Jones, 2015).

## 6.3 NAME MODEL SIMULATION OVERVIEW AND SET-UP

To simulate $XCH_4$ comparable with GOSAT measurements with a NAME model simulation, NAME back-trajectories are simulated for each individual GOSAT sounding at multiple altitudes. Due to the large quantity of GOSAT soundings this study is limited to the year 2011 and to only GOSAT Proxy $XCH_4$ retrievals which are cloud-free and pass the quality filters described in Chapter 3. This subset consists of 23,772 GOSAT soundings, with an average of 1,981 per month, ranging from 1,192 in February 2011 at the height of the wet season, to 2,988 in September 2011 during the dry season. For each of these retrievals NAME is run on two separate horizontal grids over the Amazon, one with a resolution of 0.5° $\times$ 0.5° for the main model output, and one with a lower resolution of 6° longitude by 4° latitude which is used to calculate a background concentration. Both runs are conducted on a grid centred at -54° longitude, -10° latitude, with 144 grid boxes (longitude) and 96 grid boxes (latitude) for the high resolution grid, and 12 and 6 grid boxes in each direction respectively for the lower resolution run. These both cover the same geographical area as shown in Figure 6.1 by the boxed region (high resolution); whilst the lower resolution grid is represented in Figure 6.3. This region covers the entire Amazon and extends to above the northern-most land in South America (14°N to 34°S) as well as covering a considerable extent of the Atlantic Ocean as far as Africa (18°W), (the direction of the typically expected incoming air to the Amazon), and extends to the Pacific Ocean in the west (90°W).

The model is set-up to release 1 gram of tracer particles in a one second release at the exact location and time of the corresponding GOSAT measurement at 37 separate altitude levels. These consist of 9 levels between 10 m above the surface and 90 m increasing by 10 m each, then 15 levels 100 m apart up to 1.5 km. 7 levels then extend from 1.5 km to 5 km each separated by 500 m. A further 5 levels increase in 1 km increments up to 10 km and a final uppermost level exists at 15 km. The resolution decreases with altitude since less of the air sampled at higher

altitudes is expected to have interacted with the surface over the considered time scales. The particle locations are modelled every 3 hours (the resolution of the underlying NWP model outputs which NAME uses), and outputs are given as 24-hour integrals of these for up to 10 days before the start time. For the background calculation the total column value of particles between the surface and 15 km are output. The number of particles found within 100 m of the surface is also output and is used to calculate when and where these back-trajectories are interacting with the surface, and hence where they will be influenced by surface $CH_4$ emissions. Additionally, the model is set to output the pressure, temperature and humidity at each of the release altitudes at the time of the initial release; which are taken from the METum data and are used to later convert $CH_4$ profiles into column averages. Trajectories which leave the model grid horizontally are not modelled beyond this point and with this set-up the model cannot account for them re-entering the region; however, with the large area and 10-day maximum back-trajectory time it is unlikely that there would be many trajectories which would leave and re-enter the region and interact with the land surface within this 10-day time-frame. Particles which leave the vertical boundaries of the outputs are tracked and will be included if they subsequently re-enter this range.

Figure 6.1 shows the total column averaged output of tracer particles from a NAME run based on a real GOSAT sounding at 15:33 UTC on the 1st of January 2011. The figure shows how the particles are situated on each of the 10 days before the 1st. This particular GOSAT sounding was on the East-coast as marked by the red cross on the figure, and shows that the majority of the particles travelled from the East over the Atlantic. There are also particles which originated from within the Amazon Basin, however these are far less numerous by several orders of magnitude (the data are plotted on a logarithmic scale).

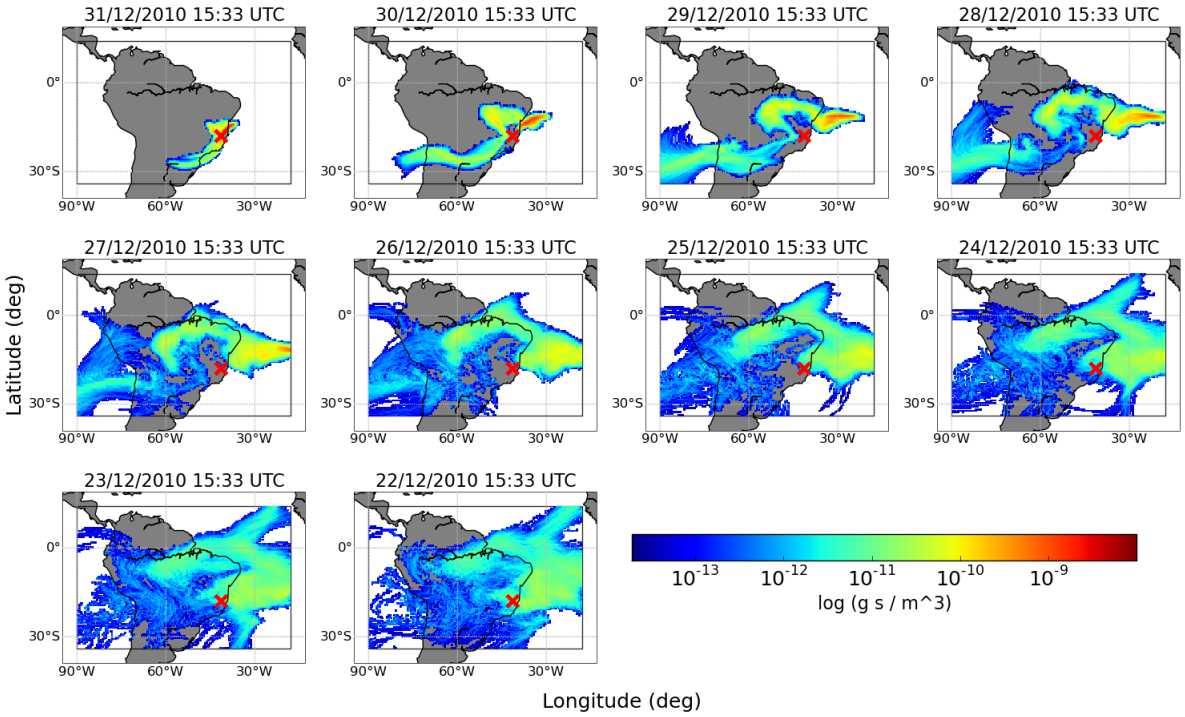


**Figure 6.1:** Maps showing the daily averaged location of released tracer particles for each day during a 10-day back-trajectory from the location of a GOSAT sounding (marked by the red cross) on January 1st 2011 at 15:33 UTC. The NAME model domain over which trajectories are tracked is shown by the black outlined rectangle which is approximately 5° smaller in all directions than the total area of map plotted. The data are plotted on a logarithmic scale with the unit as a dosage in g s $m^{-3}$ which can be difficult to consider by itself. Importantly the run represents the release of a finite number of particles during a one second period, so the relative dosage of particles at each location is best to consider.

### 6.3.1 Modelling wind directions

At this stage the NAME outputs are used to verify the choice of having aircraft sites at Rio Branco and Salinópolis, and to examine the background of incoming air. NAME runs were performed with the same horizontal grid set-up as for the GOSAT soundings for each day in 2011 at midday at the aircraft locations. The particle release was simulated at 7.5 km to represent the air at the top of the aircraft profiles. Figure 6.2 shows the average locations of the released particles for a 24-hour period 7 days before reaching the site. The daily NAME runs have further been averaged over the wet and dry seasons (January-April 2011 and July-October 2011 respectively). They are displayed on a normalised scale between the lowest and highest concentration.

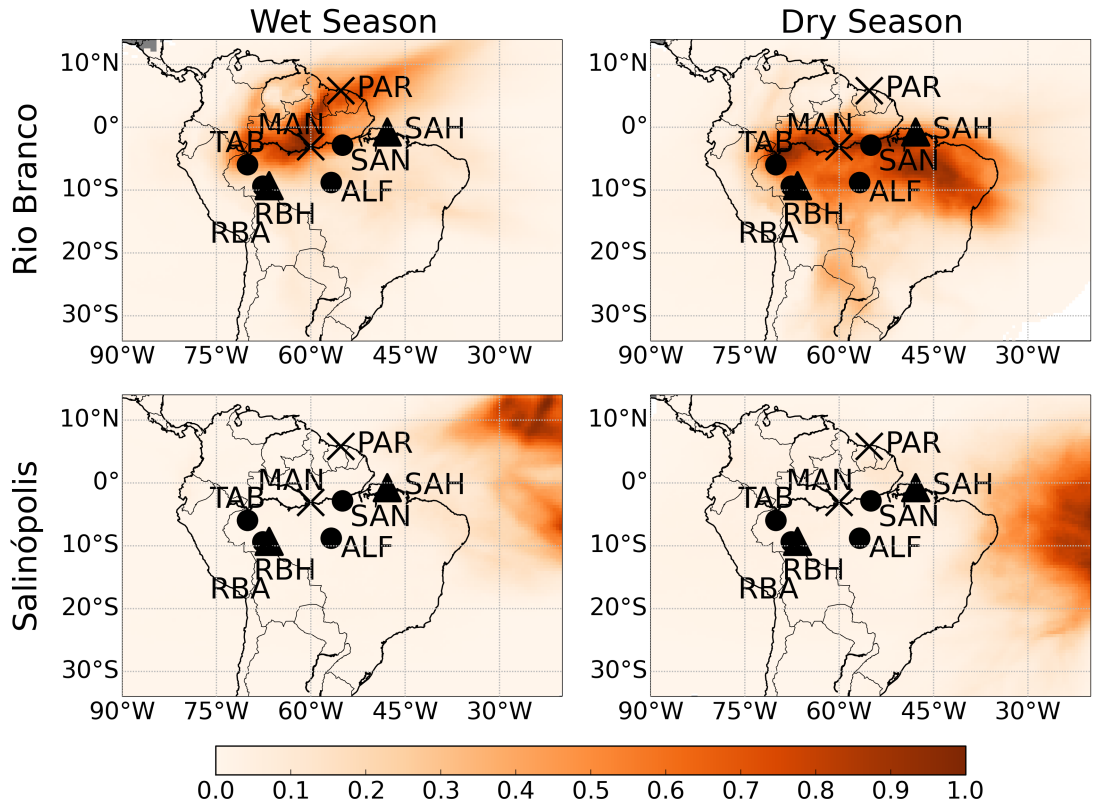


**Figure 6.2:** The mean location of incoming air sampled at Rio Branco (top row) and Salinópolis (bottom row). This is the seasonal average location of air 7 days before reaching the site at 7.5 km altitude. The left column represents an average over the wet season (Jan-Apr) and the right column represents the dry season (Jul-Oct). The data shown is a normalized particle dosage in $gsm^{-3}$ resulting from a 1 g release of particles at midday for every day in 2011, utilizing the NAME Numerical Atmospheric-dispersion Modeling Environment to calculate back-trajectories based on meteorological data to track the particles back 7 days. The locations of the aircraft sites, RBA (Rio Branco AMAZONICA), RBH (Rio Branco ACO), SAH (Salinópolis), ALF (Alta Floresta), SAN (Santarém), TAB (Tabatinga) are shown; in addition to the Paramaribo-FTS site (PAR), and Manaus TCCON site (MAN).

Figure 6.2 shows firstly that the particles released from Rio Branco do indeed almost entirely originate from an Eastwards direction across the Amazon Basin, whilst at Salinópolis the majority of particles were over the Atlantic Ocean 7 days before reaching the site. It also shows differences between the wet and dry seasons due to the varying location of the ITCZ. In the wet season the ITCZ is further to the South over the Amazon, bringing more northern air to both sites; whilst during the dry season the particles remain largely in the Southern Hemisphere.

### 6.3.2 Background calculation

To calculate $CH_4$ from the NAME outputs it is necessary to calculate the enhancement and background concentration of $CH_4$ at each GOSAT sounding location based on emission inventories and the modelled back-trajectories. The background component is calculated using MACC-II (Monitoring Atmospheric Composition and Climate) reanalysis modelled output from the ECMWF (Bergamaschi et al., 2013). This model combines state-of-the-art atmospheric modelling with Earth Observation data to produce a global record of the distribution, transport, sources, and sinks of greenhouse gases and aerosols (see `www.gmes-atmosphere.eu/about/project/` for details). The model's overall purpose is to deliver reliable operational products to support research in near real-time. The reanalysis data assimilates in situ observations from the NOAA Earth System Research Laboratory (ESRL) global air sampling network, and is available over the Amazon on a 6° longitude by 4° latitude resolution. The emission inventories used in the model are described further in the next section. The MACC-II model has been used in previous studies with the University of Leicester GOSAT retrieval results such as Alexe et al. (2015) and Parker et al. (2015).

The background is calculated by considering where the released particles reach the boundary of the NAME domain grid, which is defined as the outermost grid boxes on the lower resolution version of the grid. The sum of the total number of particles (in g s $m^{-3}$) per day for each of the 10 days of the back-trajectory and for each of these boundary grid boxes is displayed in Figure 6.3. The combined dosages of tracer particles over 10 days at each of the boundary grid boxes are then calculated as percentages of the total from these grid boxes. Figure 6.4 shows the percentages for each boundary grid box for the same NAME run as plotted in Figures 6.1 and 6.3. The largest percentage (approximately 25% of the total), is found to be in the middle grid box on the Eastern side of the NAME modelled domain, which is consistent with where the highest concentrations of particles in Figure 6.3 are seen.

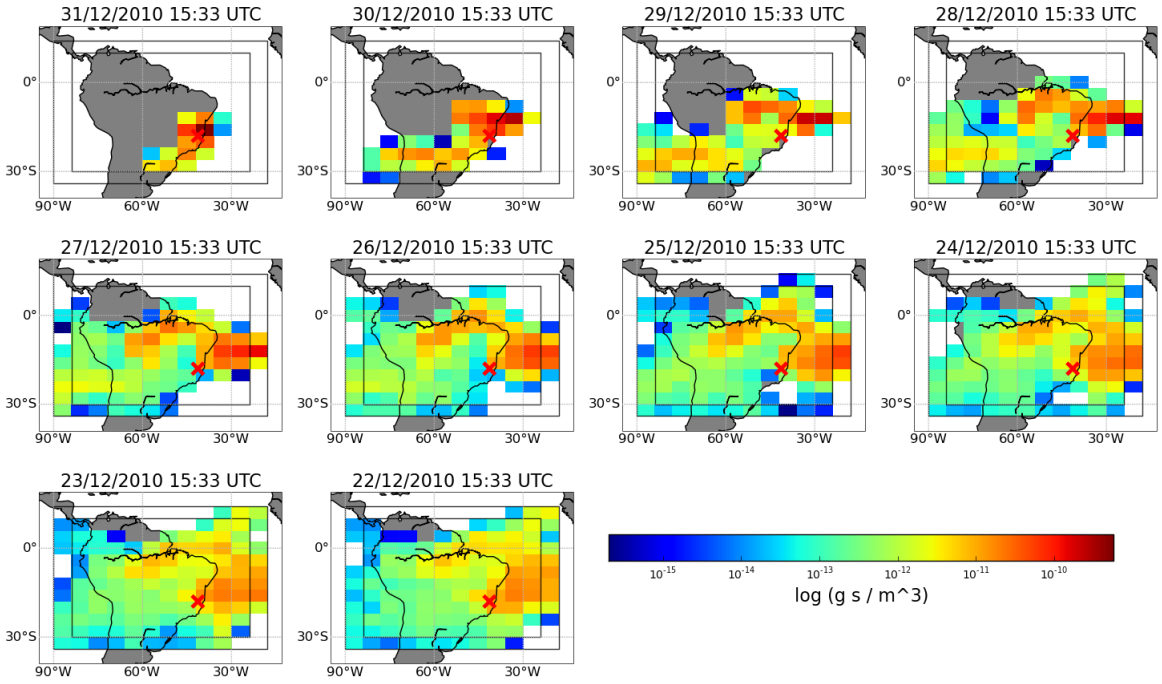


**Figure 6.3:** Maps showing the daily averaged location of released tracer particles for each day during a 10-day back-trajectory from the location of a GOSAT sounding (marked by the red cross) on January 1st 2011 at 15:33 UTC. The NAME model domain over which trajectories are tracked is shown by the outermost outlined rectangle, whilst the inner rectangle is in by one grid box. This outermost ring of pixels are the boundary grid boxes used for the background calculation. This figure is directly comparable to Figure 6.1, except this is on the lower grid resolution to match with the MACC-II model.

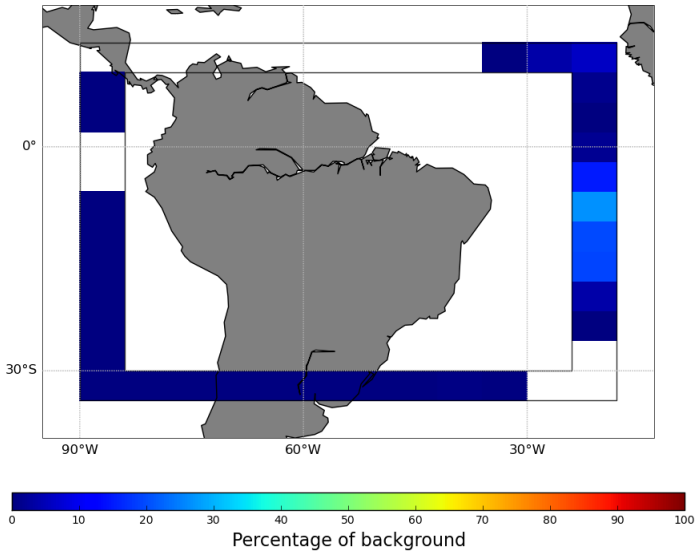


**Figure 6.4:** The percentage of tracer particles to reach each of the boundary grid boxes for a 10-day NAME back-trajectory originating from the same GOSAT sounding location on January 1st 2011 at 15:33 UTC as in Figures 6.1 and 6.3.

These percentages are then used to calculate a background $XCH_4$ value from the MACC-II data which is representative of where NAME has calculated the background air to originate from for each GOSAT sounding. The average MACC-II concentration for each of the boundary grid-boxes over the 10-day period is calculated, as shown in Figure 6.5. These values are then multiplied by the percentage which each grid box contributes to the air at the GOSAT location and summed together to calculate a background $XCH_4$ for each GOSAT sounding which will all be unique.

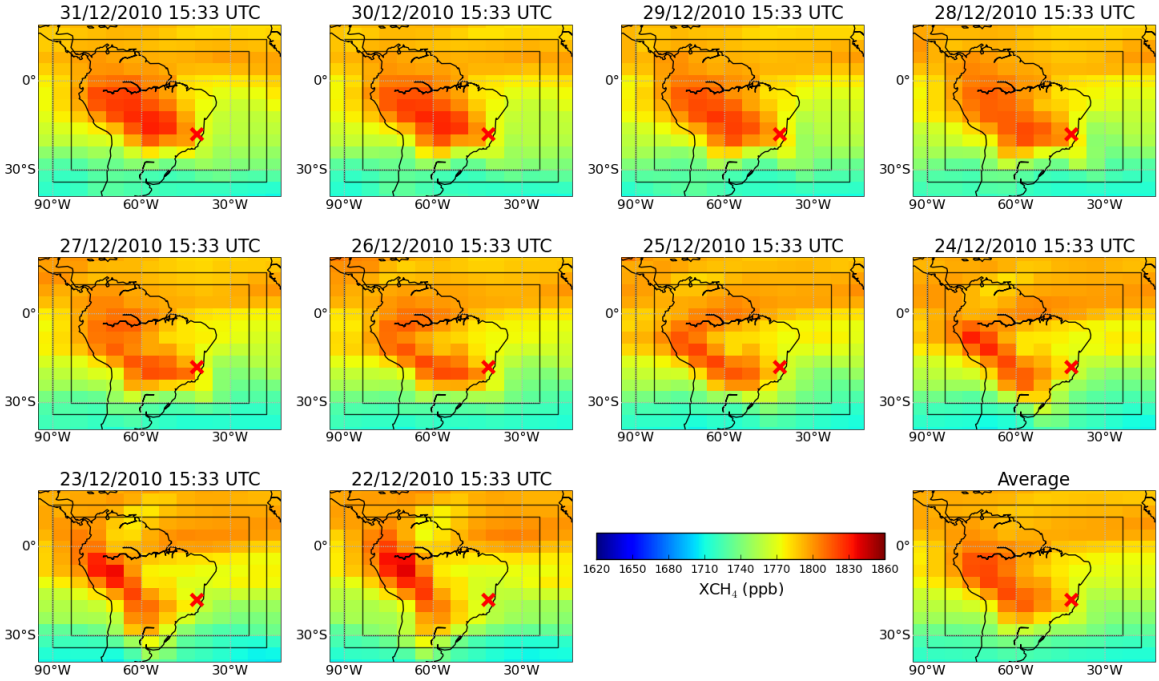


**Figure 6.5:** Maps of MACC-II $XCH_4$ for each of the days up to 10 days before the GOSAT sounding on January 1st 2011 (at the location of the red cross). The average of these 10 days of MACC-II is also shown, and the positions of the grid boxes on the boundary of the NAME modelled domain are shown.

### 6.3.3 Emission inventories

As the air modelled with NAME travels from the background to the GOSAT sounding locations, it is assumed to interact with emission sources and sinks when it is within 100 m of the surface. The NAME run outputs the daily dosage of tracer particles within this 100 m vertical area, but in order to calculate how much $CH_4$ these tracer particles are subjected to, and hence by how much the

trajectories are enhanced by, it is important to know the emissions in each grid-box. From these emission inventories I create a custom map of emissions for each day in 2011 calculated from multiple different datasets which specialise in different sources of $CH_4$ emission. For anthropogenic emissions, the Emissions Database for Global Atmospheric Research (EDGAR) v4.2 FT2010 global emissions (`edgar.jrc.ec.europa.eu`) are used, which are calculated based on energy balance statistics. These are gridded to a $0.1^\circ \times 0.1^\circ$ resolution for 2000 to 2010, and I use the 2010 emissions for 2011 since these are the newest available. EDGAR anthropogenic emissions include those from agricultural soils, energy manufacturing, fossil fuel fires, gas and oil production and distribution, road transportation, industrial processes, enteric fermentation from ruminants, manure management, soil waste disposal, waste water and from residential sources. EDGAR also contains an agricultural waste burning source which is removed. Fire emissions are very important in the tropics, so data from the Global Fire Emissions Database (GFED) v4 (`www.globalfiredata.org`) is used, which combines satellite information on fire activity and vegetation productivity to estimate the source of natural fire emissions. GFED includes emissions from savannah, grassland and shrubland fires, boreal and temperate forest fires, peatland fires, and sources from deforestation and degradation. Also included in GFED are agricultural waste burning $CH_4$ sources which I take from here instead of EDGAR. This dataset has a resolution of $0.25^\circ \times 0.25^\circ$ and is available between 1997 and 2014. Natural sources from oceans (Houweling et al., 1999), termites and hydrates, and a soil sink (Fung et al., 1991) are also included. Bloom 2012, as described in Bloom et al. (2012), is used for wetlands and rice paddies. The Bloom dataset is daily and covers 2003 to the end of 2011 with a global coverage and a resolution of $3^\circ \times 3^\circ$. They calculate $CH_4$ emissions from wetlands using surface temperature and equivalent water height (EWH) as described in Bloom et al. (2010), and use a Dynamic Methanogen-available Carbon Model (DMCM) to account for a seasonal lag between $CH_4$ columns from the SCanning Imaging Absorption spectroMeter for Atmospheric CHartographY (SCIAMACHY) and EWH (Bloom et al., 2012).

These emission inventories which I use are the same as those used for the GEOS-Chem model at the University of Edinburgh (Fraser et al., 2013); whilst those utilised by MACC-II have some differences. MACC-II also uses EDGARv4.2 for anthropogenic emissions, and GFED (v3.1) for fire emissions. Their termite, oceans and soil sink information comes from Sanderson (1996), Lambert and Schmidt (1993) and Ridgwell, Marshall, and Gregson (1999) respectively. The MACC-II wetland emissions are calculated using the GLC2000 global land cover dataset for South America and estimates methane emissions from wetlands using a scheme adapted from Christensen et al. (1996) and Kaplan (2002) to the Lund-Potsdam-Jena Dynamic Global Vegetation Model (LPJ DGVM) (Sitch et al., 2003). This method fundamentally calculates $CH_4$ emissions based on the availability of substrates for methanogenesis, the water table depth and the soil temperature. This is further detailed in Bergamaschi et al. (2007).

Figure 6.6 shows global maps of the seven separate emission inventories which are used, (GFED, EDGAR, Bloom and the Geological, Ocean, Soil Sink and Termite emissions). These emissions are shown for the 1st December 2010, since all of the inventories were available for this date, and shows their values as percentages of the total for each grid box. This shows where the individual emissions dominate and clearly shows that the Bloom wetland emissions and EDGAR anthropogenic emissions are the most dominant over land. The lower-left plot shows the total of all emissions excluding Bloom whilst the lower-right shows the total including Bloom. For these the data have been plotted between 0 and 2.5% of the total, otherwise extremely high individual point sources in the EDGAR database would dominate the plot.

In the Amazon three of the emissions inventories have considerably more of a contribution towards the total than the others. Bloom wetland emissions are the most dominant throughout the majority of the Amazon for every month in 2011 as shown by Figure 6.7 and account for more than 90% of emissions for most of the central Amazon. The EDGAR anthropogenic emissions are important outside of the central Amazon as shown by Figure 6.8, with often over 50% of emissions here coming from EDGAR. The other important emissions source in the Amazon are from fires, as expressed by the GFED emissions and shown

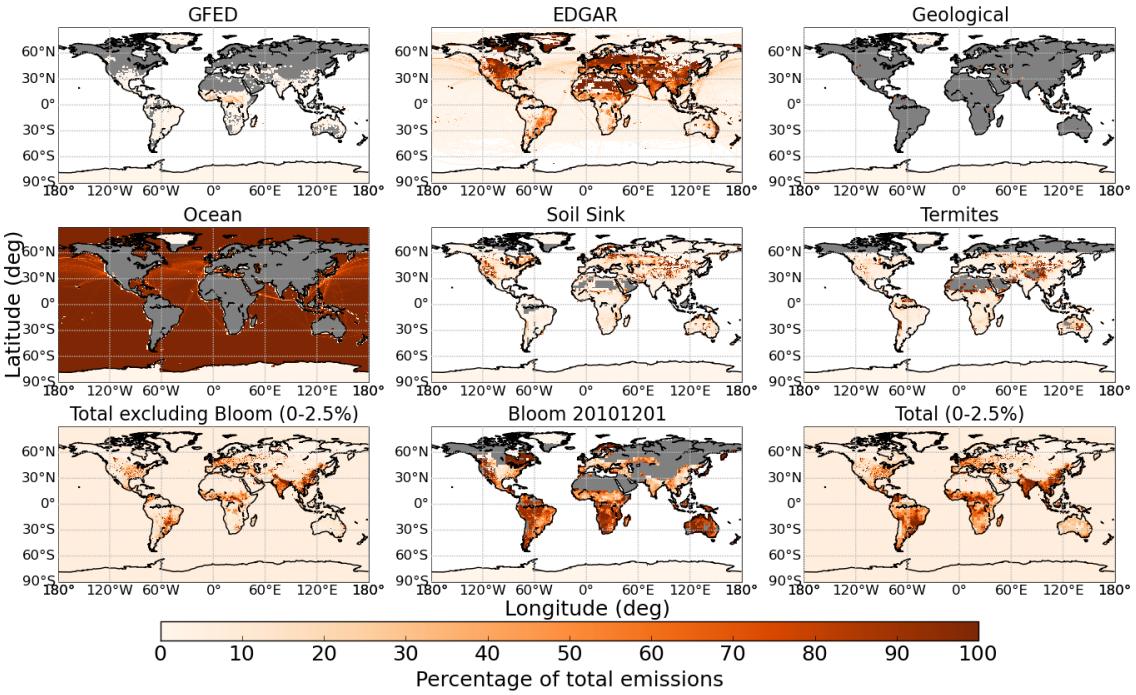


**Figure 6.6:** Emission inventories for the 1st December 2010 for GFED, EDGAR, geological sources, oceans, a soil sink term, termites, and Bloom. The values are given as percentages of the total emissions per grid box and is intended to display the relative contribution of each emission type in each grid-box. For example, ocean emissions contribute to approximately 100% of the total emissions for the grid-boxes over ocean. Also shown are maps of the total emissions, and of the total of everything excluding Bloom. These total emissions are normalised to a scale between 0 and 100, where 100 represents the highest global emission (out of all grid-boxes); although only the data between 0 and 2.5% of this are plotted, otherwise extremely high point sources in EDGAR dominate these maps.

in Figure 6.9. The GFED data shows that fire emissions can account for close to 100% of the emissions for a single $0.5^\circ \times 0.5^\circ$ grid box, and often more than 50% for a considerable area of the southern Amazon in the dry season (July–October). Figure 6.10 shows monthly averages of the combined total of all of the emission inventories for the Amazon. The many strong features visible on the coarser resolution are from the Bloom inventories, including the high values in Venezuela and Bolivia. The finer resolution features are predominately from EDGAR with only the most potent GFED fire emissions from August and September remaining significant compared to Bloom.

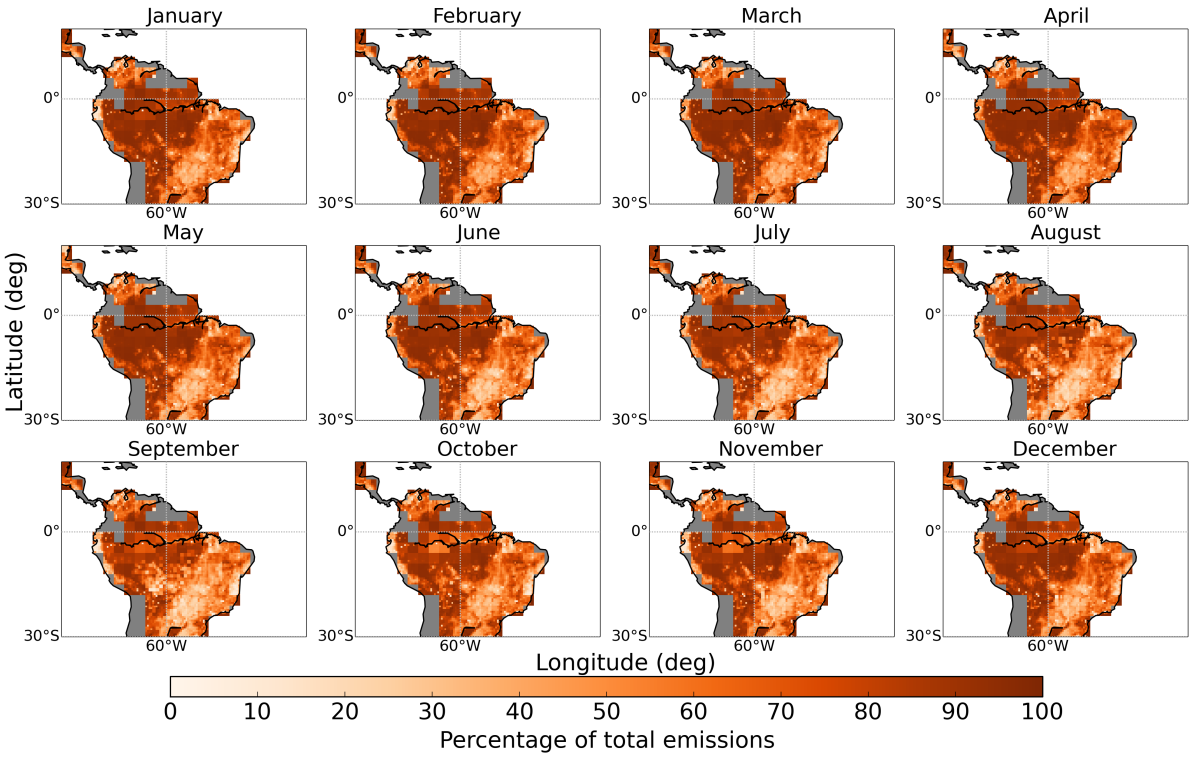


**Figure 6.7:** Monthly averaged Bloom wetland emissions for 2011 plotted as a percentage of the total emissions from all sources in each grid box.

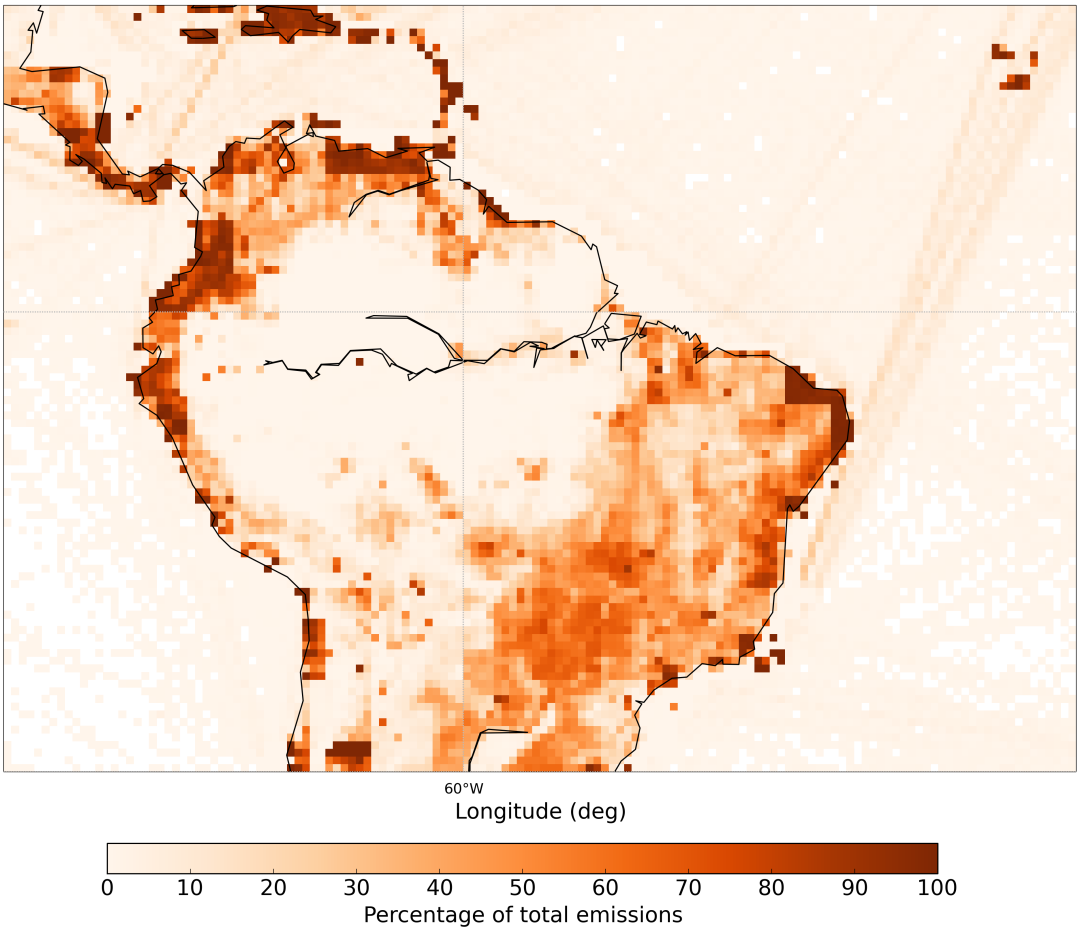


**Figure 6.8:** EDGARv4.2 anthropogenic emissions for 2010 plotted as a percentage of the total emissions from all sources in each grid box.

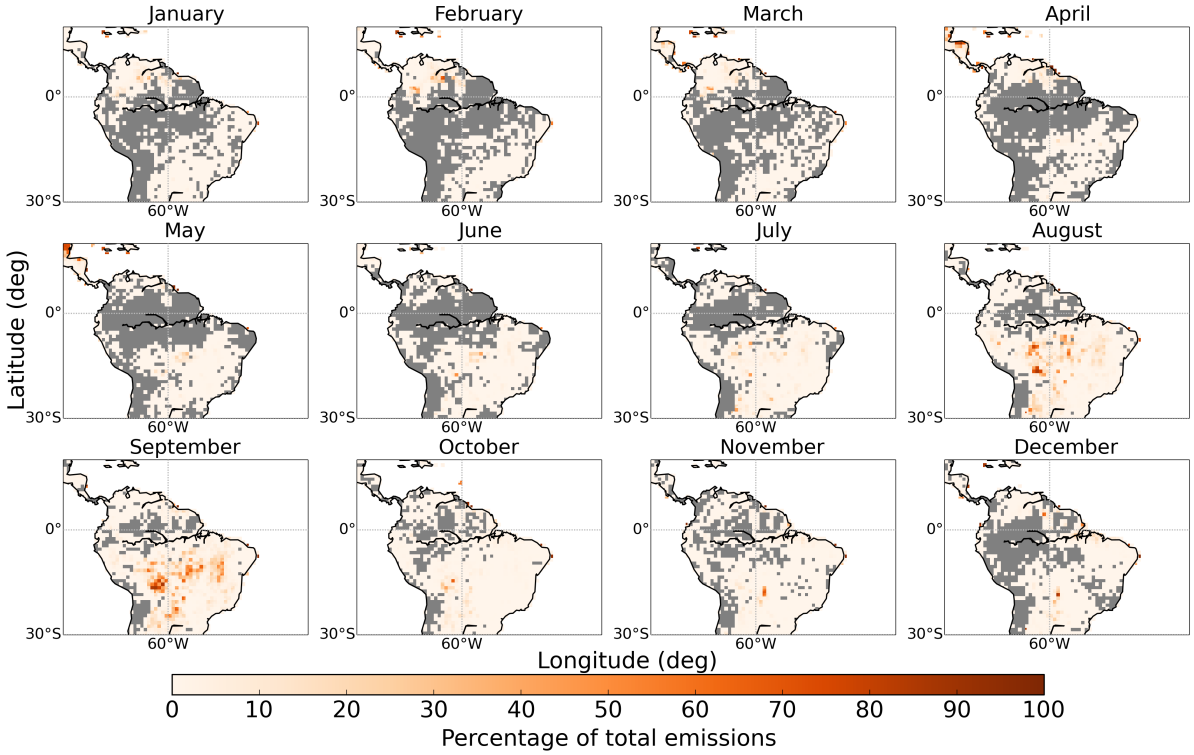


**Figure 6.9:** Monthly averaged GFEDv4 fire emissions for 2011 plotted as a percentage of the total emissions from all sources in each grid box.

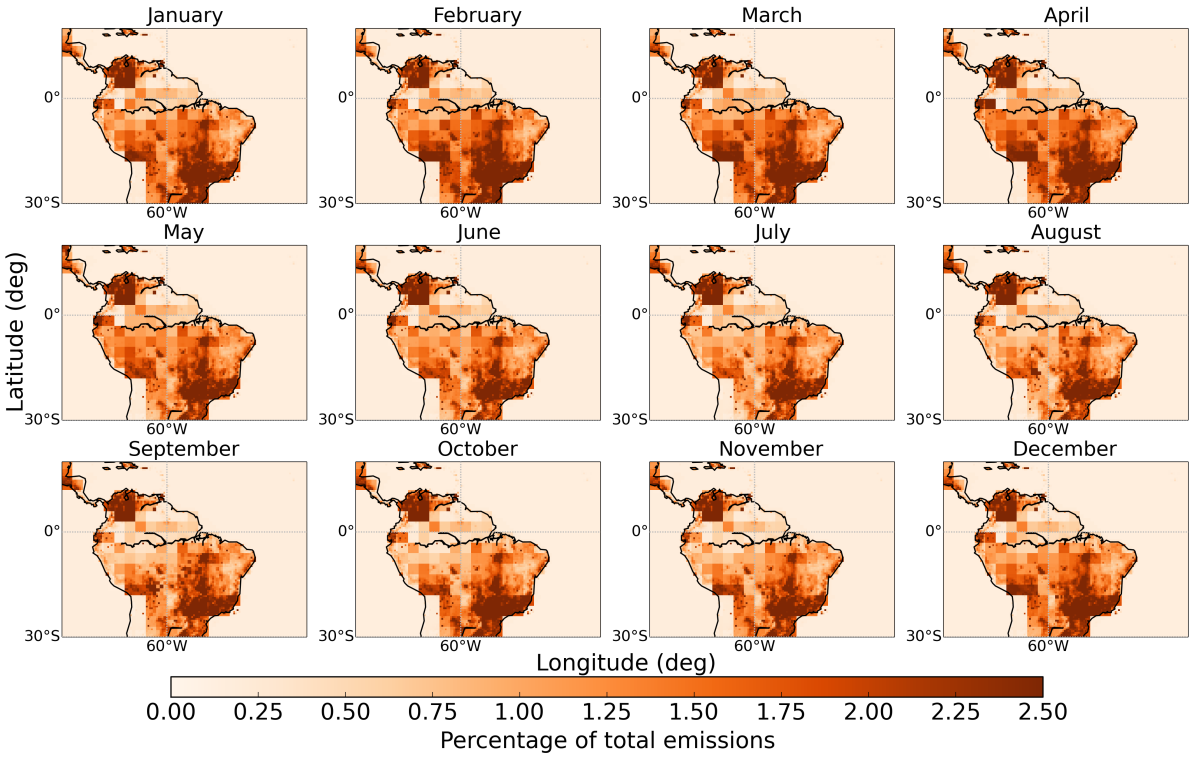


**Figure 6.10:** Monthly averages of the total of all seven emission inventories for 2011 (with 2010 EDGAR data) plotted as a percentage from 0% to 2.5% of the highest emission value in the Amazon.

### 6.3.4 Calculating $CH_4$ enhancements

To calculate the enhancements of $CH_4$ in the Amazon, the NAME outputs need to be converted from dosage matrices into dilution matrices (in s $m^{-1}$). These dilution matrices dilute a continuous emission of 1 g $m^{-2}$ $s^{-1}$ so by multiplying them by emissions with these units ($E$) the air concentration at the site can be calculated in g $m^{-3}$ as given by Equation (6.1).

$$C = \frac{D_o}{M} * A * E, \tag{6.1}$$

where $C$ is the air concentration in g $m^{-3}$, $D_o$ is the dosage, $M$ is the mass of the release and $A$ is the area of the grid-box. The area of each grid box is calculated separately since they will vary with latitude. The mass is 1 g per vertical level (37 in total). The dosages are calculated by NAME from just the particles which are within the lowest 100 m of the atmosphere, which it is realistic to assume are being influenced by local emissions. For each grid box and every day in the back-trajectory the $CH_4$ concentration is calculated by using Equation (6.1) for all 37 levels in the vertical profile. These are summed together to create the final $CH_4$ profile at the GOSAT sounding location. This air concentration can then be converted into a volume mixing ratio ($vmr$) (in ppbv) using Equation (6.2) where $R$ is the Universal Gas constant, $T$ is the temperature, $P$ is pressure and $M_W$ is the molecular weight of $CH_4$. The temperature and pressure outputs from NAME are used for this calculation.

$$vmr = \frac{C * R * T}{P * M_W}. \tag{6.2}$$

Finally the $CH_4$ profiles are converted into total column $XCH_4$ values following the method of O'Dell et al. (2012) which is outlined in Chapter 4, using the NAME calculated temperature, pressure and specific humidity directly instead of the ECMWF data used previously. By running NAME at the individual GOSAT sounding locations it is possible to directly apply each GOSAT averaging kernel to the $CH_4$ profiles.

## 6.4 RESULTS

Figures 6.11 and 6.12 show maps of the calculated background $XCH_4$ and the calculated $XCH_4$ enhancements at all GOSAT sounding locations, averaged for each month of 2011 and plotted on a $2^\circ \times 2^\circ$ grid. The background values show a north-south gradient which moves with the season as is to be expected since the higher concentrations from the Northern Hemisphere influence further south in the wet season when the ITCZ is further south. In the dry season the ITCZ is further north and as a result, lower $XCH_4$ concentrations are seen over much of the Amazon. The enhancements show their highest concentrations in the wet season as expected. Small values along the east coast and Atlantic Ocean can also be seen for all months. These concentrations become higher further inland as the air travels across the continent and picks up $CH_4$ over land.

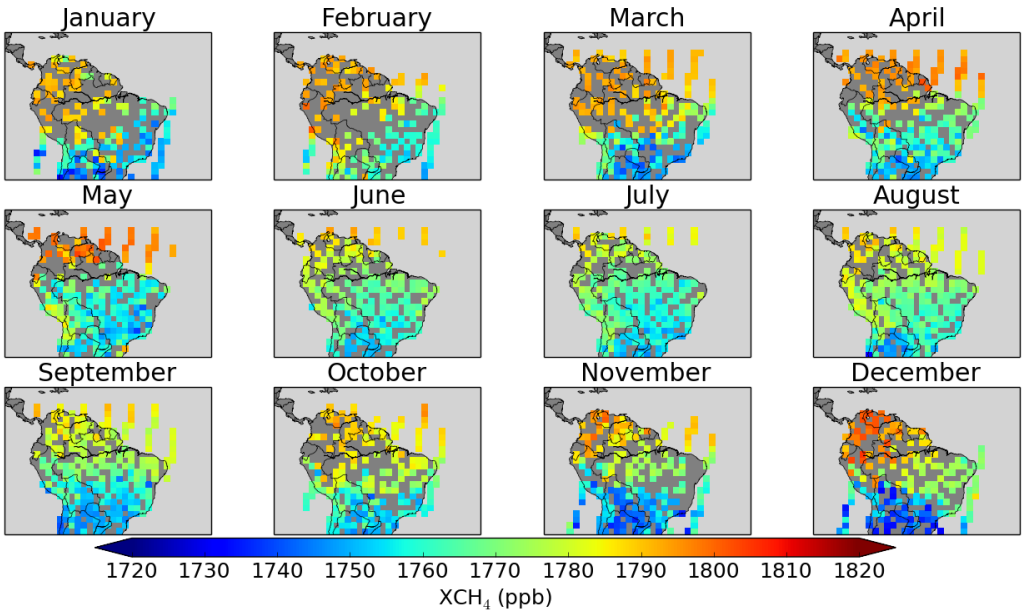


**Figure 6.11:** The calculated background from MACC-II at each GOSAT sounding location for 2011, averaged monthly on a $2^\circ \times 2^\circ$ grid.

The final $XCH_4$ values calculated from the NAME model simulation (the background plus the enhancements) are shown as monthly averages in Figure 6.13. These show that the model successfully recreates the seasonal cycle of $XCH_4$ with the highest concentrations in the northern Amazon (Venezuela) during the dry season, and higher concentrations further south in the wet season. The highest

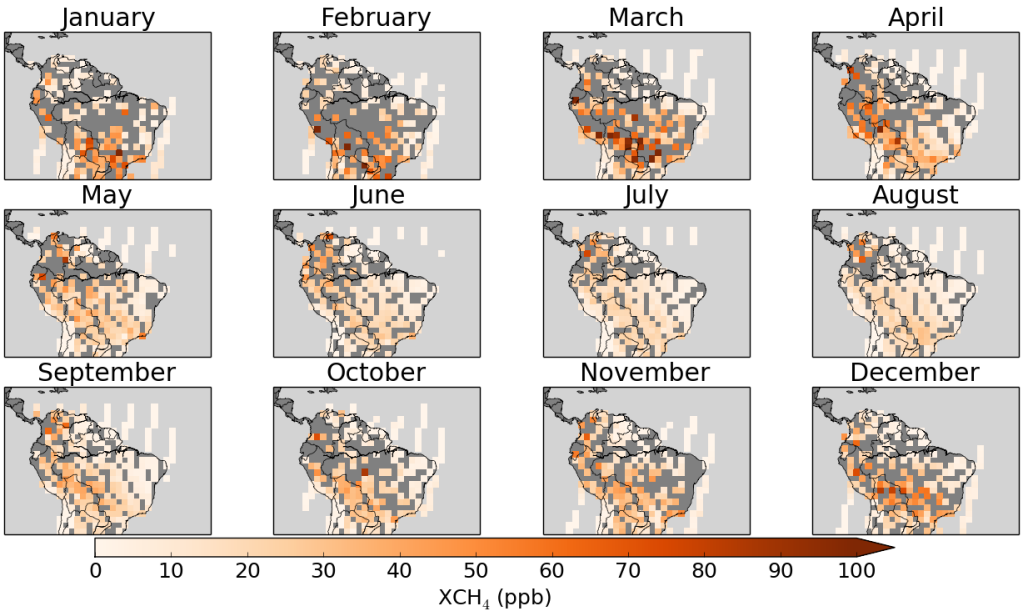


**Figure 6.12:** The calculated enhancement in $XCH_4$ seen at GOSAT sounding locations in 2011 from the interaction of incoming air with emission inventories over a 10-day period. The values are averaged for each month and plotted on a $2^\circ \times 2^\circ$ grid.

concentrations overall are seen to be in Bolivia where there are large-scale wetlands (Hess et al., 2015). However, to properly assess these results I now compare them with the GEOS-Chem model which was examined extensively in Chapter 5, with the MACC-II model from which the background was calculated, and with GOSAT.

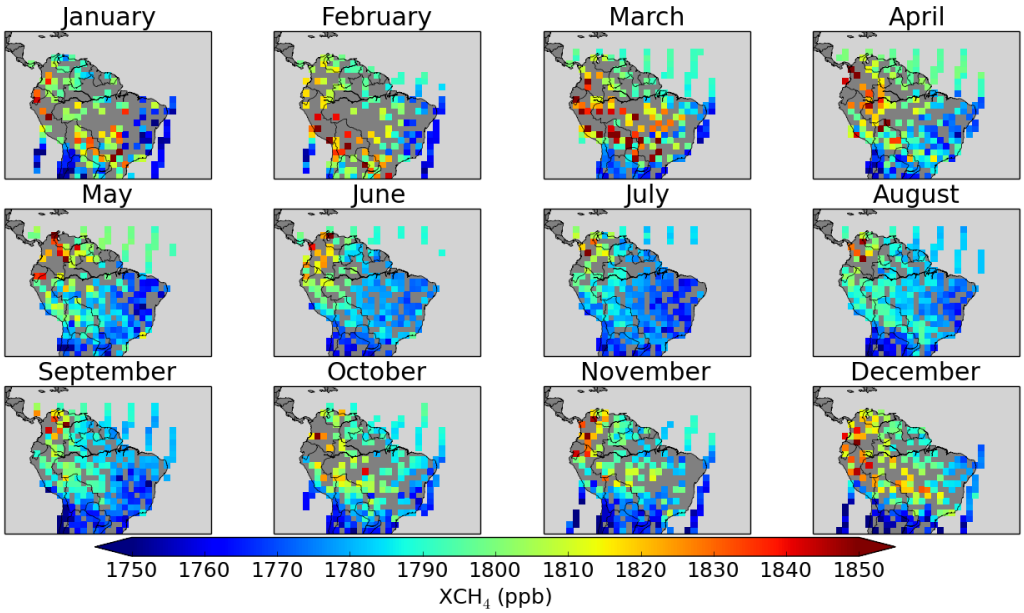


**Figure 6.13:** Monthly averaged $XCH_4$ calculated by the NAME model simulation at GOSAT sounding locations for 2011 and plotted onto a $2^\circ \times 2^\circ$ grid.

### 6.4.1 Comparisons with GOSAT and models

The $XCH_4$ was calculated at the GOSAT locations to allow a direct comparison of my results with GOSAT measured $XCH_4$ without co-location issues. Figure 6.14 shows monthly averaged maps of the difference between these results and GOSAT $XCH_4$. This figure shows that GOSAT is typically higher in concentration than my results by up to 30 ppb, although this is very regionally dependent with the opposite relationship in the south-west for many months. On average the model is 4.6 ppb lower than GOSAT with a mean monthly standard deviation of 15.4 ppb. The maximum monthly average difference is 9.7 ppb in the same direction (for April). These initial results are promising since, in Chapter 4, GOSAT $XCH_4$ was shown to be higher than (or comparable with) concentrations measured at the aircraft sites, and by up to 9.7±2.8 ppb at Salinópolis on the coast; where GOSAT is now also seen to be higher than the NAME modelled output.

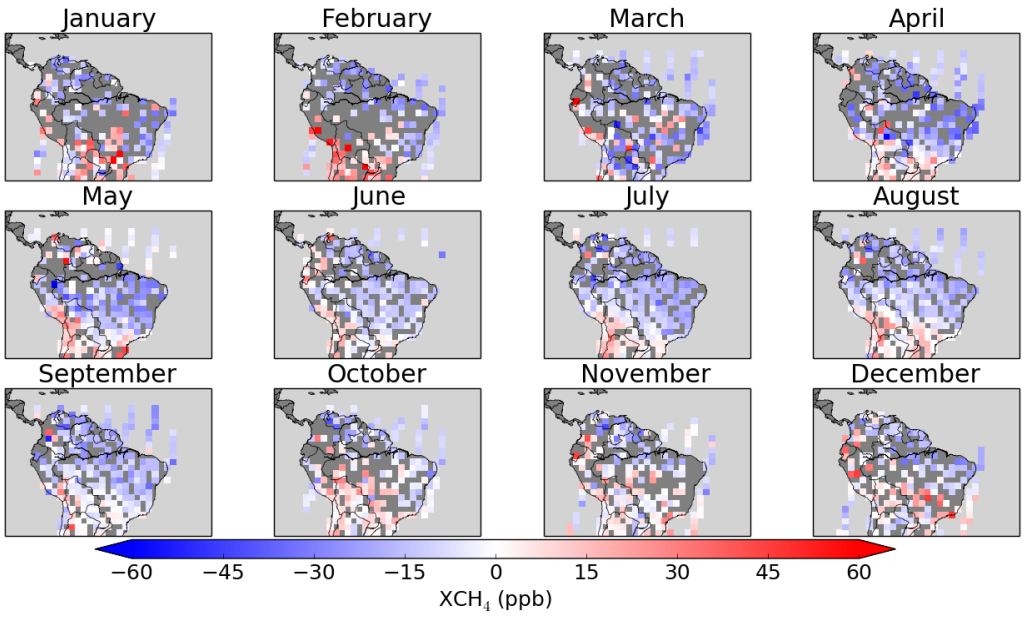


**Figure 6.14:** Monthly averaged maps for 2011 showing the difference between $XCH_4$ calculated using the NAME based model and $XCH_4$ from GOSAT, plotted on a $2° \times 2°$ grid.

I also compare my results with GEOS-Chem, sampled at the GOSAT sounding locations with the GOSAT averaging kernels applied. This is shown in Figure 6.15 which shows large differences between the model outputs in the wet season months, with GEOS-Chem lower by up to 60 ppb. However, in the dry season

GEOS-Chem can be higher than my results by up to 30 ppb in the southern Amazon; whilst remaining lower to the north and south of this. The average difference between my $XCH_4$ and $XCH_4$ calculated from GEOS-Chem is 10.5 ppb with an average monthly standard deviation of 14.4 ppb, although during the wet season the difference is as much as 19.6 ppb (February) and as little as 1.7 ppb in the dry season (July). Before concentrating on individual sub-regions in the Amazon I have also compared my model results with the MACC-II $XCH_4$, as shown in Figure 6.16. Since MACC-II $XCH_4$ is used to calculate my background concentrations before adding concentrations from the Amazon, it is expected that MACC-II and my results will typically agree over the Atlantic Ocean, although the transport models are calculated differently. They are mostly in agreement during the dry seasons when the ITCZ is more northern, and the models typically agree to within $\pm 10$ ppb over the eastern Amazon in the dry season months. They do differ further from the coast with MACC-II $XCH_4$ up to approximately 30 ppb lower in the south-west. During the wet season MACC-II concentrations are higher than mine in the Amazon by up to 40 ppb. On average MACC-II $XCH_4$ is 6.1 ppb lower than my results, and the standard deviation of the difference per month is on average 14.3 ppb.

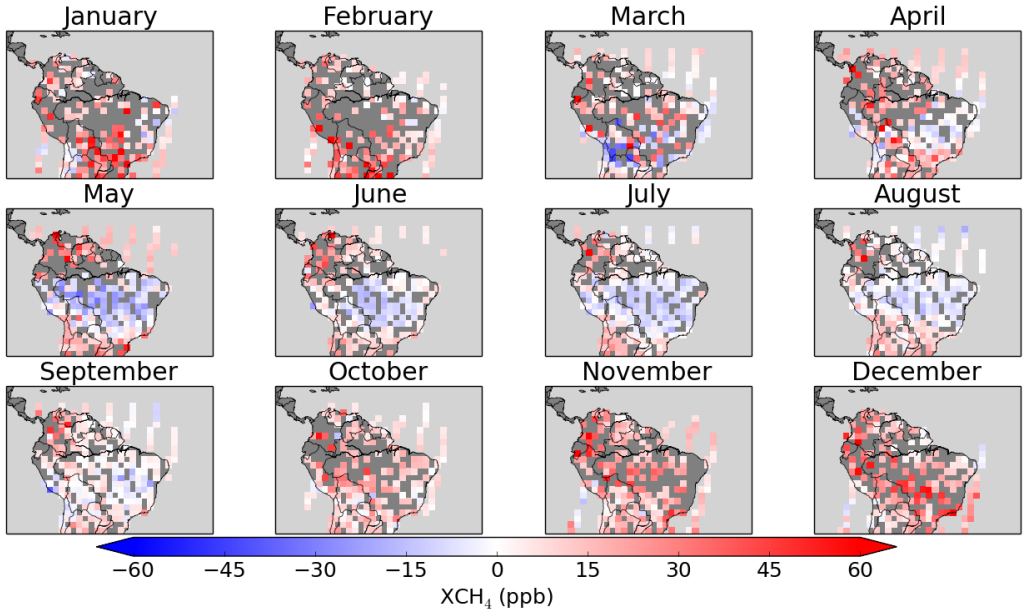


**Figure 6.15:** Monthly averaged maps for 2011 showing the difference between $XCH_4$ calculated using the NAME based model and $XCH_4$ from GEOS-Chem, sampled at GOSAT sounding locations and plotted on a $2^\circ \times 2^\circ$ grid.

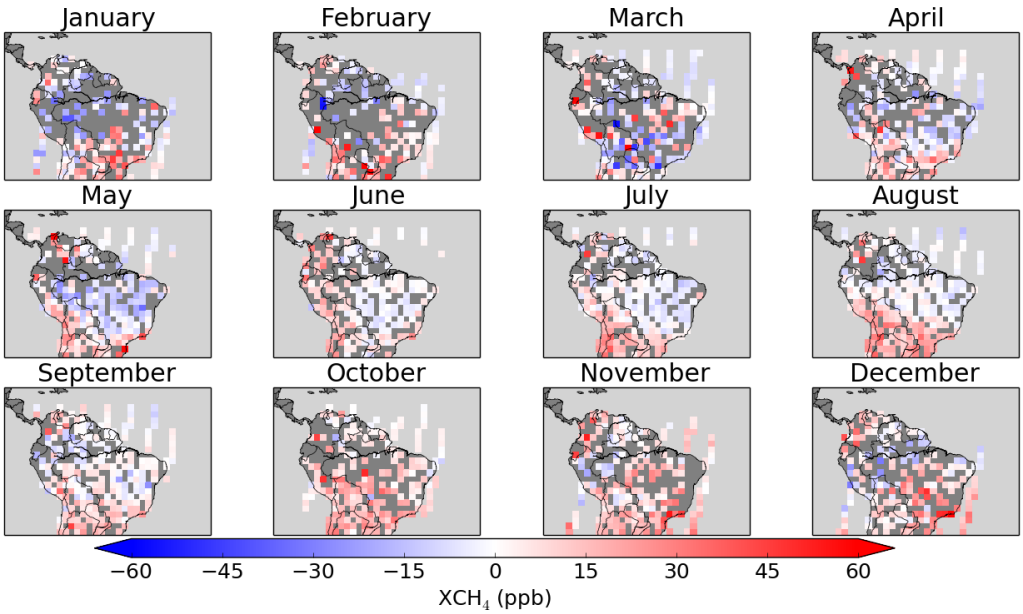


**Figure 6.16:** Monthly averaged maps for 2011 showing the difference between $XCH_4$ calculated using the NAME based model and $XCH_4$ from MACC-II, sampled at GOSAT sounding locations and plotted on a $2° \times 2°$ grid.

Figure 6.17 shows a time series of the monthly averaged $XCH_4$ from my modelled results using NAME, the calculated background, GOSAT, GEOS-Chem and MACC-II. These data are the average of all of the $XCH_4$ values for each month. All three models and GOSAT show generally similar features, all showing the highest concentration in March. The NAME modelled concentrations are closest to GOSAT for all months and are often within 5-10 ppb of MACC-II until the final three months of the year where this difference increases to approximately 10-20 ppb and becomes comparable with the standard deviations on these monthly concentrations, which are on average approximately 20 ppb for the NAME $XCH_4$. It is promising to see my model in better agreement with GOSAT over all months than MACC-II since the background is calculated from MACC-II. This suggests that either the high resolution transport modelling from NAME or the emission inventories which I use are able to better reproduce the Amazonian $CH_4$ enhancements than MACC-II. The background concentrations are considerably lower than the total and do not re-create the seasonality of the GOSAT measurements to the same extent as the total with the enhancements added. This shows that the $XCH_4$ enhancement calculated from Amazonian emission inventories provides real value in improving the background values alone.

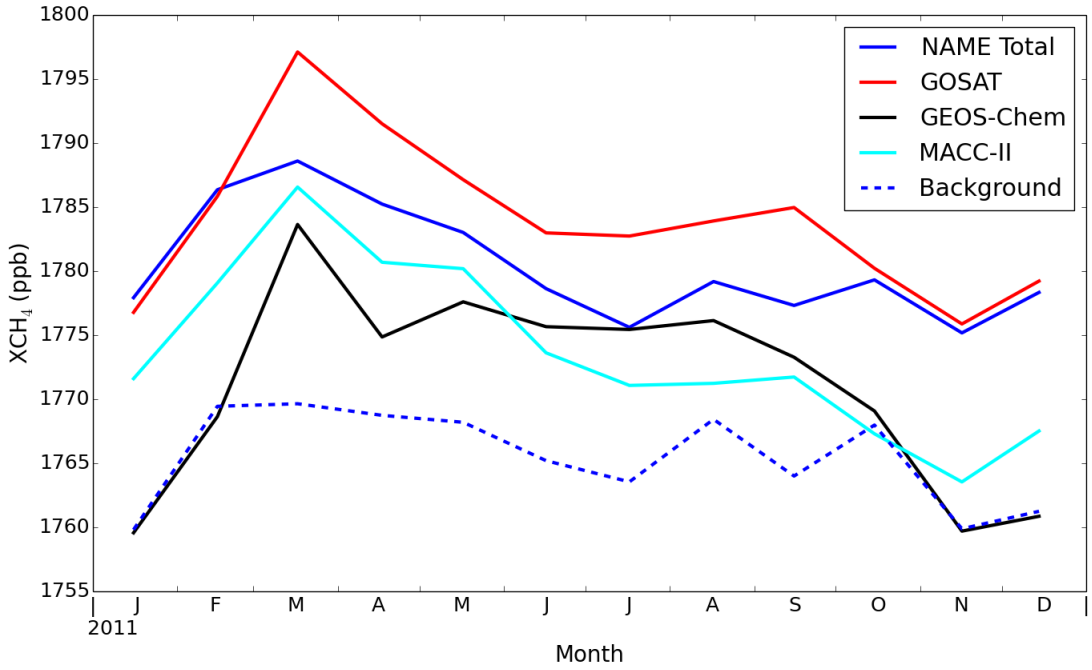


**Figure 6.17:** Time series showing monthly averages of modelled and measured $XCH_4$ at GOSAT sounding locations in the Amazon for 2011. The averaged area is for the NAME modelled domain (14°N–34°S, 90°W–18°W). In blue is the total $XCH_4$ as described in this chapter (blue dashed line is background component alone), in red is GOSAT $XCH_4$, in black is GEOS-Chem $XCH_4$ and in cyan MACC-II $XCH_4$.

### 6.4.2 Regional differences

To better understand the differences observed in Figures 6.14, 6.15 and 6.16 I now consider five sub-regions within the Amazon, which should help to determine where interesting differences can be seen between the three models and GOSAT. The five regions used are those defined in Chapter 5, Figure 5.13; where region 1 is in the Northern Amazon above the equator. Regions 2 and 3 are below this in the eastern and western Amazon respectively. Region 4 roughly covers the Bolivian wetlands and the south-western Amazon, whilst region 5 is predominantly Cerrado outside of the Amazon.

Figure 6.18 shows monthly average time series of GOSAT and the three models for each of the regions in the Amazon, in addition to the background concentration. Table 6.1 details the average differences between each model and GOSAT. The uncertainties are not shown since the number of soundings which are averaged remains high enough to generally keep them below 1 ppb, and at the maxi-

mum no more than 4.1 ppb in February for regions 2 and 4 which have the least soundings. Firstly, GOSAT $XCH_4$ concentrations are seen to be higher than the models for most months for all of these regions. In the northern-most region (region 1), the NAME model output is higher than MACC-II by on average 4.5 ppb, and higher than GEOS-Chem by on average 13.9 ppb; whilst being 12.1 ppb lower than GOSAT. The NAME model and MACC-II model are similarly close to each other throughout regions 2 and 3, without one being systematically higher than the other; albeit with considerably larger MACC-II values in region 2 at the beginning of the year (by approximately 20 ppb). In region 4 there are similarly high concentrations at the beginning of the year of up to 1840 ppb in both my model and in MACC-II which surpass the GOSAT concentrations. This region also sees GEOS-Chem in good agreement with GOSAT and my model between March and September, whilst MACC-II concentrations are lower by 10 ppb before returning to closer agreement with the NAME model in the final two months. For region 5 to the south-east of the Amazon my model and MACC-II are consistent, and typically lower than GOSAT with the exceptions of January, October, November and December where my results are very similar to GOSAT and show significant divergence from MACC-II and GEOS-Chem.

The calculated background $XCH_4$ concentration is also shown in Figure 6.18. This indicates that the background values are typically higher in the northern region than in the southern ones. The average background at region 1 is 6.3 ppb higher than for region 2 and 13.5 ppb higher than region 3. Regions 4 and 5 are 21.5 ppb and 31.6 ppb lower than region 1. The range of background values over the entire year is less than 30.1 ppb for all of the regions. This is less than the average enhancement for regions 1, 4 and 5 which are on average 2.4, 1.5 and 2.4 times as large as the background variability respectively. This suggests that the variability in the total $XCH_4$ calculated for these regions is mostly influenced by South American $CH_4$ emissions and not by the background air. The average enhancement in region 2 is approximately 83% of the variability which can be seen in the background, and in region 3 is 57%, which is expected since Figure 6.10 shows the least emissions in regions 2 and 3. Region 3 in particular is closest to the East coast where incoming air is expected to have travelled from, so

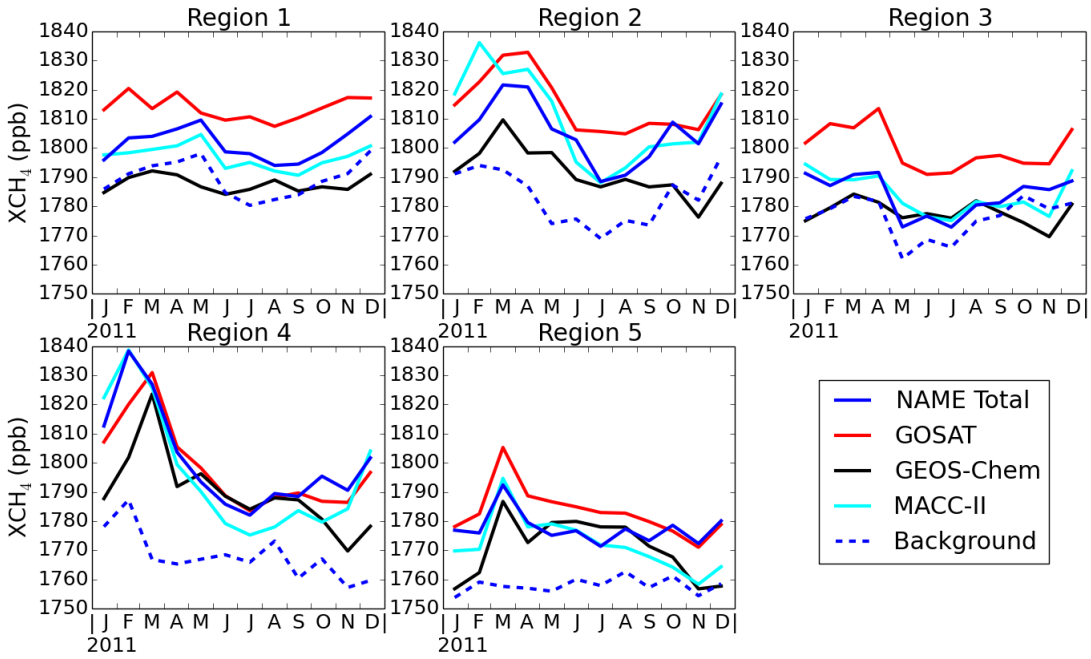


**Figure 6.18:** Time series showing the monthly mean calculated $XCH_4$ at GOSAT sounding locations in 2011 for GOSAT (red), the NAME modelled $XCH_4$ (in blue), the calculated background $XCH_4$ (blue dashed), MACC-II (in cyan) and GEOS-Chem (in black). The results are averaged over the five regions in the Amazon.

it is not surprising for it to be the most influenced by the background instead of by the emissions. For all of the regions the total $XCH_4$ concentrations from my model are closer to GOSAT and MACC-II for the majority of months than the background is. Furthermore, the enhancements are also producing features which are not found in the background but are present in GOSAT and the other models. For example, the high concentrations in region 5 in March are approximately 15 ppb higher than values on adjacent months in all three models and GOSAT, whereas the background values contain no such peak in March. This highlights that the $XCH_4$ enhancements calculated due to emissions in the Amazon are capable of making significant and real signals in the $XCH_4$ seasonality which are not just a result of changes in the background concentrations.

To better understand how the models compare with the seasonality seen by GOSAT, the yearly standard deviation of the difference between each model and GOSAT for each of the regions is considered, effectively removing the systematic offsets from the analysis. These results are summarised in Table 6.2 along with the standard deviations of the differences between each of the three

| a. | NAME - GOSAT | GEOS-Chem - GOSAT | MACC - GOSAT |
|---|---|---|---|
| Region 1 | -12.14 | -26.06 | -16.67 |
| Region 2 | -9.63 | -23.42 | -4.90 |
| Region 3 | -15.95 | -21.95 | -15.85 |
| Region 4 | 2.22 | -8.67 | -1.80 |
| Region 5 | -5.71 | -12.55 | -10.99 |
| b. | **GEOS-Chem - NAME** | **MACC - NAME** | **GEOS-Chem - MACC** |
| Region 1 | -13.92 | -4.53 | -9.39 |
| Region 2 | -13.79 | 4.73 | -18.52 |
| Region 3 | -6.00 | 0.10 | -6.10 |
| Region 4 | -10.89 | -4.02 | -6.88 |
| Region 5 | -6.84 | -5.27 | -1.56 |

**Table 6.1**: The monthly averaged differences between, a. Either the NAME model, GEOS-Chem or MACC-II $XCH_4$ with GOSAT $XCH_4$, and b. Between the three models, GEOS-Chem minus NAME $XCH_4$, MACC-II minus NAME $XCH_4$, and GEOS-Chem minus MACC-II $XCH_4$. All as averages over the five pre-defined sub-regions, with values in ppb.

models. For region 1, GEOS-Chem and MACC-II better capture the seasonality seen by GOSAT than my model, although mine is in better agreement than GEOS-Chem for the other four regions and better than MACC-II in regions 2 and 4 (the most in-land regions). Interestingly the standard deviations of the monthly differences to GOSAT across all regions are more consistent in my model (with a range of 2.13 ppb) compared to for the other models which therefore show more of a geographical dependency with their agreements to GOSAT, (a range of 4.23 ppb for GEOS-Chem and 7.49 ppb for MACC-II). The standard deviations of the differences between the three models show that for four of the regions my model agrees with the seasonality in MACC-II more than it does with GEOS-Chem. In one region the other two models agree better with each other than my model agrees to either of them. The largest differences are between MACC-II and GEOS-Chem.

### 6.4.3 MACC-II Enhancements

To examine how the emissions used in the MACC-II model compare with those I have used, I now consider the difference between my calculated $XCH_4$ enhancement and that from the MACC-II model. The background has been subtracted

| a. | NAME - GOSAT | GEOS-Chem - GOSAT | MACC - GOSAT |
|---|---|---|---|
| Region 1 | 4.19 | 3.48 | 3.60 |
| Region 2 | 5.30 | 5.41 | 7.63 |
| Region 3 | 4.63 | 5.65 | 3.71 |
| Region 4 | 6.32 | 7.71 | 9.48 |
| Region 5 | 5.13 | 6.42 | 1.99 |
| b. | **GEOS-Chem - NAME** | **MACC - NAME** | **GEOS-Chem - MACC** |
| Region 1 | 4.71 | 2.80 | 3.55 |
| Region 2 | 8.21 | 9.07 | 11.03 |
| Region 3 | 6.78 | 4.27 | 5.70 |
| Region 4 | 12.61 | 6.26 | 16.45 |
| Region 5 | 9.34 | 6.40 | 6.21 |

**Table 6.2:** The standard deviation of the monthly averaged differences between, a. Either the NAME model, GEOS-Chem or MACC-II $XCH_4$ with GOSAT $XCH_4$, and b. Between the three models, GEOS-Chem minus NAME $XCH_4$, MACC-II minus NAME $XCH_4$, and GEOS-Chem minus MACC-II $XCH_4$. All as averages over the five pre-defined sub-regions, with values in ppb.

from the MACC-II $XCH_4$ total at each GOSAT sounding location to calculate this enhancement. Whilst the transport model used for the MACC-II model is not the same as NAME, if both methods are assumed to produce similar results (which is not unreasonable for the Amazon where wind-directions are fairly predictable as previously shown), then this analysis should provide insights about the differences between the emissions which are used. Figure 6.19 shows this calculated enhancement for MACC-II as monthly averaged maps. Compared with Figure 6.12, the enhancement from MACC-II is seen to be very similar geographically with the enhancement calculated with NAME and the GEOS-Chem emission inventories. The most notable differences are in the south where MACC-II enhancements are generally lower in concentration, otherwise they do appear to be very similar. Time series for the five sub-regions are shown in Figure 6.20, showing the seasonal variation for both the NAME modelled and MACC-II enhancements. The mean difference (all given as NAME minus MACC-II) between the two is the largest for region 5 (5.27 ppb); although this is dominated by large differences at the end of the year (August onwards) of up to 15.7 ppb (in December); otherwise the remainder of the year averages only a 1.05 ppb difference. Region 3 also agrees well, with an average difference of -0.10 ppb. Regions 1 and 4 show differences of 4.53 ppb and 4.02 ppb respectively; whilst region 2 shows a similar difference in the opposite direction, -4.73 ppb. These differences in re-

gion 2 are dominated by large differences in the wet season at the beginning of the year where the models differ by as much as -26.4 ppb.

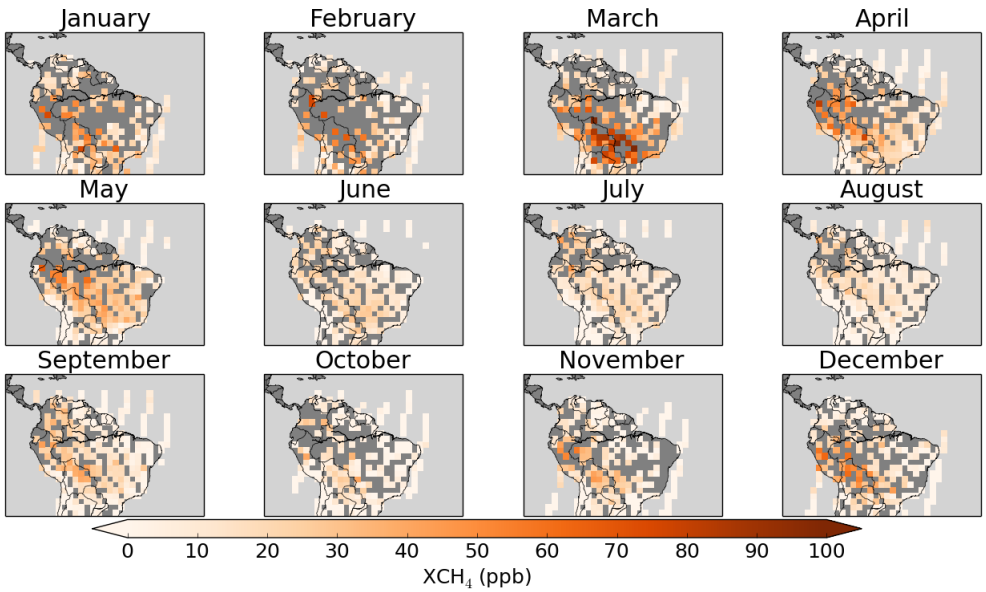


**Figure 6.19:** Monthly averaged maps of the calculated $XCH_4$ enhancement due to Amazon emissions from the MACC-II model. Averaged and plotted on a $2° \times 2°$ resolution.

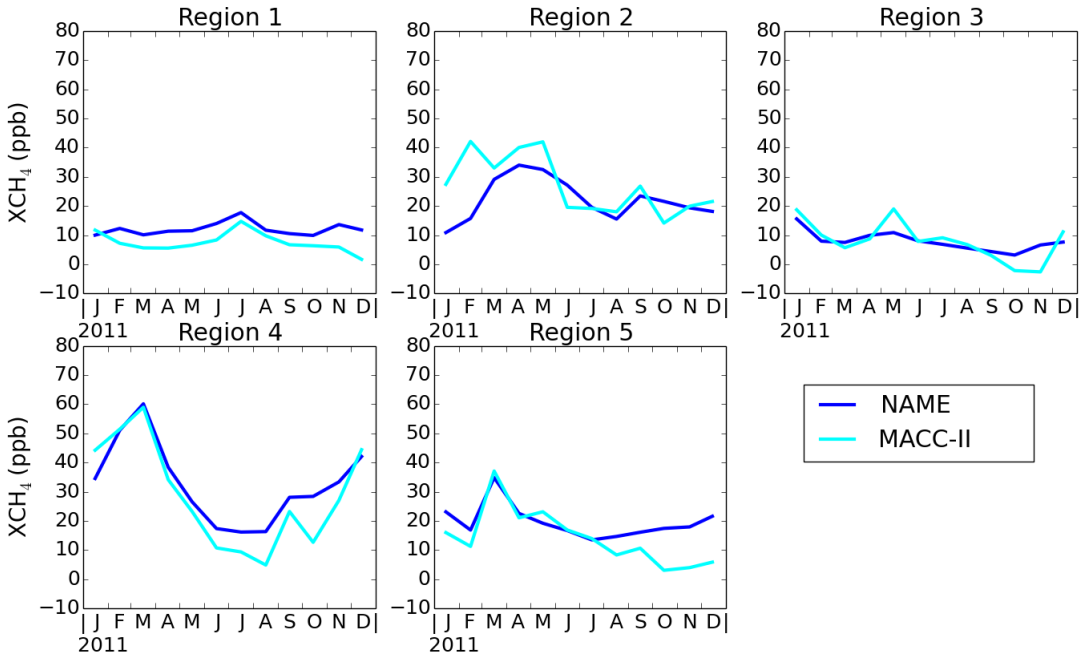


**Figure 6.20:** Time series showing the monthly averages of the $XCH_4$ enhancement for the NAME modelled output using GEOS-Chem emission inventories (in blue), and for the MACC-II calculated enhancement (in cyan).

## 6.5 CONCLUSIONS

In this chapter I have developed a model to calculate $XCH_4$ concentrations in the Amazon for 2011. This model uses the Numerical Atmospheric-dispersion Modelling Environment (NAME) to calculate the transport of tracer particles across the Amazon at high resolution using meteorological data. The model uses these back-trajectories to calculate both the origin of this air from outside of the Amazon and also where the air interacts with $CH_4$ emissions at the surface. The model was run at the times and locations of every GOSAT sounding in 2011 (in the Amazon) and these back-trajectories were used to calculate the $XCH_4$ based on $XCH_4$ concentrations from the MACC-II model outside of the Amazon by using state-of-the-art emission inventories to calculate the enhancements of $CH_4$ within the Amazon. To test the model the results are compared with the MACC-II model, which was used for background $XCH_4$ concentrations and which assimilates in situ data to produce reliable $XCH_4$ concentrations. My results are also compared with the GEOS-Chem model (which does not assimilate such data to constrain itself) and it is compared with the GOSAT satellite $XCH_4$ which was previously validated in Chapter 4.

The results show that the $XCH_4$ calculated by my model compares favourably with the other datasets. I see a north-south gradient in my calculated background $XCH_4$ which moves with the expected location of the ITCZ. The enhancements which are calculated due to the sources and sinks in the Amazon are found to match with expectations; with lower values near the east coast and gradually increased concentrations across the Amazon Basin. The seasonal cycle is also well represented, with higher concentrations calculated in the months of the wet season across regions where the emission inventories suggest such enhancements should be. The results also show high enhancements in the north-west of the Amazon in the dry season, similar to those which were observed with GOSAT in Chapter 5. The reproduction of these expected features and patterns provides confidence that the model is performing well and that the enhancements which I have calculated are providing value to the results above

that which is seen in the background values alone. Typically all three models produce lower concentrations than GOSAT, and in the northern Amazon, and overall, my model produces average values closest to those of the satellite. The scatter on all of the datasets is typically larger or similar to these differences, although the uncertainties on them are considerably lower considering the large number of soundings per averaged region. When looking at individual regions my modelled concentrations are rarely the highest or lowest concentrations for each month between the four datasets (when they are this is only by a few ppb besides a single region where the difference is approximately 9 ppb in one month). I also find that the enhancements in $XCH_4$ from emissions in the Amazon bring my results into better agreement with GOSAT concentrations in terms of magnitude and seasonality than are achieved with just the background values alone, showing that the model provides meaningful results.

To examine the seasonality agreement between the three models and GOSAT I have examined the standard deviation of the difference between the modelled results and GOSAT $XCH_4$. The standard deviation of the difference between my model and GOSAT (over the entire year) is lower than for the difference between GEOS-Chem and GOSAT for all but the northern most region. The difference between MACC-II and GOSAT is also larger than between my model and GOSAT for the two most in-land regions, whilst MACC-II is more consistent with GOSAT for the three more coastal sites. In the two in-land regions my model is also is in better agreement (concerning the seasonality) with both of the other two models than they are with each other. These results suggest that this approach has the potential to provide new insights into $XCH_4$ in the Amazon as it is able to better re-produce the magnitude of GOSAT $XCH_4$ as well as the seasonality in the western Amazon than both MACC-II and GEOS-Chem. Importantly my model is also the most consistent in its agreement to GOSAT over the five regions which I have studied compared to the other models which show more variability in their average differences to GOSAT. Finally, my calculated $XCH_4$ enhancement in the Amazon was compared to that of the MACC-II model by subtracting from it the background which had been calculated from MACC-II. These comparisons generally showed a good agreement between the two enhancements (less than a 5.3 ppb

average yearly difference), although MACC-II is typically lower in concentration at the end of the year in the south.

# 7 CONCLUSIONS AND FUTURE WORK

Natural wetlands, such as those in the Amazon, are important sources of $CH_4$ which is the second most important anthropogenic greenhouse gas in terms of radiative forcing. With a short atmospheric lifetime compared to $CO_2$, reductions in $CH_4$ emissions have the potential to mitigate global warming on much faster time scales. However, our current understanding of methane emissions is limited, with considerable disagreement between modelled wetland emissions estimates as discussed in Melton et al. (2013). There is a lack of in situ $CH_4$ measurements in the tropics where these wetland emissions are of particular importance. It is possible that satellite measurements of $XCH_4$ from GOSAT could fill this gap in knowledge and help to provide useful insights into the nature of wetland emissions in the Amazon, however they had not been validated in the Amazon until now.

In Chapter 4, measurements from GOSAT have been validated in the Amazon basin for the first time using in situ measurements from aircraft. Methane calculated from the University of Leicester Proxy $XCH_4$ retrieval algorithm (v6) was compared with aircraft profiles of $CH_4$ ranging from 300 m asl to 7.5 km asl at two sites in the Amazon (Rio Branco ACO and Salinópolis) and at four further sites where the uppermost altitude is instead 4.5 km asl, (Alta Floresta, Rio Branco AMAZONICA, Santarém and Tabatinga). This was the first time that GOSAT $XCH_4$ had been validated with regular in situ measurements in the Amazon. The aircraft profiles were first converted into total column measurements by extrapolation up to a calculated tropopause altitude and by use of a dedicated stratospheric chemical transport model (TOMCAT). The development of these extended aircraft profiles and their use to validate GOSAT $XCH_4$ was a major aim of Chapter 4; as was ascertaining the benefit of 7.5 km profiles over 4.5 km profiles. Evaluation of the uncertainties involved

with the conversion of these aircraft profiles into total columns using a high resolution model has shown that the uncertainties can be significantly reduced by measuring up to 7.5 km instead of 4.5 km. Previously the variation of $CH_4$ in the troposphere above 4.5 km was considered to be small; so this study has highlighted that this is not necessarily true, and has shown the benefits of measuring up to higher altitudes. This was one of the most important findings in Chapter 4. Another main objective of the chapter was to verify the choice of the aircraft site locations (at Salinópolis and Rio Branco). This was justified by showing that Rio Branco $CH_4$ profiles contain typically elevated concentrations over those at Salinópolis, especially near the surface, (average $CH_4$ across all altitude levels and profiles is 1834 ppb for RBH and 1815 ppb for SAH). Further analysis of average wind trajectories from both HYSPLIT and NAME (in Chapter 6) further justify the assumption that Rio Branco is representative of air which has travelled across the Amazon basin, whilst Salinópolis is representative of background air from the Atlantic Ocean.

The GOSAT $XCH_4$ measurements have been shown to agree within uncertainties with the in situ measurements at three of the aircraft sites, with differences ranging from -1.9 ppb to 6.6 ppb (GOSAT minus aircraft); whilst at two sites GOSAT $XCH_4$ is shown to be slightly higher than aircraft measurements, by 8.1 ppb and 9.7 ppb. The seasonality in $XCH_4$ seen by the aircraft profiles is also well captured by the GOSAT measurements, with correlation coefficients ranging from 0.61 to 0.90 across the five sites. A model $XCO_2$ which is used in the calculation of the GOSAT $XCH_4$ could account for part of the biases which are seen between GOSAT and aircraft $XCH_4$, although it can not account for all of the differences. Overall the fairly small difference between the extrapolated in situ data and GOSAT data is encouraging evidence which shows that GOSAT $XCH_4$ is reliable over the Amazon and can be used here to improve our understanding of Amazonian methane emissions. This successful validation of GOSAT $XCH_4$ in the Amazon for the first time is the main scientific outcome of Chapter 4 and is an important result in my work as a whole.

Building upon the promising validation results between GOSAT and in situ data, the behaviour of $XCH_4$ and its sources of emissions in the Amazon are

then studied in Chapter 5 with the aim to learn about the large-scale patterns of $XCH_4$ as observed by GOSAT. Observations from GOSAT show that $XCH_4$ concentrations in the northern Amazon are higher in the dry season by up to 30 ppb than they are in the wet season. In the wet season GOSAT concentrations are generally higher further south in the Amazon Basin by typically 45 ppb (the difference between seasonally averaged GOSAT soundings on a $2^\circ \times 2^\circ$ grid), although the largest differences can be up to as much as 60 ppb and are found in regions which are known to contain large wetlands (the Pantanal wetlands in Bolivia). This indicates that GOSAT can observe seasonal and regional differences in $XCH_4$ in the Amazon and that it can observe real enhancements in the wet season over these wetlands in clear sky conditions. This is another important finding in this thesis.

Upon validating the GOSAT data in the Amazon and discovering that it has the power to observe seasonal and regional variations across the entire Amazon Basin, the data is then used to assess the underlying emissions inventories which are used by the chemistry transport model GEOS-Chem in the Amazon. The aim: to determine whether or not GOSAT and GEOS-Chem observe differences in $XCH_4$ which could provide important information to improve the emissions inventories which models like GEOS-Chem utilise, ultimately to retrieve $CH_4$ fluxes and improve our knowledge of global methane sources. The model is sampled at GOSAT sounding times and locations, is converted from profiles into $XCH_4$ and is compared with the in situ aircraft profiles. GEOS-Chem $XCH_4$ is found to be considerably lower than the aircraft $XCH_4$, ranging from as much as 26.0 ppb lower at Santarém to 7.3 ppb lower at Alta Floresta. A special tagged tracer run of the GEOS-Chem model was conducted and analysis concluded that $XCH_4$ concentrations in the Amazon are significantly impacted by emissions originating in Northern Africa. Concentrations over the Atlantic ocean are further seen to be considerably lower from GEOS-Chem compared to with GOSAT, by between a monthly average of approximately 11–24 ppb. A background correction is then calculated for the GEOS-Chem data based upon this monthly-varying average difference between GEOS-Chem and GOSAT $XCH_4$ to remove the biases between the two which are seen in the

incoming background air before it reaches the Amazon (since this study focuses exclusively on South America).

Comparison between the background-corrected GEOS-Chem $XCH_4$ and the GOSAT $XCH_4$ show that, in general, the seasonality between the wet and the dry seasons looks similar between GOSAT and GEOS-Chem, however there are some large differences (of more than $\pm$15 ppb). For every year from 2010 to 2014 the seasonality seen by GOSAT was larger (in magnitude) than that of GEOS-Chem, especially in the region containing the Bolivian wetlands. The largest differences observed by GOSAT between the wet and the dry seasons are for 2011, which agrees well with observations stated by Gatti et al. (2014) that this was an anomalously wet year. In the dry seasons, GEOS-Chem values are noticeably more pronounced than GOSAT in the southern Amazon and over the Pantanal wetlands for 2010 and 2011. This is interesting because 2010 was an anomalously dry year in the Amazon (Gatti et al., 2014) and less rainfall would result in less wetland $CH_4$ emission. It is possible that this was not correctly attributed in the model, resulting in $XCH_4$ emissions being higher than those seen by GOSAT in 2010, which could have had a knock-on effect on the beginning of 2011. In the wet seasons it is more difficult to pick out systematic differences between them for 2010–2012, however GOSAT $XCH_4$ concentrations are considerably higher (approximately 15–30 ppb) in the Bolivian wetland region in 2013 and 2014. These findings suggest that either the modelled transport or the emissions inventories are incorrectly representing $CH_4$ sources and fluxes in the Amazon. Bloom et al. (2016) explain that their methods to determine emissions in densely vegetated wetland areas such as in the Amazon are ill-equipped for these regions and that they therefore anticipate errors in seasonal and inter-annual variability to be larger within densely vegetated wetland areas like the Amazon. GOSAT $XCH_4$ should therefore be able to help by providing accurate $CH_4$ measurements in these poorly understood regions.

Differences in the seasonal magnitude and spatial locations of $XCH_4$ concentrations between GEOS-Chem and GOSAT have highlighted that GOSAT (which agreed better with the in situ data than GEOS-Chem did) can be used to call attention to the shortcomings in the model, which are either a result of the model

transport or of the underlying emissions inventories. The aim of Chapter 6 was to develop a simulation system which can use different emission databases and produce high resolution atmospheric $XCH_4$ data which can be assessed against satellite data. This simulation system was successfully developed using the numerical atmospheric-dispersion modelling environment, NAME, to calculate the high resolution transport of $CH_4$ on a regional scale, and uses emissions inventories to calculate $CH_4$ enhancements in this region. This system was designed for a comparison with GOSAT data and was tested using the same emissions inventories used in the GEOS-Chem model, for all GOSAT soundings in the Amazon in 2011. These results were compared with GOSAT, GEOS-Chem, and the MACC-II model (which assimilates in situ data). The $XCH_4$ calculated in these simulations using NAME compare favourably with the other datasets (the difference between GOSAT and the NAME modelled $XCH_4$ ranged from 2.22 ppb to 15.95 ppb over the regions studied, whilst GEOS-Chem $XCH_4$ differed by between 8.67 ppb and 26.02 ppb from GOSAT, and MACC-II $XCH_4$ differed from GOSAT $XCH_4$ by between 1.8 ppb and 16.67 ppb). The seasonal cycle was also well represented by the NAME simulated results, with higher concentrations in the wet season in regions where the emission inventories suggest such enhancements should be, and with enhanced values in the northern Amazon in the dry season as were also seen by GOSAT previously. The enhancements in $XCH_4$ calculated from emissions in the Amazon bring the results into better agreement with GOSAT concentrations in terms of their magnitude and seasonality than with just the background values alone, showing that the model provides meaningful results and is working well.

Typically the NAME simulated $XCH_4$ concentrations, GEOS-Chem and MACC-II are all lower than GOSAT $XCH_4$, but the concentrations from the NAME simulations are closest to those of the satellite in the northern Amazon and across the Amazon Basin as a whole. Across all subregions in the Amazon, the concentrations from the NAME simulations were rarely found to be highest or lowest (monthly averages) of any of the four datasets, showing that the model is consistently performing well. The NAME simulations are also found to be in better agreement (with GOSAT) concerning seasonality than both of the other two

models in the two in-land regions studied, whilst they outperform GEOS-Chem at four out of five regions in this respect. Overall, the NAME simulations show less variability in their agreement with GOSAT than GEOS-Chem and MACC-II do; suggesting a better agreement overall with the seasonality observed by GOSAT.

In conclusion, the high-resolution NAME simulation system is working well. These results show that the use of such a system in conjunction with the newly validated GOSAT data can highlight shortcomings of different emissions inventories which I have shown (in the case of GEOS-Chem) are lacking seasonality which is observed by GOSAT. The good performance of the NAME simulated results when compared to GOSAT, coupled with the good agreement between GOSAT $XCH_4$ and in situ data in the Amazon, shows that the simulation system and GOSAT both have the capability to inform useful insights into Amazonian wetland emissions. These are the main results of this thesis: The successful first validation of GOSAT $XCH_4$ data in the Amazon, and both the development of, and demonstration that, a high-resolution transport model can to used in conjunction with emissions databases on a regional scale to help improve these databases through comparison with this newly validated GOSAT data.

## 7.1 FUTURE WORK

The next step of this research would be to perform the NAME simulations using different emission inventories, especially the ones utilised by the MACC-II model. This would allow a direct comparison between the two emissions inventories using the same background $XCH_4$ and the same transport model, allowing for an assessment into which emissions agree best with the GOSAT data and where. It would also be interesting to use the JULES emissions which, contrary to Bloom wetland emissions, are calculated using a bottom-up approach (Clark et al., 2011). Additionally, the GEOS-Chem model can be used to calculate the background $XCH_4$ instead of MACC-II. In this case the main differences between

the GEOS-Chem model output and the NAME simulated outputs would be a result of the modelled transport. If these two results proved similar it would reinforce the conclusion that GEOS-Chem $XCH_4$ concentrations are lower than in situ measurements in the Amazon due to the background $XCH_4$ from outside of the Amazon.

Ultimately these comparisons have the potential to inform where the emissions inventories are lacking in understanding in either the magnitude of their seasonal emissions or in their spatial variation. These differences could be compared with drivers such as precipitation, soil moisture and temperature to advance our current understanding into how these impact wetland emissions across the Amazon.

The Sentinel 5 Precursor satellite is due to be launched in September 2017 and will be able to accurately measure $XCH_4$ in the SWIR with the TROPOMI spectrometer (TROPOspheric Monitoring Instrument) (Butz et al., 2012). This instrument should be able to map $CH_4$ with approximately 7 million exposures per day with a ground pixel area of $7 \times 7$ km$^2$. This satellite will be able to carry forward $XCH_4$ measurements currently made by GOSAT with a similar accuracy, but with considerably more soundings, each with more likelihood of avoiding cloud than the larger GOSAT ground pixels. These observations would be of considerable benefit in the Amazon for use in evaluating $CH_4$ emissions inventories, and the NAME simulation system could easily be run for use with these measurements for such a purpose.

# LIST OF FIGURES

Figure 1.1 Global mean land-ocean temperature since 1880, with respect to a 1951-1980 base period. The dotted black line shows the annual mean, the solid red line shows a five year mean, and the green bars show the uncertainty estimate. Data is from the GISS (Goddard Institute for Space Studies) Surface Temperature Analysis (GISTEMP) project (http://data.giss.nasa.gov/gistemp/). . . . . 2

Figure 1.2 A graph showing a typical atmospheric temperature profile in Kelvin from the surface to 100 km altitude. The plot also displays the pressure profile in mb, ranging from approximately 0 mb at the top of the atmosphere to approximately 1000 mb at the surface. The profile is split into four parts which are named in boxes, whilst the names for the three transitions are written at these levels in italics (Image source www.atmos.washington.edu/~hakim/301/climo_sounding.png). . . . . 6

Figure 1.3 The radiative forcing (RF) in W $m^{-2}$ of climate change during the Industrial Era (1750 to 2011) for separate components including carbon dioxide ($CO_2$), methane ($CH_4$), nitrogen dioxide ($N_2O$), hydrofluorocarbons (HFCs), perfluorocarbons (PFCs), sulphur hexafluoride ($SF_6$), carbon monoxide (CO), non-methane volatile organic compounds (NMVOCs), ammonia ($NH_3$), sulphur dioxide ($SO_2$), ozone ($O_3$) and water vapour ($H_2O$). Horizontal bars indicate the overall uncertainty (90% confidence) whilst vertical bars are for individual components (vertical bar lengths proportional to the relative uncertainty, with the total length equal to the bar width for a $\pm$50% uncertainty). The ERF column shows the effective radiative forcing due to aerosol-cloud interactions (Stocker et al., 2013). . . . . 9

Figure 2.1 Schematic showing the fluxes and reservoirs involved with the $CH_4$ cycle in Tg $CH_4$ $yr^{-1}$ and Tg $CH_4$ respectively. These have been calculated for the time period 2000 to 2009. The black arrows denote natural fluxes, the red arrows denote anthropogenic fluxes and the brown arrow represents a combination of both natural and anthropogenic fluxes. The atmospheric reservoir is represented by two numbers; the pre-industrial inventory in black and the increase between 1750 and 2011 given in red (Ciais et al., 2014). . . . . 16

Figure 2.2 Amazonian wetland classes mapped during the (a.) dry season (October to November 1995) and the (b.) wet season (May to June 1996) by Hess et al. (2015). Black areas show non-wetland, whilst grey areas show areas within the Amazon Basin which are higher than 500 m in elevation. . . . . 19

Figure 2.3 Schematic showing the production, consumption and transfer of $CH_4$ at the atmosphere in rice fields from Le Mer and Roger (2001) (Figure 1). . . . . 20
Figure 2.4 Illustration showing the geological production and release of $CH_4$ from volcanic (geothermal) areas and hydrocarbon basins (Etiope and Klusman, 2002). . . . . 25
Figure 2.5 The principle reactions in the oxidation of atmospheric $CH_4$ into $CO_2$ and $H_2O$ (Cicerone and Oremland, 1988). . 28
Figure 2.6 Showing ice core records for the concentrations of $CO_2$, $CH_4$ and $N_2O$ over ten thousand years up until the year 1900 (Ciais et al., 2014). . . . . 30
Figure 2.7 Time series of the globally averaged $CH_4$ concentration in ppb, from 1983 to September 2016. Showing the globally averaged monthly mean values in red, (centred on the middle of each month); and the long-term trend (similar to a 12-month running mean) in black, where the average seasonal cycle has been removed. This Figure is from the National Oceanic and Atmospheric Administration (NOAA), Earth System Research Laboratory (`www.esrl.noaa.gov/gmd/ccgg/trends_ch4/`). . . . . 31
Figure 3.1 Illustration of the four fundamental modes of vibration for the $CH_4$ molecule. . . . . 35
Figure 3.2 Illustration of possible radiation paths between the Sun and a satellite. Some interacting with aerosols and clouds to shorten or lengthen the path length compared to the non-scattered case (path 1). . . . . 37
Figure 3.3 Diagram to illustrate the scattering angle $\theta$. . . . . 39
Figure 3.4 Diagram representing the directions of scattered radiation for Rayleigh scattering. The relative lengths of the arrows represent the relative amount of radiation scattered in each direction. . . . . 39

Figure 3.5 A diagram showing the relative directions of scattering radiation for the Mie scattering approximation, (the radiation is incident from the left and so there is more radiation scattered in a forward direction; to the right). The relative lengths of the arrows represent the relative amount of radiation scattering in each direction. . . . . 40

Figure 3.6 Graph showing intensity against scattering angle for Mie (solid dotted line) and Rayleigh scattering. It can be seen than when $\theta = 0^{\circ}$, the scattering is dominated by Mie scattering showing that larger particles (with respect to the incident wavelength) have larger values of $g$ (Mumford, 2000). . . . . 41

Figure 3.7 Part A (top): Showing the aerosol optical thickness at 865 nm over the Earth's water surfaces, and part B (bottom), showing the anstrom exponent. Both measured by the POLDER radiometer aboard the ADEOS satellite (Buseck and Schwartz, 2003). . . . . 44

Figure 3.8 Global sampling locations of instruments measuring $CH_4$ in 2009 from the ground, from towers, and with aircraft (`www.esrl.noaa.gov/gmd/ccgg/globalview/ch4/ch4_sites.html`). . . . . 49

Figure 3.9 Global sampling locations of instruments measuring $CO_2$ in 2013 from the ground, from towers, and with aircraft (`www.esrl.noaa.gov/gmd/ccgg/globalview/co2/co2_observations.html`). . . . . 50

Figure 3.10 Example image from the TANSO-CAI instrument on-board GOSAT. Showing the eruption of the Eyjafjallajökull volcano in Iceland in 2010. . . . . 52

Figure 3.11 Schematic of a Michelson interferometer as used for a Fourier transform spectrometer with a double pendulum design such as for GOSAT (NIES, 2009). . . . . 53

Figure 3.12 Simulated spectral coverage of TANSO-FTS. (a) The SWIR region showing bands 1, 2 and 3. (b) The TIR region showing band 4 (Kuze et al., 2009). . . . . 54
Figure 3.13 Example atmospheric spectra measured by GOSAT for bands 1, 2 and 3, indicating the regions where oxygen, carbon dioxide and methane absorption are prominent (Japan Aerospace Exploration Agency, 2009). . . . . 55
Figure 3.14 GOSAT sampling patterns for the 1st, 2nd and 3rd day of each month in 2010. . . . . 56
Figure 3.15 Example of the GOSAT 3-point CT scanning pattern for the usual case (left) and the newer dithering case (from 2014), on the right. . . . . 57
Figure 3.16 Showing the three SWIR GOSAT TANSO-FTS bands with example Jacobians for $CH_4$ at each band (Cogan, 2013). . 59
Figure 3.17 Correlation plot showing the $CH_4$ measured by GOSATv6 vs that measured by the TCCON ground based sites. The data was matched so that the GOSAT measurements were required to be within $\pm 5^{\circ}$ of the TCCON site and within two hours of the measurement taken by TCCON. The different TCCON sites are colour coded as given in the figure (Parker et al., 2015). . . . . 67
Figure 3.18 Map showing the location of current, future and past TCCON site locations in 2014 (Wunch et al., 2011). . . . . 67
Figure 4.1 Top: The aircraft used to perform measurements for the Amazonian Carbon Observatory project. Bottom left: Close-up of the air inlet. Bottom right: Air collection flasks and control box. . . . . 70
Figure 4.2 120-hour back-trajectories from Rio Branco at 4.5 km on the 28th July 2011 at 14:00 UTC; calculated using the HYSPLIT model. . . . . 71

Figure 4.3 ACO aircraft profiles between January and August 2013 at Rio Branco, showing $CO_2$ on the left in ppm, $CH_4$ in the middle in ppb, and CO on the right, also in ppb. . . . . 72
Figure 4.4 ACO aircraft profiles between January and August 2013 at Salinópolis, showing $CO_2$ on the left in ppm, $CH_4$ in the middle in ppb, and CO on the right, also in ppb. . . . . 73
Figure 4.5 Amazonian Carbon Observatory aircraft measured $CH_4$ vertical concentration profiles taken between 2013 and June 2015 at Rio Branco and Salinópolis. Profiles measured between January-April are shown in blue, July-October in red, and May-June and November-December in grey. . . . . 74
Figure 4.6 Map showing the locations of AMAZONICA sites Rio Branco (RBA), Tabatinga (TAB), Alta Floresta (ALF) and Santarém (SAN) as blue circles, in addition to ACO sites Rio Branco (RBH) and Salinópolis (SAH) as black triangles. Additionally the ground-based TCCON site at Manaus (MAN) and TCCON-like site at Paramaribo (PAR) are also shown as blue crosses. . . . . 75
Figure 4.7 ECMWF temperature profiles at Salinópolis for 11 flight dates, showing the calculated tropopause height in red and the NCEP tropopause height in blue. . . . . 77
Figure 4.8 Histograms showing the difference between the calculated tropopause height and that given by NCEP for every flight date at each of the six aircraft sites. . . . . 78
Figure 4.9 Map showing modelled $XCH_4$ data in ppb from the TOMCAT model, at 68.13 hpa (approximately 18.6 km) for January 2010. . . . . 79

Figure 4.10 $CH_4$ profiles from the TOMCAT model (in red) sampled at six TCCON sites (Lamont, Parkfalls, Bremen, Izana, Garmisch and Tsukuba), for May 2009. Compared with the TCCON apriori profiles for the same month in magenta; and with ACE-FTS satellite profiles (in blue) for the same month and sampled within $\pm 5^\circ$ of the TCCON site. Uncertainties in the TOMCAT profile are not shown, whilst those of the TCCON and ACE profiles are displayed. 80

Figure 4.11 Monthly average TOMCAT $CH_4$ profiles sampled at the locations of eight Aircore balloons launched in 2012. Since the balloons drift, GOSAT is sampled at the latitude and longitude which the balloons were each at upon reaching 10 km asl, since I am only interested in the stratosphere for this comparison. On the $14^{th}$ and $15^{th}$ of January 2012 there were two balloons released on each day, labelled here as balloons 1 and 2 for each date. TOMCAT is shown in red and the Aircore profiles in blue. . 81

Figure 4.12 TOMCAT $CH_4$ profiles for May 2009 (in red) compared with every ACE-FTS profile from this month which was made within $\pm 20^\circ$ of the equator, in blue. The latitudes and longitudes of these profiles are displayed on the figure and the y-axis extends from 35 kpa (approximately 8.1 km) to the top of the atmosphere. . . . . 82

Figure 4.13 An example extended aircraft profile with pressure levels in blue. The calculated upper (red) and lower (green) pressure levels corresponding to a pressure layer centred on the original level are shown. . . . . 87

Figure 4.14 Example of the extended aircraft profile for the ACO flight at Rio Branco on the 16th August 2014. The left panel shows the measured aircraft profile. The middle and right panels show the final complete profile with altitude and pressure on the y-axis respectively. On the right panel, the percentage contribution to the $XCH_4$ from each part is displayed (these are average values for all of the RBH extended profiles). . . . . 89

Figure 4.15 Monthly histograms of 2012 showing the difference in $XCH_4$ (partial column between 4.5 km and the tropopause) as measured by a high resolution model output (MACC ERA-Interim) and by assuming a constant $CH_4$ concentration throughout this region given by the model value at 4.5 km. The model was sampled for each day and at each grid-box within $\pm 5^\circ$ of Rio Branco, resulting in approximately 2400 comparisons per month. The solid red line marks a difference of zero ppb whilst the dotted red line marks the mean difference for that month. The numbers in red indicate the number of occurrences either side of zero. . . . . 91

Figure 4.16 Monthly histograms of 2012 showing the difference in $XCH_4$ (partial column between 7.5 km and the tropopause) as measured by a high resolution model output (MACC ERA-Interim) and by assuming a constant $CH_4$ concentration throughout this region given by the model value at 7.5 km. The model was sampled for each day and at each grid-box within $\pm 5^\circ$ of Rio Branco, resulting in approximately 2400 comparisons per month. The solid red line marks a difference of zero ppb whilst the dotted red line marks the mean difference for that month. The numbers in red indicate the number of occurrences either side of zero. . . . . 92

Figure 4.17 The median absolute deviation of (left), and median of (right) the difference in partial $XCH_4$ column (from 4.5 km to the tropopause (blue) or 7.5 km to the tropopause (red)) between a model $CH_4$ profile and a linear extrapolation method (based on the model $CH_4$ concentration at either 4.5 or 7.5 km). The model has been sampled for each day and each grid-box within $\pm 5^\circ$ of a target location to generate approximately 2400 difference values per month from which to calculate the monthly median absolute deviations and medians for 2012. The locations studied are Alta Floresta (marked by crosses), Rio Branco (marked by squares), Santarém (marked by circles), and Tabatinga (marked by triangles). . . . . 94

Figure 4.18 Comparison of TOMCAT (black) monthly mean profiles sampled at six TCCON sites for January 2011, and coincident ($\pm 5^\circ$ and same month) ACE-FTS profiles (blue). The TOMCAT profile has been shifted by $\pm 1$ km and plotted in red to indicate the scale of the uncertainty placed on the stratosphere in this analysis. . . . . 95

Figure 4.19 Time series showing the difference in daily averaged GOSAT Proxy $XCH_4$ when calculated using the usually employed model ensemble $XCO_2$ and when using GEOS-Chem alone for the $XCO_2$ (ensemble minus GEOS-Chem). GOSAT data are used within $\pm 5^\circ$ of the four AMAZONICA sites and two ACO sites. Red data show GOSAT daily averaged results with the daily standard deviation used for the error bars. The black line shows the daily mean value. The yearly mean value is displayed above the x-axes for all years of full data. . . . . 98

Figure 4.20 Time series showing daily averaged GOSAT $XCH_4$ (red) with error bars representing the standard deviation of data for each day. Extended aircraft $XCH_4$ is shown in blue. The approximate wet and dry seasons in the Amazon are displayed on the figure with 'W' and 'D' markers, respectively. . . . . 100

Figure 4.21 Ensemble of back-trajectories from the HYSPLIT model for Rio Branco, released from 4.5 km for 120 hours. The top row in order left to right show the four flight dates with the highest $XCH_4$ measurements in 2010-2011 in order starting with the highest. The bottom row shows trajectories for the four dates with the lowest $XCH_4$ values starting with the lowest. . . . . 101

Figure 4.22 Correlation plot to illustrate the data shown in Table 4.1 for the case when the co-location criteria is $\pm 5$ degrees. Showing the GOSAT $XCH_4$ on the y-axis versus the aircraft $XCH_4$ on the x-axis for the four AMAZONICA sites and two ACO sites. The black dotted line shows the one to one correlation line. The red dashed line shows the result of a linear regression with the slope set to one. From this the offset values given in Table 4.1 are the difference in intercept of each line on the y-axis, giving the mean offset between GOSAT and aircraft $XCH_4$. . . . . 102

Figure 4.23 Correlation plot showing the aircraft $XCH_4$ on the x-axis versus the average GOSAT $XCH_4$ (for the same day, within $\pm 5^\circ$ of the site) and on the y-axis for the four AMAZONICA sites and two ACO sites. The black dotted line shows the one to one correlation line. The dashed lines show the result of a linear regression with the slope set to one, for all of the flights (in black), for only flights in the dry season in red and for only flights in the wet season in blue. The intercept values quoted are the difference in intercept of each line on the y-axis (colour-coded by season). The correlation coefficients (r-values) are also quoted, along with the number of flights and the corresponding averaged GOSAT soundings. . . . . 105

Figure 4.24 Monthly histograms of 2012 showing the difference in $XCO_2$ (partial column between 7.5 km and the tropopause) as measured by a high resolution model output (MACC-II v13r $CO_2$) and by assuming a constant $CO_2$ concentration throughout this region given by the model value at 7.5 km. The model was sampled for each day and at each grid-box within $\pm 5^\circ$ of Rio Branco, resulting in approximately 2400 comparisons per month. The solid red line marks a difference of zero ppm whilst the dotted red line marks the mean difference for that month. The numbers in red indicate the number of occurrences either side of zero. . . . . 108

Figure 4.25 Correlation plot to illustrate the data shown in Table 4.2 for the case when the co-location criteria is ±5 degrees. Showing the GEOS-Chem model $XCO_2$ on the y-axis versus the aircraft $XCO_2$ on the x-axis for the four AMAZONICA sites and two ACO sites. The black dotted line shows the one to one correlation line. The red dashed line shows the result of a linear regression with the slope set to one. From this the offset values given in Table 4.2 are the difference in intercept of each line on the y-axis, giving the mean offset between the model and aircraft $XCO_2$. . . . . 111

Figure 4.26 Showing comparisons between Paramaribo-FTS (black) and GOSAT (red) for $XCH_4$. The lighter shaded scatter points show all of the Paramaribo-FTS data between 2009 and 2013 and all GOSAT until the end of 2013 which is within ±5° of the site. The average of Paramaribo-FTS data (standard deviation given in y-direction error bars) for each campaign period (shown in x-direction error bars) and coincident GOSAT within the same time period is averaged and also plotted. . . . . 112

Figure 5.1 $XCH_4$ concentration in parts per billion against the date of measurements for daily averaged GEOS-Chem sampled at GOSAT soundings within ±5° of the aircraft sites in red (error bars representing the standard error), and extended aircraft $XCH_4$ in blue. The approximate dry seasons (July–October) and wet seasons (January–April) are marked with D and W respectively. . . . . 119

Figure 5.2 Correlation plot showing GEOS-Chem $XCH_4$ on the y-axis versus the aircraft $XCH_4$ on the x-axis for the four AMAZONICA sites and two ACO sites. The black dotted line shows the one to one correlation line. The red dashed line shows the correlation line when the gradient is set to one. From this the offset values given in Table 5.1 are the difference in intercept of each line with the y-axis, giving the mean offset between GEOS-Chem and aircraft $XCH_4$. . 121

Figure 5.3 Time series of the difference between GEOS-Chem and aircraft $XCH_4$ in ppb (GEOS-Chem minus aircraft) with GEOS-Chem sampled at GOSAT sounding locations within $\pm 5^\circ$ and same day co-location of the flights. . . . . 122

Figure 5.4 GOSAT Proxy $XCH_4$ v6 UoL retrieval (in ppb) averaged for 2011. The data is plotted to a $2^\circ \times 2^\circ$ grid. . . . . 124

Figure 5.5 GOSAT Proxy $XCH_4$ v6 UoL retrieval (in ppb). Showing averages for the Northern Hemisphere seasons, December-February, March-May, June-August and September-November for the years 2009 to 2014 (winter seasons at the beginning of the year and using December from the previous year). The data is plotted to a $2^\circ \times 2^\circ$ grid. . . . . 125

Figure 5.6 Monthly averaged GOSAT $XCH_4$ for 2009. The data is plotted to a $2^\circ \times 2^\circ$ grid. . . . . 126

Figure 5.7 Monthly averaged GOSAT $XCH_4$ for 2010. The data is plotted to a $2^\circ \times 2^\circ$ grid. . . . . 126

Figure 5.8 Monthly averaged GOSAT $XCH_4$ for 2011. The data is plotted to a $2^\circ \times 2^\circ$ grid. . . . . 127

Figure 5.9 Monthly averaged GOSAT $XCH_4$ for 2012. The data is plotted to a $2^\circ \times 2^\circ$ grid. . . . . 127

Figure 5.10 Monthly averaged GOSAT $XCH_4$ for 2013. The data is plotted to a $2^\circ \times 2^\circ$ grid. . . . . 128

Figure 5.11 Monthly averaged GOSAT $XCH_4$ for 2014. The data is plotted to a $2^\circ \times 2^\circ$ grid. . . . . 128
Figure 5.12 GOSAT $XCH_4$ averaged for the wet seasons (January-April) and dry seasons (July-October) in 2010 to 2014. The third row shows the difference (wet season minus dry season) for the seasons in each year. The data is plotted to a $2^\circ \times 2^\circ$ grid. . . . . 130
Figure 5.13 GOSAT $XCH_4$ averaged for the 2009 dry season (July–October). The locations of the aircraft and Paramaribo-FTS sites are shown, in addition to the Manaus TCCON site, MAN. The five regions referred to in the text are also shown. The data is plotted to a $2^\circ \times 2^\circ$ grid. . . . . 131
Figure 5.14 Time series of monthly averaged GOSAT $XCH_4$ (in ppb) calculated from all cloud-free soundings coincident within the five sub-regions in the Amazon, as specified by Figure 5.13. Region 1 (the North Amazon) is given by the red line, region 2 (West-Central Amazon) by the green line, region 3 (East-Central Amazon) by the magenta line, region 4 (South-West Amazon) by the blue line, and region 5 (South-East Amazon) by the cyan line. . . . . 132
Figure 5.15 Maps showing the $XCH_4$ contributions from April 2010 to five different regions on May 1st 2010. The contributions are given for 11 TRANSCOM regions used in the tagged tracer run, which are coloured according to their contribution. The five geographical regions considered are bordered by black rectangles. . . . . 134

Figure 5.16 Stacked time series showing the contribution of $XCH_4$ from each month in 2010 to the first day of the next month from five of the TRANSCOM regions (Tropical South America in gold, Temperate South America in magenta, Northern Africa in cyan, Southern Africa in red, Australia in green), and the sum of the others (in blue). The five regions (labelled 1-5 in Figure 5.13 are displayed with 1-3 on the top row and 4 and 5 on the second row (both left to right). . . . . 136

Figure 5.17 GOSAT and GEOS-Chem $XCH_4$ distributions for the 2009 dry season (July–October) and 2010 wet season (January–April) with difference plots. Dry minus wet season difference plots are in column three on rows one and two, and are represented by the lowermost colour bar. The bottom row is the GOSAT minus GEOS-Chem $XCH_4$ field, and in column three is the difference between these two difference plots. All plotted to a $2^\circ \times 2^\circ$ grid. . . 137

Figure 5.18 Surface altitude at GOSAT sounding locations shown as monthly averages for 2010 and plotted on a $2^\circ \times 2^\circ$ grid. . 138

Figure 5.19 Showing the monthly varying correction between GOSAT and GEOS-Chem for the case where all of the GOSAT values between 20°N, 30°S, 90°W and 20°W are used in blue, and in black where just values over the Atlantic Ocean between $\pm 4^\circ$ of the equator are used. The black crosses represent measurements in the Atlantic Ocean correction where there are less than 10 grid boxes that contain GOSAT data (72 total). The uncertainties shown represent the standard deviation of the data. . . . . 139

Figure 5.20 Time series of monthly averaged GEOS-Chem $XCH_4$ (in ppb) calculated by sampling at the locations of all cloud-free GOSAT soundings coincident within the five sub-regions in the Amazon, as specified by Figure 5.13. Region 1 (the North Amazon) is given by the red line, region 2 (West-Central Amazon) by the green line, region 3 (East-Central Amazon) by the magenta line, region 4 (South-West Amazon) by the blue line, and region 5 (South-East Amazon) by the cyan line. . . . . 140

Figure 5.21 Time series of monthly averaged GEOS-Chem $XCH_4$ (with the background correction applied) calculated by sampling at the locations of all cloud-free GOSAT soundings coincident within the five sub-regions in the Amazon, as specified by Figure 5.13. Region 1 (the North Amazon) is given by the red line, region 2 (West-Central Amazon) by the green line, region 3 (East-Central Amazon) by the magenta line, region 4 (South-West Amazon) by the blue line, and region 5 (South-East Amazon) by the cyan line. . . . . 141

Figure 5.22 Time series showing the monthly averaged GOSAT $XCH_4$ minus GEOS-Chem $XCH_4$ (with the background correction applied) calculated from all cloud-free GOSAT soundings coincident within the five sub-regions in the Amazon, as specified by Figure 5.13, and using GEOS-Chem model values sampled at these locations. Region 1 (the North Amazon) is given by the red line, region 2 (West-Central Amazon) by the green line, region 3 (East-Central Amazon) by the magenta line, region 4 (South-West Amazon) by the blue line, and region 5 (South-East Amazon) by the cyan line. . . . . 142

Figure 5.23 GOSAT and GEOS-Chem $XCH_4$ distributions for the 2009 dry season (July–October) and 2010 wet season (January–April) with difference plots. Dry minus wet season difference plots are in column three on rows one and two, and are represented by the lowermost colour bar, except with twice the range. The bottom row is the GOSAT minus GEOS-Chem $XCH_4$ field, and in column three is the difference between these two difference plots. The locations of the aircraft and Paramaribo-FTS sites are shown, in addition to the Manaus TCCON site, MAN. All plotted to a $2^\circ \times 2^\circ$ grid. . . . . 144

Figure 5.24 The Bloom wetland $CH_4$ emissions used in the GEOS-Chem model, for March 2010. Plotted to a $2^\circ \times 2^\circ$ grid. . . . . 145

Figure 5.25 Showing GOSAT and GEOS-Chem $XCH_4$ distributions for multiple dry seasons (July–October) with difference plots. 147

Figure 5.26 Showing GOSAT and GEOS-Chem $XCH_4$ distributions for multiple wet seasons (January–April) with difference plots. 148

Figure 5.27 GEOS-Chem $XCH_4$ averaged for the wet seasons (January-April) and dry seasons (July-October) in 2010 to 2014. The third row shows the difference (wet season minus dry season) for the seasons in each year. The data is plotted to a $2^\circ \times 2^\circ$ grid. . . . . 149

Figure 5.28 Showing the difference between GOSAT and GEOS-Chem $XCH_4$ distributions for consecutive dry seasons (July–October). . . . . 151

Figure 5.29 Showing the difference between GOSAT and GEOS-Chem $XCH_4$ distributions for consecutive wet seasons (January–April). . . . . 152

Figure 6.1 Maps showing the daily averaged location of released tracer particles for each day during a 10-day back-trajectory from the location of a GOSAT sounding (marked by the red cross) on January 1st 2011 at 15:33 UTC. The NAME model domain over which trajectories are tracked is shown by the black outlined rectangle which is approximately 5° smaller in all directions than the total area of map plotted. The data are plotted on a logarithmic scale with the unit as a dosage in g s $m^{-3}$ which can be difficult to consider by itself. Importantly the run represents the release of a finite number of particles during a one second period, so the relative dosage of particles at each location is best to consider. . . 159

Figure 6.2 The mean location of incoming air sampled at Rio Branco (top row) and Salinópolis (bottom row). This is the seasonal average location of air 7 days before reaching the site at 7.5 km altitude. The left column represents an average over the wet season (Jan-Apr) and the right column represents the dry season (Jul-Oct). The data shown is a normalized particle dosage in $gsm^{-3}$ resulting from a 1 g release of particles at midday for every day in 2011, utilizing the NAME Numerical Atmospheric-dispersion Modeling Environment to calculate back-trajectories based on meteorological data to track the particles back 7 days. The locations of the aircraft sites, RBA (Rio Branco AMAZONICA), RBH (Rio Branco ACO), SAH (Salinópolis), ALF (Alta Floresta), SAN (Santarém), TAB (Tabatinga) are shown; in addition to the Paramaribo-FTS site (PAR), and Manaus TCCON site (MAN). . . . . 160

Figure 6.3 Maps showing the daily averaged location of released tracer particles for each day during a 10-day back-trajectory from the location of a GOSAT sounding (marked by the red cross) on January 1st 2011 at 15:33 UTC. The NAME model domain over which trajectories are tracked is shown by the outermost outlined rectangle, whilst the inner rectangle is in by one grid box. This outermost ring of pixels are the boundary grid boxes used for the background calculation. This figure is directly comparable to Figure 6.1, except this is on the lower grid resolution to match with the MACC-II model. . . . . 162

Figure 6.4 The percentage of tracer particles to reach each of the boundary grid boxes for a 10-day NAME back-trajectory originating from the same GOSAT sounding location on January 1st 2011 at 15:33 UTC as in Figures 6.1 and 6.3. . . 162

Figure 6.5 Maps of MACC-II $XCH_4$ for each of the days up to 10 days before the GOSAT sounding on January 1st 2011 (at the location of the red cross). The average of these 10 days of MACC-II is also shown, and the positions of the grid boxes on the boundary of the NAME modelled domain are shown. 163

Figure 6.6 Emission inventories for the 1st December 2010 for GFED, EDGAR, geological sources, oceans, a soil sink term, termites, and Bloom. The values are given as percentages of the total emissions per grid box and is intended to display the relative contribution of each emission type in each grid-box. For example, ocean emissions contribute to approximately 100% of the total emissions for the grid-boxes over ocean. Also shown are maps of the total emissions, and of the total of everything excluding Bloom. These total emissions are normalised to a scale between 0 and 100, where 100 represents the highest global emission (out of all grid-boxes); although only the data between 0 and 2.5% of this are plotted, otherwise extremely high point sources in EDGAR dominate these maps. . . . . 166

Figure 6.7 Monthly averaged Bloom wetland emissions for 2011 plotted as a percentage of the total emissions from all sources in each grid box. . . . . 167

Figure 6.8 EDGARv4.2 anthropogenic emissions for 2010 plotted as a percentage of the total emissions from all sources in each grid box. . . . . 168

Figure 6.9 Monthly averaged GFEDv4 fire emissions for 2011 plotted as a percentage of the total emissions from all sources in each grid box. . . . . 169

Figure 6.10 Monthly averages of the total of all seven emission inventories for 2011 (with 2010 EDGAR data) plotted as a percentage from 0% to 2.5% of the highest emission value in the Amazon. . . . . 169

Figure 6.11 The calculated background from MACC-II at each GOSAT sounding location for 2011, averaged monthly on a $2^\circ \times 2^\circ$ grid. . . . . 171

Figure 6.12 The calculated enhancement in $XCH_4$ seen at GOSAT sounding locations in 2011 from the interaction of incoming air with emission inventories over a 10-day period. The values are averaged for each month and plotted on a $2^\circ \times 2^\circ$ grid. . . . . 172
Figure 6.13 Monthly averaged $XCH_4$ calculated by the NAME model simulation at GOSAT sounding locations for 2011 and plotted onto a $2^\circ \times 2^\circ$ grid. . . . . 172
Figure 6.14 Monthly averaged maps for 2011 showing the difference between $XCH_4$ calculated using the NAME based model and $XCH_4$ from GOSAT, plotted on a $2^\circ \times 2^\circ$ grid. . . . . 173
Figure 6.15 Monthly averaged maps for 2011 showing the difference between $XCH_4$ calculated using the NAME based model and $XCH_4$ from GEOS-Chem, sampled at GOSAT sounding locations and plotted on a $2^\circ \times 2^\circ$ grid. . . . . 174
Figure 6.16 Monthly averaged maps for 2011 showing the difference between $XCH_4$ calculated using the NAME based model and $XCH_4$ from MACC-II, sampled at GOSAT sounding locations and plotted on a $2^\circ \times 2^\circ$ grid. . . . . 175
Figure 6.17 Time series showing monthly averages of modelled and measured $XCH_4$ at GOSAT sounding locations in the Amazon for 2011. The averaged area is for the NAME modelled domain (14°N–34°S, 90°W–18°W). In blue is the total $XCH_4$ as described in this chapter (blue dashed line is background component alone), in red is GOSAT $XCH_4$, in black is GEOS-Chem $XCH_4$ and in cyan MACC-II $XCH_4$. . . . . 176

Figure 6.18 Time series showing the monthly mean calculated $XCH_4$ at GOSAT sounding locations in 2011 for GOSAT (red), the NAME modelled $XCH_4$ (in blue), the calculated background $XCH_4$ (blue dashed), MACC-II (in cyan) and GEOS-Chem (in black). The results are averaged over the five regions in the Amazon. . . . . 178

Figure 6.19 Monthly averaged maps of the calculated $XCH_4$ enhancement due to Amazon emissions from the MACC-II model. Averaged and plotted on a $2^\circ \times 2^\circ$ resolution. . . . . 181

Figure 6.20 Time series showing the monthly averages of the $XCH_4$ enhancement for the NAME modelled output using GEOS-Chem emission inventories (in blue), and for the MACC-II calculated enhancement (in cyan). . . . . 181

# LIST OF TABLES


Table 4.1 Correlation results with varying degrees of filtering criteria for the extended aircraft profile $XCH_4$ vs same day averaged GOSAT $XCH_4$. Only criteria with at least 10 coincident GOSAT retrievals are shown. Offset is calculated as described in text. . . . . 107

Table 4.2 Correlation results with varying degrees of filtering for extended aircraft profile $XCO_2$ vs same day averaged model $XCO_2$ which is used in the University of Leicester Proxy methane retrieval (GEOS-Chem in this study). The aircraft profile $XCO_2$ is calculated in the same way as for the $XCH_4$ but instead using an ECMWF MACC $CO_2$ model for the stratosphere and a high resolution version for the extrapolated region error analysis. The offset is calculated as the intercept on the Model $XCO_2$ axis when a linear function of gradient 1 is fit to the data. . . . . 110

Table 5.1 Correlation results with varying degrees of filtering for the extended aircraft profile $XCH_4$ verses the same day averaged GEOS-Chem $XCH_4$ sampled at the same GOSAT locations. Only criteria with at least 10 coincident GOSAT retrievals are shown. . . . . 120

Table 6.1 The monthly averaged differences between, a. Either the NAME model, GEOS-Chem or MACC-II $XCH_4$ with GOSAT $XCH_4$, and b. Between the three models, GEOS-Chem minus NAME $XCH_4$, MACC-II minus NAME $XCH_4$, and GEOS-Chem minus MACC-II $XCH_4$. All as averages over the five pre-defined sub-regions, with values in ppb. 179

Table 6.2 The standard deviation of the monthly averaged differences between, a. Either the NAME model, GEOS-Chem or MACC-II $XCH_4$ with GOSAT $XCH_4$, and b. Between the three models, GEOS-Chem minus NAME $XCH_4$, MACC-II minus NAME $XCH_4$, and GEOS-Chem minus MACC-II $XCH_4$. All as averages over the five pre-defined sub-regions, with values in ppb. . . . . 180

# REFERENCES


Aben, I, O Hasekamp, and W Hartmann (2007). "Uncertainties in the space-based measurements of CO 2 columns due to scattering in the Earth's atmosphere". In: *Journal of Quantitative Spectroscopy and Radiative Transfer* 104.3, pp. 450–459.

Alexe, M. et al. (2015). "Inverse modelling of CH4 emissions for 2010-2011 using different satellite retrieval products from GOSAT and SCIAMACHY". In: *Atmospheric Chemistry and Physics* 15.1, pp. 113–133.

Aragão, Luiz E. O. C. et al. (2014). "Environmental change and the carbon balance of Amazonian forests". In: *Biol Rev* 89.4, pp. 913–931.

Archer, David, Bruce Buffett, and Victor Brovkin (2009). "Ocean methane hydrates as a slow tipping point in the global carbon cycle". In: *Proceedings of the National Academy of Sciences* 106.49, pp. 20596–20601.

Baker, David F et al. (2010). "Carbon source/sink information provided by column CO2 measurements from the Orbiting Carbon Observatory". In: *Atmos. Chem. Phys.* 10, pp. 4145–4165.

Barkley, Michael P, Udo Friess, and Paul S Monks (2006). "Measuring atmospheric CO 2 from space using Full Spectral Initiation (FSI) WFM-DOAS". In: *Atmospheric Chemistry and Physics* 6.11, pp. 3517–3534.

Barry, Roger Graham and Richard J Chorley (1992). *Atmosphere, weather, and climate*. CUP Archive.

Basso, Luana S. et al. (2016). "Seasonality and interannual variability of CH 4 fluxes from the eastern Amazon Basin inferred from atmospheric mole fraction profiles". In: *Journal of Geophysical Research: Atmospheres* 121.1, pp. 168–184.

Bastviken, David et al. (2011). "Freshwater methane emissions offset the continental carbon sink". In: *Science* 331.6013, pp. 50–50.

Basu, S et al. (2013). "Global CO 2 fluxes estimated from GOSAT retrievals of total column CO 2". In: *Atmospheric Chemistry and Physics* 13.17, pp. 8695–8717.

Berchet, A et al. (2015). "Atmospheric constraints on the methane emissions from the East Siberian Shelf". In: *Atmospheric Chemistry and Physics Discussions* 15.18, pp. 25477–25501.

Bergamaschi, P. et al. (2007). "Satellite chartography of atmospheric methane from SCIAMACHY on board ENVISAT: 2. Evaluation based on inverse model simulations". In: *J. Geophys. Res.* 112.D2.

Bergamaschi, P. et al. (2013). "Atmospheric CH 4 in the first decade of the 21st century: Inverse modeling analysis using SCIAMACHY satellite retrievals and NOAA surface measurements". In: *Journal of Geophysical Research: Atmospheres* 118.13, pp. 7350–7369.

Bergamaschi, Peter et al. (2009). "Inverse modeling of global and regional CH4 emissions using SCIAMACHY satellite retrievals". In: *J. Geophys. Res.* 114.D22.

Bey, Isabelle et al. (2001). "Global modeling of tropospheric chemistry with assimilated meteorology: Model description and evaluation". In: *Journal of Geophysical Research: Atmospheres* 106.D19, pp. 23073–23095.

Bloom, Anthony A. et al. (2010). "Large-scale controls of methanogenesis inferred from methane and gravity spaceborne data". In: *Science* 327.5963, pp. 322–325.

Bloom, Anthony A et al. (2012). "Seasonal variability of tropical wetland CH 4 emissions: the role of the methanogen-available carbon pool". In: *Biogeosciences* 9.8, pp. 2821–2830.

Bloom, Anthony A. et al. (2016). "A global wetland methane emissions and uncertainty dataset for atmospheric chemical transport models". In: *Geoscientific Model Development Discussions*, pp. 1–37.

Boesch, Hartmut et al. (2006). "Space-based near-infrared CO2 measurements: Testing the Orbiting Carbon Observatory retrieval algorithm and validation concept using SCIAMACHY observations over Park Falls, Wisconsin". In: *Journal of Geophysical Research: Atmospheres* 111.D23.

Boesch, Hartmut et al. (2011). "Global characterization of CO2 column retrievals from shortwave-infrared satellite observations of the Orbiting Carbon Observatory-2 mission". In: *Remote Sensing* 3.2, pp. 270–304.

Boucher, O et al. (2013). "Clouds and Aerosols". In: *Climate Change 2013: The Physical Science Basis. Contribution of Working Group I to the Fifth Assessment Report of the Intergovernmental Panel on Climate Change*. Cambridge University Press.

Buchwitz, Michael, Vladimir V Rozanov, and John P Burrows (2000). "A near-infrared optimized DOAS method for the fast global retrieval of atmospheric CH4, CO, CO2, H2O, and N2O total column amounts from SCIAMACHY Envisat-1 nadir radiances". In: *Journal of Geophysical Research: Atmospheres* 105.D12, pp. 15231–15245.

Buseck, PR and SE Schwartz (2003). "Tropospheric aerosols". In: *Treatise on geochemistry* 4, p. 347.

Butz, A et al. (2011). "Toward accurate CO2 and CH4 observations from GOSAT". In: *Geophysical Research Letters* 38.14.

Butz, A. et al. (2012). "TROPOMI aboard Sentinel-5 Precursor: Prospective performance of CH4 retrievals for aerosol and cirrus loaded atmospheres". In: *Remote Sensing of Environment* 120, pp. 267–276.

Chipperfield, M. P. (1999). "Multiannual simulations with a three-dimensional chemical transport model". In: *Journal of Geophysical Research: Atmospheres* 104.D1, pp. 1781–1805.

Christensen, T. R. et al. (1996). "Methane flux from northern wetlands and tundra. An ecosystem source modelling approach". In: *Tellus B* 48.5, pp. 652–661.

Ciais, Philippe et al. (2014). "Carbon and other biogeochemical cycles". In: *Climate Change 2013: The Physical Science Basis. Contribution of Working Group I to the Fifth Assessment Report of the Intergovernmental Panel on Climate Change*. Cambridge University Press, pp. 465–570.

Cicerone, Ralph J and Ronald S Oremland (1988). "Biogeochemical aspects of atmospheric methane". In: *Global biogeochemical cycles* 2.4, pp. 299–327.

Clark, D. B. et al. (2011). "The Joint UK Land Environment Simulator (JULES), model description – Part 2: Carbon fluxes and vegetation dynamics". In: *Geoscientific Model Development* 4.3, pp. 701–722.

Cogan, AJ et al. (2012). "Atmospheric carbon dioxide retrieved from the Greenhouse gases Observing SATellite (GOSAT): Comparison with ground-based TCCON observations and GEOS-Chem model calculations". In: *Journal of Geophysical Research: Atmospheres* 117.D21.

Cogan, Austin James (2013). "Atmospheric Carbon Dioxide Retrieved from the Greenhouse Gases Observing SATellite; Method, Comparisons and Algorithm Development". PhD thesis. University of Leicester.

Comiso, J C et al. (2011). "Variability and trends in sea ice extent and ice production in the Ross Sea". In: *J. Geophys. Res.* 116.C04021.

Connor, Brian J et al. (2008). "Orbiting Carbon Observatory: Inverse method and prospective error analysis". In: *Journal of Geophysical Research: Atmospheres* 113.D5.

Cook, John et al. (2016). "Consensus on consensus: a synthesis of consensus estimates on human-caused global warming". In: *Environmental Research Letters* 11.4, p. 048002.

Crisp, David et al. (2012). "The ACOS CO2 retrieval algorithm-Part II: Global XCO2 data characterization". In: *Atmospheric Measurement Techniques* 5.

Dai, Aiguo (2011). "Drought under global warming: a review". In: *Wiley Interdisciplinary Reviews: Climate Change* 2.1, pp. 45–65.

Deuzé, JL et al. (1999). "Characterization of aerosols over ocean from POLDER/ADEOS-1". In: *Geophysical Research Letters* 26.10, pp. 1421–1424.

Devenish, B.J. et al. (2012). "A study of the arrival over the United Kingdom in April 2010 of the Eyjafjallajökull ash cloud using ground-based lidar and numerical simulations". In: *Atmospheric Environment* 48, pp. 152–164.

Dils, B. et al. (2014). "The Greenhouse Gas Climate Change Initiative (GHG-CCI): comparative validation of GHG-CCI SCIAMACHY/ENVISAT and TANSO-FTS/GOSAT CO2 and CH4 retrieval algorithm products with measurements from the TCCON". In: *Atmos. Meas. Tech.* 7.6, pp. 1723–1744.

Dlugokencky, E. J. (2003). "Atmospheric methane levels off: Temporary pause or a new steady-state?" In: *Geophys. Res. Lett.* 30.19.

Dlugokencky, E. J. et al. (1994). "The growth rate and distribution of atmospheric methane". In: *J. Geophys. Res.* 99.D8, p. 17021.

Dlugokencky, Edward J et al. (2011). "Global atmospheric methane: budget, changes and dangers". In: *Philosophical Transactions of the Royal Society of London A: Mathematical, Physical and Engineering Sciences* 369.1943, pp. 2058–2072.

Draxler, R.R and G. D. Hess (1997). "Description of the HYSPLIT4 modeling system". In: *NOAA Tech. Memo. ERL ARL-224*, 24 pp.

Dubey, Manvedra et al. (2014). *Total Column Carbon Observing Network (TCCON) Site: Manaus*. Tech. rep. Total Carbon Column Observing Network (Carbon Dioxide Information Analysis Center, ORNL).

Etiope, Giuseppe and Ronald W Klusman (2002). "Geologic emissions of methane to the atmosphere". In: *Chemosphere* 49.8, pp. 777–789.

Etiope, Giuseppe et al. (2008). "Reappraisal of the fossil methane budget and related emission from geologic sources". In: *Geophysical Research Letters* 35.9.

Feng, L. et al. (2009). "Estimating surface CO2 fluxes from space-borne CO2 dry air mole fraction observations using an ensemble Kalman Filter". In: *Atmospheric Chemistry and Physics* 9.8, pp. 2619–2633.

Feng, L. et al. (2011). "Evaluating a 3-D transport model of atmospheric CO2 using ground-based, aircraft, and space-borne data". In: *Atmospheric Chemistry and Physics* 11.6, pp. 2789–2803.

Fiore, A. et al. (2003). "Variability in surface ozone background over the United States: Implications for air quality policy". In: *Journal of Geophysical Research: Atmospheres* 108.D24.

Frankenberg, C. et al. (2006). "Satellite chartography of atmospheric methane from SCIAMACHY on board ENVISAT: Analysis of the years 2003 and 2004". In: *J. Geophys. Res.* 111.D7.

Fraser, A. et al. (2013). "Estimating regional methane surface fluxes: the relative importance of surface and GOSAT mole fraction measurements". In: *Atmospheric Chemistry and Physics* 13.11, pp. 5697–5713.

Fraser, A. et al. (2014). "Estimating regional fluxes of CO2 and CH4 using space-borne observations of XCH4: XCO2". In: *Atmospheric Chemistry and Physics* 14.23, pp. 12883–12895.

Fung, I et al. (1991). "Three-dimensional model synthesis of the global methane cycle". In: *Journal of Geophysical Research: Atmospheres* 96.D7, pp. 13033–13065.

Gatti, L. V. et al. (2014). "Drought sensitivity of Amazonian carbon balance revealed by atmospheric measurements". In: *Nature* 506.7486, pp. 76–80.

Gavin, Henri (2011). "The Levenberg-Marquardt method for nonlinear least squares curve-fitting problems". In: *Department of Civil and Environmental Engineering, Duke University*, pp. 1–15.

Gloor, M et al. (2012). "The carbon balance of South America: a review of the status, decadal trends and main determinants". In: *Biogeosciences* 9.12, pp. 5407–5430.

Gloster, J et al. (2007). "Assessing the risk of windborne spread of bluetongue in the 2006 outbreak of disease in northern Europe". In: *The Veterinary Record* 160(2).54.

Guliyev I, S and A Feizullayev A (1997). *All About Mud Volcanoes*. page 120. Baku Institute of Geology of the Azerbaijan National Academy of Sciences.

Hess, Laura L et al. (2015). "Wetlands of the lowland Amazon basin: Extent, vegetative cover, and dual-season inundated area as mapped with JERS-1 Synthetic Aperture Radar". In: *Wetlands* 35.4, pp. 745–756.

Heymann, J et al. (2012). "SCIAMACHY WFM-DOAS XCO 2: reduction of scattering related errors". In: *Atmospheric Measurement Techniques* 5.10, pp. 2375–2390.

Houweling, Sander et al. (1999). "Inverse modeling of methane sources and sinks using the adjoint of a global transport model". In: *Journal of Geophysical Research: Atmospheres* 104.D21, pp. 26137–26160.

Inoue, M. et al. (2014). "Validation of XCH4 derived from SWIR spectra of GOSAT TANSO-FTS with aircraft measurement data". In: *Atmos. Meas. Tech.* 7.9, pp. 2987–3005.

Inoue, Makoto et al. (2016). “Bias corrections of GOSAT SWIR XCO2 and XCH4 with TCCON data and their evaluation using aircraft measurement data”. In: *Atmos. Meas. Tech.* 9.8, pp. 3491–3512.

Jackson, R B et al. (2014). “Natural gas pipeline leaks across Washington, DC”. In: *Environmental science and technology* 48.3, pp. 2051–2058.

Japan Aerospace Exploration Agency, JAXA (2009). *Greenhouse Gases Observing Satellite "IBUKI" (GOSAT) "First Light" Acquired by Onboard Sensors*. Press Release.

Jones, A. R et al. (2007). “The U.K. Met Office’s next-generation atmospheric dispersion model, NAME III”. In: *Borrego C. and Norman A.-L. (Eds) Air Pollution Modeling and its Application XVII (Proceedings of the 27th NATO/CCMS International Technical Meeting on Air Pollution Modelling and its Application)* 62. Ed. by Carlos Borrego and Ann-Lise Norman, pp. 580–589.

Jones, Andrew (2015). *User Guide for NAME: MD15/8(version 2.0)*. Met Office.

Kalney, E et al. (1996). “The NCEP/NCAR 40-Year Reanalysis Project”. In: *Bull. Amer. Meteor. Soc.* 77, pp. 437–471.

Kaplan, Jed O. (2002). “Wetlands at the Last Glacial Maximum: Distribution and methane emissions”. In: *Geophys. Res. Lett.* 29.6, pp. 3–1–3–4.

Keesee, Bob (2014). *The Upper Atmosphere A ATM 101*. University at Albany Upton Campus. www.albany.edu/faculty/rgk/atm101/structur.htm.

Keppler, Frank et al. (2006). “Methane emissions from terrestrial plants under aerobic conditions”. In: *Nature* 439.7073, pp. 187–191.

Kirschke, Stefanie et al. (2013). “Three decades of global methane sources and sinks”. In: *Nature Geoscience* 6.10, pp. 813–823.

Kort, Eric A et al. (2014). “Four corners: The largest US methane anomaly viewed from space”. In: *Geophysical Research Letters* 41.19, pp. 6898–6903.

Kuze, Akihiko et al. (2009). “Thermal and near infrared sensor for carbon observation Fourier-transform spectrometer on the Greenhouse Gases Observing Satellite for greenhouse gases monitoring”. In: *Appl. Opt.* 48.35, p. 6716.

Kuze, Akihiko et al. (2016). “Update on GOSAT TANSO-FTS performance, operations, and data products after more than 6 years in space”. In: *Atmos. Meas. Tech.* 9.6, pp. 2445–2461.

Lambert, Gérard and Sabine Schmidt (1993). "Reevaluation of the oceanic flux of methane: Uncertainties and long term variations". In: *Chemosphere* 26.1-4, pp. 579–589.

Le Mer, Jean and Pierre Roger (2001). "Production, oxidation, emission and consumption of methane by soils: A review". In: *European Journal of Soil Biology* 37.1, pp. 25–50.

Manning, A. J. (2003). "Estimating European emissions of ozone-depleting and greenhouse gases using observations and a modeling back-attribution technique". In: *J. Geophys. Res.* 108.D14.

Manning, A. J. et al. (2011). "Estimating UK methane and nitrous oxide emissions from 1990 to 2007 using an inversion modeling approach". In: *J. Geophys. Res.* 116.D2.

Mazière, M. De et al. (2008). "Validation of ACE-FTS v2.2 methane profiles from the upper troposphere to the lower mesosphere". In: *Atmospheric Chemistry and Physics* 8.9, pp. 2421–2435.

McKay, N P, J T Overpeck, and B L Otto-Bliesner (2011). "The role of ocean thermal expansion in Last Interglacial sea level rise". In: *Geophys. Res. Lett.* 38.L14605.

McMichael, Anthony J (2013). "Globalization, climate change, and human health". In: *New England Journal of Medicine* 368.14, pp. 1335–1343.

Melack, John M et al. (2004). "Regionalization of methane emissions in the Amazon Basin with microwave remote sensing". In: *Global Change Biology* 10.5, pp. 530–544.

Melton, J. R. et al. (2013). "Present state of global wetland extent and wetland methane modelling: conclusions from a model inter-comparison project (WETCHIMP)". In: *Biogeosciences* 10.2, pp. 753–788.

Miller, John B. et al. (2007). "Airborne measurements indicate large methane emissions from the eastern Amazon basin". In: *Geophys. Res. Lett.* 34.10.

Miller, S. M. et al. (2013). "Anthropogenic emissions of methane in the United States". In: *Proceedings of the National Academy of Sciences* 110.50, pp. 20018–20022.

Miyamoto, Y. et al. (2013). "Atmospheric column-averaged mole fractions of carbon dioxide at 53 aircraft measurement sites". In: *Atmospheric Chemistry and Physics* 13.10, pp. 5265–5275.

Mumford, Jonathan Reid (2000). "Atmospheric horizontal uniformity measured by a steerable laser system at the High Resolution Fly's Eye". PhD thesis. The University of Utah.

NIES (2009). *Thermal And Near infrared Sensor for carbon Observation (TANSO) On board the Greenhouse gases Observing SATellite (GOSAT). Appendix A.* Tech. rep. NIES.

Nisbet, Euan G, Edward J Dlugokencky, and Philippe Bousquet (2014). "Methane on the rise–again". In: *Science* 343.6170, pp. 493–495.

Nisbet, RER et al. (2009). "Emission of methane from plants". In: *Proceedings of the Royal Society of London B: Biological Sciences* 276.1660, pp. 1347–1354.

O'Connor, Fiona M et al. (2010). "Possible role of wetlands, permafrost, and methane hydrates in the methane cycle under future climate change: A review". In: *Reviews of Geophysics* 48.4.

O'Dell, C. W. et al. (2012). "The ACOS CO2 retrieval algorithm – Part 1: Description and validation against synthetic observations". In: *Atmos. Meas. Tech.* 5.1, pp. 99–121.

Oshchepkov, Sergey et al. (2012). "Effects of atmospheric light scattering on spectroscopic observations of greenhouse gases from space: Validation of PPDF-based CO2 retrievals from GOSAT". In: *Journal of Geophysical Research: Atmospheres* 117.D12.

Pandey, S. et al. (2015). "On the use of satellite-derived CH4 : CO2 columns in a joint inversion of CH4 and CO2 fluxes". In: *Atmospheric Chemistry and Physics* 15.15, pp. 8615–8629.

Pandey, Sudhanshu et al. (2016). "Inverse modeling of GOSAT-retrieved ratios of total column CH4 and CO2 for 2009 and 2010". In: *Atmospheric Chemistry and Physics* 16.8, pp. 5043–5062.

Pangala, Sunitha R et al. (2015). "The contribution of trees to ecosystem methane emissions in a temperate forested wetland". In: *Global change biology* 21.7, pp. 2642–2654.

Parker, Robert (2015). *Product User Guide v3 for the University of Leicester Proxy XCH4 GOSAT Data Product*. Tech. rep. University of Leicester.

Parker, Robert et al. (2011). "Methane observations from the Greenhouse Gases Observing SATellite: Comparison to ground-based TCCON data and model calculations". In: *Geophysical Research Letters* 38.15.

Parker, Robert et al. (2015). "Assessing 5 years of GOSAT Proxy XCH4 data and associated uncertainties". In: *Atmos. Meas. Tech.*

Parker, Robert J. et al. (2016). "Atmospheric CH4 and CO2 enhancements and biomass burning emission ratios derived from satellite observations of the 2015 Indonesian fire plumes". In: *Atmospheric Chemistry and Physics Discussions*, pp. 1–33.

Peters, Glen P et al. (2013). "The challenge to keep global warming below 2 C". In: *Nature Climate Change* 3.1, pp. 4–6.

Pollard, David, Robert M DeConto, and Richard B Alley (2015). "Potential Antarctic Ice Sheet retreat driven by hydrofracturing and ice cliff failure". In: *Earth and Planetary Science Letters* 412, pp. 112–121.

Prather, Michael J. (1986). "Numerical advection by conservation of second-order moments". In: *J. Geophys. Res.* 91.D6, p. 6671.

Rayner, PJ and DM O'Brien (2001). "The utility of remotely sensed CO2 concentration data in surface source inversions". In: *Geophys. Res. Lett.* 28.1, pp. 175–178.

Reichler, Thomas, Martin Dameris, and Robert Sausen (2003). "Determining the tropopause height from gridded data". In: *Geophys. Res. Lett.* 30.20.

Reuter, M et al. (2010). "A method for improved SCIAMACHY CO 2 retrieval in the presence of optically thin clouds". In: *Atmospheric Measurement Techniques* 3.1, pp. 209–232.

Reuter, M et al. (2011). "Retrieval of atmospheric CO2 with enhanced accuracy and precision from SCIAMACHY: Validation with FTS measurements and comparison with model results". In: *Journal of Geophysical Research: Atmospheres* 116.D4.

Reuter, M et al. (2013). "A joint effort to deliver satellite retrieved atmospheric CO 2 concentrations for surface flux inversions: the ensemble median algorithm EMMA". In: *Atmospheric Chemistry and Physics* 13.4, pp. 1771–1780.

Ridgwell, Andy J., Stewart J. Marshall, and Keith Gregson (1999). "Consumption of atmospheric methane by soils: A process-based model". In: *Global Biogeochem. Cycles* 13.1, pp. 59–70.

Rigby, M. et al. (2008). "Renewed growth of atmospheric methane". In: *Geophys. Res. Lett.* 35.22.

Rockström, Johan et al. (2009). "Future water availability for global food production: the potential of green water for increasing resilience to global change". In: *Water Resources Research* 45.7.

Rodgers, Clive D (2000). *Inverse methods for atmospheric sounding: theory and practice*. Vol. 2. World scientific.

Ross, Adrian N. et al. (2013). "First satellite measurements of carbon dioxide and methane emission ratios in wildfire plumes". In: *Geophys. Res. Lett.* 40.15, pp. 4098–4102.

Sanderson, MG (1996). "Biomass of termites and their emissions of methane and carbon dioxide: A global database". In: *Global Biogeochemical Cycles* 10, pp. 543–558.

Sawadogo, JB, AS Traoré, and D Dianou (2012). "Seasonal CO and CH Emissions from Termite Mounds in the Sub-Sahelian Area of Burkina Faso". In: *Botany Research International* 5.3, pp. 49–56.

Schaeffer, Michiel et al. (2012). "Long-term sea-level rise implied by 1.5∘C and 2∘C warming levels". In: *Nature Climate Change* 2.12, pp. 867–870.

Schepers, D et al. (2012). "Methane retrievals from Greenhouse Gases Observing Satellite (GOSAT) shortwave infrared measurements: Performance comparison of proxy and physics retrieval algorithms". In: *Journal of Geophysical Research: Atmospheres* 117.D10.

Schneising, O et al. (2012). "Atmospheric greenhouse gases retrieved from SCIAMACHY: comparison to ground-based FTS measurements and model results". In: *Atmospheric Chemistry and Physics* 12.3, pp. 1527–1540.

Schneising, Oliver et al. (2014). "Remote sensing of fugitive methane emissions from oil and gas production in North American tight geologic formations". In: *Earth's Future* 2.10, pp. 548–558.

Schuckmann, K von et al. (2016). "An imperative to monitor Earth's energy imbalance". In: *Nature Climate Change* 6, pp. 138–144.

Schulz, Michael et al. (2006). "Radiative forcing by aerosols as derived from the AeroCom present-day and pre-industrial simulations". In: *Atmospheric Chemistry and Physics* 6.12, pp. 5225–5246.

Sitch, S. et al. (2003). "Evaluation of ecosystem dynamics, plant geography and terrestrial carbon cycling in the LPJ dynamic global vegetation model". In: *Global Change Biol* 9.2, pp. 161–185.

Smith, Felisa A et al. (2015). "The importance of considering animal body mass in IPCC greenhouse inventories and the underappreciated role of wild herbivores". In: *Global change biology* 21.10, pp. 3880–3888.

Stocker, TF et al. (2013). *IPCC, 2013: summary for policymakers in climate change 2013: the physical science basis, contribution of working group I to the fifth assessment report of the intergovernmental panel on climate change*.

Swick, C. H. (1942). "Pendulum Gravity Measurements and Isostatic Reductions". In: *U. S. Coast and Geodetic Survey special publication* 232, pp. 61–65.

Taylor, Thomas E et al. (2012). "Comparison of cloud-screening methods applied to GOSAT near-infrared spectra". In: *Geoscience and Remote Sensing, IEEE Transactions on* 50.1, pp. 295–309.

Thornton, Philip K et al. (2014). "Climate variability and vulnerability to climate change: a review". In: *Global change biology* 20.11, pp. 3313–3328.

Van Aardenne J, A et al. (2005). "The EDGAR 3.2 Fast track 2000 dataset (32FT2000)". In: *Emission Database for Global Atmospheric Research: Description of* 32.

Verma, S et al. (2017). "Extending methane profiles from aircraft into the stratosphere for satellite total column validation using the ECMWF C-IFS and TOMCAT/SLIMCAT 3-D model". In: *Atmos. Chem. Phys.* 17, pp. 6663–6678.

Wang, James S. et al. (2004). “A 3-D model analysis of the slowdown and interannual variability in the methane growth rate from 1988 to 1997”. In: *Global Biogeochem. Cycles* 18.3.

Warneke, T. et al. (2010). “Co-located column and in situ measurements of CO2 in the tropics compared with model simulations”. In: *Atmospheric Chemistry and Physics* 10.12, pp. 5593–5599.

Webb, Alex J. et al. (2016). “$CH_4$ concentrations over the Amazon from GOSAT consistent with in situ vertical profile data”. In: *Journal of Geophysical Research: Atmospheres* 121.

Werf, G. R. van der et al. (2010). “Global fire emissions and the contribution of deforestation, savanna, forest, agricultural, and peat fires (1997–2009)”. In: *Atmospheric Chemistry and Physics* 10.23, pp. 11707–11735.

Wilson, Chris et al. (2016). “Contribution of regional sources to atmospheric methane over the Amazon Basin in 2010 and 2011”. In: *Global Biogeochem. Cycles* 30.3, pp. 400–420.

Worden, John et al. (2013). “El Niño, the 2006 Indonesian peat fires, and the distribution of atmospheric methane”. In: *Geophysical Research Letters* 40.18, pp. 4938–4943.

Wunch, D. et al. (2010). “Calibration of the Total Carbon Column Observing Network using aircraft profile data”. In: *Atmos. Meas. Tech.* 3.5, pp. 1351–1362.

Wunch, Debra et al. (2011). “The total carbon column observing network”. In: *Philosophical Transactions of the Royal Society of London A: Mathematical, Physical and Engineering Sciences* 369.1943, pp. 2087–2112.

Yevich, Rosemarie and Jennifer A. Logan (2003). “An assessment of biofuel use and burning of agricultural waste in the developing world”. In: *Global Biogeochem. Cycles* 17.4.

Yokota, T et al. (2009). “Global concentrations of CO2 and CH4 retrieved from GOSAT: First preliminary results”. In: *Sola* 5, pp. 160–163.

Yoshida, Y et al. (2011). “Retrieval algorithm for CO 2 and CH 4 column abundances from short-wavelength infrared spectral observations by the Greenhouse gases observing satellite”. In: *Atmospheric Measurement Techniques* 4, pp. 717–734.